IMAGING OF THE WATER VELOCITY DISTRIBUTION IN WATER CONTINOUS MULTIPHASE FLOWS USING INDUCTIVE FLOW TOMOGRAPHY(IFT)

YIQING MENG

BEng,MSc

A thesis submitted to the University of Huddersfield in partial fulfilment of the requirements for the degree of Doctor of Philosophy

The University of Huddersfield

January 2016

Copyright statement

The following notes on copyright and the ownership of intellectual property rights must be

included as written below:

i. The author of this thesis (including any appendices and/or schedules to this thesis) owns any copyright in it (the "Copyright") and s/he has given The University of Huddersfield the right to use such Copyright for any administrative, promotional, educational and/or teaching purposes.

ii. Copies of this thesis, either in full or in extracts, may be made only in accordance with the regulations of the University Library. Details of these regulations may be obtained from the Librarian. This page must form part of any such copies made.

iii. The ownership of any patents, designs, trademarks and any and all other intellectual property rights except for the Copyright (the "Intellectual Property Rights") and any reproductions of copyright works, for example graphs and tables ("Reproductions"), which may be described in this thesis, may not be owned by the author and may be owned by third parties. Such Intellectual Property Rights and Reproductions cannot and must not be made available for use without the prior written permission of the owner(s) of the relevant Intellectual Property Rights and/or Reproductions.

Declaration

No portion of the work referred to in this thesis has been submitted to support an application for another degree or qualification at this or any other university or other institute of learning.

Acknowledgment

My deepest gratitude goes first and foremost to Professor Lucas, my supervisor, for giving me the opportunity to carry out this research. I would also like to thank for his continuing support and guidance during my PhD. Without his help, this thesis would not be finished.

Secondly, I would like to express my heartfelt gratitude to the technicians at the University of Huddersfield for their assistance in repairing, manufacturing different experimental apparatus that I have needed. Additionaly, I would like to thank the researcher at University of Cambridge, Dr Bartlett and Dr Sederman, for providing MRI data and experimental facilities. I would also like to acknowledge the members of Schlumberger Gould Research (SGR) Centre for their considerable assistance in providing reference measurement and setting up of apparatus at SGR, in particular, Dr Oddie and Dr Xie.

I would like to extend my thanks to my colleagues in the Systems Engineering Research Group at University of Huddersfield for their support during this research. Several researchers were especially helpful to me: Dr Kollar Laszlo, Dr Zhang Zhichao, Dr Teerachai Leeuncgulsatien, Dr Muhamedsalih.Yousif, Dr Abdurazzaq Mussbah.

Last, but not least, I would like to thank my parents and my wife for their endless love and support during these years. Without them, I would never reach my goal.

Abstract

In the oil-gas fields, slurry flows, gas-in-water two phase flows, and oil-gas-water three phase flows are frequently encountered. Generally, the measurement of volumetric flow rate for each phase is of most interest, especially in subsea oil-gas production applications, where it is essential to obtain oil, water and gas flow rates in inclined oil wells. The problem of how to accurately measure these flow parameters for such complicated flow phenomena, without using expensive and large test separators, is a major challenge for the industry.

Most conventional multiphase flow meters have severe limitations regarding types of flow and their measurement reliability. Some useful techniques containing radioactive sources are available but they are expensive and potentially harmful to humans. Thus, many academic and industrial researchers are working to develop a multiphase flow meter based on tomographic techniques that does not contain a radioactive source. Such a device would normally involve at least two independent flow metering techniques.

Tomographic techniques have been successfully used in multiphase flows to determine the local volume fraction distributions of the various phases; however, only a very small number of results can be found in the published literature concerning the equally significant problem of local velocity distribution. Therefore, the aim of this research is to develop a non-intrusive flow measurement technique, without the use of radioactive sources, for measuring the local axial velocity distribution of the electrically conducting continuous phase in multiphase flows.

This thesis reports the development of a multi-electrode electromagnetic flow metering technique, the so-called Inductive Flow Tomography (IFT), for obtaining the local flow velocity distributions of the electrically conducting continuous phase in multiphase flows, with particular relevance to gas-in-water two phase and oil-gas-water three phase flows.

Previous research has indicated that the electromagnetic flow meter (i.e. Electromagnetic Velocity Profiler) is a promising technique for measuring the local axial water velocity in single phase and solid-in-water two phase flow. However, that technique has several limitations, which means it is valid only for determining water velocity profiles in seven regimes of the pipe cross-section. A novel multi-electrodes electromagnetic IFT flow metering system has been developed

in the research described in this thesis, which is capable of determining the local conducting continuous phase velocity at any position in the flow cross-section (in vertical and inclined pipes). The theoretical work carried out in developing the IFT system includes a completely novel flow velocity distribution "image reconstruction algorithm", which is described in the thesis. This thesis also describes the design and subsequent implementation of the hardware and software for the IFT system.

In the final sections of this thesis, a series of experiments, which include inclined gas-oil-water three phase flow and gas-in-water two phase flow, were performed to investigate the performance of the IFT system. The experimental results obtained show a good agreement between the reference measurements and velocity measurements obtained using the IFT system.

Table of contents

COPYRIGHT STATEMENT **1**

DECLARATION **2**

ACKNOWLEDGMENT **3**

ABSTRACT **4**

TABLE OF CONTENTS **6**

TABLE OF FIGURES **11**

LIST OF TABLES **21**

NOMENCLATURE **23**

1 INTRODUCTION **34**

1.1 INTRODUCTION 34

1.2 SIGNIFICANCE OF MULTIPHASE FLOW MEASUREMENT AND DEVELOPMENT OF MPFMS 35

1.2.1 Multiphase flow regime 36

1.2.2 Test separator-based measurement system and its limitations 42

1.3 OVERVIEW OF CONVENTIONAL MPFM TECHNIQUES 45

1.3.1 Measurement strategies of conventional MPFMs 45

1.3.2 Limitations of conventional MPFMs and Process Tomography (PT) techniques 49

1.4 AIM AND OBJECTIVES OF THE PRESENT STUDY 53

2 LITERATURE REVIEW **54**

2.1 INTRODUCTION 54

2.2 PREVIOUS RELEVANT RESEARCH ON MULTIPHASE FLOW MEASUREMENT 55

2.2.1 Mean volume fraction and velocity measurement for dispersed phase using impedance techniques 55

2.2.2 Local volume fraction and velocity measurement for the dispersed phase using impedance techniques 59

2.2.3 Local volume fraction and velocity distribution measurement using tomography 60

2.3 TECHNIQUES FOR MEASURING THE VELOCITY PROFILE OF THE CONDUCTING CONTINUOUS PHASE IN MULTIPHASE FLOWS 69
2.3.1 Conventional optical techniques 69
2.3.2 Magnetic resonance imaging 70
2.3.3 Electromagnetic velocity profiler 73
2.4 SUMMARY 81
2.5 THESIS OUTLINE 81
3 BACKGROUND THEORY FOR INDUCTIVE FLOW TOMOGRAPHY 83
3.1 INTRODUCTION 83
3.2 THE THEORETICAL BACKGROUND OF AN ELECTROMAGNETIC FLOW METER 84
3.2.1 Fundamental theory of electromagnetic flow meters 84
3.2.2 Two dimensional analysis of an electromagnetic flow meter 86
3.3 ELECTROMAGNETIC FLOW METER WITH ANTI-HELMHOLTZ COIL CONFIGURATION 89
3.4 NUMERICAL MODELLING OF AN INDUCTIVE FLOW TOMOGRAPHY SYSTEM 93
3.4.1 Software platform for numerical modelling 93
3.4.2 Geometrical design for numerical simulation 94
3.4.3 Defining the physical boundary conditions and specifying object properties 96
3.4.4 Meshing the model 97
3.5 DETERMINING AXISYMMETRIC 'POWER LAW' VELOCITY PROFILES USING IFT 100
3.5.1 Power law velocity profile 100
3.5.2 Influence of axisymmetric velocity profile on electrical potential distribution 101
3.5.3 Evaluation of the power-law exponent q 112
3.6 VELOCITY PROFILE RECONSTRUCTION ALGORITHM FOR NON-AXISYMMETRIC FLOW VELOCITY PROFILE 117
3.6.1 Study of the relationship between boundary potential distribution and a polynomial velocity profile 118
3.6.1.1 Determining coefficient of n^{th} order velocity profile 121
3.6.1.2 Determination of angle of direction of velocity profile 127
3.7 EXTENDING THE RECONSTRUCTION ALGORITHM TO INCLUDE AXISYMMETRIC VELOCITY COMPONENTS 136
3.7.1 Applying an axisymmetric velocity component into a polynomial velocity profile 137
3.7.2 Study of the effects of polynomial velocity components on DFT component $\mathrm{Im}\hat{X}_2$ 140
3.8 SUMMARY 146

4 IMPLEMENTATION OF THE VELOCITY PROFILE RECONSTRUCTION ALGORITHMS 147

4.1 INTRODUCTION 147
4.2 DETERMINING AN OPTIMUM VELOCITY PROFILE SOLUTION 148
4.3 APPLICATION OF THE VELOCITY PROFILE RECONSTRUCTION ALGORITHM 151
4.3.1 Simulation velocity profile 151
4.3.2 Software prototype of velocity reconstruction procedure in MATLAB 154
4.3.3 Reconstruction results for simulation velocity profiles 169
4.4 SUMMARY 174

5 EXPERIMENTAL APPARATUS 176

5.1 INTRODUCTION 176
5.2 THE INDUCTIVE FLOW TOMOGRAPHY FLOW METER 176
5.2.1 The IFT flow conduit design 178
5.2.2 Excitation coil specifications 179
5.2.3 The electrode array 183
5.3 THE ELECTRONIC SYSTEMS FOR IFT 184
5.3.1 Coil excitation 185
5.3.2 Coil excitation control circuitry 188
5.3.3 Potential difference measurement circuitry 197
5.4 SUMMARY 204

6 IFT SYSTEM CONTROL AND SIGNAL PROCESSING 206

6.1 INTRODUCTION 206
6.2 SIGNAL ACQUISITION AND CONTROL SOFTWARE DESIGN 206
6.2.1 Parallel processing of signal acquisition and data storage based on a graphical program 207
6.2.2 Coil excitation signal control program 209
6.3 PROCEDURES FOR PROCESSING THE MEASURED IFT DATA 214
6.4 SUMMARY 222

7 EXPERIMENTAL TESTS OF IFT AND ANALYSIS OF RESULTS 223

7.1 INTRODUCTION 223
7.2 MULTIPHASE FLOW LOOP FACILITY 224
7.2.1 Multiphase flow loop in the Schlumberger Gould Research (SGR) Centre 224

7.2.2 Vertical two phase flow loop in the Magnetic Resonance Research Centre (MRRC) of the University of Cambridge 228
7.3 REFERENCE FLOW MEASUREMENT TECHNIQUES USED IN THE PRESENT EXPERIMENTAL INVESTIGATION 230
7.3.1 Differential pressure technique 230
7.3.2 Electrical resistance tomography 233
7.3.3 Magnetic resonance imaging technique 235
7.4 CORRECTION OF ELECTRICAL POTENTIALS MEASUREMENT Φ_J 236
7.4.1 Procedure for correction of electrical potential 239
7.5 TESTING THE PERFORMANCE OF THE IFT SYSTEM IN INCLINED AND VERTICAL FLOWS 248
7.5.1 Reference measurement parameters and experimental flow conditions 248
7.5.2 Reconstructed local water velocity distribution for non-vertical oil-gas-water three phase flows using IFT 250
7.5.2.1 Reconstructed local water velocity distribution by using the reconstruction algorithm without the use of an axisymmetric velocity component 252
7.5.2.2 Reconstructed local water velocity distribution using reconstruction algorithm with use of an axisymmetric velocity component 263
7.5.2.3 Comparison of experimental results for both reconstruction algorithms with reference measurement in oil-gas-water three phase flows 267
7.5.3 Reconstructed local water velocity distribution for vertical multiphase flow (oil-in-water two phase and oil-gas-water three phase) and water only single phase flow using IFT 269
7.5.3.1 Reconstructed velocity profiles for water only single phase flow 271
7.5.3.2 Reconstructed velocity profiles for oil-in-water two phase flow and oil-gas-water three phase flow in a vertical pipe. 279
7.5.4 Discussion of selection of the original and the improved velocity profile reconstruction algorithms 288
7.6 COMPARING THE PERFORMANCE OF IFT AGAINST MRI IN VERTICAL GAS-IN-WATER TWO PHASE FLOWS 292
7.6.1 Reference measurement parameters and experimental flow conditions 292
7.6.2 Reconstructed local water velocity distribution for vertical gas-in-water two phase flows using the IFT system 294
7.6.2.1 Comparison of the local water velocity distributions obtained by IFT and MRI 305
7.6.2.2 Comparison of averaged velocity results obtained by MRI and IFT with reference measurements 306
7.7 SUMMARY 310

8 CONCLUSIONS AND SUGGESTIONS FOR FUTURE WORK 313

8.1 INTRODUCTION 313

8.2 CONCLUSIONS 313

8.3 CONTRIBUTION TO KNOWLEDGE 318

8.4 FUTURE WORK 319

9 REFERENCES 322

APPENDIX A 329

APPENDIX B 345

Table of Figures

Fig. 1-1 Flow regime classification map of oil-water flow [4]. 35
Fig. 1-2 Flow regimes in vertical gas-liquid flows 38
Fig. 1-3 Flow regimes in inclined and horizontal gas-liquid flow [9] 39
Fig. 1-4 The flow regime map for deviation angle of 89 degree, 90 degree and 91 degree to vertical. Note that : DB is dispersed bubble flow, SW is wavy stratified flow, SS is stratified flow, A is annular flow, PL is plug flow and SL is slug flow[10] 39
Fig. 1-5 Flow regime map for liquid-liquid(oil-water) flows in vertical pipe [12] 40
Fig. 1-6 Solids-liquid flow in inclined pipe[13] 42
Fig. 1-7 Schematic diagram of the multiphase flow measurement system (a) traditional test separator-based measurement system; (b) inline MPFMs system [3] 44
Fig. 1-8 Schematic diagram of compact separator MPFM[27] 46
Fig. 1-9 Structure of Schlumberger Vx MPFM[33] 49
Fig. 1-10 Effect of flow regimes on solids volume fraction measurement using a common capacitance sensor (a) Stratified flow regime, (b)Annular flow regime [37] 50
Fig. 1-11 A multiphase flow meter based on PT technique 51
Fig. 2-1 Configuration of half-ring electrode for impedance measurement technique [46] 56
Fig. 2-2 Conductance measurement circuit[13] 56
Fig. 2-3 The six-electrodes probe conductance measurement circuit[14] 60
Fig. 2-4 Six-electrode conductivity probe as designed by Lucas and Cory [14] 60
Fig. 2-5 Electrical Resistance Tomography (a) Adjacent pair strategy, (b) Opposite pair strategy 62
Fig. 2-6 Schematic diagram of dual-plane ERT system 65
Fig. 2-7 Schematic diagram of local dispersed phase velocity distribution measurement based on pixel-pixel cross-correlation. 66
Fig. 2-8 Location of CoA for Configurations I, II and III for each of the eight electrode configurations [13, 47] 68
Fig. 2-9 A bipolar gradient pulse sequence with pulses of length δ, amplitude ±G and cycle time Δ [78] 72
Fig. 2-10 Transformer signal when a single particle passed through the meter [82] 77

Fig. 2-11 Geometry of EVP device [83] 80
Fig. 2-12 Pixel arrangement and electrodes arrangement for EVP [65, 83, 85] 80
Fig. 3-1 Conventional electromagnetic flow meter with circular pipe and two point electrodes[88] 86
Fig. 3-2 Contours of the weight function 89
Fig. 3-3 Coordinates and variables describing two circular loop used to express magnetic field 91
Fig. 3-4 Magnetic flux density distributions of anti-Helmholtz magnetic field in the *x*-*y*-plane (a) By component(unit: tesla), (b) Bx component (unit: tesla) and (c) vector plot of magnetic field 92
Fig. 3-5 Geometry of IFT device in x-y plane 95
Fig. 3-6 Geometrical model used for simulation and relevant coordinate system (a) view on x-y plane (b) 3D view 95
Fig. 3-7 Magnetic flux density in a uniform magnetic field (unit: Tesla) 96
Fig. 3-8 A plot of magnetic flux density B_y profile for different mesh elements (a) B_y along *y*-axis of pipe, (b) B_y along *x*-axis of pipe 98
Fig. 3-9 Pipe mesh elements with different mesh geometry setting. 99
Fig. 3-10 The magnetic flux density B_y profile for the model with the same size element (total mesh number is 32851) and the model with optimum mesh (total mesh number is 32050). (a) B_y along y-axis of pipe, (b) B_y along x-axis of pipe 99
Fig. 3-11 Power law velocity profiles with different values of the exponent *q* 101
Fig. 3-12 Three axisymmetric velocity profiles (a) Profile 1: Velocity profile uniform across the whole pipe cross-section (q = 0), (b) Profile 2: Velocity profile for q=1, and (c) Profile 3: Velocity profile for q=5 103
Fig. 3-13 Electrical potential distribution for three velocity profiles in uniform magnetic field (a) Profile 1, q = 0, (b) Profile 2, q = 1, (c) Profile 3, q = 5 and (d) the 16 electrode positions on the pipe cross-section 105
Fig. 3-14 Comparison of the boundary potential difference distribution U_j for profiles 1 ,2 and 3 106
Fig. 3-15 Electrical potential distribution of three velocity profiles in a non-uniform magnetic field produced by an anti-Helmholtz coil (a) Profile 1, q = 0, (b) Profile 2, q = 1, (c) Profile 3, q = 5 and (d) the 16 electrode positions on the pipe cross-section 109
Fig. 3-16 Comparison of the boundary potential difference U_j for profiles 1, 2 and 3 110

Fig. 3-17 Electrical potential difference U_3 associated with exponent q (a) the mean velocity $\bar{v}_z$ =5m/s, and (b) the mean velocity $\bar{v}_z$ =0.5m/s 111

Fig. 3-18 A_q versus q curve with different mean velocity $\bar{v}_z$ =0.5 and 5 m/s 113

Fig. 3-19 Third and sixth order polynomials fitted to data points for exponent q plotted as a function of A_q 115

Fig. 3-20 The geometry of IFT device in the x-y plane 118

Fig. 3-21 Definition of the direction angle $\theta_{Q,n}$ [96] 121

Fig. 3-22 Relationship between $\theta_{Q,1}$ and ψ_2 for linear velocity profile 129

Fig. 3-23 Relationship between $\theta_{Q,2}$ and ψ_3 for quadratic velocity profile 132

Fig. 3-24 Relationship between $\theta_{Q,3}$ and ψ_4 for cubic velocity profile 133

Fig. 3-25 Relationship between $\theta_{Q,4}$ and ψ_5 for quartic velocity profile 133

Fig. 3-26 Relationship between $\theta_{Q,5}$ and ψ_6 for quintic velocity profile 134

Fig. 3-27 Relationship between $\theta_{Q,6}$ and ψ_7 for 6th order velocity profile 134

Fig. 3-28 Magnitude of DFT components for three axisymmetric velocity profiles with mean velocity 5m/s and q = 0, 1, 5 (see Section 3.5.2) in a uniform magnetic field 138

Fig. 3-29 Applying DFT into boundary potential distribution in a non-uniform magnetic field (a) imaginary parts of DFT components for three axisymmetric velocity profiles; (b) real parts of DFT components for three velocity profiles (see Section 3.5.2) 139

Fig. 3-30 The imaginary part $\mathrm{Im}\,\hat{X}_2$ for polynomial velocity components 1st to 6th order with varying angle 141

Fig. 3-31 Effects of different quadratic velocity profiles on $\mathrm{Im}(\hat{X}_2)_2$ 143

Fig. 3-32 $A_{2,\theta}$ as a function of $\theta_{Q,2}$ 144

Fig. 4-1 Schematic diagram of the flow regions [93] 150

Fig. 4-2 Axial velocity profile in two phase oil-in-water flow in a pipe with inclination of 25 ºto vertical (solid line is predicted velocity profile and circles represent experimental velocity profiles) [28] 152

Fig. 4-3 Imposed velocity as defined by Equation 4-6 and Equation 4-7: (a) the imposed asymmetric "first" velocity profile is defined by Equation 4-6 (b) the imposed axisymmetric "second" velocity profile is defined by Equation 4-7 153
Fig. 4-4 (a) potential difference distribution for the first imposed velocity profile in the uniform magnetic field (see Equation 4-5); (b) potential differences distribution for the second imposed velocity profile in the uniform magnetic field (see Equation 4-7); (c) potential difference distribution for the first imposed velocity profile in the non-uniform magnetic field ; (d) potential difference distribution for the second imposed velocity profile in the non-uniform magnetic field; (e) asymmetric velocity profile(first velocity profile) Equation 4-5; and (f) axisymmetric velocity profile(second velocity profile) Equation 4-7 155
Fig. 4-5 The chosen optimum velocity profile: (a) reconstructed by using the method without use of an axisymmetric component referring to Section3.6; (b) reconstructed by using the method with use of an axisymmetric component referring to Section 3.7; and (c) potential difference distribution for imposed and reconstructed velocity profiles in the non-uniform(anti-Helmholtz) magnetic field..... 171
Fig. 4-6 Local percentage error between imposed velocity and reconstructed velocity; colour bar is in % 172
Fig. 4-7 Reconstructed velocities for imposed velocity profile defined by Equation 4-7: (a) optimum velocity profile obtained using reconstruction algorithm without use of an axisymmetric component; (b) optimum velocity profile obtained using reconstruction algorithm with use of an axisymmetric component; (c) potential difference distributions in the non-uniform magnetic field of simulated and reconstructed velocity profiles for reconstruction algorithm without use of an axisymmetric velocity component; and (d) potential difference distributions in the non-uniform magnetic field of simulated and reconstructed velocity profiles for reconstruction algorithm with the use of an axisymmetric velocity component. 173
Fig. 4-8 Local percentage error between reference velocity defined by Equation 4-7 and reconstructed velocity in Fig. 4-7(b); colour bar is in% 174
Fig. 5-1 Fully assembled IFT device and overall dimensions 177
Fig. 5-2 Component parts of the IFT device ① rubber O-Ring ② 2" BSP thread ③ electrodes holes ④grooves 179

Fig. 5-3 IFT device in anti-Helmholtz configuration..... 180
Fig. 5-4 Electrode assembly inside the flow conduit ("inside" or "in the side of") 184
Fig. 5-5 The structure of IFT flow measurement system..... 185
Fig. 5-6 (a) electrical potential difference Uj, (b) magnetic flux density B_y, and..... 188
Fig. 5-7 Overview of Helmholtz coil circuit and coil current monitoring circuit..... 189
Fig. 5-8 Schematic diagram of reference voltage unit..... 190
Fig. 5-9 H bridge of SSRs coil excitation circuitry 192
Fig. 5-10 coil excitation control circuitry of IFT system..... 192
Fig. 5-11 (a) Measured temperature on the coil surface, (b) dynamic measurement of the magnetic flux density [1] 195
Fig. 5-12 Coil current monitor circuitry 197
Fig. 5-13 Overview of potential difference measurement circuitry..... 197
Fig. 5-14 Physical potential signal U_9 with excitation frequency of 0.0167Hz..... 199
Fig. 5-15 Part I Signal detection and amplifier[note that signal at 'a' is fed into the circuit shown in Fig. 5-16 and that the signal at 'Reference point' is the output from the circuit in Fig. 5-16]200
Fig. 5-16 Part Ⅱ DC offset control circuit [Note that signal at 'a' is the output from the circuit in Fig. 5-15 and the signal at ' Reference point' is fed into the circuit shown in Fig. 5-15]..... 202
Fig. 5-17 Part Ⅲ second amplification within bias voltage control circuit and Butterworth low pass filter [note that the input is effectively equal to zero duo to the action of the DC offset control circuit (see Fig. 5-16)] 203
Fig. 5-18 Photograph of the 15 channels potential differences measurement circuit..... 204
Fig. 6-1 Framework of IFT LabVIEW based software..... 207
Fig. 6-2 Signal acquisition block diagram with DAQmx code..... 209
Fig. 6-3 Coil excitation routine..... 212
Fig. 6-4 LabVIEW program for coil excitation routine..... 213
Fig. 6-5 One cycle of averaged electrical potential difference signal $U_{j,a}$ 217
Fig. 6-6 Coil current signal U_r and 'square wave' digital control signal for one cycle..... 217
Fig. 6-7 Flow chart of signal processing software..... 221

Fig. 7-1 Diagram showing the features of the multiphase flow loop in SGR [110]. Note that: ① represents flow loop working section in vertical position. ② represents flow loop working section inclined at an angle ɵ to the vertical 226
Fig. 7-2 Photographs of the Schlumberger Gould Research (SGR) multiphase flow loop. ① Mounting position of the IFT flowmeter ② working section with 50mm diameter bore 227
Fig. 7-3. Schematic of MRRC flow loop at the University of Cambridge. 1) storage tank; 2) pump; 3) liquid flowmeter; 4) compressed air feed; 5) gas rotameter; 6) mixing section; 7) differential pressure tapping; 8) MRI system; 9) IFT sensor with clear section of pipe for visual observation. 229
Fig. 7-4 The modular flow loop with vertical working section and with IFT and MRI installed. 1) storage tank, 2) compressed air feed, 3) MRI system, 4) IFT flowmeter, 5) return line to tank. 229
Fig. 7-5 Schematic of the differential pressure connections for measuring $\overline{\alpha}_g$ (see also item "7" in Fig. 7-3)..... 232
Fig. 7-6 The dual-plane ERT flowmeter device used in the present study (developed and constructed by University of Leeds) (a) photograph of the ERT system, and (b) circular image with 316 pixels..... 235
Fig. 7-7 Sixteen electrodes on pipe wall rotated by angle η relative to the *y*-axis 237
Fig. 7-8 Electrical potential distribution on pipe boundary for vertical water-only single phase flow conditions (uniform magnetic field) with electrodes rotated by angle η 238
Fig. 7-9 Potential difference distribution on the pipe boundary for vertical water-only single phase flow conditions (non-uniform magnetic field) with electrodes rotated by angle η 238
Fig. 7-10 Measured potential distribution φ_j vs. actual electrode position j; corrected potential distribution φ_j'' vs. virtual electrode position j' ; (a) uniform magnetic field, (b) non-uniform magnetic field..... 240
Fig. 7-11 DC offset value is found in the real part of the DFT..... 241
Fig. 7-12 Comparison of potential measurement values of φ_j and φ_j' (uniform magnetic field) 242
Fig. 7-13 Polynomial curve fitting for φ_j' order 15..... 243

Fig. 7-14 Electrical potential φ_j'' was determined by using the linear interpolation technique. 244

Fig. 7-15 Corrected potential measurement distribution φ_j'' using the polynomial interpolation method..... 245

Fig. 7-16 Comparison of φ_j, φ_j' and φ_j'' 246

Fig. 7-17 Corrected potential measurement distribution φ_j'' against j' using the linear interpolation method 246

Fig. 7-18 φ_j'' against j' (corrected using the polynomial interpolation method) in a non-uniform magnetic field..... 247

Fig. 7-19 φ_j'' against j' (corrected using the linear interpolation method) in a non-uniform magnetic field..... 248

Fig. 7-20 Corrected potential difference measurements $U_j^{''}$ vs j' for non-vertical oil-gas-water three phase flows (a) uniform magnetic field (b) non-uniform magnetic field 251

Fig. 7-21 Magnitude of DFT components for potential distributions $U_j^{''}$ for uniform magnetic field, for experimental conditions fm1 to fm5 252

Fig. 7-22 Reconstructed velocity profiles in non-vertical oil-gas-water three phase flows. The water velocity in this colour bar is in ms^{-1} 255

Fig. 7-23 Flow characteristics observed in vertical and non-vertical oil-in-water two phase flows. As the angle of deviation θ increases, buoyancy forces cause more bubbles (oil and gas) to congregate along the upperside of the inclined working section (Vigneaux [112]) 256

Fig. 7-24 Flow patterns for flow condition fm5; note elongated bubble along upper side of inclined pipe in this flow condition : Q_w =5m^3/hr Q_o =2m^3/hr Q_g =3.4m^3/hr inclination angle θ =60). 257

Fig. 7-25 Local water volume fraction distribution and local dispersed phase(oil and gas) volume fraction distribution..... 260

Fig. 7-26 Distribution parameter values $C_{o\theta}$ for various experimental data sets [116]..... 262

Fig. 7-27 Reconstructed velocity profiles for different velocity flow conditions (fm1 to fm5) by using the improved reconstruction algorithm. The water velocities in the colour bars are in ms^{-1} 266

Fig. 7-28 Potential difference distribution $U_j^{''}$ vs. j' for all flow conditions shown in Table 7-3: (a) uniform magnetic field, (b) non-uniform magnetic field 270
Fig. 7-29 (a) The real parts of the DFT components for a uniform magnetic field, (b) the imaginary parts of the DFT components for a non-uniform magnetic field. 271
Fig. 7-30 Local water velocity distributions in water only single phase flow in vertical pipe as reported by Leeungculsatien [1]. The water velocity in the colour bar is in ms^{-1} 274
Fig. 7-31 Flow condition fv1: (a) reconstructed velocity profile using the reconstruction algorithm with use of an axisymmetric component; (b) reconstructed velocity profile using the reconstruction algorithm without use of an axisymmetric component. Note that the water velocity profile with higher resolution (100×100) is on the left of the figure, and the water velocity profile with low resolution (20×20 ERT grid) is on the right. The water velocities in the colour bars are in ms^{-1} 275
Fig. 7-32 Flow condition fv2: (a) reconstructed velocity profile using the reconstruction algorithm with use of an axisymmetric component; (b) reconstructed velocity profile using the reconstruction algorithm without use of an axisymmetric component. Note that the water velocity profile with higher resolution (100×100) is on the left of the figure and the water velocity profile with low resolution (20×20 ERT grid) is on the right. The water velocities in the colour bars are in ms^{-1} 276
Fig. 7-33 Flow condition fv3: (a) reconstructed velocity profile using the reconstruction algorithm with use of an axisymmetric component; (b) reconstructed velocity profile using the reconstruction algorithm without use of an axisymmetric component. Note that the water velocity profile with higher resolution (100×100) is on the left of the figure and the water velocity profile with low resolution (20×20 ERT grid) is on the right. The water velocities in the colour bars are in ms^{-1} 277
Fig. 7-34 Flow condition fv4: (a) reconstructed velocity profile using the reconstruction algorithm with use of an axisymmetric component; (b) reconstructed velocity profile using the reconstruction algorithm without use of an axisymmetric component. Note that the water velocity profile with higher resolution (100×100) is on the left of the figure and the water velocity profile with low resolution (20×20 ERT grid) is on the right. The water velocities in the colour bars are in ms-1 278

Fig. 7-35 Local oil volume fraction distribution in oil-in-water two phase flow in vertical pipe from Panagiotopuolos [117]. 280
Fig. 7-36 Local water volume fraction distribution and local dispersed phase (oil or oil and gas) volume fraction distribution for flow conditions fv5 to fv8. 283
Fig. 7-37 Flow condition fv5: (a) reconstructed velocity profile using the reconstruction algorithm with use of an axisymmetric component; (b) reconstructed velocity profile using the reconstruction algorithm without use of an axisymmetric component. Note that the water velocity profile with higher resolution (100×100) is on the left of the figure and the water velocity profile with low resolution (20×20 ERT grid) is on the right. The water velocities in the colour bar are in ms^{-1} 284
Fig. 7-38 Flow condition fv6: (a) reconstructed velocity profile using the reconstruction algorithm with use of an axisymmetric component; (b) reconstructed velocity profile using the reconstruction algorithm without use of an axisymmetric component. Note that the water velocity profile with higher resolution (100×100) is on the left of the figure and the water velocity profile with low resolution (20×20 ERT grid) is on the right. The water velocities in the colour bar are in ms^{-1} 285
Fig. 7-39 Flow condition fv7: (a) reconstructed velocity profile using the reconstruction algorithm with use of an axisymmetric component; (b) reconstructed velocity profile using the reconstruction algorithm without use of an axisymmetric component. Note that the water velocity profile with higher resolution (100×100) is on the left of the figure and the water velocity profile with low resolution (20×20 ERT grid) is on the right. The water velocities in the colour bar are in ms^{-1} 286
Fig. 7-40 Flow condition fv8: (a) reconstructed velocity profile using the reconstruction algorithm with use of an axisymmetric component; (b) reconstructed velocity profile using the reconstruction algorithm without use of an axisymmetric component. Note that the water velocity profile with higher resolution (100×100) is on the left of the figure and the water velocity profile with low resolution (20×20 ERT grid) is on the right. The water velocities in the colour bar are in ms^{-1} 287
Fig. 7-41 Percentage difference ε plotted against the angle of deviation θ for multiphase flow condition 289

Fig. 7-42 Percentage difference ε plotted against the angle of deviation, θ, for water-only single phase flow 290
Fig. 7-43 (a) IFT flow cross-section (b) MRI flow cross-section 292
Fig. 7-44 Measured potential differences for gas-in-water two phase vertical flows: (a) uniform magnetic field, (b) non-uniform magnetic field 294
Fig. 7-45 Applying DFT method to the potential distributions shown in Fig. 7-27: (a) the real parts of the DFT components for the uniform magnetic field, (b) the imaginary parts of the DFT components for the non-uniform magnetic field. 295
Fig. 7-46 Comparison of local water velocity distribution results for vertical flows. Left side: reconstructed velocity profiles using MRI. Right side: reconstructed velocity profiles using IFT. The water velocities in the colour bars are in ms^{-1} 297
Fig. 7-47 Local gas volume fraction distribution and local gas velocity distribution in vertical air-water flow. Mean gas volume fraction is 0.0248, superficial water velocity is 0.9m/s ,superficial gas velocity is 0.033m/s [111] 299
Fig. 7-48 Local water velocity profiles for vertical gas-in-water two phase flows. The black curve is the corrected MRI velocity profile, the blue curve is the power law approximation to the corrected MRI velocity profile and the red curve is the velocity profile obtained from IFT. 301
Fig. 7-49 Exponent q vs. mean volume fraction[90] 303
Fig. 7-50 Plots of power law exponent q vs. mean gas volume fraction (a) q vs. $\overline{\alpha}_g$ for IFT system, (b) q vs. $\overline{\alpha}_g$ for MRI system 304
Fig. 7-51 Local relative differences between velocities 306
Fig. 7-52 Averaged water velocity vs. reference water velocity: (a) averaged water velocity obtained by IFT vs. reference mean water velocity, (b) averaged water velocity obtained using uncorrected MRI data vs. reference mean water velocity 309

List of Tables

Table 3-1 Calculation for supply current components for Helmholtz coil 96

Table 3-2 Potential difference measurement between electrode position e_j and e_5 106

Table 3-3 Calculated value of mean velocity $\bar{v}_{z,m}$ and q for the three velocity profiles 114

Table 5-1 the working state of relays and voltages across Helmholtz coil for uniform and non-uniform magnetic fields 191

Table 7-1 Flow measurement techniques and related reference measurement parameters 249

Table 7-2 Flow conditions used in the oil-gas-water three phase flow in non-vertical pipe experiments 250

Table 7-3 Flow conditions used in the water only single phase, oil-in-water two phase , oil-gas-water three phase flows in vertical pipe experiments 250

Table 7-4 Percentage difference between reference measurement $Q_{w,ref}$ and water volumetric flow rate $Q_{w,IFT}$ based on velocity results calculated by using the reconstruction algorithm without use of an axisymmetric velocity component (see Section 3.6)..... 268

Table 7-5 Percentage difference between reference measurement $Q_{w,ref}$ and water volumetric flow rate $Q_{w,IFT}$ based on velocity results calculated by using the reconstruction algorithm with use of an axisymmetric velocity component(see Section 3.7)..... 269

Table 7-6 Percentage difference between reference measurement $Q_{w,ref}$ and water volumetric flow rate $Q_{w,IFT}$ based on velocity results calculated by using the reconstruction algorithm without use of an axisymmetric velocity component (see Section 3.6)..... 274

Table 7-7 Percentage difference between reference measurement $Q_{w,ref}$ and water volumetric flow rate $Q_{w,IFT}$ based on velocity results calculated by using the reconstruction algorithm with use of an axisymmetric velocity component(see Section 3.7)..... 274

Table 7-8 Percentage difference between reference measurement $Q_{w,ref}$ and water volumetric flow rate $Q_{w,IFT}$ based on velocity results calculated by using the reconstruction algorithm without use of an axisymmetric velocity component (see Section 3.6)..... 281

Table 7-9 Percentage difference between reference measurement $Q_{w,ref}$ and water volumetric flow rate $Q_{w,IFT}$ based on velocity results calculated by using the reconstruction algorithm with use of an axisymmetric velocity component(see Section 3.7) 281
Table 7-10 This table relates to Fig. 7-41 and shows the phase volumetric flow rates corresponding to the colour of the data points in Fig. 7-41 289
Table 7-11 This table relates to Fig. 7-42 and shows the phase volumetric flow rates relating to the colour of the data points in Fig. 7-42 290
Table 7-12 Relevant reference measurement parameters 293
Table 7-13 Gas-in-water two phase vertical flow conditions 293
Table 7-14 Averaged water velocity determined using IFT and reference measurement for vertical gas-in-water two phase flow 308

Nomenclature

Symbols:

σ	Conductivity
$\bar{v}$	Mean flow velocity
$v_{z,1}$	The 1st case flow velocity in *z* direction
$v_{z,2}$	The 2nd case flow velocity in *z* direction
$v_{z,3}$	The 3rd case flow velocity in *z* direction
$\bar{v}_{z,m1}$	The 1st case flow mean velocity in *z* direction
$\bar{v}_{z,m2}$	The 2nd case flow mean velocity in *z* direction
$\bar{v}_{z,m3}$	The 3rd case flow mean velocity in *z* direction
$\bar{v}_w$	Mean water velocity
$\bar{v}_g$	Mean gas velocity
$v_{d,i}$	Dispersed phase velocity in i^{th} region
$\bar{v}_d$	Mean velocity of dispersed phase
$\boldsymbol{E}$	Electric field
$\boldsymbol{v}$	velocity vector
q	Exponent q
U_j	Potential difference between j^{th} electrode pair

U_e	Induced voltage
j	Electrode number
φ_j	Electrical potential at j th electrode
$\boldsymbol{B}$	Magnetic field vector
B	Magnetic flux density
$\overline{B}$	Mean magnetic flux density
B_y	Magnetic flux density (y component)
B_x	Magnetic flux density (x component)
A_q	Parameter (see Equation 3-88)
B_{op}	Magnetic flux density for a non-uniform magnetic field
$\overline{\alpha}_w$	Mean water volume fraction
$\overline{\alpha}_{o+g}$	Mean oil and gas volume fraction
$\varphi_j^{"}$	Corrected potential distribution
j'	Virtual electrode
$\overline{\alpha}_d$	Mean dispersed phase volume fraction
U_d	Mean dispersed phase velocity
U_h	Homogeneous velocity of the mixture
U_{dj}	Drift velocity of the dispersed phase

$U_j^{''}$	Corrected potential differences distribution
$C_{o\theta}$	An inclination dependent distribution parameter
α_l	Local volume fraction of the dispersed phase
j_m	Sum of the local flux densities of the two flow components
α_c	Local volume fraction of the continuous phase
α_d	Local volume fraction of the dispersed phase
$\alpha_{d,i}$	Dispersed phase volume fraction in i^{th} region
$\overline{\alpha}_o$	Mean oil volume fraction
$\overline{\alpha}_g$	Mean gas volume fraction
Q_c	Volumetric flow rate of continuous phase flow
Q_d	Volumetric flow rate of dispersed phase flow
Q_w	Volumetric flow rate of water
Q_l	Volumetric flow rate of liquid
Q_o	Volumetric flow rate of oil
q_t	Inclined angle from horizontal line.
σ_m	Measured conductivity of the mixture
σ_w	Water conductivity
$R_{xy}(\tau)$	Cross-correlation function between *x(t)*and *y(t)*

K_s	Cell constant
G_f	Fluid conductance
V_{out}	Output voltage signal
$V_{out,w}$	Ouput voltage when the measured flow is water only
$\lvert V_{out} \rvert$	Amplitude of output voltage signal
$V(t)$	Excitation signal
$\lvert V(t) \rvert$	Amplitude of excitation signal
R_{fb}	Feedback resistor
R_f	Resistance of fluid
$R_{t,c}$	Total resistance of the Helmholtz coil
L	Distance
$L_{t,c}$	Total inductance of the Helmholtz coil
τ	Delay time
τ_p	Value of time delay for which the cross-correlation function is at maximum
V_c	Voltage output of sensor C for six electrodes probe
V_{ref}	Reference voltage measurement on reference resistor
$\varphi_e(x,y)$	Electrical potential distribution
n	Order number of polynomial expression

a_n	Coefficient of polynomial expression
$\theta_{Q,n}$	The angle between the direction and the *x*-axis
v_n	n^{th} velocity component
$\tilde{U}(\theta)$	Overall boundary potential distribution
$U_n(\theta)$	n^{th} order velocity component and associated boundary potential distribution
$\hat{U}_j$	Potential difference measurement in a non-uniform magnetic field
$a_{n,n}$	Coefficient of the n^{th} velocity component
U_p	Discretised potential distribution
A_0	Peak amplitude of the sinewave component of the input signal
K_n	Coefficient
X_n	n^{th} DFT component in a uniform magnetic field
$\hat{X}_n$	n^{th} DFT component in a non-uniform magnetic field
ψ_{n+1}	The argument ψ_{n+1} of the $(n+1)^{th}$ DFT component, X_{n+1}
$A_{2,\theta}$	Parameter (see Equation 3-86)
$v_{axi}(x;y)$	Axisymmetric velocity component
$w_{i,j}$	Weight value
$\hat{U}_{wt,j}$	Potential difference measurements between j^{th} electrode pair in a non-uniform magnetic field (see Equation 4-2)

$\widehat{U}_{j,ref}$	The reference potential differences (a non-uniform magnetic field)
S_U	Parameter (see Equation 4-4)
$v_{\max}$	The maximum velocity at the centre of the axisymmetric velocity profile
δv	The mean deviance of local velocities
$\widetilde{M}$	Number of sub-regions of pipe cross-section
$v_{in,\max}$	The maximum velocities in the imposed velocity profile
$v_{in,\min}$	The minimum velocities in the imposed velocity profile
δv_i	The local error between velocities
μ_0	The permeability of free space
n_c	Number of turns in each coil
I_c	The coil current
U_r	The output voltage signal obtained from coil monitor circuit
$I_{c,t}$	Total coil current
U_{DC}	DC power supply
R_p	Coil resistance at coil temperature T_p ($^{\circ}$C)
R_{ini}	Coil resistance at initial temperature
T_{ini}	Initial temperature of coil
T_p	Actual temperature of coil

$I_{p,c}$	Coil current at actual coil operating temperature
R_{ref}	Precision resistor
f_{ct}	Cutting –off frequency
$U_{R,ref}$	Voltage drop across the precision resistor
U_{dc}	DC offset
U_{BV}	The bias voltage
$U_{j,a}$	Amplified potential difference measurements
$U_{j,cp}$	Compensated amplified potential difference measurements
J_C	Conduction current density
J_D	Displacement current density
J_{total}	Total current density
E	The electric field
σ_w	The conductivity of water
ε_0	The permittivity of vacuum
ε_r	The relative permittivity of the water
ω	The angular frequency of the excitation signal
e_w	Counter-emf noise
U_j^+	The maximum is value of the potential difference during the time period t_1

U_j^-	The minimum value of the electrical potential difference during the time period t_3
U_{ds}	Combined digital control signal
$U_{r,ref}$	Coil current at initial coil temperature
ΔP	Differential pressure
ρ_w	Density of water
g	Acceleration due to gravity
η	Rotation angle
A_i	Sub-region of the flow cross-section
A	Pipe cross-sectional area
$Q_{w,IFT}$	Volumetric flow rate of water is calculated by IFT
$v_{i,MRI,\max}$	Maximum velocities in the MRI velocity profile
$v_{i,MRI,\min}$	Minimum velocities in the MRI velocity profile
$\varepsilon_{v,w}$	Relative error
ξ^{th}	Configuration number
ς^{th}	Rotation number
Δx_d	Particle displacement
Δt	Time interval between laser flashes
$G(t)$	Applied gradient

$r(t)$	Spatial location of the spin
$\phi(t)$	The phase shift
γ	Gyromagnetic ratio
δ	Length of pulse
B_1	Mean magnetic flux density for the first EMFM
B_2	Mean magnetic flux density for the second EMFM
D_1	Internal diameter of the first EMFM
D_2	Internal diameter of the second EMFM
U_{E1}	Induced voltage of the first EMFM
U_{E2}	Induced voltage of the second EMFM
V_1	Mean conducting continuous phase velocity in the first EMFM
V_2	Mean conducting continuous phase velocity in the second EMFM
U_k	Potential difference measurement
R_g	Radius of the gas core
L^*	Distance between two peak value of signal (see Fig.2-10)
$U_{j,evp}$	Potential difference measurements from EVP
U_{p1}	First peak value of transformer signal
U_{p2}	Second peak value of transformer signal
i^{th}	Number of the pixel for the flow cross-section

M_{ind}	Independent measurements
$S_{i,j}$	A normalized sensitivity
V_p	Vector velocity for each sub-area

Acronyms:

AC	Alternating Current
ADC	Analogue-to-Digital Converter
CoA	Centre of Action
DAC	Digital-to-Analogue Converter
DAQ	Data Acquisition Board
DA	Differential Amplifier
DP	Differential Pressure
DC	Direct Current
e.m.f	Electromotive force
EMFM	Electro Magnetic Flow Meter
ERT	Electrical Resistance Tomography
ECT	Electrical Capacitance Tomography
EVP	Electromagnetic Velocity Profiler
FEA	Finite Element Analysis
HGA	High Gain Amplifier
LPF	Low-Pass Filter

LSV	Laser Speckle Velocimetry
PIV	Particle Image Velocimetry
PT	Process Tomography
MRI	Magnetic resonance imaging
NMR	Nuclear magnetic resonance
NI	National Instrument
IPT	Industrial Process Tomography
ICC	Impedance Cross Correlation
IFT	Inductive Flow Tomography
3D	3 Dimensional
VF	Voltage Follower
SSR	Solid State Relay
SNR	Signal to Noise ratio

1 Introduction

1.1 Introduction

The world's relentless need for oil and gas is a strong motivation for the oil industries to continuously develop new, more effective and efficient, oil and gas production techniques [1,2]. Although there are a large number of techniques for measuring multiphase flow in use worldwide, and research has successfully investigated and developed new devices, the problem of how to accurately measure the flow rate of each phase in multiphase flow (e.g. in oil-gas-water mixture) in a pipeline remains a great challenge. This is because, in multiphase flow, the interactions between the phases determine the flow properties and these are difficult to predict and/or measure.

The most important flow properties to be measured include both phase local volume fraction distribution and phase local velocity distribution [2, 3]. Many flow measuring techniques have been developed and are in current use measuring these quantities, but no individual technique can successfully meet all measurement requirements in the field. The common method for obtaining multiphase flow information is based on integrating multiple measurement techniques, such as Electrical Resistance Tomography, dual-energy gamma ray and Venturi differential pressure. Unfortunately, most existing techniques are only valid for obtaining the local volume fraction distribution and velocity distribution of the dispersed phase in the flow.

The motivation of the present research is to advance and implement a novel multi-electrode electromagnetic flow meter to be applied in the imaging of the local velocity distribution of the conducting continuous phase in multiphase flows. With reference to Fig. 1-1, it can be seen that 'oil-in-water' and 'transition' flow regimes constitute a high proportion of the oil-water two phase flow regime map. This means that the water being the continuous phase is the most commonly encountered regime in oil-water two phase flow. Thus, multiphase flows in which the continuous phase is not electrically conducting are not considered in this thesis, such as the water-in-oil flow or pure oil flow.

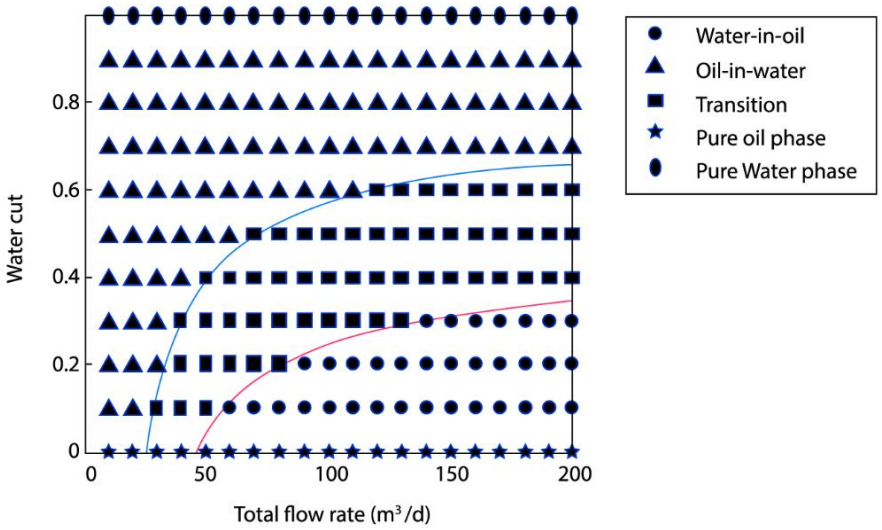

Fig. 1-1 Flow regime classification map of oil-water flow [4].

This chapter starts by discussing why multiphase flow measurement is important, and why such a difficult problem needs to be solved. This chapter also describes how Multiphase Flow Meter (MPFM) techniques are currently trending towards techniques based on process tomographic flow imaging. Some potential techniques and existing commercial MPFMs are described. In the last section, the aim and objectives of the present research are given.

1.2 Significance of multiphase flow measurement and development of MPFMs

Previously, Crowe [5] described multiphase flow as a term used to define flow where more than one phase or component is present in the flowing stream. In industrial applications, slurry flows, solids-in-water two phase flows and oil-gas-water three phase flows are commonly encountered. The measurement of various parameters of the flows is the key for solving safety and fiscal issues in many industrial applications (e.g. off-shore oil exploration). The most important parameters to be measured include the volume fraction distribution and the velocity distribution of each individual phase. As a consequence of these measurements, the volumetric flow rate for each individual phase can be calculated by using the following equations:

$$Q_c = \int_A \alpha_c v_c dA$$ Equation 1-1

$$Q_d = \int_A \alpha_d v_d dA$$ Equation 1-2

where α_c and α_d, respectively, represent the local volume fraction of the continuous phase and a particular dispersed phase; v_c and v_d, respectively, denote the local velocity of the continuous phase and dispersed phase; and A is the flow cross-sectional area. Since, for two phase flow, $\alpha_c + \alpha_d = 1$, only one of the phase local volume fraction distributions needs to be measured (i.e. in general, the dispersed phase α_d is measured). Equation 1-1 can be rewritten as:

$$Q_c = \int_A (1-\alpha_d) v_c dA$$ Equation 1-3

As stated earlier, oil-gas-water three phase flow is frequently encountered in oil fields. In such a case, it is more difficult to make direct measurements of the parameters for each individual flowing phase. A review of previous research indicated that there are two common methods used for measuring phase flow rates in multiphase flow in industrial applications: test separator-based measurement systems and inline MPFM systems [6, 7].

1.2.1 Multiphase flow regime

Before discussing the multiphase flow measurement techniques, it is worth introducing another important concept, the so-called 'flow regime' or 'flow pattern' in multiphase flow. This is because some multiphase flow metering techniques rely upon identification of the flow regime of the flowing mixture (see Section 1.3.2). In what follows, a description of the main flow regimes that characterise gas-liquid, liquid-liquid and solids-in-liquid flows is presented.

Gas-liquid flows

With reference to previous research work, the most common flow regimes encountered in vertical upward gas-liquid flow are shown in Fig. 1-2. In the five cases shown the volumetric flow rate of liquid is fixed and the volumetric flow rate of gas is constantly increased [8].

a) Bubbly flow:

In this type of flow regime, the gas is in the dispersed phase and flows as bubbles of various sizes in the liquid phase.

b) Slug flow

The average gas bubble size rises when the volumetric flow rate of gas starts increasing. The 'slug flow' occurs when the volumetric flow rate of gas reaches a certain value and numerous bubbles coalesce to form a Taylor bubble. These Taylor bubbles have a bullet shape with spherical noses and are of a similar size to the pipe cross-section. There is a thin liquid film between the Taylor bubbles and pipe wall. Some small bubbles will be entrained in the fluid separating the Taylor bubbles.

c) Churn flow

As the volumetric flow rates of gas become even higher , the Taylor bubbles break down and the flow starts to become chaotic.

d) Annular flow and annular mist flow

Further increasing the volumetric flow rate of gas causes both two phases to become separated; the gas phase flows in the centre of the fluid and the liquid phase flows as an annular film. If the flow rate is increased even further, liquid drops are carried in the core, causing annular flow with droplets.

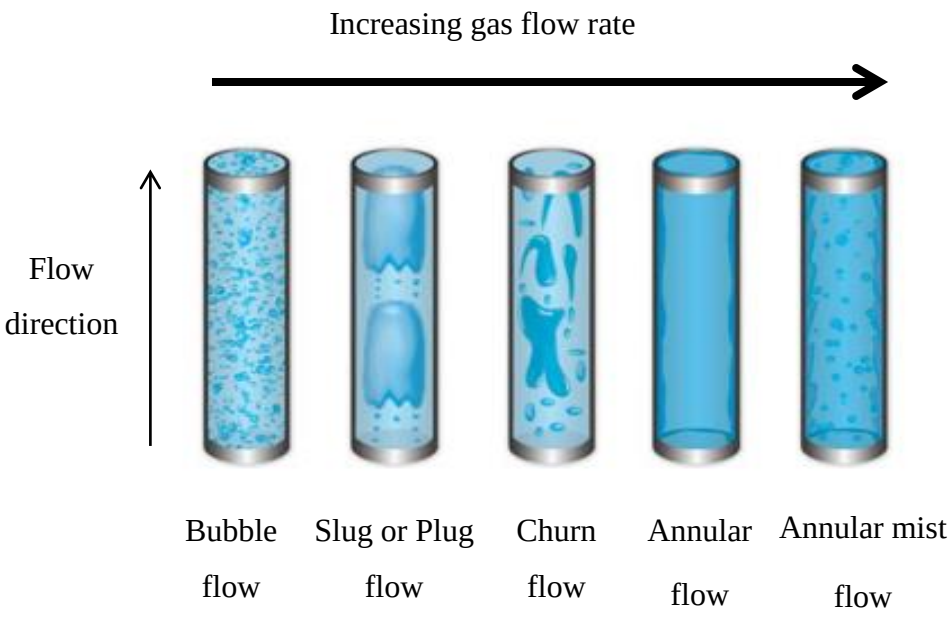

Fig. 1-2 Flow regimes in vertical gas-liquid flows

Unlike vertical flow regimes, multiphase flow in an inclined or horizontal pipe will be affected by gravitational forces that cause the gas phase to cluster towards the top side of the pipe. Shoham [9] has shown the most commonly encountered gas-liquid flow regimes when the pipe was inclined at different angles (see Fig. 1-3). From inspection, it can be seen that, for the inclined gas-liquid, the same flow regimes occur, as shown in Fig. 1-2. Akhnoukh *et al*, [10] demonstrated that the conversion to slug flow regimes was affected by varied pipe deviation angles. Changing the deviation angle slightly, led to a significant change in the flow pattern map (see Fig. 1-4). From Fig. 1-4, it can be seen that a one degree variation influenced the flow regime distribution.

Oddie [11] also presented the observed flow regimes for gas-liquid two phase flows. The results showed that, at two different deviation angles of 90 ° and 85 ° to the vertical, bubbly and churn flows were commonly observed. When the deviation angle was increased from 10 ° to 20 °, there were two typical flow regimes observed: Taylor bubble flows and large bubble flows. When the working section was in the horizontal , stratified and wavy stratified flow were observed.

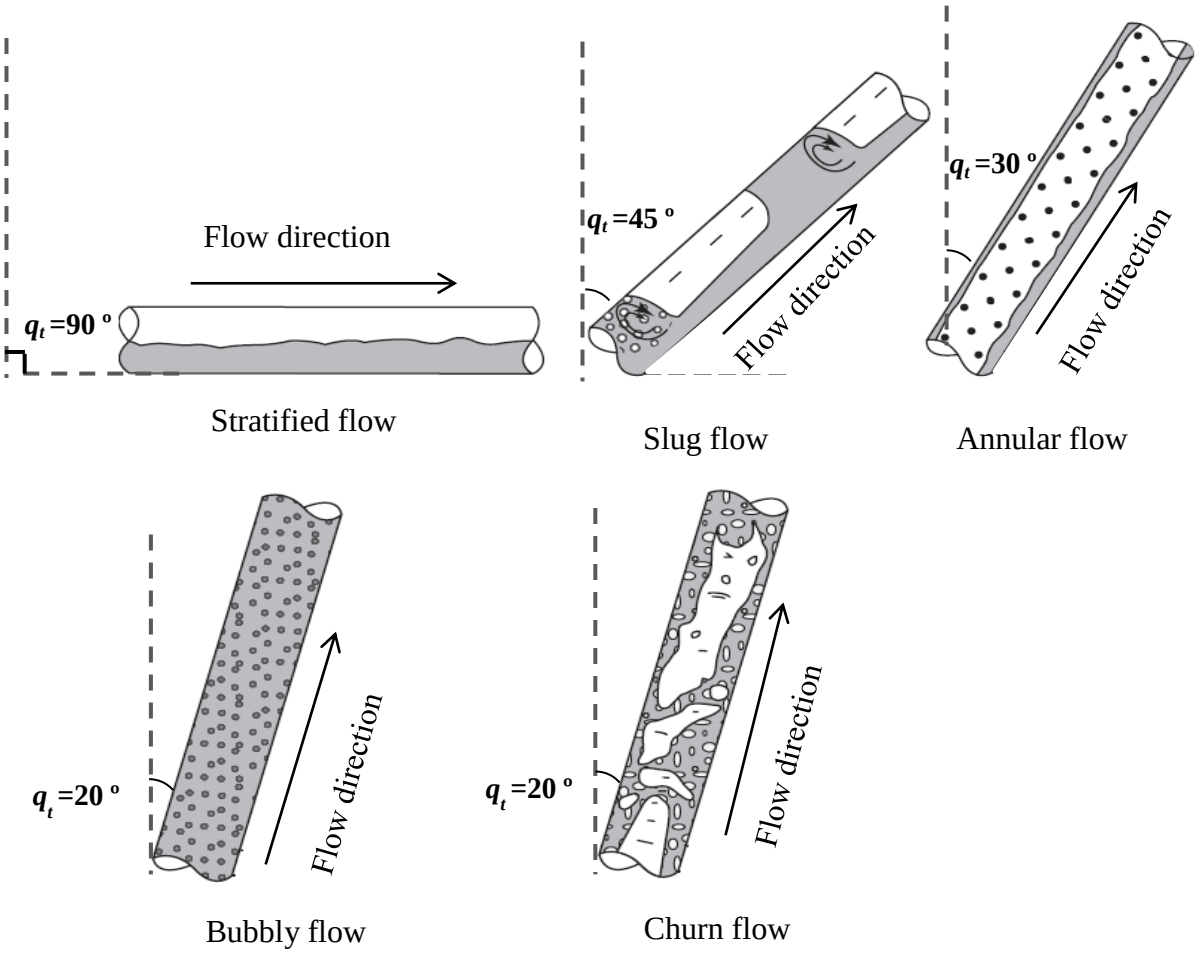

Fig. 1-3 Flow regimes in inclined and horizontal gas-liquid flow [9]

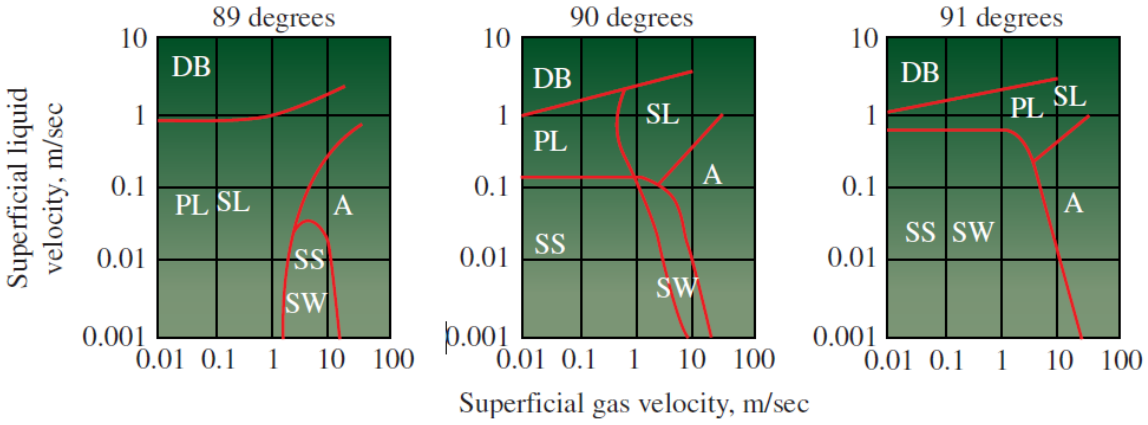

Fig. 1-4 The flow regime map for deviation angle of 89 degree, 90 degree and 91 degree to vertical. Note that : DB is dispersed bubble flow, SW is wavy stratified flow, SS is stratified flow, A is annular flow, PL is plug flow and SL is slug flow[10]

Liquid-liquid flows

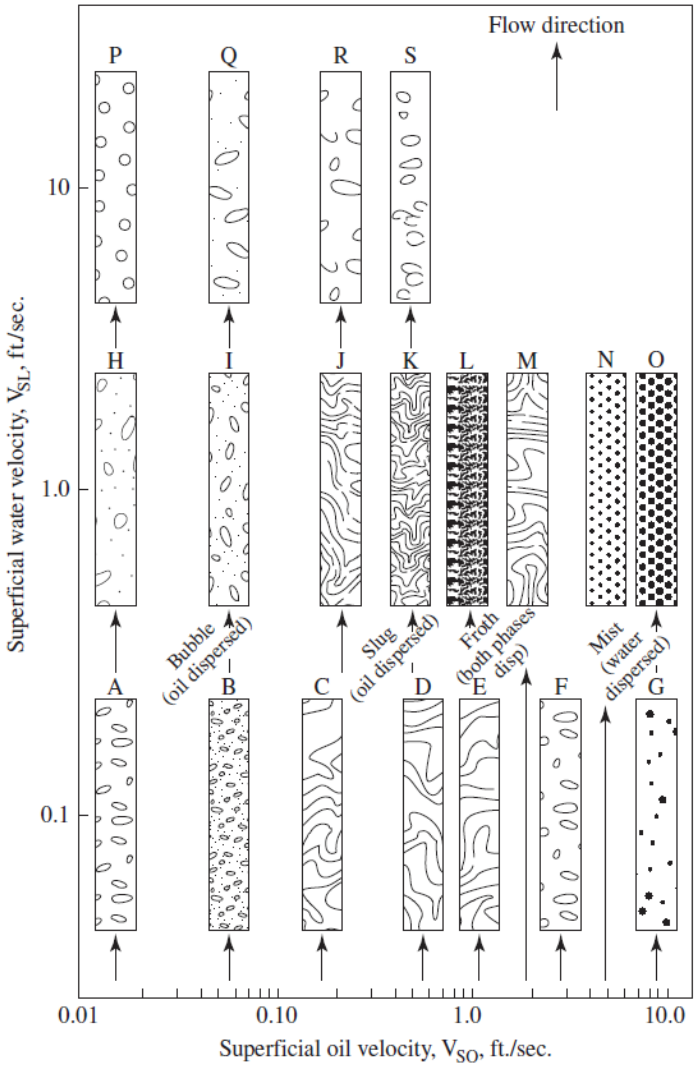

Fig. 1-5 Flow regime map for liquid-liquid(oil-water) flows in vertical pipe [12]

Liquid –liquid mixture flow, especially oil-water flow, is commonly encountered in the chemical and oil industry. Govier *et al.* [12] used a 0.025metre diameter pipe to investigate flow regimes of oil-water flow in a vertical pipe. Fig. 1-5 demonstrates the observation of oil-water flow patterns at different levels of superficial water velocity and superficial oil velocity. As seen from the diagram, at the lower level of superficial water velocity, there were four different flow regimes: (A, B)oil bubbly flow, (C)slug flow , (D, E) churn flow and , (F, G) water bubbly flow(water is the dispersed phase) [12].

When the superficial oil velocity is increased from 0.01 to 0.3ft/sec at a fixed superficial water velocity of 0.1ft/sec, the dispersed oil bubbles congregated to form a larger and longer bubble, the so-called Taylor bubble. As with the behaviour shown in gas-water vertical flow, there were some small oil bubbles found between these Taylor bubbles. As the oil velocity was increased still further, Taylor bubbles were collapsed, leading to the churn flow. However, once the oil velocity was increased to about 5 or 10 ft/sec, the oil became the continuous phase in oil-water flow , which contained small bubbles of water.

By increasing water velocity (1ft/sec) for the flow regime A and B, as shown in Fig. 1-5, the number of oil bubbles was apparently reduced. For the slug flow and churn flow, the longer and larger oil bubbles were no longer present. The flow regimes were close to bubbly flow. For F and G, we can see that the fluid contains more water bubbles in the pipe.

Solids-liquid flow

Solids-liquid flow is often also called slurry flow and is a frequently encountered flow phenomenon in the processes of mineral transportation industries. Solids-liquid flow represents the flow of a liquid, which is the continuous phase carrying solids as the dispersed phase. When the mixture flows in a vertical pipe, the particle distribution is radially symmetric in the liquid. Unlike gas-liquid flows there is no slug flow or churn flow [13]. Slurry flows in inclined pipes demonstrate more complicated flow phenomena due to the densities of solids being greater than the liquid.

Both Lucas and Cory [14] and Al-Hinai[15] have investigated inclined solids-in-water flows. A commonly observed flow regime is shown in Fig. 1-6. It is clear that the solids distribution is highly non-uniform. This is because of the action of the gravitational force. The solid particles sink to the bottom of the pipe. When this solid accumulation reaches a specific value, it will flow backwards down the pipe.

Solid recirculation occurs in the middle region of the pipe due to the action of so-called Kelvin-Helholtz waves. Lucas *et al.* showed, that in the region at the upper side of the inclined pipe the solids velocity is relatively higher than in the region towards the lower side [14, 15] [16]. On the

other hand, the volume fraction of solids close to the lower side of the pipe is higher than near the upper side of the pipe.

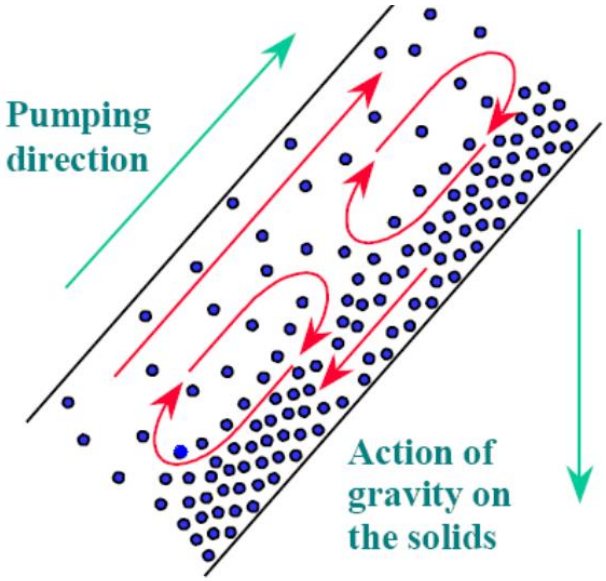

Fig. 1-6 Solids-liquid flow in inclined pipe[13]

1.2.2 Test separator-based measurement system and its limitations

The traditional test separator-based measurement system is shown in Fig. 1-7 (a). It can be seen from the figure that the different phases are separated before measurement takes place. By using different types of single phase flow meter, the volumetric flow rate (or mass flow rate) for each phase can then be measured from the outlet streams of the test separator. However, their large size and heavy weight limits their use on offshore platforms where space is extremely valuable. Moreover, they depend on the action of gravity to separate the various phases, and this generally requires stabilisation times of several hours or days before reliable measurements can be made. This could result in lost profits for oil companies as oil prices fluctuate significantly and rapidly. In addition, despite each phase being individually measured by a single phase flow meter, the accuracy varies from ±5% to ±10% for each phase flow rate which is only just acceptable [6, 17].

Considering the above limitations of test separators, the use of MPFMs (multiphase flowmeters) has been suggested as a means of overcoming such difficulties and better achieving the requirements of industrial applications [18]. By comparing Fig. 1-7(a) with (b), it is clear that an MPFM measurement system only needs a multiphase flow meter and multiphase pump, which substantially reduces the physical footprint of the entire system, thereby leading to capital cost savings in the initial installation. In the particular case of exploring new oil and gas fields in deep water, the extremely expensive deep-water pipelines costs can be reduced (i.e. deep-water pipelines can cost up to $10 million per kilometre), which will effectively improve project viability [19].

Because inline MPFM measurement systems do not require phase separation, they have the ability to continuously provide flow information in subsea applications [20]. This characteristic is useful to prevent flow assurance risks (e.g. pipeline blocking problems). Specifically, when oil-gas-water multiphase flows are exploited from the same well, several types of solids deposits may occur in the pipeline, such as hydrates, asphaltenes, emulsions and waxes, which can cause blockages. In such cases, the field engineer can make appropriate risk mitigation decisions using MPFM online flow measurements. For example, once the blockage is found, the prevention programs start running, which may include injecting an appropriate flow rate of hydrate-formation inhibitors or heating the pipes [20-23].

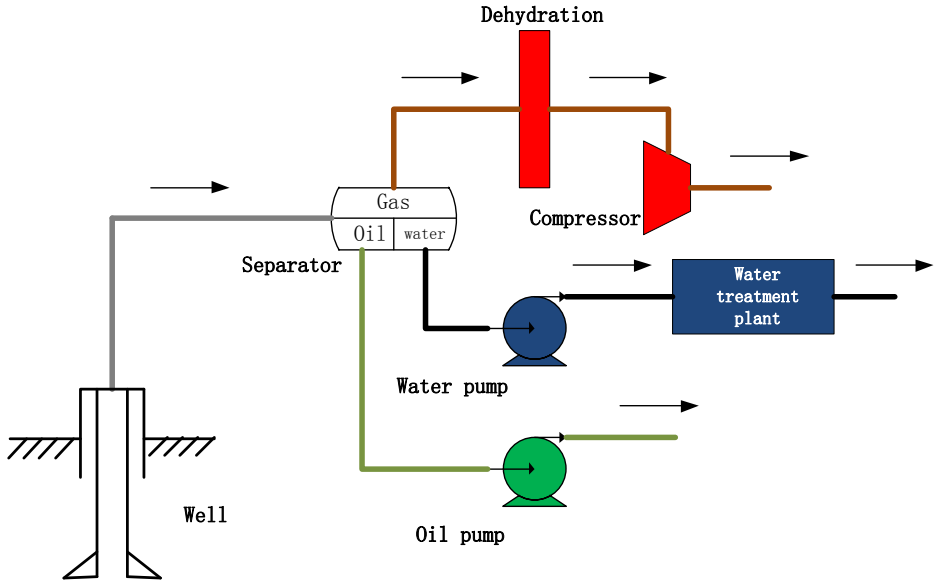

(a)

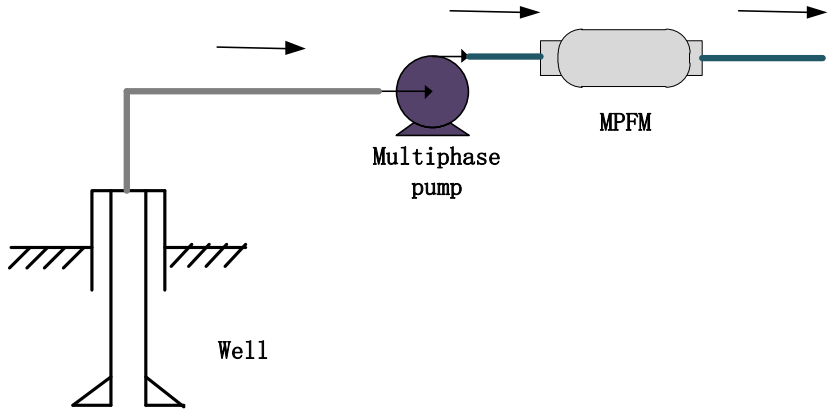

(b)

Fig. 1-7 Schematic diagram of the multiphase flow measurement system (a) traditional test separator-based measurement system; (b) inline MPFMs system [3]

1.3 Overview of conventional MPFM techniques

The last section demonstrated the importance of multiphase flow measurement in industrial applications (especially in oil-gas industrial applications). By comparing a traditional separator-based flow measurement system with inline MPFMs, it can be seen that the inline MPFM is an attractive technique for use in oil-gas industrial applications. This section describes the basic principles of conventional MPFMs and also their measurement problems.

1.3.1 Measurement strategies of conventional MPFMs

As stated earlier, the most important parameters normally used to analyse a multiphase flow are the volumetric flow rates of each phase. For oil-gas-water three phase flow produced from wells, the volumetric flow rate of each of the gas, oil and water phases are needed. The expression of oil volumetric flow rate, gas volumetric flow rate and water volumetric flow rate are given by Equation 1-4, Equation 1-5 and Equation 1-6, respectively. From these equations, the essential parameters to be determined include mean gas volume fraction, $\overline{\alpha}_g$, mean oil volume fraction, $\overline{\alpha}_o$, and mean gas velocity, $\overline{v}_g$, mean oil velocity, $\overline{v}_o$, and mean water velocity, $\overline{v}_w$.

$$Q_o = A\overline{\alpha}_o\overline{v}_o \qquad \text{Equation 1-4}$$

$$Q_g = A\overline{\alpha}_g\overline{v}_g \qquad \text{Equation 1-5}$$

$$Q_w = A[1-(\overline{\alpha}_g+\overline{\alpha}_o)]\overline{v}_w \qquad \text{Equation 1-6}$$

where A is pipe cross-sectional area.

It is worth noting that the relationships given in Equations 1-4 to 1-6 are only valid for homogeneous flows.

There is no existing single technique that can be used to directly measure all the above parameters. Thus, inline MPFMs currently in use are based on two basic measuring strategies, which are described below:

Indirect measurement of multiphase flow

Because of the many difficulties of directly measuring flow parameters in oil-gas-water three phase flows, the 'indirect measurement' method has been proposed to simplify the process. The conventional inline MPFM with this method comes in two typical types:

1. Compact separator system type

As Fig. 1-8 shows, this type of MPFM includes a compact separator, which is used to extract the gas phase flow from the three phase mixture fluid before measurement takes place. The volumetric flow rate of the gas phase is measured by using a single phase flow meter (e.g. a Vortex shedding flow meter) while the remaining two phase oil-in-water flow is passed through a liquid flow meter and a water cut flow meter [6, 24-26]. Note that the water cut flow meter is used to obtain the mean water volume fraction in the liquid. The basic principle of this type of flow meter is to reduce the measurement problem from a three phase flow to the combination of a single and two phase flow.

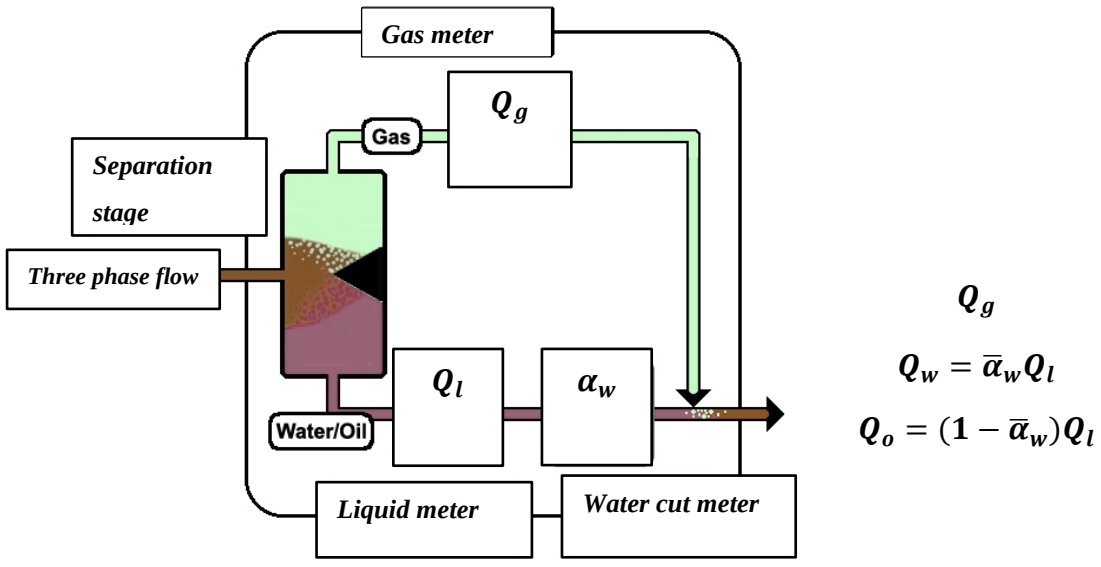

Fig. 1-8 Schematic diagram of compact separator MPFM[27]

The volumetric flow rate of oil and water can be determined by using the following equations:

$$Q_w = \overline{\alpha}_w Q_l$$ Equation 1-7

$$Q_o = (1 - \overline{\alpha}_w) Q_l$$ Equation 1-8

where $\overline{\alpha}_w$ is mean water volume fraction, which is measured by using a water cut meter and Q_l is the liquid (water and oil) volumetric flow rate, which is measured by using a liquid flow meter.

It is claimed that the average accuracy of volumetric flow rate measurement for commercial MPFMs based on this technique is about ±2%, but the size issue remains, and the device is still too large for many applications [27].

2. Inferential measurement type

The basic principle of the inferential measurement type of MPFM is to estimate flow parameters for each phase by using as few measurements as possible in conjunction with an adequate mathematical model.

Lucas [28] developed a mathematical model which predicted oil and water local axial velocity profiles in inclined oil-in-water two phase flows dependent on simple auxiliary measurement (i.e. local water volume fraction and axial pressure gradient). The reported prediction results were in good agreement with the reference measurement results. However, it was shown that this model is only valid for specific cases, for example, the oil-water mixture must be locally well mixed and the mean properties of the flow cannot vary significantly with time. To increase the range of application, other methods involve the use of an empirical mathematical model to determine the parameters of the flow. However, they are still not immune from the dependency problem associated with flow regimes.

In order to overcome this issue, pattern recognition and neural network techniques have been suggested to provide a relationship between the measurements from three independent sensors and the volumetric flow rate of each phase in the flow. Once the measurements of three sensors have been obtained, the volumetric flow rate of each phase can be determined from these techniques. It is worth noting that the pattern recognition techniques require calibration in known multiphase flows which are established in laboratory flow loops. Similarly, neural network methods require that the neural network is trained in known flows [29]. According to several

papers in the literature, the calibration and training processing are considered to be the major limitations of these methods due to the calibration procedure being relatively complicated and the fact that results obtained in laboratory calibration flow loops may not be valid for multiphase flows in real oil wells [8, 29-31].

Direct measurement of multiphase flow

The direct measurement multiphase flow meter, as the name suggests, is characterised by the fact that there is no need for pre-separation or homogenising of the flow before measurement. By using two or more measurement techniques, this type of flow meter can directly obtain the volumetric flow rate for each phase from online measurement of the mean volume fraction and velocity for the flowing phases.

The Schlumberger Vx MPFM is an example for this type of flow meter, which uses a Venturi-based differential pressure measurement and dual-energy gamma ray absorption measurement [32] (see Fig. 1-9).

By inspection of Fig. 1-9, it can be seen that this device contains three main and distinct sections. First, a Venturi section and differential pressure transmitter are used to measure total volumetric flow rate. Second, the nuclear system, which includes a gamma source and detector, is used to obtain the mean volume fractions of the oil, gas, and water phases across the cross-section of the Venturi throat. Third, a compact flow computer is used to process the online measured data and provide the online volumetric flow rate results.

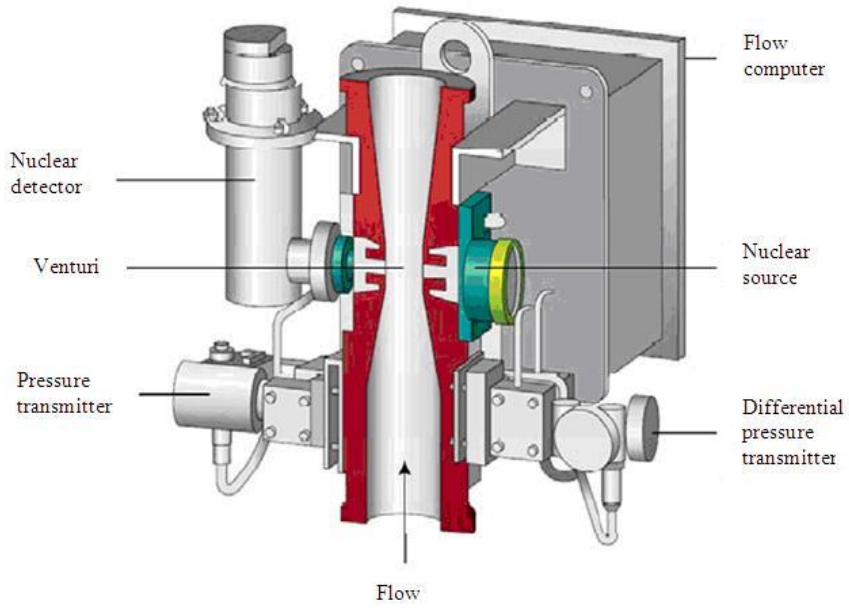

Fig. 1-9 Structure of Schlumberger Vx MPFM[33]

Al-Bourni *et al.* [34] experimentally tested five Schlumberger Vx MPFMs in the offshore-Khafji field in comparison with a reference conventional test separator measurement system. The test report shows that the relative error for the oil and water flow rates is in the range of 5-10% and, for the gas phase, the relative error is over 15%, although a separator was not installed in the system.

From the above results, it can be seen that this type of conventional MPFM still has some limitations.

1.3.2 Limitations of conventional MPFMs and Process Tomography (PT) techniques

From the discussion in Section 1.3.1, it is clear that the MPFMs with different measurement methods can continuously obtain the necessary flow information for multiphase flows from oil and gas wells. However, the conventional MPFM techniques still have limitations. One major limitation is that the measurement is flow regime-dependent. Ismail *et al.* [35], Caniere *et al.* [36] and Irons *et a.l* [37] have demonstrated that, when the flow regime of two phase flow (air-water or solids-air) was changed, the phase volume fraction measurements obtained by conventional MPFMs would be influenced. An example, as shown in Fig. 1-10**,** is the work of Caniere *et al.*

[37] who investigated the differences between the capacitance measurements for the annular and the stratified air-water flow regime using a capacitance sensor. By looking at Fig. 1-10 , it is apparent that, with the same air volume fraction, the output of capacitance measurement for stratified flow is greater than the annular flow until the air volume fraction reaches 0.6. Therefore, if the capacitance measurements have an inaccuracy, the volume fraction measurements might have greater errors.

To minimise the effect of flow regime variations on the accuracy of measurements, most existing multiphase flow meters must be installed in the vertical working section,which makes the flow profile axisymmetric. In addition, some conventional MPFMs homogenise the flow by using an inline mixer or blind tee joint [6]. However, these methods for overcoming flow regime dependency bring new problems, e.g. increased cost of flow pipe allocation and maintenance cost.

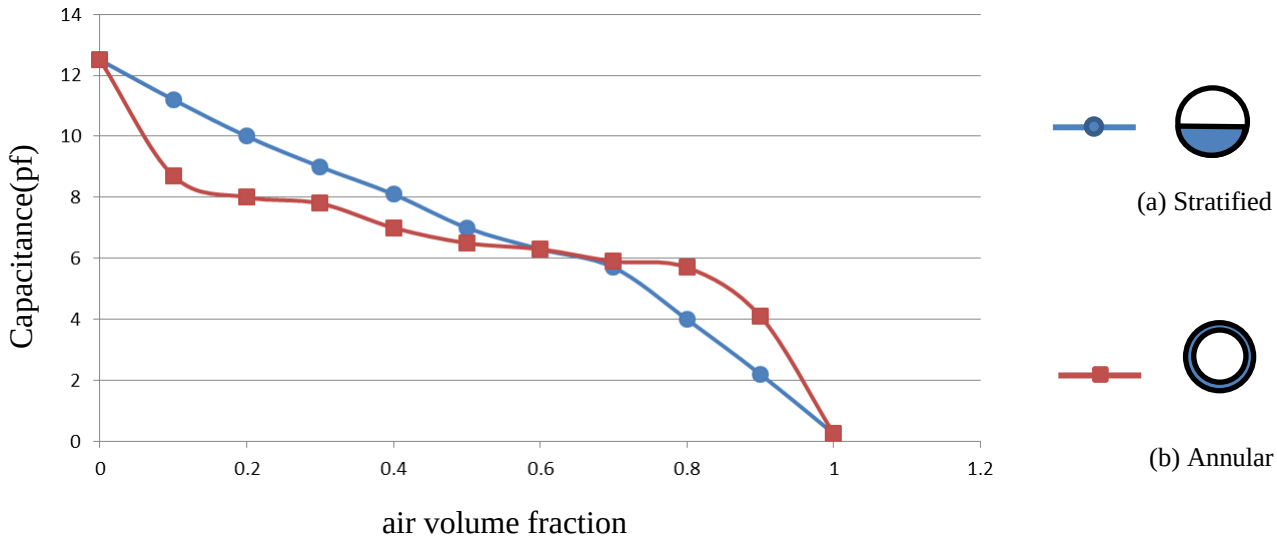

Fig. 1-10 Effect of flow regimes on solids volume fraction measurement using a common capacitance sensor (a) Stratified flow regime, (b)Annular flow regime [37]

A relatively new approach, Process Tomography (PT), has been proposed for use in multiphase flow measurement. The basic concept of Process Tomography(PT) technique for multiphase

flow measurement application is to image the cross-section of a multiphase flow by using a number of independent measurements(such as electrical resistance) from multiple sensors. By using the reconstructed image in conjunction with an appropriate mathematical model, the desired flow parameters, such as local volume fraction distribution and local velocity distribution, for each phase can be determined[6, 8, 35, 38].

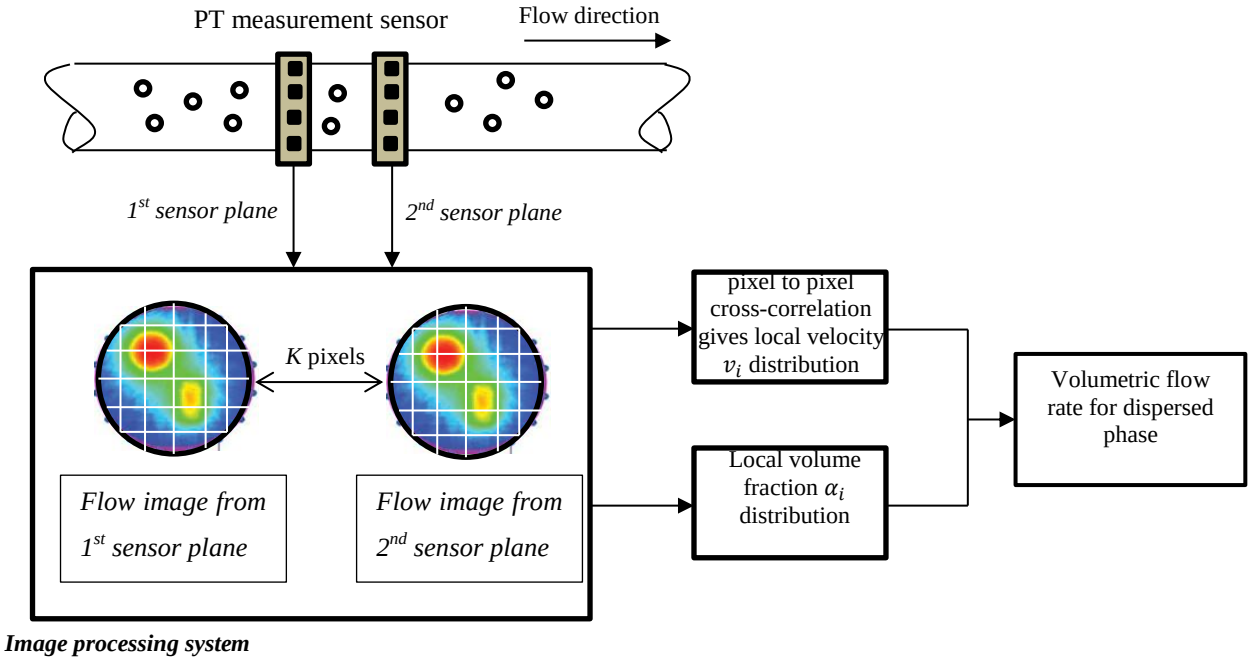

Fig. 1-11 A multiphase flow meter based on PT technique

A typical PT technique, Electrical Resistance Tomography (ERT)-based multiphase flow meter (MPFM) is shown in Fig. 1-11. From the diagram, it can be seen that the ERT system contains two sensor arrays. When the multiphase flow passes through them, the measurements from the sensors are used to provide a flow image for each sensor plane respectively. The flow cross-sections for the 1st and 2nd sensor planes are divided into K pixels with areas A_i. With this feature, the non-conductive dispersed phase volume fraction for each pixel $\alpha_{d,i}$ can be determined by converting conductivity measurements according to a mathematical model. More details will be described in Section 2.2.3. In this technique, pixel by pixel cross-correlation (see

Section 2.2.3) is used to determine the non-conductive dispersed phase velocity profile $v_{d,i}$. Therefore, the volumetric flow rate of the non-conductive dispersed phase can be calculated by the following equation:

$$Q_d = \sum_{i=1}^{K} \alpha_{d,i} v_{d,i} A_i \qquad \text{Equation 1-9}$$

Once the local volume fraction and local velocity distribution are accurately obtained, the volumetric flow rate can be determined regardless of the flow regime. Because of this advantage, MPFM accuracy can be improved by reducing flow regime dependency. There are many types of tomographic technique used in MPFMs, including gamma ray and X-ray tomography, Electrical Impedance Tomography (EIT) and , Electrical Capacitance Tomography (ECT) [35, 39-41]. More details of tomographic MPFMs are given in Chapter 2.

1.4 Aim and objectives of the present study

From the discussion as presented in Section 1.3.1, it can be seen that direct measurement commercial inline MPFMs generally have an accuracy of ±10%. Ismail *et al*.[35] and Thorn *et al*.[6] have concluded that the main factor affecting the accuracy of inline MPFMs is flow regime dependency. This has generated considerable interest from industry in introducing PT-based techniques into a multiphase flow meter. Over the past ten years, a number of different PT-based MPFM techniques have been developed and applied into oil industrial application. Because most existing tomographic techniques can only be used to obtain flow parameters for the non-conductive dispersed phase flow, such as volume fraction profile and velocity profile for non-conducting dispersed phase flow, there is a need for a new measurement technique for measuring the local velocity distribution of the conducting continuous phase to enable calculations of the volumetric flow rate of the conducting continuous phase (see Equation 1-1 and Equation 1-3).

For this reason, the aim of the present research is to construct an innovative multi-electrode electromagnetic flow meter capable of measuring the local velocity distribution of the conducting continuous phase (water) in oil-gas-water three phase flows or air-in-water two phase flows.

The main objectives of this research work are:

1. To investigate and develop a methodology which is capable of determining the local conducting continuous phase velocity profile in multiphase flow for both vertical and inclined flows.
2. To develop a physical flow meter capable of measuring the local velocity distribution of a conducting continuous phase in multiphase flow without the use of a radioactive source or an instrusive homogenizing mixer.
3. To combine the technique in objective 2 with existing techniques (e.g. ERT) for measuring the local volume fraction distribution of the dispersed and continuous phases to enable calculation of the volumetric flow rate of the continuous phase.
4. To experimentally investigate the performance of the physical flow meters in 2 and 3 above .

2 Literature review

2.1 Introduction

From the discussion presented in the previous chapter, it is clear that the development of inline Multiphase Flow Metering (MPFM) is an important research topic for the oil and gas industry. After decades of research, academics and industrialists have developed and implemented many commercial devices using different measurement methods (see Section 1.3). However, they are all flow regime dependent (most are valid only for homogeneous flows), which reduces their applicability and reliability. There is, thus, the need to develop a MPFM flow device which combines a number of Process Tomography (PT) techniques, such as electrical tomography (impedance, capacitance, resistance, etc.) (see Section 1.3.2).

Most research efforts have been invested in more accurate profiling of the local dispersed phase volume fraction and velocity distribution, based on the resistance (or capacitance) tomography technique. However, for the continuous phase which is conducting (e.g. continuous water phase), few tomographic techniques have been developed or results published. Thus, today, there is an increasing demand for a reliable, low cost and non-radioactive technique that can be used to obtain the local velocity profile for the conducting continuous phase in multiphase flow (e.g. flows where water is the continuous phase). The later parts of the chapter focus on a review of continuous phase velocity measurement techniques in multiphase flow.

Section 2.2 contains a brief review of previous research into measurement of the non-conducting dispersed phase volume fraction and velocity for two/three phase flows where water is the continuous phase. In Section 2.3, techniques for measuring the conducting continuous phase flow velocity in multiphase flow are described, including information on basic working principles, design, applications and limitations.

2.2 Previous relevant research on multiphase flow measurement

2.2.1 Mean volume fraction and velocity measurement for dispersed phase using impedance techniques

A popular technique for determining the mean volume fraction of dispersed solids or oil in water continuous flows has been by measuring the electrical impedance of the flow using different arrangements of electrodes placed around the perimeter of the pipe containing the flow [42-45]. A typical electrode arrangement is shown Fig. 2-1. From the diagram, we can see that two sensors (upstream and downstream) were fully immersed in the fluid with each sensor containing two electrodes. In each sensor, the current is injected from one electrode. The other electrode is connected to a voltage measurement circuit. Referring to the review of impedance techniques by Ceccio and George [46], this technique is only for an electrically conducting continuous phase flow (e.g. water) with non-conducting dispersed phase (e.g. solids/oil/gas).

A number of researchers [14, 15, 38, 47] have shown it is possible to determine the mean dispersed phase volume fraction $\overline{\alpha}_d$ by using Maxwell's extension function, as shown in Equation 2-1 [38, 48] :

$$\overline{\alpha}_d = \frac{2\sigma_w - 2\sigma_m}{\sigma_m + 2\sigma_w} \qquad \text{Equation 2-1}$$

where σ_m is the measured conductivity of the mixture and σ_w is the water conductivity,

By inspection of Equation 2-1, it can be seen that it was necessary to determine the value of σ_m before calculating the volume fraction $\overline{\alpha}_d$. The following procedure shows how to determine the value of σ_m :

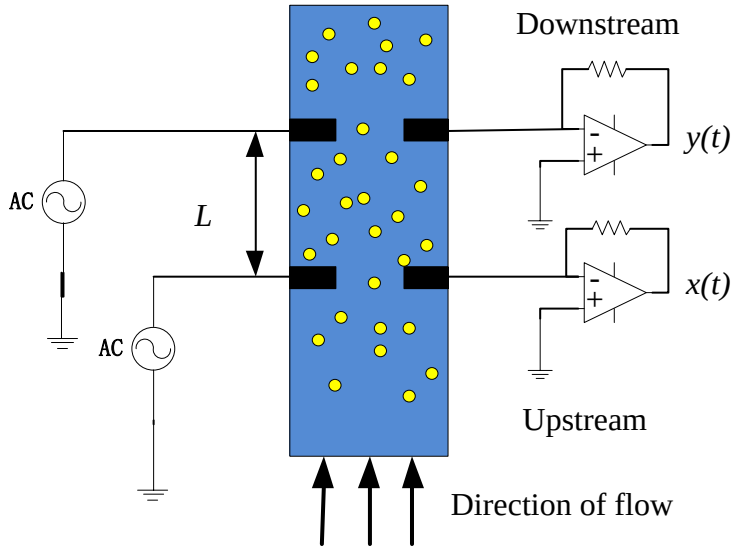

Fig. 2-1 Configuration of half-ring electrode for impedance measurement technique [46]

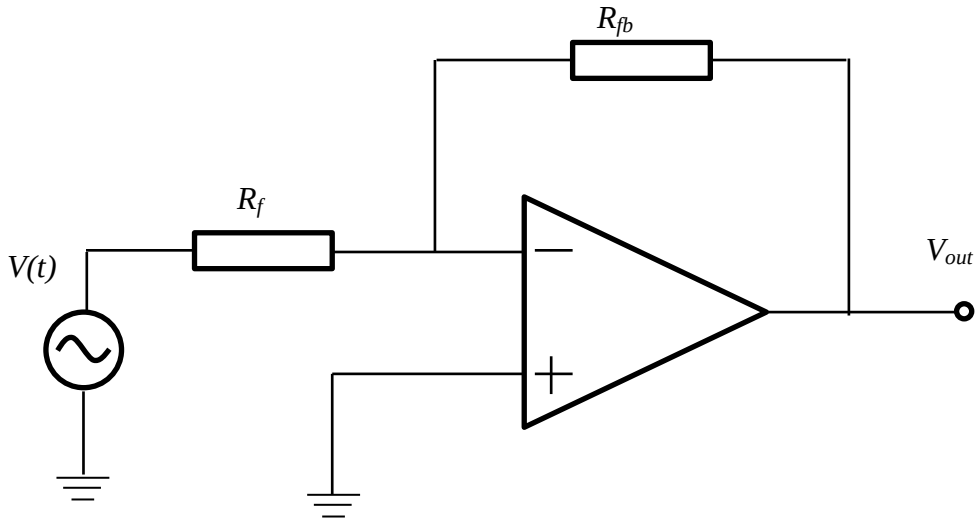

Fig. 2-2 Conductance measurement circuit[13]

As mentioned at the beginning of this section, both electrodes were fully contacting the flow and one of them was connected to the conductance measurement circuit, as shown in Fig. 2-2 . In Fig. 2-2 R_f represents the resistance of fluid between the two electrodes. Because the entire

measurement circuit is based on an inverting amplifier circuit, the output signal V_{out} can be written as:

$$V_{out} = -V(t)\frac{R_{fb}}{R_f} \qquad \text{Equation 2-2}$$

where $V(t)$ is excitation signal and , R_{fb} is the feed back resistor.

If the fluid conductance is defined as G_f , Equation 2-2 can be expressed as:

$$V_{out} = -V(t)R_{fb}G_f \qquad \text{Equation 2-3}$$

Referring to Al-Hinai [13], Lucas and Cory [14], the fluid conductance G_f is given by:

$$G_f = K_s\sigma_m \qquad \text{Equation 2-4}$$

where K_s is system constant, or so-called cell-constant[47] .

Hence, by substituting Equation 2-4 into Equation 2-3, the result is:

$$V_{out} = -V(t)R_{fb}K_s\sigma_m \qquad \text{Equation 2-5}$$

Equation 2-5 can be re-written as:

$$|V_{out}| = |V(t)|R_{fb}K_s\sigma_m \qquad \text{Equation 2-6}$$

where $|V_{out}|$ and $|V(t)|$ represent amplitude of output signal and amplitude of input excitation signal, respectively.

From Equation 2-6 it is now possible to write that:

$$\sigma_m = \frac{|V_{out}|}{|V(t)|}\frac{1}{K_s R_{fb}} \qquad \text{Equation 2-7}$$

It is worth noting that the cell constant K_s can be found by:

$$K_s = \frac{V_{out,w}}{\sigma_w}$$ Equation 2-8

where $V_{out,w}$ is the output voltage obtained when the measured flow is water only. .

For dispersed phase velocity measurement, the technique most widely reported in the literature and widely used in industrial applications is the cross-correlation technique [14, 49-53]. Referring to the above electrode configuration, when the dispersed phase passes through an upstream sensor, a change is generated in the output signal. The same dispersed phase particles travel with the flow and pass through the downstream sensor, where a similar change is generated in the output signal. From these changes in output signal for the two sensors, the delay time can be found that is equal to the time taken for these solid particles to travel between the sensors. Specifically, as shown in Fig. 2-1, according to Beck and Plaskowski [54] , if the time-dependent signal *x(t)* is from the upstream sensor and the signal *y(t)* is from the downstream sensor, the cross-correlation function $R_{xy}(\tau)$ is defined as:

$$R_{xy}(\tau) = \lim_{T\to\infty} \frac{1}{T} \int_0^T x(t)\, y(t+\tau) dt$$ Equation 2-9

In the above equation, *T* is the time period over which the signals *x(t)* and *y(t)* are sampled. If the signals *x(t)* and $y(t+\tau)$ match, the integral value is maximised. This occurs when the signals are aligned. Therefore, the time taken for the dispersed phase (i.e. solids, gas or oil) to move from the upstream to downstream sensor is τ_p, where τ_p is the value of time delay for which the cross-correlation function $R_{xy}(\tau)$ is at maximum. The average dispersed phase velocity $\bar{v}_d$ is then given by:

$$\bar{v}_d = \frac{L}{\tau_p}$$ Equation 2-10

where *L* is the distance between the upstream and downstream sensors.

2.2.2 Local volume fraction and velocity measurement for the dispersed phase using impedance techniques

Lucas and Cory [14] developed a conductivity probe with six flush-mounted ring electrodes which has been successfully used to determine the local volume fraction and local velocity distribution for the dispersed phase of solids-in-water two phase flows . A PC-based controller mechanism was used to traverse the local probe throughout the pipe cross-section. Using a similar principle to that described in Section 2.2.1, two sensors (A and B in Fig. 2-4) were used to measure the varying voltage drop when the dispersed particles passed by the probe. With reference to the conductance measurement circuit, as shown in Fig. 2-3, the mixture conductivity σ_m can be determined using Equation 2-11 [55]:

$$\frac{\sigma_m}{\sigma_w} = \left(\frac{V_{ref}}{V_c}\right)_m \left(\frac{V_c}{V_{ref}}\right)_w \qquad \text{Equation 2-11}$$

where V_c is measured voltage drop with the mixture fluid by using sensor C and V_{ref} is the reference voltage measurement of reference resistance.

By substituting Equation 2-11 into Equation 2-1, the local dispersed phase volume fraction in that specific position can be calculated.

Furthermore, referring to Fig. 2-4, it is apparent that the measured voltage from both sensor A and B can be used to determine the local dispersed phase velocity by using a cross-correlation method. By repeating the above procedures several times, the local dispersed phase volume fraction and local dispersed phase velocity distribution can be obtained. However, it should be noted that the six electrode conductive probe is an intrusive technique whose use is restricted by the flow condition (i.e. too much solid in the flow would damage the probe). In addition, an intrusive measuring device will affect the velocity and volume fraction distribution. Clearly, this technique is best suited for laboratory applications.

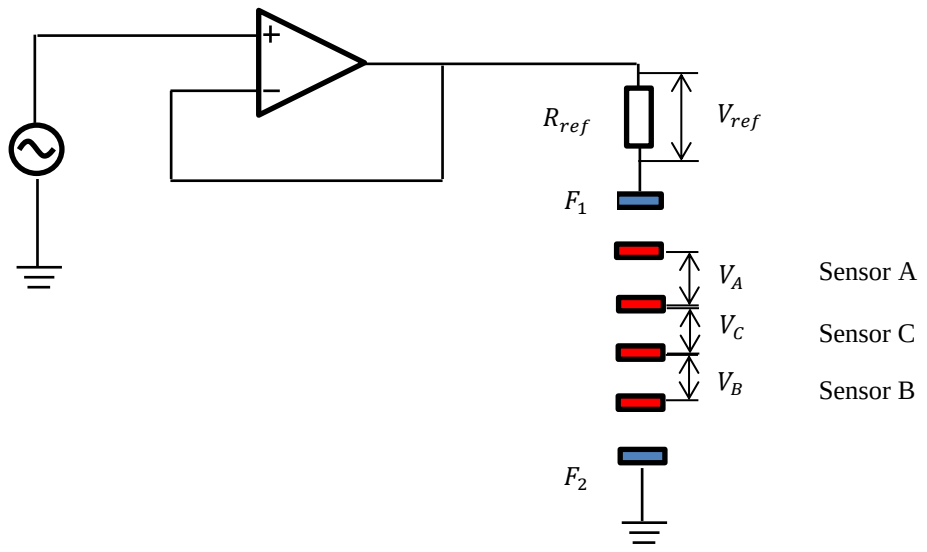

Fig. 2-3 The six-electrodes probe conductance measurement circuit[14]

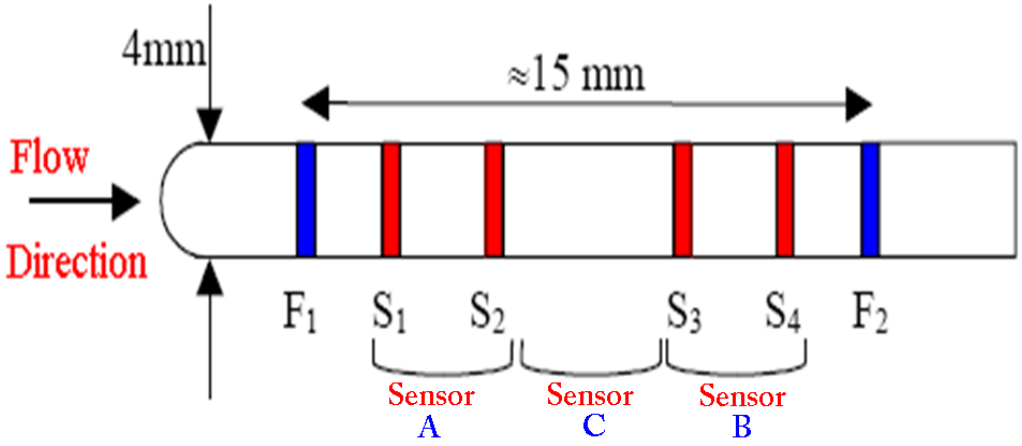

Fig. 2-4 Six-electrode conductivity probe as designed by Lucas and Cory [14]

2.2.3 Local volume fraction and velocity distribution measurement using tomography

To overcome the limitations of intrusive flow measurement devices, a number of researchers have proposed using tomography techniques for measuring multiphase flow parameters. As described in Section 1.3.2, tomography techniques, also called Industrial Process Tomography (IPT), provide a two-dimensional image of a slice through an object. A number of images can

then be used to reconstruct a complete image representing the original object. Various tomography techniques are based on this principle, such as X-ray Computed Tomography which is widely used in medical applications[56]. However, the use of tomography technique to investigate multiphase flows has been developed and reported by, amongst others, Williams and Beck [37], Dyakowski [56], Wang *et al.* [50], Ismail *et al.* [34], Tan and Dong [48].

Referring to previous and current work, it is clear that several forms of tomography have been used to obtain the concentration and velocity distribution of the dispersed and continuous phase in two (or three) phase flows. These tomographic techniques generally can be categorised into two types: 'hard field' and 'soft field'. In 'hard field' tomography, the energy and direction of the electromagnetic radiation generated by the power source is constant, irrespective of the material or medium. Typical 'hard field' techniques include X-rays, gamma rays and magnetic resonance imaging (MRI). Compared to 'hard field' tomography, 'soft field' tomography is much more complicated. Taking a typical 'soft field' technique, Electrical Capacitance Tomography(ECT), as an example, capacitance is measured between pairs of electrodes to establish the permittivity distribution in the flow cross-section. From this perimittivity distribution the volume fraction distribution of one or more phases can be determined [41, 57]. Some common examples of 'soft field' tomography techniques are Electrical Resistance Tomography (ERT) and Impedance Cross Correlation (ICC) [51].

This section presents descriptions of some common tomography techniques for determining local dispersed phase volume fraction and velocity distribution in multiphase flow.

- ***Electrical Resistance Tomography (ERT)***

ERT is based on the impedance measurement principle as presented in Section 2.2.1. The aim of the ERT system is to obtain the conductivity distribution in the flow cross-section area. As a current is injected into an electrode, it is possible to obtain the conductivity distribution by measuring currents received at other electrodes [39]. Referring to Fig. 2-3, it can be seen that a number of electrodes are mounted around the pipe circumference and in direct contact with the fluid. Several common sensing strategies with different applications have been used and reported since the late 1980s [39].

In the first method, termed “adjacent pair strategy”, a known current is injected between pairs of electrodes and voltage measurements are obtained between other electrode pairs. The entire measurements will be finished when the full rotation is complete (see Fig. 2-5(a)). For an eight electrode configuration, by repeating the above procedure 20 times, all 20 possible independent measurements are obtained. It is worth noting that, for the adjacent pair strategy, the total number of independent measurements is simply calculated by $M_{ind} = N(N-3)/2$, where N is number of electrodes. However, by inspecting Fig. 2-5(a), it can be seen that for this excitation strategy, the sensitivity near the pipe wall is higher than the sensitivity at the centre of the pipe [58, 59]. This is because the current was injected into adjacent electrodes, which results in a higher current density near to the boundary of the pipe and lower current density in the centre of the pipe.

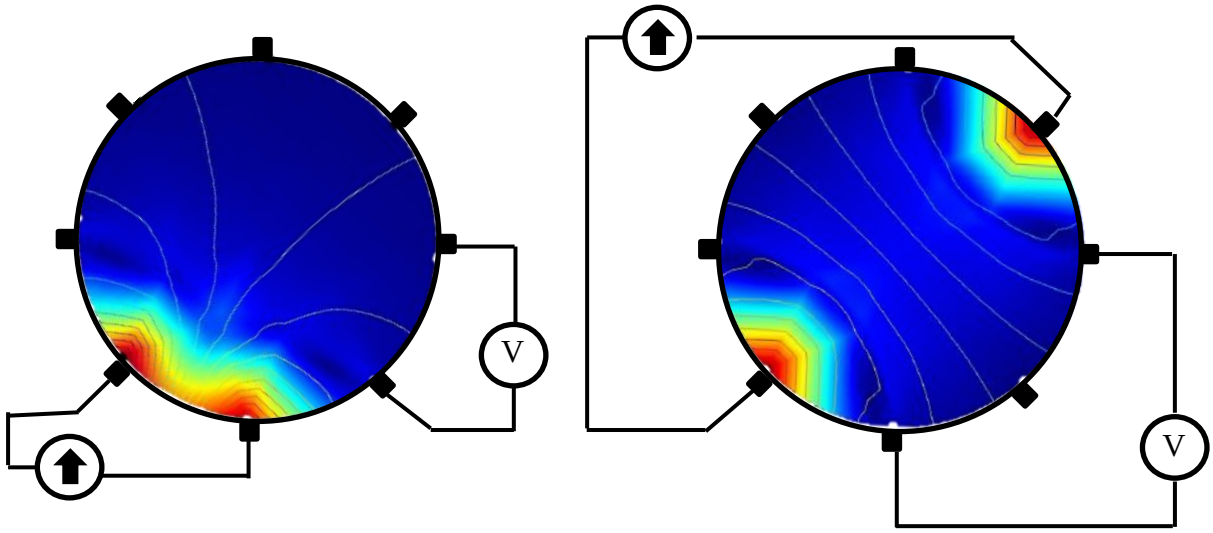

(a) (b)

Fig. 2-5 Electrical Resistance Tomography (a) Adjacent pair strategy, (b) Opposite pair strategy

The second method is called “opposite pair strategy”. By inspection of Fig. 2-5 (a) and (b), it can be seen that the main differences between the first and second method is that the current is applied into the oppositely aligned electrode pairs. The reason for this is to increase the current density at the centre of the pipe. However, the opposite pair strategy provides only

$M_{ind} = N \cdot (N-4)/2$ independent measurements, which is lower than the adjacent pairs strategy. For the eight electrode configuration, the number of independent measurements is 16, which means the image resolution will be reduced by 20% compared to adjacent pairs strategy [59-61]; this could then result in the reconstructed image having less information. Harikumar [62] stated that this excitation strategy provides better sensitivity distribution in comparison to the adjacent pair strategy. This means the reconstructed image can provide more information of objects at the centre of pipe in comparison with the adjacent pair strategy.

With the different sensing strategies, independent measurements of conductivity distribution are obtained using a reconstruction algorithm, and these can be used to obtain the local dispersed phase volume fraction distribution. The basic principle of the reconstruction algorithm is briefly outlined below.

Referring to the paper published by Ismail [35], the standard governing equation of an ERT system can be written as:

$$\nabla \cdot [\sigma(x,y) \nabla \varphi_e(x,y)] = 0 \qquad \text{Equation 2-12}$$

where $\sigma(x,y)$ is the conductivity distribution in the flow cross-section and $\varphi_e(x,y)$ is the electrical potential distribution[35].

A relationship can be obtained between the j^{th} voltage measurement $\Delta\varphi_{e,j}$ between a pair of electrodes on the boundary for a small conductivity change $\Delta\sigma_i$ in the i^{th} pixel and is given by:

$$\Delta\varphi_{e,j} = \sum_{i=1}^{p} -S_{i,j}\Delta\sigma_i \qquad \text{Equation 2-13}$$

where $S_{i,j}$ is a normalised sensitivity coefficient relating changes in the conductivity in the i^{th} pixel to changes in the j^{th} boundary voltage measurement (j=1,2,… M_{ind}) and P is the total number of pixels in the flow cross-section[35, 39].

Equation 2-14 can be expressed in matrix form as:

$$[\varphi_e] = -[S][\Delta\sigma] \qquad \text{Equation 2-14}$$

where $[\varphi_e]$ is a boundary potential difference matrix, $[\Delta\sigma]$ is the matrix representing conductivity changes in the P pixels and $[S]$ is the sensitivity matrix.

By inspection of Equation 2-15, it can be seen that the conductivity change matrix $[\Delta\sigma]$can be calculated using a matrix inversion algorithm, which can be expressed in the form:

$$[\Delta\sigma] = -[S]^{-1}[\varphi_e] \qquad \text{Equation 2-15}$$

Generally, the number of unknowns in ERT is greater than the number of voltage measurements, which means that the problem is ill-posed. Thus, a huge amount of computing power is needed to reconstruct the conductivity change image by performing iterative calculations. Once the conductivity change image has been reconstructed, the local dispersed phase volume fraction distribution can be obtained by using Equation 2-1 [49-51].

In order to determine the local dispersed phase velocity distribution, dual plane ERT systems have been developed and used. Referring to Fig. 2-6, a second electrode plane has been placed down-stream of the first electrode plane by a known distance *L*. Using a similar method to that shown in Section 2.2.1, the dispersed phase velocity can be measured by means of cross correlating changes in conductivity between corresponding pixels in the two image planes (i.e. plane *x* and plane *y*) using a technique known as pixel-pixel correlation [63]. Consider a simple example image which has 12 pixels, as shown in Fig. 2-7. If the spatial distribution of the

dispersed phase does not vary much during the transition from plane *x* to plane *y*, the discrete cross-correlation function is defined as:

$$R_{xy,k}(p\Delta t) = \frac{1}{N}\sum_{i=1}^{N} x_k(i\Delta t)\, y_k(i\Delta t + p\Delta t) \qquad \text{Equation 2-16}$$

$p = 0,1,2...m$ and $m < N$, $k = 1,2,3...12$

where Δt is the sampling time between successive images at each plane, k is the pixel number, $p\Delta t$ is the frame delay time, and N is the length of data series for cross-correlation [63].

Once the peak value of the cross-correlation function is determined, the peak delay time τ_k for the k^{th} pixel can be obtained. Referring to Equation 2-17, the axial velocity $[v_d]_k$ of the dispersed particles at the k^{th} pixel can be expressed as :

$$[v_d]_k = \frac{L}{\tau_k} \qquad \text{Equation 2-17}$$

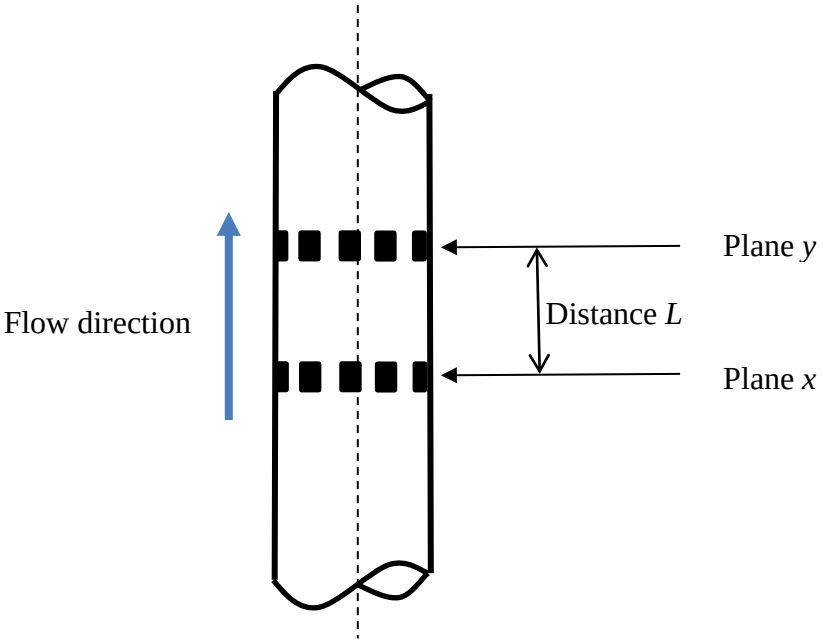

Fig. 2-6 Schematic diagram of dual-plane ERT system

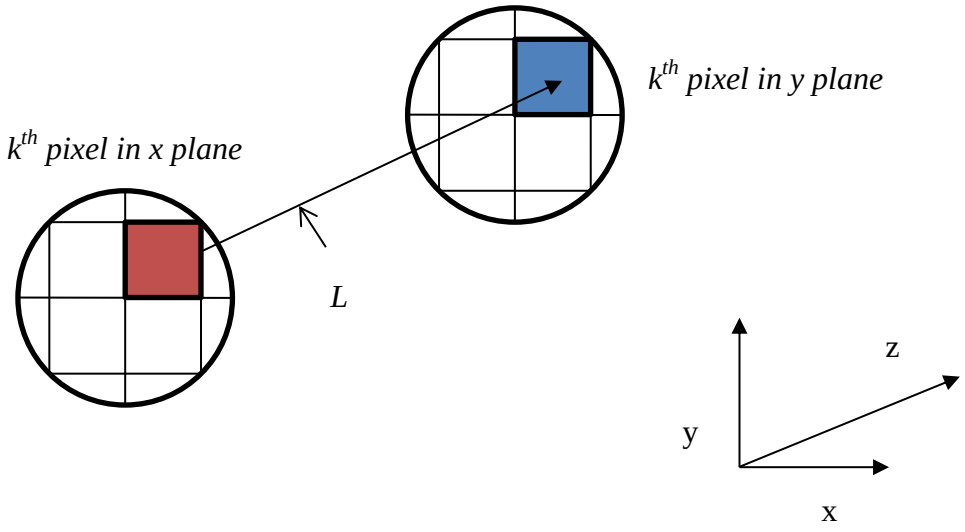

Fig. 2-7 Schematic diagram of local dispersed phase velocity distribution measurement based on pixel-pixel cross-correlation.

- ***Impedance Cross Correlation technique***

Another non-intrusive flow measurement technique that has been successfully used for determining the local solids volume fraction and velocity distribution in solids-in-water two phase flows is Impedance Cross Correlation (ICC). This technique was developed by Lucas and Al-Hinai [15, 64] and Muhamedsalih [16]. The ICC device has a similar structure to the dual-plane ERT system and consists of two arrays of electrodes separated by an axial distance of 50 mm, with each array containing eight electrodes equally spaced around the internal perimeter of 80mm diameter flow pipe. Every electrode in each array can be selected to be 'excitation', 'measurement' or 'ground'. An amplifier circuit is used to measure the fluid conductance between the excitation and measurement electrodes, which, in turn, can be related to the fluid conductivity and hence the local volume fraction of the solids and water phases [47]. To ensure the sensing region covers the whole pipe cross-section, the ICC measurement strategy consists of three different configurations which are described below. For each configuration, there are eight possible rotational positions. For the ξ^{th} configuration and ς^{th} rotational position a 'Centre of

action' (CoA) is defined with the solids and water volume fractions being measured at each of these CoAs [13].

Configuration I: similar to the adjacent pairs strategy of the ERT system, one electrode is selected as 'excitation'. An adjacent electrode is selected as 'measurement'. The remaining electrodes are set at 'ground' (i.e. earthed)[16]. This procedure is repeated for all eight possible rotational positions. With reference to the results reported by Al-Hinai [13], it can be seen that the corresponding eight regions which are interrogated are all relatively close to the internal face of the pipe wall.

Configuration II: in this configuration, one electrode is selected as 'excitation' and both adjacent electrodes are selected as 'measurement' and the five remaining electrodes are connected to 'ground' [16]. As with Configuration I, eight different rotational positions are possible for Configuration II .

Configuration III: in this configuration, two adjacent electrodes are selected as 'excitation', and the adjacent electrodes are set as 'measurement', while the remaining four electrodes are set at 'ground'[16]. Again, with this configuration eight different rotational positions are possible.

Referring to the Centre of Action (CoA) parameter and results developed by Al-Hinai [13] and Muhamedsalih [47] , it can be seen from Fig. 2-8 that, for Configuration III, the CoA is closer to the centre of the pipe than for Configuration I and II. Similarly, the CoA for Configuration II is closer to the pipe centre than for Configuration I. Al-Hinai [13] has also stated that, by using this CoA parameter, the measured local mixture conductivity $(\sigma_m)_{\xi,\varsigma}$ for a given configuration ξ and given rotational position ς can be used to estimate the local mean solids volume fraction $(\alpha_s)_{\xi,\varsigma}$. This calculation for ICC can be done by using Equation 2-18 [13, 65]:

$$(\alpha_s)_{\xi,\varsigma} = \frac{2\sigma_w - 2(\sigma_m)_{\xi,\varsigma}}{2\sigma_w + (\sigma_m)_{\xi,\varsigma}} \qquad \text{Equation 2-18}$$

As mentioned earlier, the ICC device has dual-plane sensors. Consequently, for a given configuration ξ and rotational position ς, the measured output voltages from the amplifier circuit for each measurement plane can be cross correlated to provide information on the local

solids velocity at each CoA corresponding to an interrogation region. This cross correlation function $R_{\xi,\varsigma}(\tau)$ can be written as:

$$R_{\xi,\varsigma}(\tau)=\frac{1}{T}\int_{0}^{T}(V_a)_{\xi,\varsigma}(t)(V_b)_{\xi,\varsigma}(t+\tau)dt \qquad \text{Equation 2-19}$$

where V_a and V_b represent the measured voltage signals from the amplifier circuit from upstream sensor plane 'a' and downstream sensor plane 'b', respectively. Again, once the peak delay time $\tau_{p,\xi,\varsigma}$ is obtained for the ξ^{th} configuration and ς^{th} rotational position, the local solid velocity for the corresponding CoA can be calculated by using Equation 2-10.

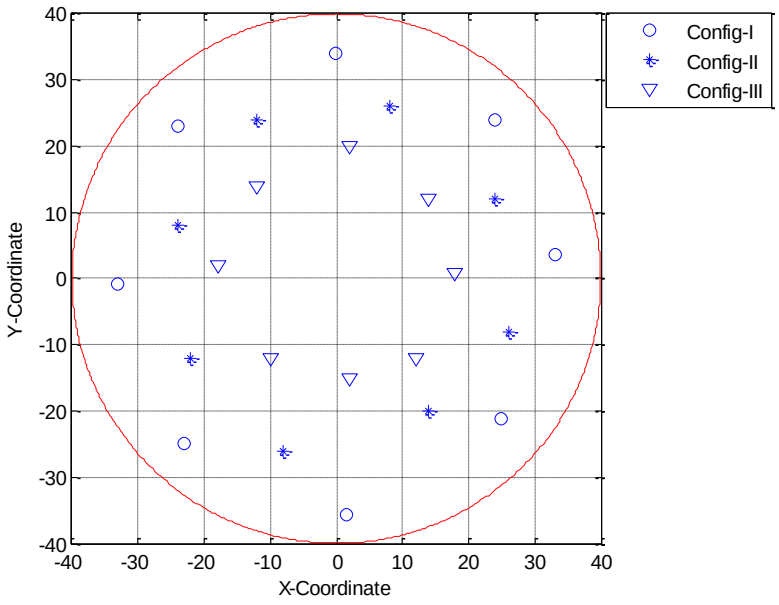

Fig. 2-8 Location of CoA for Configurations I, II and III for each of the eight electrode configurations [13, 47]

2.3 Techniques for measuring the velocity profile of the conducting continuous phase in multiphase flows

Referring to Section 1.4, most multiphase flow measurement techniques are still limited to determining local volume fraction and local velocity distributions of the dispersed phase while the continuous phase is a conducting medium. This section presents three existing techniques for measuring the velocity profile of the continuous phase in multiphase flow. As mentioned earlier, intrusive flow measurement techniques disturb the flow profile, so this section will focus mainly on non-intrusive tomographic techniques.

2.3.1 Conventional optical techniques

A popular non-intrusive technique used to investigate the flow velocity is optical visualisation. Among these techniques, Particle Image Velocimetry (PIV) is used for studying the velocity field in multiphase flow [66]. In this technique, tracer particles are inserted into the flow and a specific area of the flow is illuminated multiple times by a laser sheet at a very high frequency. Simultaneously, one or more high-resolution digital cameras are used to record the light scattered by the particles. Once the images for each light pulse are obtained, the displacement of the particles can be determined [67]. The vector velocity for each sub-area can be calculated using:

$$V_p = \frac{\Delta x_d}{\Delta t} \qquad \text{Equation 2-20}$$

where Δx_d is the vector particle displacement and Δt the time interval between laser flashes.

Another well-know technique is Laser Speckle Velocimetry (LSV). The basic principle of this technique is also to determine the placement of the tracer particles by using a laser light. The only difference is that the number of tracer particles used in the LSV technique is much greater than the PIV technique [67].

Although these optical techniques are capable of accurately obtaining the velocity profiles in a transparent single phase flow, they are much less accurate in multiphase flow measurement, particularly in the majority of oil industrial applications [8, 67, 68].

2.3.2 Magnetic resonance imaging

This section summarises some of the developments in MRI velocimetry that are most relevant to the work described in this thesis.

Magnetic resonance imaging (MRI) is an imaging technique based on the principle of nuclear magnetic resonance (NMR), which is used in many industrial and medical applications. MRI has many advantages over other imaging methods; it is non-intrusive, chemically inert and is not affected by optical factors (e.g. opacity), thus, as noted by Sederman [69], it is a technique that is being actively developed for continuous phase velocity measurement of multiphase flows.

For further information, the reader should refer to the numerous published reviews of MRI techniques for single and two phase flow characterisation, including Pope and Yao [70], Gladden [71], Fukushima [72] , Hogendoorn [73, 74] and Sederman[75].

There are numerous established MRI-based methods for measuring the velocity distribution of steady flows. One of the most common techniques for MRI velocimetry is the phase shift method, wherein a pair of equal but opposing field gradients are incorporated into the pulse program (see Fig. 2-9) [74]. The fundamental basis of the phase shift velocity method is based on the effects of the applied gradient $G(t)$ on the phase of moving spins[76]. Gladden [77] has shown that, if the spatial location of the spin is time-dependent, $r(t)$, the phase shift $\phi(t)$ is written in following form:

$$\phi(t) = \gamma \int_0^t G(t) r(t) \qquad \text{Equation 2-21}$$

where $G(t)$ is the applied gradient and γ is the gyromagnetic ratio.

The time-dependent position $r(t)$ is given by:

$$r(t) = r_0 + v_0 t + \frac{1}{2} a_0 t^2 + \ldots \quad \text{Equation 2-22}$$

where r_0 is the initial position , v_0 is the velocity and a_0 is acceleration.

Equation 2-22 can be rewritten as:

$$\phi(t) = \gamma \left[r_0 \int_0^t G(t)dt + v_0 \int_0^t G(t)tdt + \frac{1}{2} a_0 \int_0^t G(t)t^2 dt + \ldots \right] \quad \text{Equation 2-23}$$

These integrals are so-called moments of the gradient with time, which can be expressed as:

$$M_0 = r_0 \int_0^t G(t)dt \quad \text{Equation 2-24}$$

$$M_1 = v_0 \int_0^t G(t)tdt \quad \text{Equation 2-25}$$

$$M_2 = \frac{1}{2} a_0 \int_0^t G(t)t^2 dt \quad \text{Equation 2-26}$$

Applying a gradient pulse signal as shown in Fig. 2-9, the zero moment can be expressed using Equation 2-28. From Equation 2-28, it is found that the total relative phase shift, $M_0^{\pm G}$ is zero.

$$M_0^{\pm G} = \int_0^{\delta} G(t)dt + \int_{\Delta}^{\delta+\Delta} G(t)dt = G\delta + (-G\delta) = 0 \quad \text{Equation 2-27}$$

where Δ is the cycle time of the bipolar gradient pulse signal and δ is the length of pulse, as shown in Fig. 2-9

Similarly, the total first moment, $M_1^{\pm G}$, is given by:

$$M_1^{\pm G} = \int_0^{\delta} G(t)tdt + \int_{\Delta}^{\delta+\Delta} G(t)tdt = \frac{1}{2}G\left(\delta^2 - 0 - \Delta^2 - 2\delta\Delta - \delta^2 + \Delta^2\right) = -G\delta\Delta$$

Equation 2-28

Combining Equation 2-29 and Equation 2-24, relates the phase shift ϕ of the MRI signal to the velocity v_0 as:

$$\phi = \gamma v_0 G\Delta\delta$$ Equation 2-29

By inspection of Equation 2-29 it can be seen that the measured phase shift is linearly proportional to the velocity. From this relationship, a 2D map of the signal phase can be converted to a velocity image.

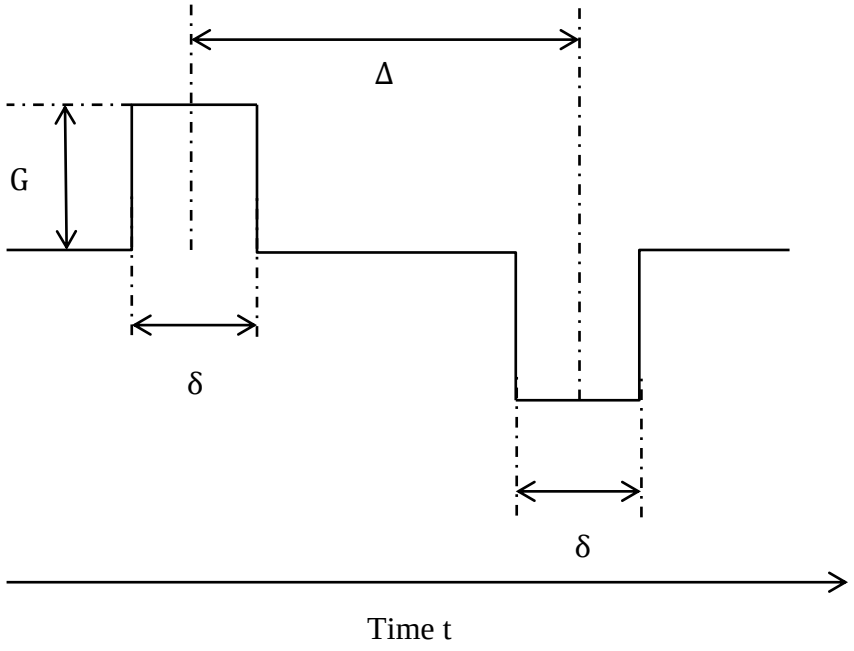

Fig. 2-9 A bipolar gradient pulse sequence with pulses of length δ, amplitude ±G and cycle time Δ [78]

Although MRI imaging techniques have many advantages in multiphase flow measurement, they have a number of intrinsic limitations, the most important of which have been discussed by Sederman [75].

- High cost and size issue

With reference to the published literature, it is found that one of the significant disadvantages of MRI is the high cost. The cost of an entire MRI system, which includes a permanent magnet system and superconducting magnet, is estimated to be more than £300,000 [75]. Furthermore, in order to reduce temperature effects in the coils, they must be immersed in liquid Helium. This would mean high maintenance costs. In addition, the MRI flow metering system might need more space than other inline MPFMs due to the generally huge size of the meter body. It is probably unsuitable for most oil industrial applications.

- Limitation of material and geometries of pipes

Because MRI systems generate strong magnetic fields, only non-ferromagnetic materials are applicable. Moreover, the geometries of the flow pipe are also restricted to ensure it passes through the bore of the magnet.

- SNR and resolution

Sederman [75] has shown that the imaging resolution is inversely proportional to the SNR and imaging time. This means that the higher the resolution, the longer must be the scanning time and the lower the SNR. However, for most multiphase flow conditions, especially for the fluctuating flow, it is necessary to increase the scanning frequency, which will lead to reduced spatial resolution.

2.3.3 Electromagnetic velocity profiler

Another popular technique for measuring the water velocity in many industrial applications is the magnetic flow meter. This technique involves establishing a magnetic field over a pipe cross-section and then simultaneously measuring the induced voltage when a conducting liquid passes through the flow meter. Based on Faraday's Law, the mean volumetric flow rate of the conducting phase can be obtained. Note that a detailed theory of conventional magnetic flow

meter will be given in the next chapter. However, this conventional magnetic flow metering technique is limited to measuring the mean volumetric flow rate in single phase flow.

For many years, engineers and scientists have been working on developing an electromagnetic flow metering technique which is able to obtain the flow parameters in multiphase flow. Heineman *et al.* [77] have reported using an electromagnetic flow meter (EMFM) to study a gas-in-liquid metal two phase flow. They found that there is a relationship between the predicted vapour volume fraction and the induced voltage signal. In order to verify their theoretical work, they placed two electromagnetic flow meters (EMFMs) in series in the working section of flow loop. When only the conducting liquid phase flow passed through the first meter, the induced voltage was obtained. That single conducting liquid phase was then mixed with a gas phase prior to the second meter. Using both measured induced voltage signals, the vapour volume fraction was determined with the following procedures.

When the fluid passed through the two electromagnetic flow meters, the induced voltage for each flow meter is shown by:

$$U_{E1} = B_1 D_1 V_1 \qquad \text{Equation 2-30}$$

$$U_{E2} = B_2 D_2 V_2 \qquad \text{Equation 2-31}$$

where B_1 and B_2 represent the mean magnetic flux density for the first EMFM and second EMFM, respectively; D_1 and D_2 represent the internal diameter of the first EMFM and second EMFM, respectively; and V_1 and V_2 represent the mean conducting continuous phase velocity in the first EMFM and second EMFM, respectively.

Because both EMFMs have the same geometry and features, we have $B_1 = B_2$ and $D_1 = D_2$. Combining Equation 2-30 and Equation 2-31, the induced voltage U_{E1} and U_{E2} can be expressed as:

$$\frac{U_{E1}}{U_{E2}} = \frac{V_1}{V_2} \qquad \text{Equation 2-32}$$

The volumetric flow rate of the mixture flowing is given by:

$$Q_{mix} = AV_1 = (1-\overline{\alpha}_d)AV_2$$ Equation 2-33

where A is the pipe cross-sectional area and $\overline{\alpha}_d$ is the mean volume fraction of the dispersed phase

Equation 2-33 can be re-written as:

$$\frac{V_1}{V_2} = 1-\overline{\alpha}_d$$ Equation 2-34

Substituting Equation 2-34 into Equation 2-32 :

$$\frac{U_{E1}}{U_{E2}} = 1-\overline{\alpha}_d$$ Equation 2-35

Hence,

$$\overline{\alpha}_d = 1-\left(\frac{U_{E1}}{U_{E2}}\right)$$ Equation 2-36

By comparing predicted vapour volume fraction with reference measurements, it was found the mean error was in a range of nine to twenty percent.

Following on from Heineman *et al.'s* work, Hori *et al.* [79] used two EMFM flow meters based on the same method as shown above to determine the volume fraction of inserted non-conducting plastic rods in Mercury and water flow. After a series of experiments, it was found that the measured volume fraction of non-conducting rods was generally slightly lower than that calculated from the ratio of the pipe cross-section and the cross-section of rods.

In 1983, a study of two phase flow using a transverse EMFM was reported by Bernier and Brennan [80]. Their conclusions reveal that, if a homogeneous mixture of two phases exists in the pipe, then the potential difference U_k can be expressed in the form:

$$U_k = \frac{2\overline{B}Q_c}{\pi R(1-\overline{\alpha}_d)}$$ Equation 2-37

where Q_c is the volumetric flow rate of the continuous phase flow and $\overline{\alpha}_d$ is the volume fraction of the dispersed phase, $\overline{B}$ is the mean magnetic flux density and R is pipe radius. Bernier [80] also investigated another special case of two phase flow: annular flow with a concentric gas core in the centre of the pipe. For this case, Bernier [80] published the following exact solution :

$$U_k = \frac{2R\overline{B}}{\pi(R^2 - R_g^2)} \int_{R_g}^{R} 2\pi r v(r) dr \qquad \text{Equation 2-38}$$

where R_g is the radius of the gas core and $v(r)$ represents the axisymmetric water velocity profile. When substituting the volume fraction $\overline{\alpha}_d = R_g^2 / R^2$ into this equation, it is same as the solution for homogeneous two phase flow (see Equation 2-38). Bernier and Brennen also quantified this technique's performance, which showed good agreement with their predictions (i.e. the error was about $\pm 2\%$) [80].

A new method for determining flow parameters in multiphase flow with EMFM was proposed by Velt *et al.* [81] and Krafft [82]. The basic principle of operation for this EMFM is based on measuring a voltage signal produced by the unequal eddy current. The eddy current is generated by applying a sinusoidal current into the coil to create an alternating magnetic field within the conducting phase. Velt *et al.* [81] found that when a non-conducting phase, such as gas bubbles, passed through the EMFM, the eddy current distribution in the flow became unequal and then produced a signal on the electrodes.

By inspection of this signal, as shown in Fig. 2-10, it is shown that, when the non-conducting phase (gas) moves from z1 to z0, the magnitude of signal increases until a maximum value U_{p1} and then falls to 0. When the non-conducting phase moves from z0 to z2, the magnitude of signal starts increasing until reaching another maximum value U_{p2} and then decreases to 0. Krafft [82] experimentally proved that the maximum value U_{p1} and U_{p2} occurred when the non-conducting phase (gas) reached a particular position. This position relies upon the design of the electrode and meter body. Once the distance L^* between the positions of U_{p1} and U_{p2} is determined, the

velocity of the non-conducting dispersed phase can be calculated by using a cross correlation method (see Equation 2-10). The delay time can be found by finding the maximum value of the cross correlation function of U_{p1} and U_{p2}.

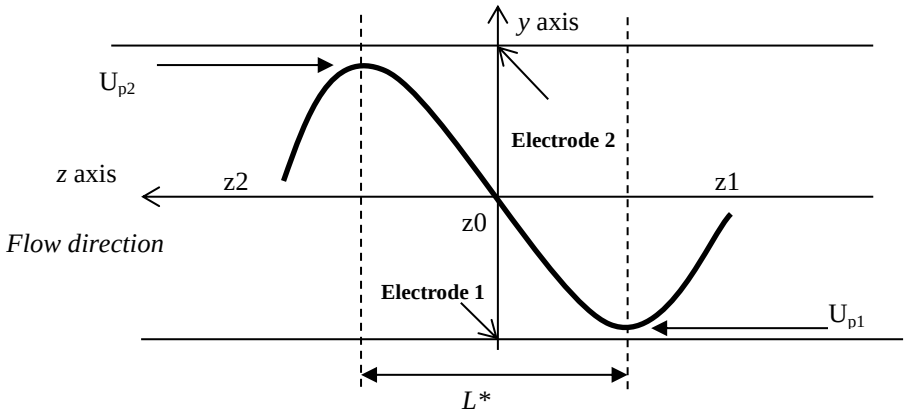

Fig. 2-10 Transformer signal when a single particle passed through the meter [82]

From the above descriptions of previous research, it can be seen that many flow measuring techniques have been developed for multiphase flow. However, techniques involving the use of a magnetic or electromagnetic field for obtaining the local water velocity distribution in two or three phase flows are not mentioned in any great number in the literature.

Lucas and Leeungculsatien [1, 83] have proposed a multi-electrode electromagnetic flow measuring device, the so-called Electromagnetic Velocity Profiler (EVP), which is based on Shercliff's[84] weight function theory. The profiler has been successfully applied in reconstructing the local axial water velocity profile in solids-in-water two phase flow. Fig. 2-11 shows the EVP device, which consists of a Helmholtz coil and flush-mounted electrodes. Based on this geometry, Lucas and Leeungculsatien [1, 83] divided the EVP flow cross-section into seven regions, as shown in Fig. 2-12. Specifically, with a single magnetic field projection, there are fourteen electrodes configured to measure seven electrical potential differences to obtain the average velocity in each independent region (pixel). By using this pixel arrangement in conjunction with the weight function theory described in Chapter 3, Lucas and Leeungculsatien

[1, 83] found that, for the case described above, the electrical potential difference $U_{j,evp}$ can be expressed as:

$$U_{j,evp} = \frac{2\overline{B}}{\pi R}\sum_{i=1}^{N} v_i w_{ij} A_i \qquad \text{Equation 2-39}$$

where R is internal pipe radius, $\overline{B}$ is the mean magnetic flux density in the flow cross-section and N is the total number of regions into which the flow cross-section is divided (here equal to seven), A_i denotes area of the i^{th} region and $U_{j,evp}$ is the j^{th} measured electrical potential difference corresponding to j^{th} electrode pair. The term w_{ij} is the area weight value which relates the flow velocity in the i^{th} region to the j^{th} electrical potential difference [1, 83]. The weight value is used to describe the contribution of the flow velocity at different points in the cross-section to the measured potential difference signal, as proposed by Shercliff [84]. Note that the weight function theory is described in more detail later in Section 3.2.

The axial velocity distribution can be calculated by applying matrix inversion to Equation 2-40 as:

$$\mathbf{V} = \frac{\pi a}{2\overline{B}}\left[\mathbf{WA}\right]^{-1}\mathbf{U_{evp}} \qquad \text{Equation 2-40}$$

where $\mathbf{V}$ is a single column matrix containing the pixel velocities v_i, $\mathbf{W}$ is a square matrix containing the relevant weight values w_{ij}, $\mathbf{A}$ is a diagonal matrix containing information on the pixel areas A_i and $\mathbf{U_{evp}}$ is a single column matrix containing the measured potential differences $U_{j,evp}$ [1].

After a series of solids-in-water two phase experiments, local axial water velocity profiles in multiphase flow were reconstructed by using the system described above.The measured water

velocity profile in solids-in-water flows is in good qualitative agreement with visual observation [1].

Although this technique does show some accurate results, it has several limitations. Overcoming these limitations has become the main thrust of this research to obtain the local conducting continuous phase flow velocity distribution in multiphase flows.

The major limitations of an EVP flow meter are:

1. Low spatial resolution of the local axial velocity. As mentioned earlier, the EVP flow cross-section was divided into seven pixels (see Fig. 2-13). Pixel 1 was at the top of the pipe and the pixel 7 was at the bottom. This pixel arrangement was limited and gave average velocities over relatively large regions. There are only seven values of the local conducting continuous flow velocity across the whole pipe cross-section, which may be insufficient for volumetric flow rate calculations in some multiphase flows. If the local volume fraction distribution can be obtained to a higher degree of spatial resolution using existing techniques, e.g. ERT or ICC, the local water velocity distribution with the same spatial resolution becomes essential for accurate calculation of water volumetric flow rate.
2. The EVP velocity reconstruction algorithm cannot be used to predict axisymmetric velocity profiles. Because of the seven pixel arrangement, variations of the reconstructed axial velocity are determined only along the *y* axis of flow cross-section (see Fig. 2-13). Thus, for measuring the velocity profile in vertical single phase or multiphase phase flows, the measurement of EVP is inaccurate. This is because, since most vertical flow velocity profiles are axisymmetric, the variation of velocity in two mutually orthogonal directions is required and this cannot be achieved using the EVP velocity reconstruction algorithm.

From the above brief discussion on the limitations of EVP, it can be seen that, in order to improve the accuracy of the reconstructed velocity profile, increasing spatial resolution of the EVP is essential. However, when increasing the spatial resolution, ill-posed problems may occur. It would require a more sophisticated reconstruction algorithm to overcome this problem. Furthermore, it might also need more magnetic field projections and electrical potential measurements, which could increase the cost of the flow meter.

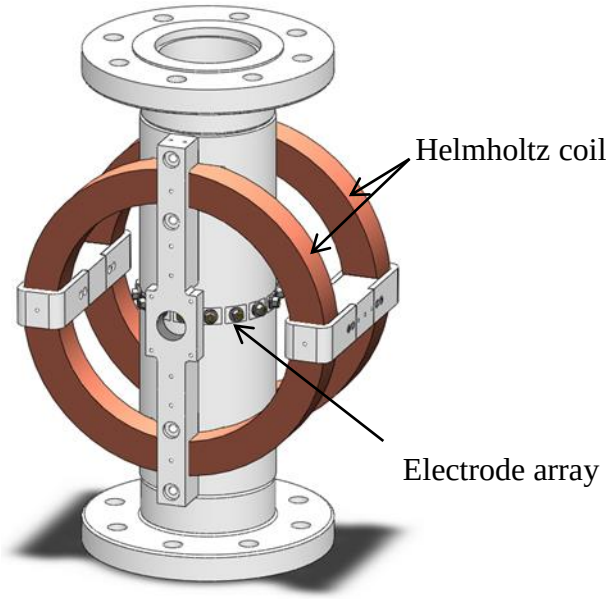

Fig. 2-11 Geometry of EVP device [83]

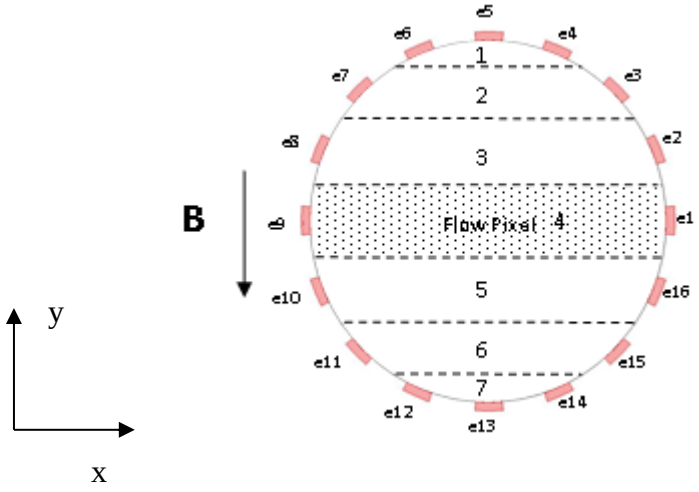

Fig. 2-12 Pixel arrangement and electrodes arrangement for EVP [65, 83, 85]

2.4 Summary

In this chapter, the principles of common and some selected techniques for the investigation of multiphase flows have been presented. These were: the mean volumetric flow rate measurement technique, intrusive measurement techniques for determining local volume fraction and velocity, and tomographic techniques. As a consequence of the discussion in the previous chapter, Section 2.2.3 presented most of the existing PT techniques, such as ERT, ECT and ICC, which were only used for obtaining information on local volume fraction and the velocity of the non-conducting dispersed phase in multiphase flow. Although these techniques have been commonly applied to MPFM devices, they are limited in determining the volumetric flow rate of the electrically conducting continuous phase (i.e. water). As described in Chapter 1, in multiphase flow, it is often necessary to measure the volumetric flow rate of both the dispersed and continuous phase, which can only be calculated by integrating the product of local phase velocity and local phase volume fraction in the flow cross-section. The local volume fraction of the conducting continuous phase can be found by $\alpha_{c,i} = 1 - \alpha_{d,i}$, where $\alpha_{d,i}$ is the local volume fraction of the non-conducting dispersed phase. Thus, the local velocity distribution of the conducting continuous phase becomes very important. Through reviewing previous published literature , we can see that a very small number of techniques for measuring local velocity distribution of the conducting continuous phase have been invented (see Section 2.3). By discussing the disadvantages of the different techniques, it has been shown that there is a demand for a novel measuring technique based on the multi-electrode EMFM technique, which may fill the gap left by previous research.

2.5 Thesis outline

In Chapter 1, the author attempts to demonstrate that the inline MPFM technique can save cost and valuable space on oil-gas exploration wells and also can provide continuous measurement of each phase flow parameter.

Chapters 1 and 2 refer to conventional inline MPFM devices, which commonly have an accuracy of ±10% and involve at least two independent techniques which are valid only for determining local dispersed phase flow parameters (i.e. velocity and volume fraction). In order to

overcome this limitation, the basic objective is proposed which indicates that the multi-electrode electromagnetic flow meter technique is selected in the current study. The technique used in this thesis, the so-called Inductive Flow Measurement Tomography (IFT), can be used for obtaining the local conducting continuous phase velocity distribution in oil-gas-water three phase and gas-in-water two phase flows. The main objectives are presented in Chapter 2.

Chapter 3: This chapter describes the background theory of the electromagnetic flow meter technique as well as the reconstruction algorithm used in the current study. In addition, this chapter also presents the investigation of the magnetic flux density distribution and electrical potential distribution in the pipe cross-section under a Helmholtz and anti-Helmholtz coil configuration by using numerical and analytical simulation methods.

Chapter 4: This chapter starts with an explanation of the method which can be used to determine the optimum velocity profile from several possible solutions. In this chapter, the implementation of the reconstruction algorithm is also described. Furthermore, based on the simulation model which is completed by COMSOL, the reconstructed local axial velocity distribution from the potential difference using two velocity reconstruction algorithms is presented.

Chapter 5: This chapter depicts the mechanical and electronic design of the IFT system.

Chapter 6: This chapter mainly describes the PC based program for data acquisition and electronics circuit control. In addition, it also explains the electrical potential signal analysis software , which is programmed using MATLAB.

Chapter 7: The experimental apparatus used in this study is introduced, such as the multiphase flow loops in SCR and the University of Cambridge. Several relevant flow metering techniques used in this study are also briefly described, such as, differential pressure measurement, ERT and MRI. Furthermore, there is a description of the data correction method used to correct the measured potential differences. Finally, the experimental results are discussed and analysed.

Chapter 8: The thesis finishes with conclusions, a discussion of the main results and the different reconstruction algorithms and suggestions for future works.

3 Background theory for inductive flow tomography

3.1 Introduction

Chapter 2 describes attempts by previous researchers to develop a technique for measuring the local velocity profiles for both continuous and dispersed phase in multiphase flow and demonstrates that few non-intrusive instruments have the potential for determining the local velocity distribution of the electrically conductive continuous phase of such flows. Among these techniques, only the electromagnetic flow meter (EVP) has successfully measured the local water velocity distribution in highly non-uniform multiphase flow. The major limitation of the EVP technique has been the low spatial resolution of the local water velocity measurements. This chapter discusses the theoretical background of the electromagnetic flow meter and develops a measurement methodology for Inductive Flow Tomography (IFT) devices to provide greater spatial resolution of the local water velocity distribution measurement in vertical and inclined multiphase flows.

In Section 3.2, the background theory of the conventional electromagnetic flow meter(EMF) is presented. The analysis shows that the conventional EMF can be used only to determine mean water volumetric flow rate for flows with an axisymmetric velocity profile and for a uniform magnetic field. Based on the mathematical modelling work done by Shercliff(1987), [84] it is seen that there is a parameter, the so-called 'weight value', which can describe the contribution of the local flow velocity to the overall flow induced electrical potential distribution over the pipe cross-section. This theory is used as the basis for a novel velocity profile reconstruction technique.

Referring to previous research, the EMF has been limited to a uniform magnetic flux density distribution. The analysis of involving the use of a non-uniform magnetic field is described in Section 3.3.

In order to investigate the performance of IFT in different physical environments, and to validate the reconstruction techniques, COMSOL software-based simulation models are described.

Section 3.4 describes the COMSOL simulation model geometry and the physical boundary conditions for the IFT flow meter.

Based on the characteristics of a non-uniform " anti-Helmholtz " magnetic flux density distribution, the power law exponent q of a 'power-law' expression of the form $V = V_{max}(1 - r/R)^q$ for the fluid velocity profile in axisymmetric flows can be determined (see Section 3.5).

In Section 3.6, a newly proposed flow velocity reconstruction algorithm is presented. For non-axisymmetric flows, this technique leads to multiple possible velocity profile solutions and it is shown how the use of the non-uniform anti-Helmholtz magnetic field enables selection of the optimum of these solutions. In Section 3.7, the velocity reconstruction algorithm, for non-axisymmetric flows, is combined with the reconstruction technique for "power law" axisymmetric flows to enable the reconstruction of velocity profiles containing both an axisymmetric velocity component and also a highly non-uniform velocity component.

3.2 The theoretical background of an electromagnetic flow meter

3.2.1 Fundamental theory of electromagnetic flow meters

For conventional EMFMs, the key principle is Faraday's Law, which states that a voltage is induced between two ends of a conductor when it moves through a magnetic field in a direction perpendicular to the direction of the magnetic field. The magnitude of the electrical potential between the two ends of the conductor is described by:

$$E = \frac{d\phi}{dt} = \frac{BdA}{dt} = B\frac{Ddl}{dt} = BD\bar{v} \qquad \text{Equation 3-1}$$

where ϕ is magnetic flux (weber,Wb), B is magnetic flux density (weber/m^2, tesla), A is the area of the loop completed by the moving conductor in the magnetic field, D is the length of the conductor and $dl/dt = \bar{v}$ is simply the speed of the conductor perpendicular to the magnetic

field. It should be noted that *E* in Equation 3-1 is the magnitude of the induced electromotive force (e.m.f) [86].

Fig. 3-1 shows the same principle applied to an EMF with point electrodes *b* and *c*. In this figure, the conductive fluid with axial velocity **V** is flowing through a magnetic field $\mathbf{B_y}$ in the positive "z" direction parallel to the z-axis. The flow induced electrical voltage between electrodes *b* and *c* is generated in a perpendicular direction, both to the flow velocity **V** and the magnetic field $\mathbf{B_y}$. It is apparent that in the flow cross-sectional area *A*, where the distance between electrodes *a* and *b* is L (i.e. L is the pipe diameter), the induced voltage U_e is given by:

$$U_e = BLV \qquad \text{Equation 3-2}$$

where *B* is magnitude of $\mathbf{B_y}$, and *V* is magnitude of **V**

Furthermore, if the volumetric flow rate of the conductive fluid is *Q*, Equation 3-2 can be written as:

$$U_e = BL\frac{Q}{A} = \frac{4BQ}{\pi L} \qquad \text{Equation 3-3}$$

It is clear from Equation 3-3 that the volumetric flow rate *Q* of the conductive fluid can be obtained from the measured value of U_e when the conductive fluid passes through the magnetic field. Note that the above equations are valid only for a uniform magnetic field [87].

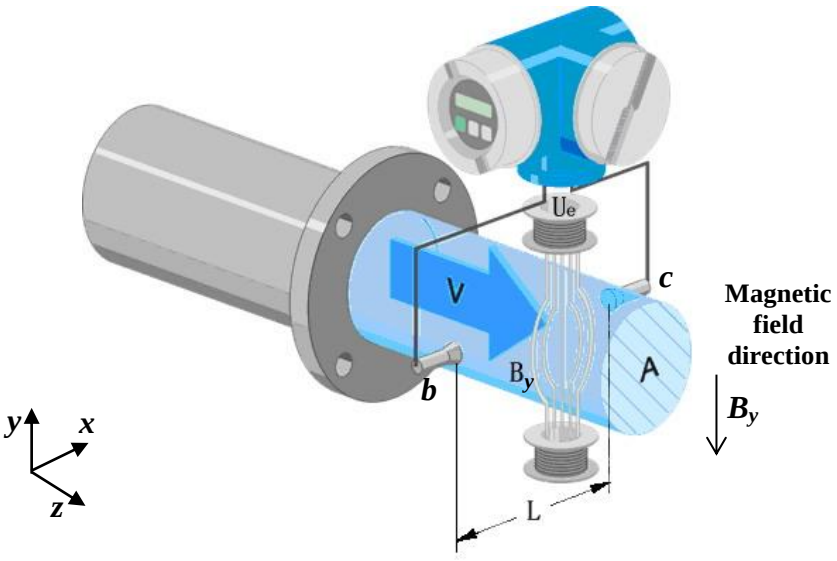

Fig. 3-1 Conventional electromagnetic flow meter with circular pipe and two point electrodes[88]

3.2.2 Two dimensional analysis of an electromagnetic flow meter

Shercliff [84] developed a theory of the EMF based on the assumption that the flow induced signal obeys Ohm's Law, as expressed in the form shown in Equation 3-4.It is assumed that the conductivity of the fluid across the flow cross-section is uniform, the circular pipe wall is insulated and the fluid is non-magnetic. It follows that:

$$\boldsymbol{j} = \sigma\,(\boldsymbol{E} + \boldsymbol{v} \times \boldsymbol{B}) \qquad \text{Equation 3-4}$$

where σ is the local fluid electrical conductivity, $\boldsymbol{j}$ is the local current density, the expression of $\boldsymbol{v} \times \boldsymbol{B}$ represents the local electric field induced by the fluid motion, $\boldsymbol{E}$ is the electric field due to charges distributed in and around the fluid and $\boldsymbol{B}$ is the magnetic flux density.

In circumstances whereby the coil excitation is a DC signal, the magnetic flux density can be considered constant, $\partial \boldsymbol{B} / \partial t = 0$, and we can define it in the form:

$$\nabla \times \boldsymbol{E} = 0$$ Equation 3-5

The electric field at a given point is equal to the negative gradient of the electrical potential *U*, written as:

$$\boldsymbol{E} = -\nabla U$$ Equation 3-6

From Equation 3-4 , it can be expressed as :

$$\boldsymbol{E} = \frac{\boldsymbol{j}}{\sigma} - \boldsymbol{v} \times \boldsymbol{B}$$ Equation 3-7

From Equation 3-6, the divergence of the electric field can be written as :

$$\nabla \cdot \boldsymbol{E} = -\nabla^2 U$$ Equation 3-8

Combining Equation 3-6 , Equation 3-7 and Equation 3-8, we obtain:

$$\nabla \cdot (\frac{\boldsymbol{j}}{\sigma} - \boldsymbol{v} \times \boldsymbol{B}) = -\nabla^2 U$$ Equation 3-9

Because the coil excitation signal is DC or has a low frequency, the local accretion of charge caused by the magnetic field is negligible. It is worth noting that the conductivity of flow is assumed uniform. Thus, it can be written as:

$$\nabla \cdot \boldsymbol{j} = \boldsymbol{0}$$ Equation 3-10

Substituting Equation 3-10 into Equation 3-9 , we obtain:

$$\nabla^2 U = \nabla \cdot (\boldsymbol{v} \times \boldsymbol{B})$$ Equation 3-11

Shercliff's work made the assumptions that (i) the magnetic flux density distribution over the flow cross-section, is relatively constant, and (ii) the flow velocity does not vary. Under these conditions, Equation 3-11 can be re-written as:

$$\nabla^2 U = \frac{\partial(B_y v_z - B_z v_y)}{\partial x} + \frac{\partial(B_z v_x - B_x v_z)}{\partial y} + \frac{\partial(B_x v_y - B_y v_x)}{\partial z} \qquad \text{Equation 3-12}$$

Equation 3-12 simplifies to Equation 3-13 in the case where the magnetic flux density $B_z = 0$, $B_x = 0$ and $B_y = -B$; the flow velocity has only one component, in the z direction, so $v_x = 0$, $v_y = 0$ and $v_z = v$.

$$\nabla^2 U = -B\frac{\partial v_z}{\partial x} \qquad \text{Equation 3-13}$$

By considering the pipe wall as non-conductive, on the pipe wall boundary we have $v = 0$ and $\partial U/\partial r = 0$, where $r = a$.

By solving Equation 3-13, Shercliff proposed a method that can be used to predict the effect of a general velocity profile via a so-called weight function. The weight function value at a point in the flow cross-section relates the contribution of the axial velocity at that point to the flow induced potential difference U_{bc} between the electrodes, according to Equation 3-14:

$$U_{bc} = 2a\bar{B}v_m \frac{\iint v(x,y)W(x,y)dxdy}{\iint v(x,y)dxdy} \qquad \text{Equation 3-14}$$

where $\bar{B}$ is mean magnetic flux density, $W(x,y)$ is the weight function, a is the inner radius of the pipe cross-section, v_m is mean velocity in the flow cross-section and $v(x,y)$ is the velocity component at (x,y) in the flow cross-section.

The weight function $W(x,y)$ is given by:

$$W(x,y) = \frac{a^4 + a^2(y^2 - x^2)}{a^4 + 2a^2(y^2 - x^2) + (y^2 + x^2)^2} \qquad \text{Equation 3-15}$$

Using Equation 3-15, the distribution of weight value for the pipe cross-section is shown in Fig. 3-2. It can be seen from the figure that, for a pipe of radius a, the weight values at the centre of the pipe cross-section are approximately equal to 1 and the minimum weight value of 0.5 occurs

when $x = 0$ and $y = \pm a$. In addition, when $x = \pm a$ and $y = 0$, the weight value is infinity at the left-hand pipe wall (electrode *b*) and decreases to 1.105 at the centre of the pipe and then increases to infinity again at the right-hand pipe wall (electrode *c*) [84]. Note that the pipe radius $a = 0.025\text{m}$ in Fig. 3-2.

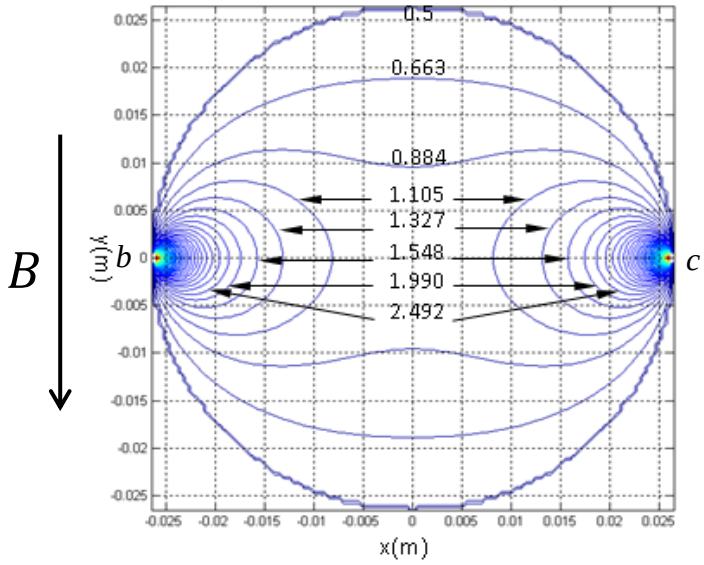

Fig. 3-2 Contours of the weight function

3.3 Electromagnetic flow meter with anti-Helmholtz coil configuration

With reference to previous publications, it is clear that, for most conventional EMFs, a uniform magnetic field with flux density B_y in the *y* direction is obtained by using a Helmholtz coil (see Fig. 3-2). This field is applied over the flow cross-section perpendicular to the flow velocity v_z and the electrical potential difference is along the *x* axis. In the present study, the Helmholtz coil was used not only to create a uniform magnetic field in the flow cross-section of the IFT system, but also to generate a highly non-uniform magnetic flux density distribution in the flow cross-section. This was obtained when the current was flowing through the two coils in opposite directions (known as an anti-Helmholtz coil configuration).

For a circular current loop, its magnetic field components at any position ρ and y can be computed from the vector potential $\boldsymbol{B}=\nabla\times\boldsymbol{A}$, where $\boldsymbol{B}$ is magnetic flux density, and $\boldsymbol{A}$ is the magnetic vector potential. Detroye and Chase [89] proposed an expression for the magnetic field of a single coil as:

$$B_\rho(\rho,y)=\frac{\mu_0 I}{2\pi}\frac{y}{\rho\sqrt{(\rho+a)^2+y^2}}\left[\frac{a^2+\rho^2+y^2}{(a-\rho)^2+y^2}E(k)-K(k)\right] \quad \text{Equation 3-16}$$

$$B_y(\rho,y)=\frac{\mu_0 I}{2\pi}\frac{1}{\rho\sqrt{(\rho+a)^2+y^2}}\left[\frac{a^2-\rho^2-y^2}{(a-\rho)^2+y^2}E(k)-K(k)\right] \quad \text{Equation 3-17}$$

where:

$$K(k)=\int_0^{\frac{\pi}{2}}\frac{d\phi}{\sqrt{1-k^2\sin^2\phi}} \quad \text{Equation 3-18}$$

$$E(k)=\int_0^{\frac{\pi}{2}}\sqrt{1-k^2\sin^2\phi}\,d\phi \quad \text{Equation 3-19}$$

and μ_0 is permeability of free space, I is current through the coil, a is radius of coil and ϕ is the angle between the x-axis and the relevant point on the coil (see Fig. 3-3). Referring to Fig. 3-3, any point P can be defined by using a cylindrical coordinate system so that radial distance ρ is the Euclidean distance from the y-axis to the point P and the height y is the signed distance of the point P to the x-y plane.

The expression for the magnetic field of an anti-Helmholtz coil can be written in terms of summing the individual fields from each loop and is given by:

$$B_{\rho}^{total}(\rho,y)=B_{\rho}(\rho,y+\frac{a}{2})-B_{\rho}(\rho,y-\frac{a}{2})$$ Equation 3-20

$$B_{y}^{total}(\rho,y)=B_{y}(\rho,y+\frac{a}{2})-B_{y}(\rho,y-\frac{a}{2})$$ Equation 3-21

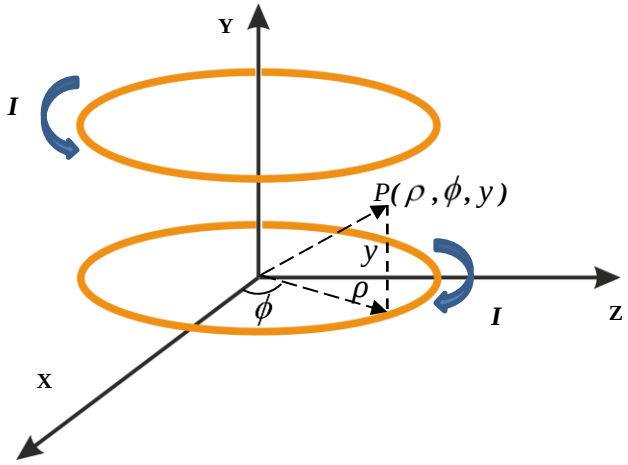

Fig. 3-3 Coordinates and variables describing two circular loop used to express magnetic field

In the region of interest (where the measurement are taken), the distribution of magnetic flux density on the *x*-*y* plane for anti-Helmholtz coils is shown in Fig. 3-4.

In the case of coil radius $a=0.149m$ and pipe radius is 0.025m, Fig. 3-4 (a) shows that the maximum magnitude of the magnetic flux density is $5e^{-3}$ T and minimum magnitude is -$5e^{-3}$ T. Across the pipe cross-section at y = 0, the magnitude of the magnetic flux density is zero. It is clear that the magnetic flux density distribution between the coils is also not uniform along the *y*-axis, the vertical axis in the figure. Note that the B_x component shown in Fig. 3-4(b) is equivalent to the radial component of the magnetic flux density (see Equation 3-20). This figure is valid for showing the radial magnetic field component for any vertical plane centred on the *y*-axis.

In Fig. 3-4 (c), the arrows indicate the magnitude and direction of the local magnetic flux density in the *x-y* plane. The z component of the local magnetic field vector is negligible in the plane z =0. By inspecting the magnetic field vector, it can be seen that the magnetic flux density distribution between two coils moves in different directions, depending on position in the field, as would be expected of a magnetic quadrupole effect.

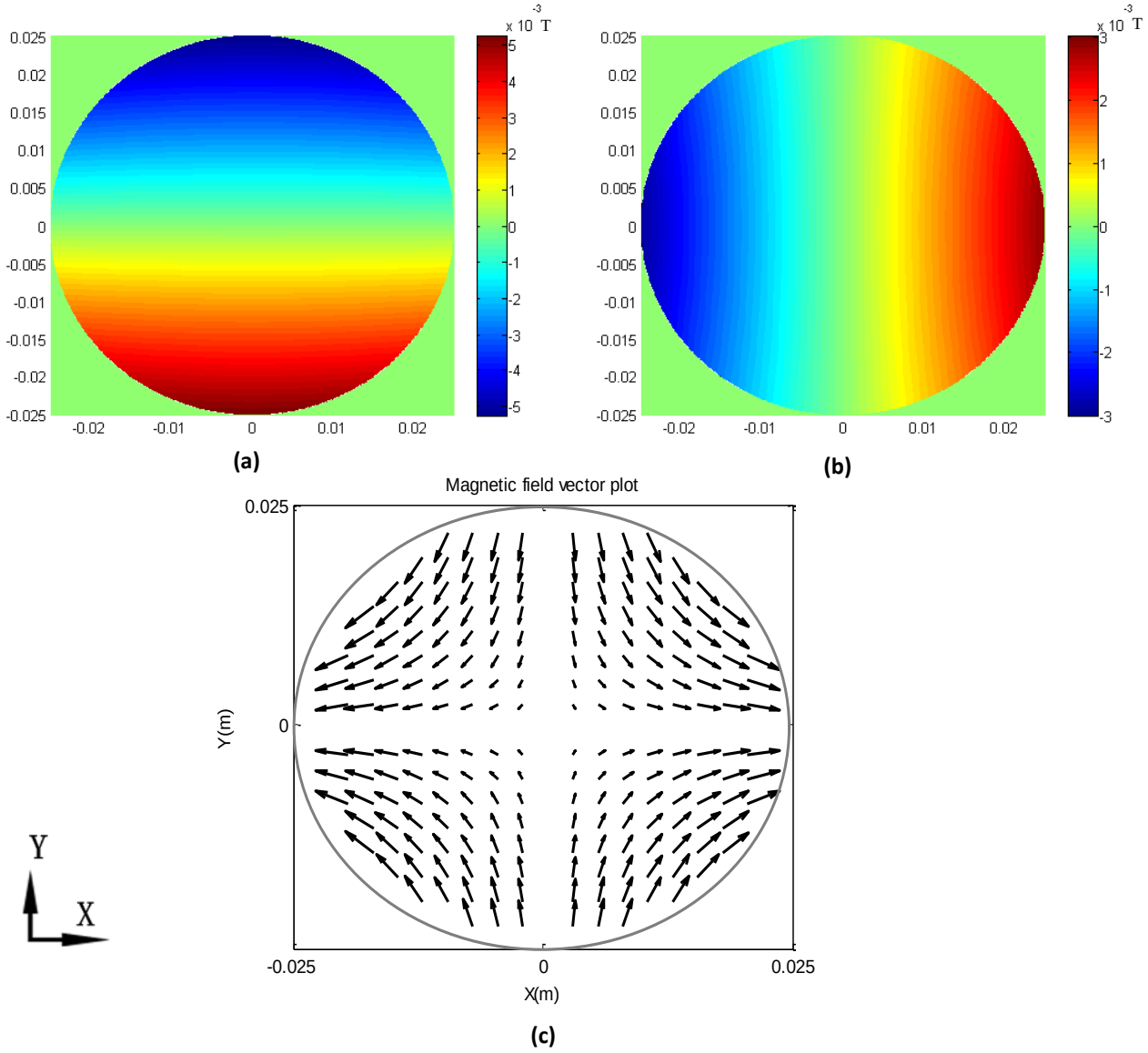

Fig. 3-4 Magnetic flux density distributions of anti-Helmholtz magnetic field in the *x-y*-plane (a) By component(unit: tesla), (b) Bx component (unit: tesla) and (c) vector plot of magnetic field

3.4 Numerical modelling of an Inductive Flow Tomography system

Inductive Flow Tomography (IFT), intended to reconstruct the velocity field of electrically conducting fluids, is based on a multi-electrode EMFM. For the development of such a device it is important to know the distribution of magnetic flux density and also the distribution of flow induced electrical potential under the specific conditions that the device will be expected to operate. The present study uses numerical modelling to investigate the influence of physical geometry on factors such as (i) magnetic flux density distribution, (ii) flow induced electrical potential distribution with different velocity profiles, and (iii) the reconstruction algorithm for the water velocity profile.

Details which are relevant to the numerical modelling of IFT are given below. The numerical modelling will analyse the electrical potentials induced when a specific fluid flow passes through the uniform and non-uniform magnetic fields generated when the electrical current in the two coils of the electromagnetic flow meter flow in the same direction (uniform field) or in the opposite directions (non-uniform field). From the simulation results, a theoretical approach is presented to reconstruct the water velocity profile. Further investigation of numerical modelling using the IFT is presented in the next chapter.

3.4.1 Software platform for numerical modelling

The software platform chosen to model the IFT was COMSOL3.5a Multiphysics (also known as FEMLAB) for all simulations. The IFT system modelling work was completed using the AC/DC module because it is suitable for simulating electric current and static electromagnetic field applications in a 3D environment. The electromagnetic package contains customised user interfaces and has been optimised for the analysis of electromagnetic systems. Electromagnetic analysis at the microscopic level is performed by solving the Maxwell equations subject to given boundary conditions. In the present study, the ‘Electric and Induction Currents’ module with the time-harmonic stationary linear solver was chosen to generate simulation models for the electromagnetic flow meter with a Helmholtz coil, and to solve the magnetic flux density and flow induced potential.

3.4.2 Geometrical design for numerical simulation

The dimensions and geometry of the EMFM studied in this research are shown in Fig. 3-5. The first stage of creating the model in a COMSOL environment is to build a Helmholtz coil and a pipe cross-section with their corresponding dimensions in a 2D work-space (i.e. the *x-y* plane), as shown in Fig. 3-6 (b). The cross-section of the circular pipe carrying the flow had a 50mm internal diameter (shown as blue in Fig. 3-5). The 5mm thick pipe wall is typically made from an engineering material such as PTFE (polytetrafluoroethylene); this is shown in green in Fig. 3-5. The two rectangles marked co1 and co2 represent parallel Helmholtz coils, each with width of 35mm, placed at the top and bottom of the pipe, separated by a distance of 114mm, which is equal to the mean radius of the coils.

After the geometries of the different parts of the EMFM were specified in the 2-D work-space, they were converted to a 3D model using the 'Revolve' and 'Extrude' functions of the software package.

The following procedures were used to form a completed model:

- Firstly, the whole pipe cross-section is specified as a 50 mm circular flow cross-section enclosed by a 60mm diameter circular ring, as shown in the figure. This 2D model was extended by 300mm in the z direction using the 'Extrude' function with distance set at 0.3m.
- The second step in configuring a Helmholtz coil is to highlight both squares, co1and co2, open the 'Revolve' function and set the angle of revolution between 0 ºand 360 º, as required, and also to set the resolution axis to x=0,y=0.
- Once the IFT meter body model was completed, the last step was to build a computing domain in terms of the geometry of the IFT model. In this case, a cylindrical shaped computing domain boundary was created using the 'Cylinder' function and setting a radius of 0.15m and height of 0.34m. Note that all the geometries are referenced to the origin of the workspace, which is x=0 , y=0 and z=0.

The final IFT simulation model in 3D is as shown in Fig. 3-6 (b).

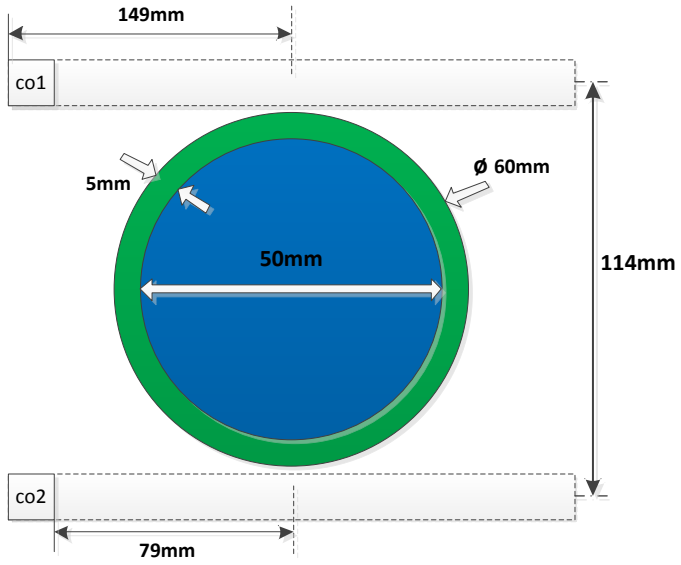

Fig. 3-5 Geometry of IFT device in x-y plane

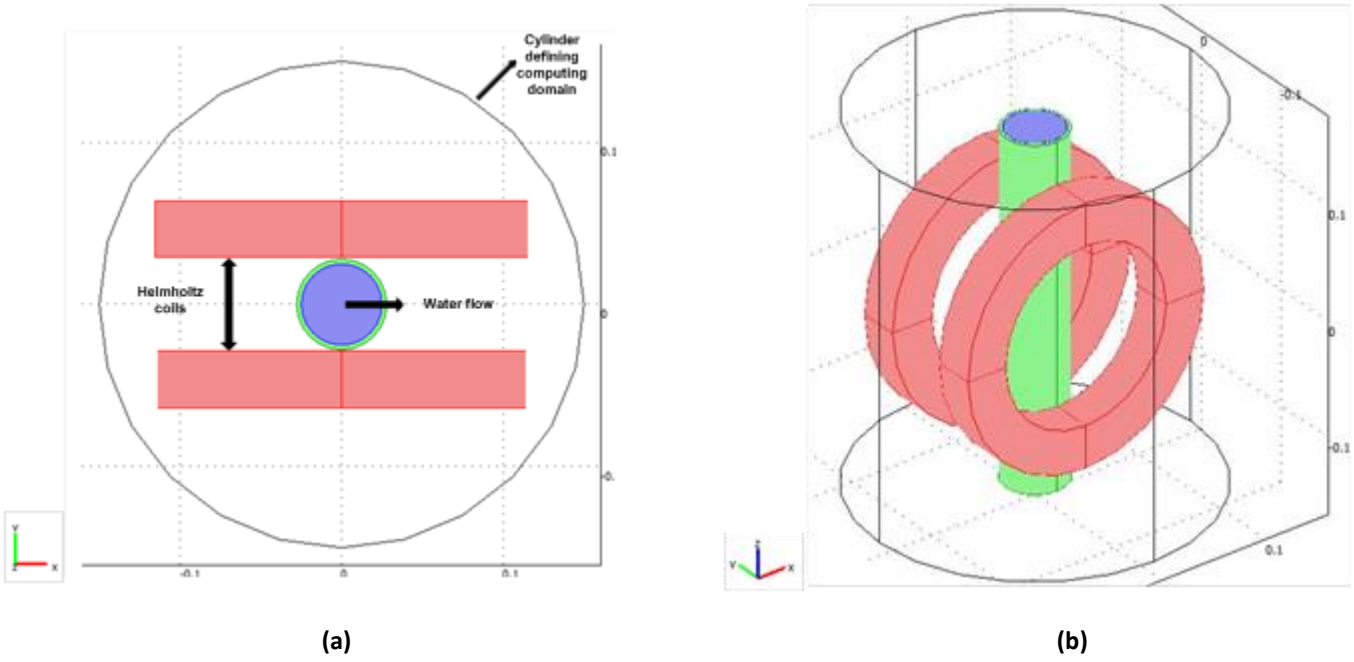

Fig. 3-6 Geometrical model used for simulation and relevant coordinate system (a) view on x-y plane (b) 3D view

3.4.3 Defining the physical boundary conditions and specifying object properties

After defining the geometry of the EMFM, the physical parameters had to be identified for each sub-domain: i.e. material property, initial conditions, etc. In this simulation, as stated earlier, the entire investigation is concerned with the electrical potential distribution in the flow cross-section, which is influenced by the magnetic field and velocity distribution of the flowing conductive fluid. To determine the magnetic field, it is necessary to define the current supplied to the Helmholtz coil. The coils are of copper wire with a conductivity of 5.998×10^{7} S/m (obtained from the 'Library materials' option within the software). The supply current density vector components are defined in Cartesian coordinates according to the COMSOL guidelines. These are shown in Table 3-1.

Components	Expression
J_x	$-J_0*z/(\sqrt{(x^2+z^2)})$
J_y	0
J_z	$J_0*x/(\sqrt{(x^2+z^2)})$

Table 3-1 Calculation for supply current components for Helmholtz coil

The input electrical current density J_0 can be defined as a required value in the 'Constants' under the options menu. The value of J_0 is set to be 3.4×10^{8} Am^{-2}, which was used in the present investigation (refer to Section 3.5). The reason for setting this specific value is to achieve sufficient uniform magnetic field strength in the pipe cross-section (see Fig. 3-7).

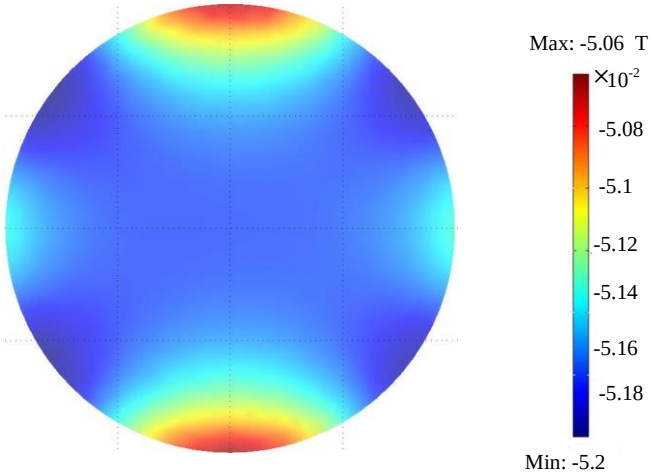

Fig. 3-7 Magnetic flux density in a uniform magnetic field (unit: Tesla)

The region of interest is the pipe, which includes the flow channel and pipe wall. The electrical conductivity of fluid in the pipe is set to 1.5 $\times 10^{-2}$ S/m, which is the typical value of tap water in northern England. The conductivity of the pipe wall is set at 1×10^{-15} S/m, as it is assumed to be made from a non-conducting material. For the purposes of the present investigation, the rest of the computing domain is assumed to be air with magnetic insulation condition.

After setting all the required physical and sub-domain parameters, the model can be meshed and solved. This is explained in the next section.

3.4.4 Meshing the model

In finite element analysis, meshing a model is an essential procedure before beginning the simulation process. The purpose of the mesh is to divide a modelled geometry into small cells or elements. The governing equations are then discretised and solved in these small areas. It is apparent that the size of the meshing elements is crucial for achieving the best results in a reasonable time. The higher the resolution, the smaller the mesh, which gives a more accurate solution. However, it also increases the time and computational power required for the computation process. Thus, it is necessary to find a credible mesh, which can provide adequate resolution with the computer power available.

With reference to the methodology of mesh convergence, the same geometry model was tested using a different number of mesh elements. The results of magnetic flux density in the flow cross-section have been determined and are shown in Fig. 3-8. Fig. 3-8 (a) and (b), respectively, show the variation in the magnetic flux density B_y (y component of the magnetic flux density) along the *x*-axis and *y*-axis for the different number of mesh elements.

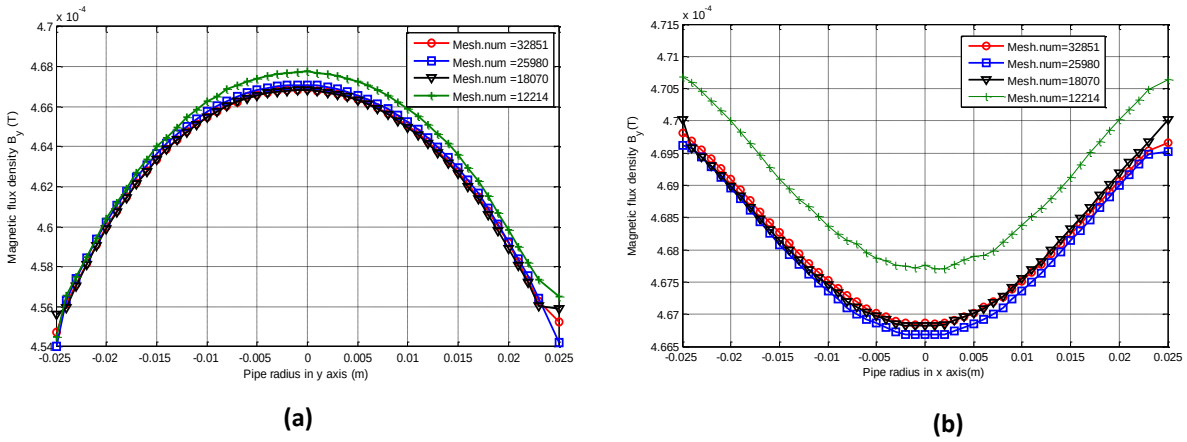

Fig. 3-8 A plot of magnetic flux density B_y profile for different mesh elements (a) B_y along *y*-axis of pipe, (b) B_y along *x*-axis of pipe

As can be seen from both Fig. 3-8 (a) and (b), there is no great change in the magnetic flux density results as the mesh number increases beyond approximately 18000 elements. However, the value of B_y on the very edge of the flow cross-section converges more slowly than in the pipe's central area. This is probably because the mesh elements are insufficiently small to accurately construct discontinuities occurring at the boundary of the pipe.

Based on the mesh convergence results shown in Fig. 3-8, it was found to be necessary to insert more mesh elements in the region of the pipe wall where the error is estimated to be large. However, it is inefficient to give the entire geometry the same mesh size and, thus, the normal mesh (i.e. the element size is default setting, which is bigger than 'finer mesh' size) was used in the remaining cross-section. Given the present model and computational capability of the PC to be used, it was decided that the total number of mesh elements would be 32050. Through experiment and observation, the mesh element at the "edges" of the segment of circular pipe was improved by setting the 'maximum size of element' at 0.006mm and 'element growth rate' at 1.2. Fig. 3-9 (a) shows the normal mesh and Fig. 3-9 (b) is an optimum mesh with a custom element size and element growth rate. It is clear that the Fig. 3-9 (b) mesh geometry has smaller elements on the edge of the flow cross-section, which can provide more detailed results in that region.

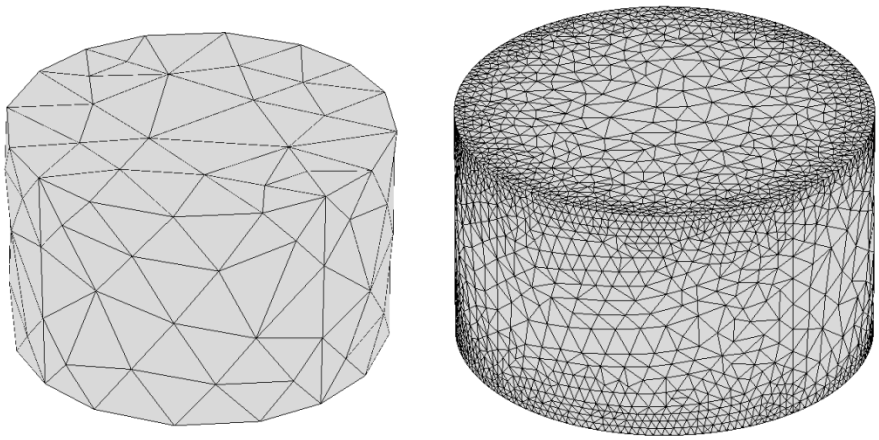

(a) **(b)**

Fig. 3-9 Pipe mesh elements with different mesh geometry setting.

Fig. 3-10 shows that, by using the optimum mesh (Mesh.num=32050), the magnetic flux density B_y distribution in the *x*-axis and *y*-axis is more uniform. The calculated magnetic flux density distribution of the B_y component, shown in Fig. 3-10 (a) and (b), respectively, has the variation of ±0.3% and ±0.1% from the mean value in the pipe cross-section, which was too small to be considered significant. This value is also smaller than the variation of ±1.5 from previous research [1]. Therefore, the magnetic flux density distribution can be considered to be uniform on the *x*-*y* plane inside of the pipe, and this satisfies our expectation, because the magnetic flux density at any position of the pipe should be the same due to the geometry of the Helmholtz coil.

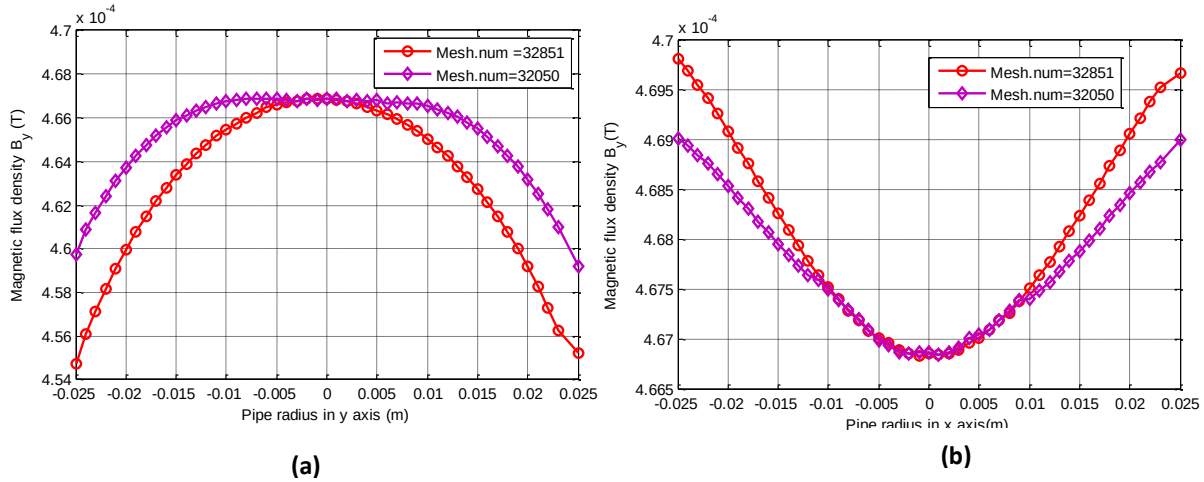

Fig. 3-10 The magnetic flux density B_y profile for the model with the same size element (total mesh number is 32851) and the model with optimum mesh (total mesh number is 32050). (a) B_y along y-axis of pipe, (b) B_y along x-axis of pipe

3.5 Determining axisymmetric 'power law' velocity profiles using IFT

3.5.1 Power law velocity profile

In single phase and multiphase flow, numerous different types of model have been proposed to describe the velocity profile for flow in circular pipes. However, there is a vast body of literature showing that, in fully developed single phase flow in circular pipes, the velocity profile is axisymmetric. Significant previous research by Lucas [88] and van der Welle [89] has also shown that, in well developed vertical upward multiphase flows, the velocity profiles of the flowing phases are also axisymmetric [90, 91]. Furthermore, in both the single phase and multiphase flows described above, previous research has shown that the axisymmetric phase velocity profiles may be accurately represented by a power law expression of the form:

$$\frac{v}{v_{\max}} = (1 - \frac{r}{R})^{q} \qquad \text{Equation 3-22}$$

where $v_{\max}$ is the maximum local axial flow velocity at the centre of the pipe, r is the radial position within the pipe, R is the inner radius of pipe cross-section, and q is the power law exponent. The value $q = 1/7$ generally approximates the velocity profile of typical well-developed single phase turbulent flows (see Fig. 3-11).

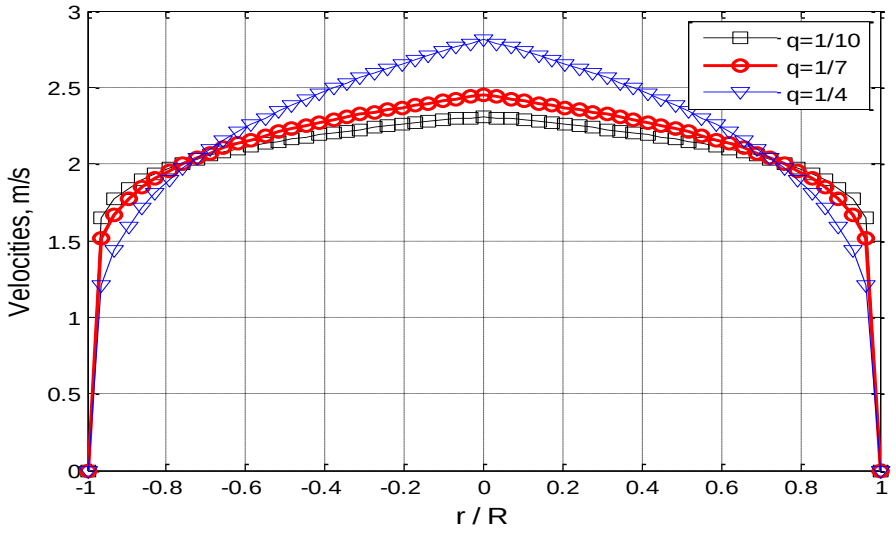

Fig. 3-11 Power law velocity profiles with different values of the exponent *q*

The velocity profile can also be expressed in terms of the average phase flow velocity $\bar{v}$, enabling Equation 3-22 to be re-written as:[1, 90]

$$v = 0.5 \cdot \bar{v} \cdot (1 - \frac{r}{R})^q \cdot (1+q) \cdot (2+q) \qquad \text{Equation 3-23}$$

Equation 3-22 shows that the phase velocity profile can be determined by finding the appropriate values of q and $\bar{v}$. Thus, obtaining the values of q and $\bar{v}$ for different flow conditions is important. This section is concerned with describing how to evaluate the exponent q by investigating the relationship between the value of q and potential difference measurements from the IFT flow meter in a number of axisymmetric flow conditions.

3.5.2 Influence of axisymmetric velocity profile on electrical potential distribution

This section investigates the axisymmetric flow of a conducting fluid through a pipe across which a magnetic field is applied. The purpose is to find out how the distribution of the flow velocity can affect the distribution of the induced electrical potential. Three axisymmetric

velocity profiles have been chosen for the finite element analysis (COMSOL) based on the power law equation given in Equation 3-23.

From inspection of Equation 3-23, it is obvious that, if the mean velocity of the fluid $\bar{v}$ is kept constant, then, as q increases, the velocity at the centre of the flow increases. At the same time, the velocity near the pipe wall decreases. Thus, as q increases the velocity distribution profile looks more 'peaky'. Three velocity profiles are shown in Fig. 3-12, q = 0, 1 and 5, with same mean velocity of $\bar{v}$ = 5m/s.

With these three different axisymmetric velocity profiles flowing through a uniform and non-uniform magnetic field, the electrical potential distribution formed around the pipe cross-section was determined on each electrode, i.e. from e_1 to e_{16} using COMSOL. The boundary potential distribution, once determined, can be used to distinguish between these velocity profiles. This will be explained later this section.

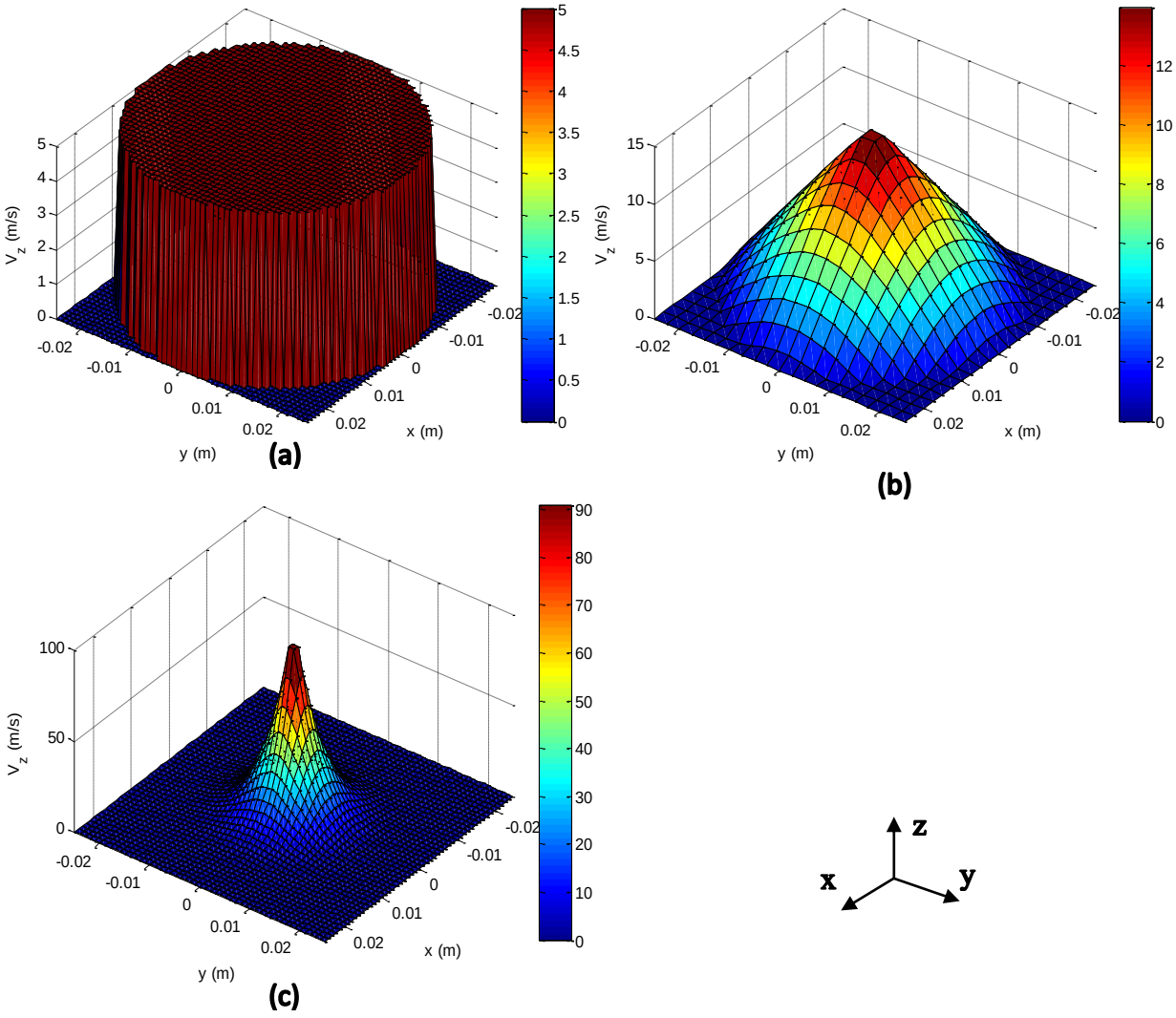

Fig. 3-12 Three axisymmetric velocity profiles (a) Profile 1: Velocity profile uniform across the whole pipe cross-section (*q* = 0), (b) Profile 2: Velocity profile for *q*=1, and (c) Profile 3: Velocity profile for *q*=5

The conductivity of the water filling the pipe is $\sigma = 1.5 \times 10^{-2}\, Sm^{-2}$

(i) In the first instance, Fig. 3-12(a), it is proposed that the water has a uniform velocity distribution across the entire pipe with mean velocity $\bar{v}$ =5m/s. The reason for assuming such a high velocity is to achieve sufficient numerical precision for the electrical potential results at the boundary obtained using COMSOL. This velocity profile is described by the power law velocity distribution when *q*=0. Because water flow velocity $\bar{v}$ is considered in the *z* direction only, the local water velocity distribution for this first case, $v_{z,1}$, can be expressed as:

$$v_{z,1} = \bar{v}_z$$ Equation 3-24

(ii) In the second instance, Fig. 3-12 (b), q = 1 is not a condition normally found in practice. Again, the mean water velocity has been set to $\bar{v}_z$ =5m/s. The local axial velocity of water for this second case, $v_{z,2}$, is given by:

$$v_{z,2} = 3 \cdot \bar{v}_z \cdot (1 - \frac{r}{R})$$ Equation 3-25

The local axial velocity $v_{z,2}$ varies from zero at r =0.025 m, to 15 m/s at r=0 (in the centre of the pipe).

(iii) In the third instance, Fig. 3-12 (c), q = 5. Here the flow velocity profile is clearly more "peaky" than for the second case [90]. If the mean flow velocity is held constant, i.e. $\bar{v}_z$ =5m/s, the water velocity at the pipe centre (r = *0*), is equal to 105m/s. At the boundary of the pipe, the water velocity is very close to zero and is considered stationary. The local axial velocity of water for this third case, $v_{z,3}$, is given by:

$$v_{z,3} = 21 \cdot \bar{v}_z \cdot (1 - \frac{r}{R})^5$$ Equation 3-26

For each simulated flow condition, the electrical potential was determined from COMSOL based on the IFT model geometry as described in Section 3.4.2 (see Fig. 3-6). Fig. 3-13 presents the corresponding results for the simulated electrical potential distribution when the fluid passed through a uniform magnetic field (as shown in Fig. 3-7) i.e. The mean magnetic flux density is equal to -5.13×10^{-2}T.

The next stage of this study was to obtain the measured electrical potential φ at sixteen measurement positions (e_1 to e_{16}). The measured electrical potential was obtained at each electrode and is represented as φ_j (j =1 to 4 and 6 to16). This investigation was to find the potential differences between φ_j and φ_5 (Note that e_5 was chosen as a reference measurement position). Thus, with respect to the potential at e_5, the fifteen potential differences U_j were defined as:

$$U_j = \varphi_j - \varphi_5$$ Equation 3-27

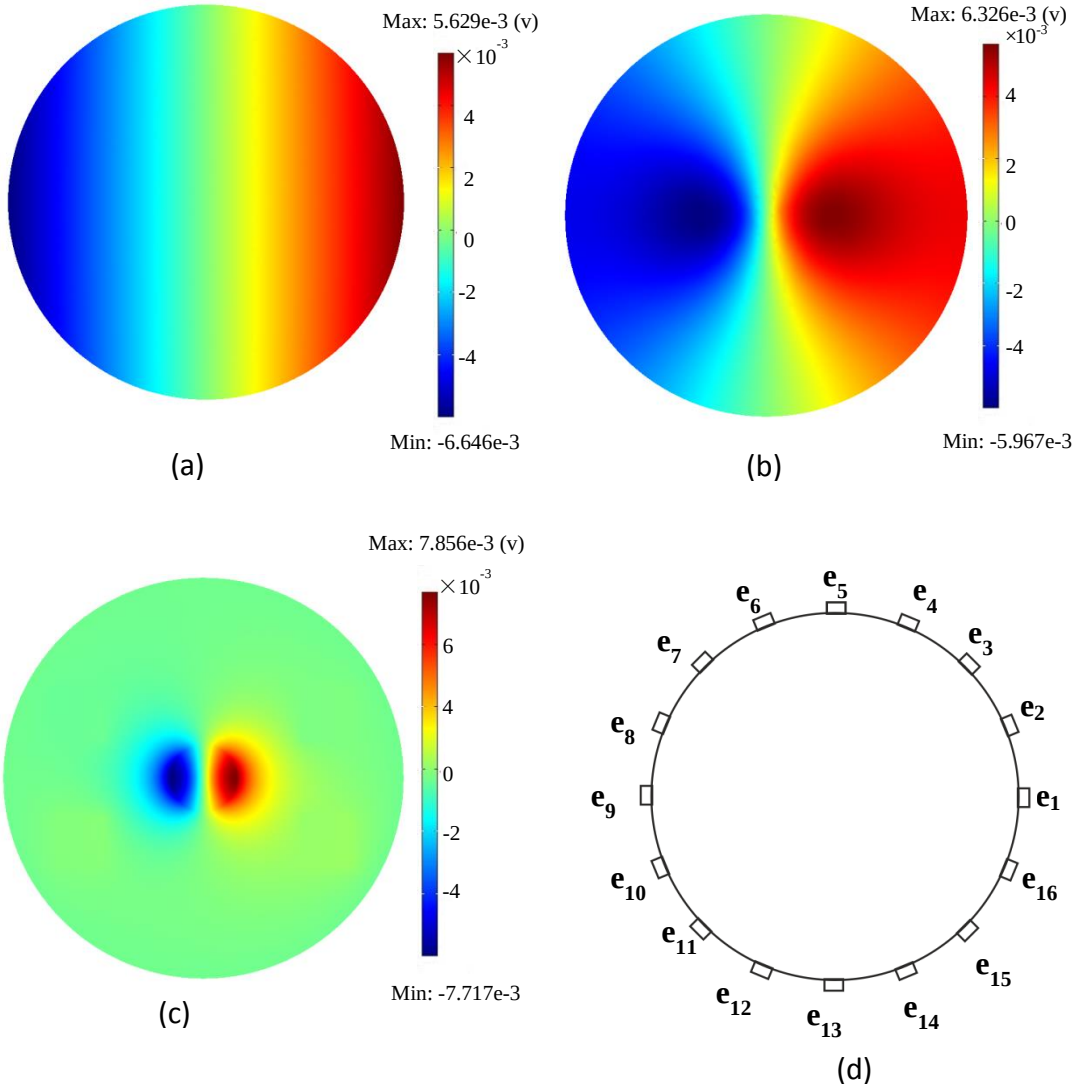

Fig. 3-13 Electrical potential distribution for three velocity profiles in uniform magnetic field (a) Profile 1, *q* = 0, (b) Profile 2, *q* = 1, (c) Profile 3, *q* = 5 and (d) the 16 electrode positions on the pipe cross-section

The boundary potential difference distribution U_j shown in Fig. 3-14 was determined from the simulated results of electrical potential distribution, as shown in Fig. 3-13, according to Table 3-2.

U_j	$\boldsymbol{\varphi_j - \varphi_5}$	Electrode pair
$\boldsymbol{U_1}$	$\varphi_1 - \varphi_5$	e1-e5
$\boldsymbol{U_2}$	$\varphi_2 - \varphi_5$	e2-e5
$\boldsymbol{U_3}$	$\varphi_3 - \varphi_5$	e3-e5
$\boldsymbol{U_4}$	$\varphi_4 - \varphi_5$	e4-e5
$\boldsymbol{U_5}$	$\varphi_6 - \varphi_5$	e6-e5
$\boldsymbol{U_6}$	$\varphi_7 - \varphi_5$	e7-e5
$\boldsymbol{U_7}$	$\varphi_8 - \varphi_5$	e8-e5
$\boldsymbol{U_8}$	$\varphi_9 - \varphi_5$	e9-e5
$\boldsymbol{U_9}$	$\varphi_{10} - \varphi_5$	e10-e5
$\boldsymbol{U_{10}}$	$\varphi_{11} - \varphi_5$	e11-e5
$\boldsymbol{U_{11}}$	$\varphi_{12} - \varphi_5$	e12-e5
$\boldsymbol{U_{12}}$	$\varphi_{13} - \varphi_5$	e13-e5
$\boldsymbol{U_{13}}$	$\varphi_{14} - \varphi_5$	e14-e5
$\boldsymbol{U_{14}}$	$\varphi_{15} - \varphi_5$	e15-e5
$\boldsymbol{U_{15}}$	$\varphi_{16} - \varphi_5$	e16-e5

Table 3-2 Potential difference measurement between electrode position e_j and e_5

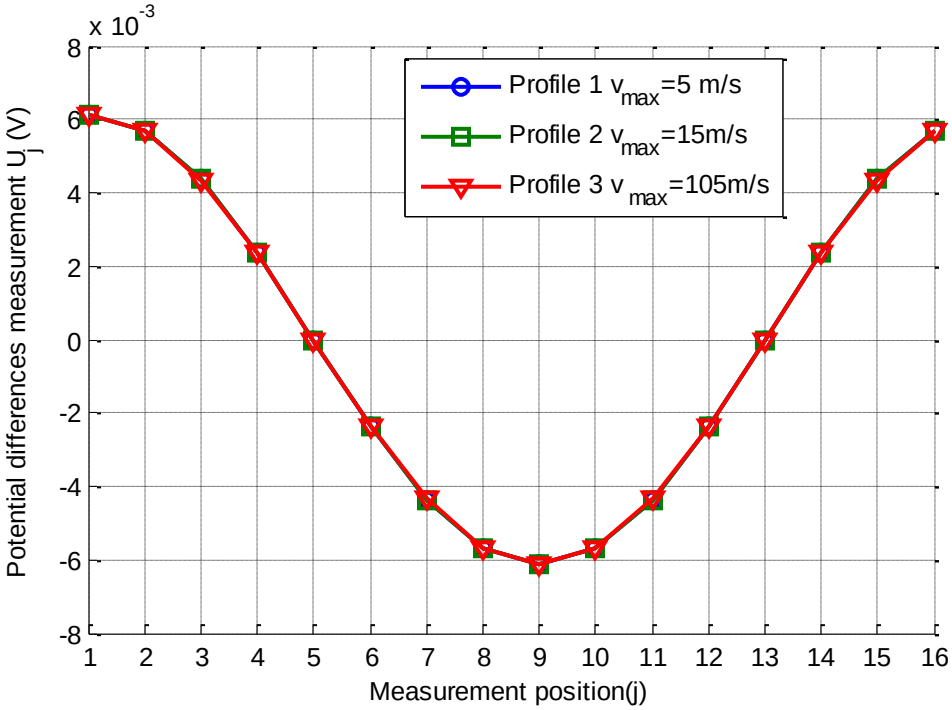

Fig. 3-14 Comparison of the boundary potential difference distribution U_j for profiles 1 ,2 and 3

By inspection of Fig. 3-14, it can be seen that there are no distinguishing differences in the boundary potential difference distribution U_j between velocity profiles 1, 2 and 3. That is

because they all have the same mean axial velocity, $\bar{v}_z$. The result can also be explained by reference to the work of Shercliff [83], Horner [90] and Zhang and Lucas [92], who showed that, in single phase flow when the mean volumetric flow rate is unchanged for different axisymmetric velocity profiles, the electrical potential distribution on the boundary is the same for all flows.

In the case of a uniform axial flow $\bar{v}_z$ in the z direction (i.e. out of page) passing through a uniform magnetic field B in the negative y-direction, then, with reference to Kollar and Lucas [93], provided the potential at $\theta = 90°$ on the pipe boundary is held equal to zero, the electrical potential at any measurement point on the boundary can be expressed as Equation 3-28.

$$\varphi(\theta) = BR\bar{v}_z \cos\theta \qquad \text{Equation 3-28}$$

From Equation 3-28 , we have:

$$\varphi(0°) = BR\bar{v}_z \qquad \text{Equation 3-29}$$

$$\varphi(180°) = -BR\bar{v}_z \qquad \text{Equation 3-30}$$

It can be seen from Equation 3-29 and Equation 3-30 that, when θ is equal to 0 º and 180 º, the difference between φ_1 and φ_9 is greater than for other measurement positions, and is easy to calculate. The axial water velocity can be written as:

$$\varphi(0°) - \varphi(180°) = 2BR\bar{v}_z \qquad \text{Equation 3-31}$$

$$\bar{v}_z = \frac{\varphi(0°) - \varphi(180°)}{2BR} \qquad \text{Equation 3-32}$$

Referring to Table 3-2, the Equation 3-32 can be rewritten as :

$$\bar{v}_z = \frac{U_1 - U_9}{2BR} \qquad \text{Equation 3-33}$$

where the magnetic field is uniform, the boundary potential difference between electrodes 1 and 9 is used only to determine the mean axial velocity, $\bar{v}_z$, in terms of conventional EMFM, as given by Equation 3-33. The term R is the pipe radius. The next aim is to find a unique signature

from the electrical potential distribution which can be used to distinguish different velocity profiles. Referring to the characteristics of the non-uniform magnetic field produced by an anti-Helmholtz coil (see Section 3.3), the simulated results of electrical potential distribution for velocity profiles 1, 2 and 3 are shown in Fig. 3-15. For results shown in Fig. 3-15 give the value of the magnetic flux density in the *y* directionat e_{13} and state (with reference to future Section 3.5.3) that this magnetic flux density is also known as B_{op}. It is worth noting that ,for this study, the B_{op} is 3×10^{-2} T.

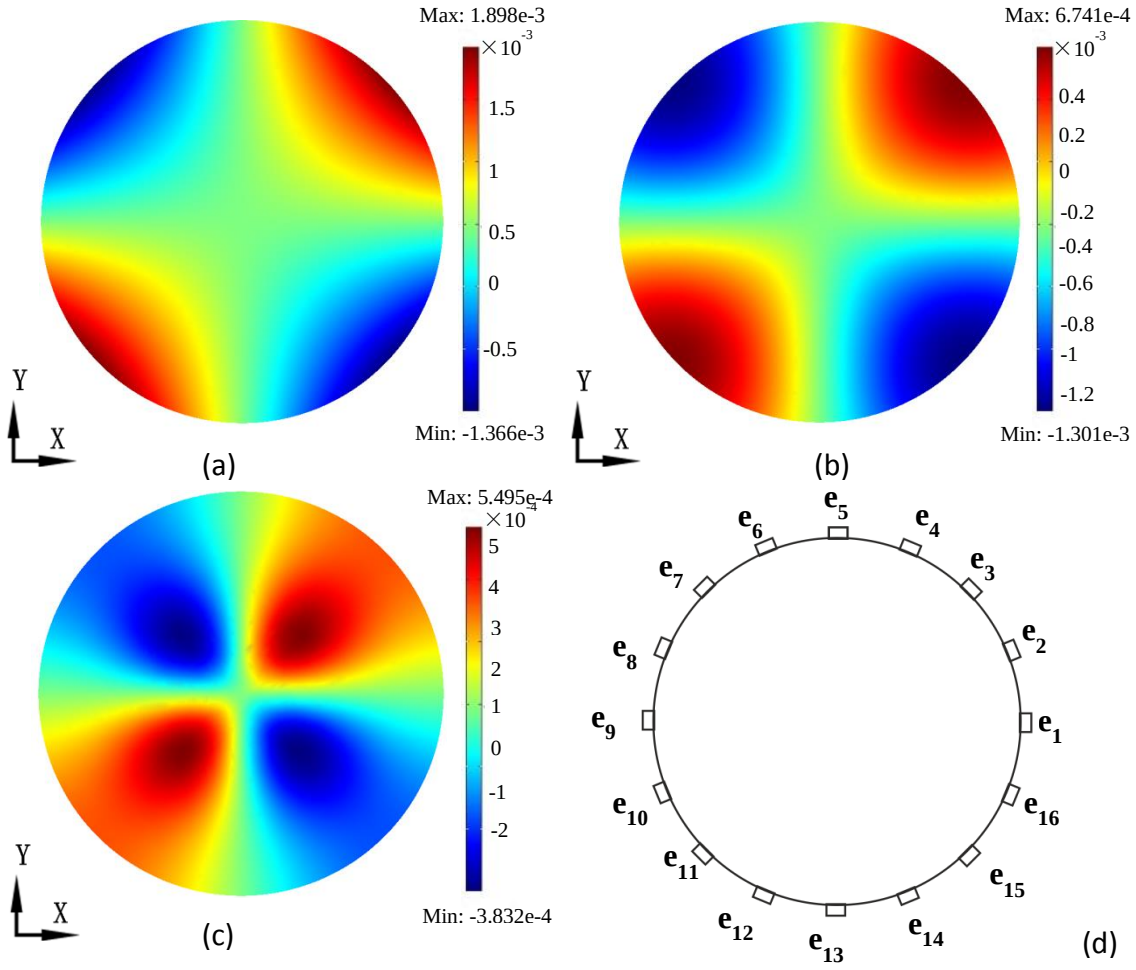

Fig. 3-15 Electrical potential distribution of three velocity profiles in a non-uniform magnetic field produced by an anti-Helmholtz coil (a) Profile 1, q = 0, (b) Profile 2, q = 1, (c) Profile 3, q = 5 and (d) the 16 electrode positions on the pipe cross-section

Using the definition of potential difference U_j given in Equation 3-27, it is obvious that there are clear dissimilarities in the potential differences obtained for flow profiles 1, 2 and 3 (see Fig. 3-16). Inspection of Fig. 3-16 also shows that the potential differences, U_j, obtained for the velocity profiles all show twice the frequency obtained with the uniform field produced by the Helmholtz coil, as shown in Fig. 3-14. This is because the magnetic field produced by an anti-Helmholtz coil is a magnetic quadrupole with a magnetic component that is zero at the centre of the pipe and along the axes of symmetry (x and y axis). The highest magnitudes of the flow induced potential differences (with respect to electrode e_5) are found near electrodes 3, 7, 11 and

15. Thus, referring to Fig. 3-16, it can be seen that the potential difference $U_3 = \varphi_3 - \varphi_5$ represents one of the two maximum values of the boundary potential differences distribution, U_j and U_3, chosen for the current study.

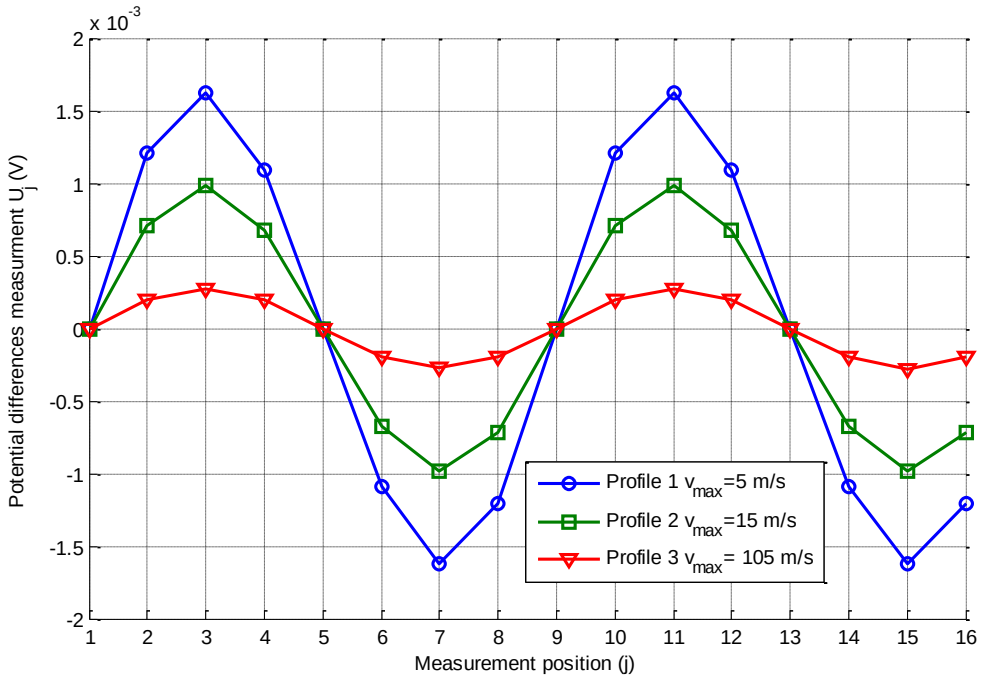

Fig. 3-16 Comparison of the boundary potential difference Uj for profiles 1, 2 and 3

For the simulation results described above, the mean velocity of water $\bar{v}_z$ was assumed to be fixed at the relatively high value of 5m/s. It was decided to investigate the effect of varying the mean velocity of water $\bar{v}_z$ and a second value of 0.5m/s was selected. In Fig. 3-17 (a) and (b) the results of this investigation are presented. The maximum potential difference U_3 is shown plotted against exponent q for q= 0, 0.1, 0.2…to 1 for the two different mean velocity conditions. It can be seen from the figure that, as q increases the maximum potential difference U_3 decreases for both values of $\bar{v}_z$. It is also apparent that the relationship between the maximum potential difference U_3 and the exponent q is changed when the mean velocity $\bar{v}_z$ is changed. Note that

the pipe radius R is fixed and the value of the magnitude of the magnetic flux density at any point in the flow cross- section is also fixed.

(a)

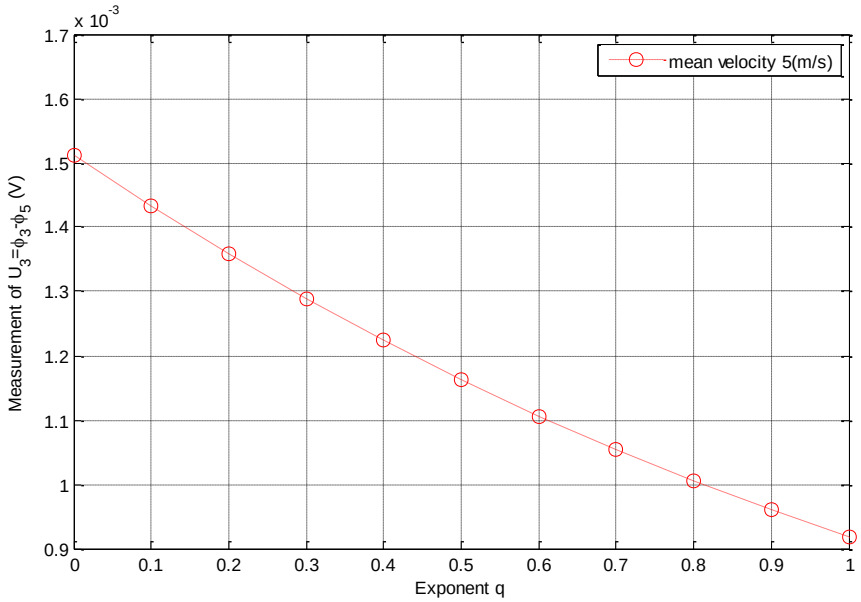

(b)

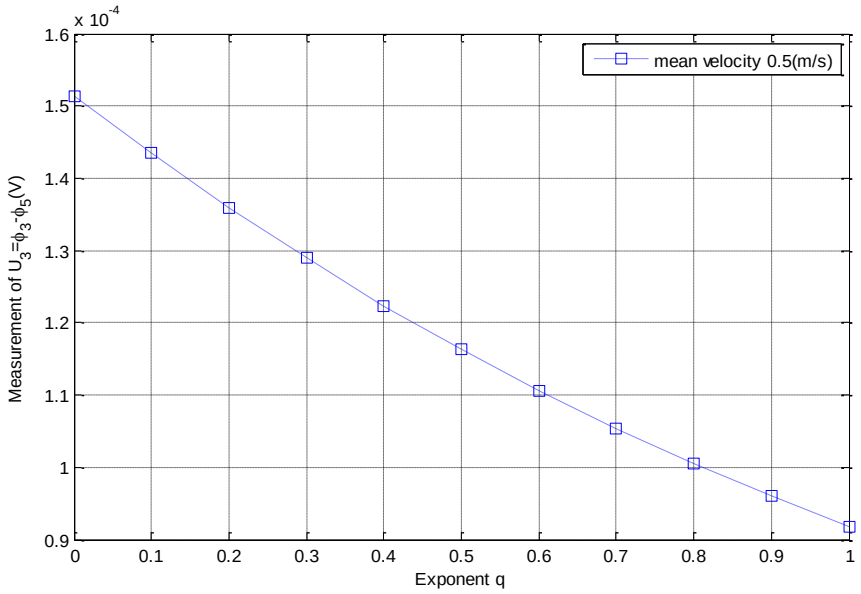

Fig. 3-17 Electrical potential difference U_3 associated with exponent q (a) the mean velocity $\overline{v}_z$=5m/s, and (b) the mean velocity $\overline{v}_z$=0.5m/s

3.5.3 Evaluation of the power-law exponent *q*

With reference to Section 3.5.2 above, it is clear that the value of maximum potential difference $\varphi_3 - \varphi_5$ is dependent upon the power law exponent q and the mean flow velocity $\bar{v}_z$. In fact, its value is also related to the magnetic flux density and pipe radius. For the purposes of this section, it is convenient to assume that there is a relationship between the exponent q and a new defined variable, A_q, that includes the mean flow velocity $\bar{v}_z$, the pipe radius R, the y-component of magnetic flux density B_{op} at the position (0, -*R*) (i.e. at electrode e_{13}) in the non-uniform magnetic field and the maximum potential difference U_3 (i.e. $U_3 = \varphi_3 - \varphi_5$). A_q is defined as:

$$A_q = \frac{\varphi_3 - \varphi_5}{B_{op} R \bar{v}_z} \qquad \text{Equation 3-34}$$

In Section 3.5.2, the mean velocity of water $\bar{v}_z$ was calculated using Equation 3-3, which assumes that the flow velocity of the conducting continuous phase is distributed axisymmetrically in the flow cross-section. Simulation provided the magnitude of the y-component of the magnetic flux density in the non-uniform magnetic field B_{op} =3×10^{-2} T. Combining this information, it is possible to calculate the variation of the value of A_q for a series of power law exponents, *q*, for the two flow conditions: mean velocity $\bar{v}_z$ =5m/s and mean velocity $\bar{v}_z$ =0.5m/s. In Fig. 3-18, the red solid line with circles corresponds to mean velocity $\bar{v}_z$ =5m/s, and the blue solid line with squares corresponds to the mean velocity $\bar{v}_z$ =0.5m/s. It is clear that both curves are very similar to each other. A percentage difference term $A_{q,E}$ can be defined as:

$$A_{q,E} = \left| \frac{A_{q,0.5} - A_{q,5}}{A_{q,0.5}} \right| \times 100 \qquad \text{Equation 3-35}$$

where $A_{q,0.5}$ is the value of A_q for $\bar{v}_z$ =0.5m/s; and $A_{q,5}$ is the value of A_q for $\bar{v}_z$ =5m/s.

From Equation 3-34 and Equation 3-35 , and by inspection of Fig. 3-18, it can be shown that, for *q* from 0.4 to 1, the value of $A_{q,E}$ is less than 0.03%. For the exponent *q* below 0.3, the

percentage error $A_{q,E}$ remains less than 0.144%. From the results of the numerical analysis, it is confirmed that, as the mean velocity $\bar{v}_z$ varied, the relationship between A_q and the exponent q can be considered to remain constant.

The reason for selecting such a limited range of values for q (i.e. q=0, 0.1, 0.2…1) was that the same range of values are observed in previous research [90]. Note that values of q outside of the range are rarely observed in normal pipe flow (single phase or multiphase).

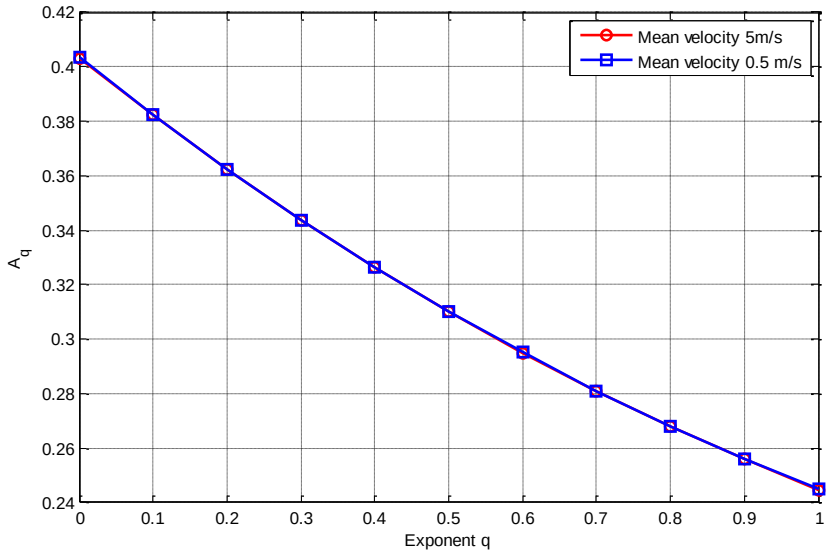

Aq	
$\bar{v}_z$=0.5m/s	$\bar{v}_z$=5m/s
0.403538	0.402957
0.382494	0.382302
0.362519	0.362374
0.343764	0.343489
0.326315	0.326249
0.310138	0.310045
0.295102	0.294996
0.281111	0.280988
0.268149	0.268141
0.256023	0.255926
0.244838	0.244694

Fig. 3-18 A_q versus q curve with different mean velocity $\bar{v}_z$=0.5 and 5 m/s

As shown Fig. 3-18 and discussed in detail below, an appropriate polynomial curve (i.e. polynomial function) was fitted to the A_q versus q relationship. This curve (function) is used in conjunction with the calculated value of A_q and the measured potential difference U_3 in the non-uniform magnetic field to estimate the exponent q of the flow. Note that the measured value of $U_1 - U_9$ in the uniform magnetic field is also required in order to determine $\bar{v}_z$ using Equation 3-33. The error associated with q will depend upon the number of data points and accuracy of the polynomial fitting curve. This implies that, to determine relatively accurate values of q, it would

require more data points (A_q and q) and a polynomial function of an appropriate order to fit all the data points. The polynomial interpolation method used in this study is discussed below.

According to theory of the polynomial interpolation, the interpolation error depends upon the order and distance between data points; therefore, it is possible to investigate the effect of using different numbers of data points and order of the polynomial function. Fig. 3-19 shows two polynomial curves with different numbers of data points. The curve shown in Fig. 3-19 (a) is of a third order polynomial, which was fitted to the eleven data points (i.e. q=0, 0.1, 0.2…1) using the least squares approach. Fig. 3-19 (b) shows a 6th order polynomial fitted to the nineteen data points (i.e. q=0, 0.1, 0.2…1, 1.5, 2,…5), again using the least squares approach [94].

In order to find an appropriate form of polynomial equation for this study, three imposed power law velocity profiles were applied into a simulation model; the calculated A_q for three velocity profiles was respectively substituted into the two polynomial equations. The estimates of exponent q were obtained from two polynomial equations. The results are shown in Table 3-3.

Case NO.	Imposed velocity profile		Calculate velocity and Aq		q ,using 3rd &6th order polynomial equation	
	$\bar{v}_z$ (m/s)	exponent q	$\bar{v}_{z,m}$ (m/s)	A_q	q_{3rd}	q_{6th}
1	2	0.21	2.0053	0.360504	0.211	0.206
2	1	0.124	1.0251	0.3775	0.125	0.119
3	5	0.038	5.0312	0.3954	0.0382	0.0366

Table 3-3 Calculated value of mean velocity $\bar{v}_{z,m}$ and q for the three velocity profiles

The three velocity profiles used with the simulation model were:

(i) In the first case, the mean axial water velocity was $\bar{v}_z$ =2m/s, and exponent q=0.21;

(ii) For the second case, the mean axial water velocity $\bar{v}_z$ =1m/s, exponent q=0.124;

(iii) For the third case, the mean axial water velocity $\bar{v}_z$ =5m/s, exponent q=0.038.

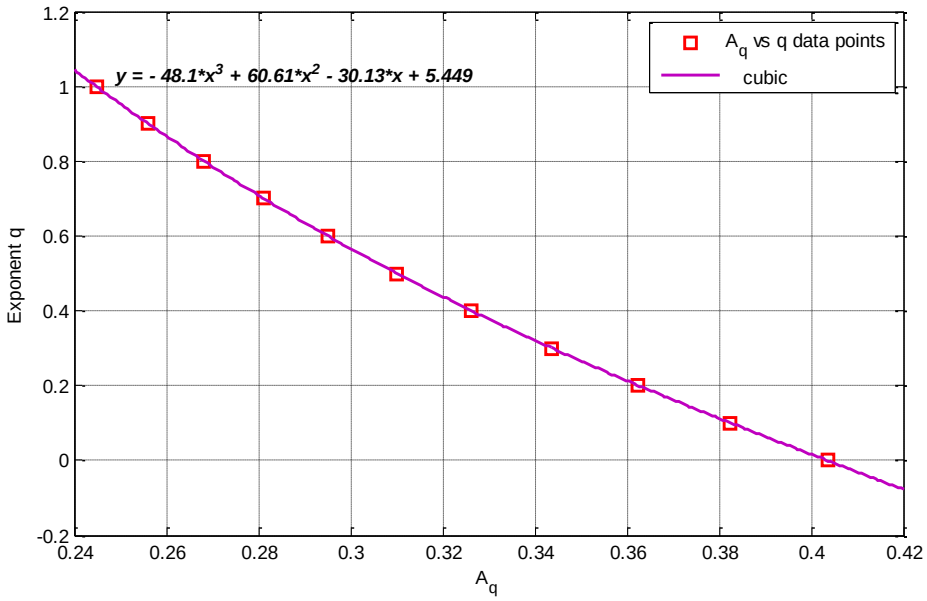

(a)

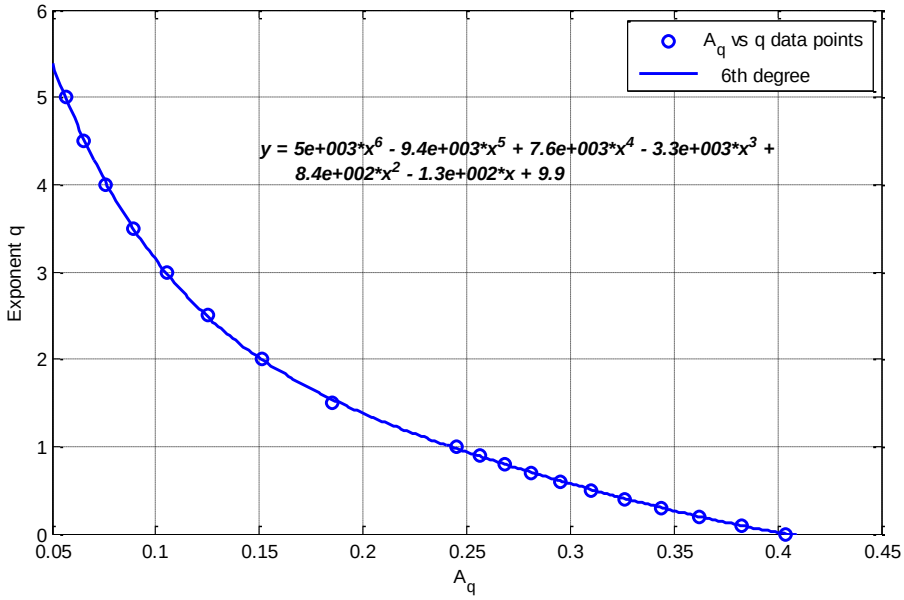

(b)

Fig. 3-19 Third and sixth order polynomials fitted to data points for exponent q plotted as a function of Aq

With different imposed velocity profiles flowing through a uniform magnetic field, the electrical potential can be measured on the pipe boundary using electrode pairs e_j (j = 1 to 4 and 6 to 16)

and e_5 (Equation 3-27) to give an electrical potential difference $U_1 - U_9$. Using Equation 3-33, the electrical potential difference $U_1 - U_9$ can be used to calculate the mean velocity $\bar{v}_{z,m1}$, $\bar{v}_{z,m2}$ and $\bar{v}_{z,m3}$ for the three cases. In this simulation, the magnetic flux density B_y (y component) was determined for the uniform magnetic field. The values of magnetic flux density B_y were averaged in the flow cross-section to give a mean value of 5.13×10^{-2} T.

Similarly, the electrical potential difference $\varphi_3 - \varphi_5$ was obtained respectively for each of the three velocity profiles flowing through an anti-Helmholtz non-uniform magnetic field. By combining the value of mean velocity (i.e. $\bar{v}_{z,m1}$, $\bar{v}_{z,m2}$ and $\bar{v}_{z,m3}$) with electrical potential $\varphi_3 - \varphi_5$, A_q can be determined using Equation 3-34. Note that B_{op} was equal to 3×10^{-2}T. The value of A_q can be used in the polynomial equations in Fig. 3-19 to obtain the exponent *q*. The comparison results between using 3rd order and 6th order polynomial equations are shown in Table 3-3.

Inspection of Table 3-3 reveals that there is reasonable agreement between the calculated values (i.e. $\bar{v}_{z,m}$, q_{3rd} and q_{6th}) and reference values of the imposed velocity profile. The maximum relative error between imposed mean velocity $\bar{v}_z$ and measured mean velocity $\bar{v}_{z,m}$ is only 0.62%. Furthermore, the relative errors between the exponent *q* and q_{3rd} are 0.48%, 0.81% and 0.53% for cases 1, 2 and 3, respectively. The relative errors in the calculated exponent q_{6th} from the original value of exponent *q* are 1.90%, 4.03%, and 3.69%.

Based on results shown in Table 3-3 and Fig. 3-19, it is apparent that the accuracy of calculating the exponent *q* would be reduced if the polynomial curve includes data points in the range of $1<q<5$, even though the polynomial order is up to 6. This reduction of the accuracy of *q* decreased the accuracy of reconstructing the local conducting continuous phase velocity distribution (see Section 3.5.1). As mentioned earlier, the value of exponent *q* was commonly in a range of $0<q<1$, thus the curve shown in Fig. 3-19 (a) should be used to determine the exponent *q* for the majority of axisymmetric velocity profiles, in order to achieve higher accuracy for the value of *q*.

3.6 Velocity profile reconstruction algorithm for non-axisymmetric flow velocity profile

The main assumption of the velocity reconstruction algorithm described in Section 3.5 is that the distribution of the water velocity in multiphase flow is axisymmetric across the pipe cross-section. However, axisymmetric distribution is rarely encountered in an inclined flow pipe. Particularly, in inclined oil-in-water flows, the local volume fraction distribution of the dispersed phase (oil) is highly non-uniform due to the density differences between water and oil. This will result in the flow velocity at the top of the pipe being faster than the bottom. Note that the reason for this phenomenon is explained in Section 1.2.1 and Section 7.5.2. Thus, it is necessary to develop an alternative technique that can be used to determine the local velocity distribution of water in non-axisymmetric flow (i.e. asymmetric velocity profile).

Referring to the review of previous research in Section 2.3.3, the working concept of the EVP flow meter is based upon the tomography technique which requires that the pipe cross-section is divided into seven pixels. To avoid ill-conditioned problems, the resolution of the local axial velocity distribution has been limited to seven pixels, which does not provide adequate local flow velocity information. However, the higher the resolution of the local axial velocity distribution, the more individual measurements are required. In practical work, there is only a limited number of measurement sensors that can be mounted on the pipe due to the physical size of the sensor.

The following sections describe a novel analytical method for the reconstruction of velocity from the sixteen electrical potential difference measurements, to determine the local water axial velocity distribution at any position in the flow cross-section in highly non-uniform flow conditions.

3.6.1 Study of the relationship between boundary potential distribution and a polynomial velocity profile

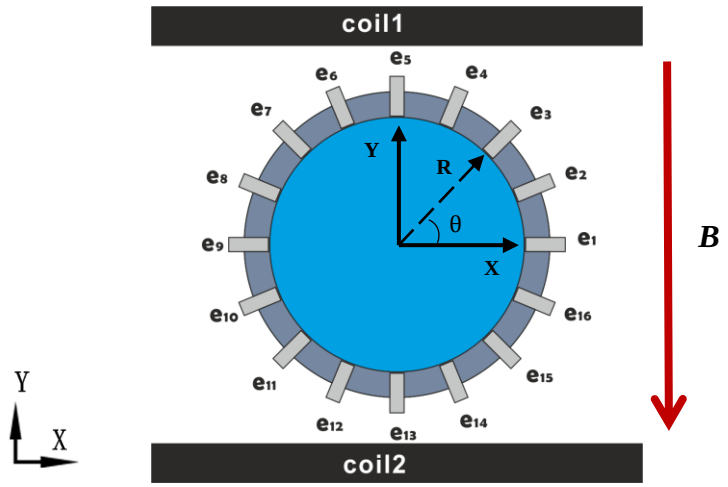

Fig. 3-20 The geometry of IFT device in the x-y plane

The aim of the analysis described in this section is the investigation of the relationship between a polynomial velocity profile and the potential distribution on the boundary of the pipe carrying the flow. As mentioned earlier, the Helmholtz coil configuration is applied to the IFT device to generate a magnetic field in the pipe cross-section (see Fig. 3-20). The electrical potential difference measurements on the boundary are obtained by the sixteen electrodes pairs, (see Equation 3-27). Shercliff and Horner [95] proposed an analytical expression of boundary potential ,which is given by a surface integral over the pipe cross-section, Ω.

$$U(\vec{x}') = \iint_{\Omega} \vec{v} \cdot [\vec{B}(\vec{x}) \times gradG(\vec{x}, \vec{x}')] d^2x$$

$$= \iint_{\Omega} v_z (B_x \frac{\partial G}{\partial Y} - B_y \frac{\partial G}{\partial x}) d^2x \qquad \text{Equation 3-36}$$

where $\vec{v}(\vec{x})$ is assumed to have a component only in the z direction, v_z, $\vec{B}(\vec{x})$ is the magnetic flux density vector, $G(\vec{x}, \vec{x}')$ is the Green's function of the second kind, the pipe cross-section, Ω, is

circular with radius R, $\vec{x}'$ is the electrode measurement position and $\vec{x}$ is the integration variable[95]. Horner[95] used Equation 3-36 to show that the electrical potential measurement at each electrode position is given by the following expression:

$$U(\theta) = B[M_1(c_0)\cos\theta + \sum_{k=1}^{\infty} M_{k+1}(c_k)\cos(k+1)\theta + M_{k+1}(s_k)\sin(k+1)\theta] \qquad \text{Equation 3-37}$$

with

$$M_{k+1}(c_k) = \int_0^R c_k(r)(\frac{r}{R})^{k+1} dr \qquad k = 0,1,2... \qquad \text{Equation 3-38}$$

$$M_{k+1}(s_k) = \int_0^R s_k(r)(\frac{r}{R})^{k+1} dr \qquad k = 0,1,2... \qquad \text{Equation 3-39}$$

$$c_k(r) = \frac{1}{\pi}\int_0^{2\pi} v_z(r,\vartheta)\cos k\vartheta d\vartheta \qquad k = 0,1,2... \qquad \text{Equation 3-40}$$

$$s_k(r) = \frac{1}{\pi}\int_0^{2\pi} v_z(r,\vartheta)\cos k\vartheta d\vartheta \qquad k = 0,1,2... \qquad \text{Equation 3-41}$$

where v_z is the velocity component in the z-direction, B is the magnitude of magnetic flux density and θ is the angle of potential measurement position (see Fig. 3-20). Equation 3-40 and Equation 3-41 represent the Fourier coefficients of the Fourier series expansion of the velocity field.

To determine more accurately the velocity distribution in the flow cross-sectional area, the velocity profile can be defined as the sum of a series of polynomial velocity components with the n^{th}-order polynomial component ($0 \le n \le 6$) written as:

$$v_n(x;y) = a_n \frac{(x\cos\theta_{Q,n} + y\sin\theta_{Q,n})^n}{R^n}$$ Equation 3-42

where $\theta_{Q,n}$ denotes the angle measured with respect to the *x*-axis (see Fig. 3-21), R is the radius of the pipe cross-section and a_n is a constant. Referring to Fig. 3-21, it is clear that the n^{th} velocity component v_n is only varies with changing distance along the direction $\theta_{Q,n}$. In addition, the velocity component v_n is constant along the lines orthogonal to the direction $\theta_{Q,n}$. It is worth noting that the velocity profile is assumed to be uniform $v_0 = a_0$ when the order n=0. The 0^{th} order velocity profile will later be replaced by an axisymmetric velocity component, which will be described in the next section.

Combining Equation 3-37 and Equation 3-42 gives the potential distribution on the pipe boundary associated with the n^{th} velocity component, is given below:

$$U_n(\theta) = \frac{1}{(n+1)2^n} a_{n,n} BR \times \sum_{k=0}^{[\frac{n}{2}]} \binom{n+1}{k} [\cos(n-2k)\theta_{Q,n}\cos(n-2k+1)\theta + \sin(n-2k)\theta_{Q,n}\sin(n-2k+1)\theta]$$

where

$$\left[\frac{n}{2}\right] = \begin{cases} \frac{n}{2} & \text{for } n \text{ is even} \\ \frac{n-1}{2} & \text{for } n \text{ is odd} \end{cases}$$ Equation 3-43

Note that B is the magnetic flux density and R represents the pipe radius.

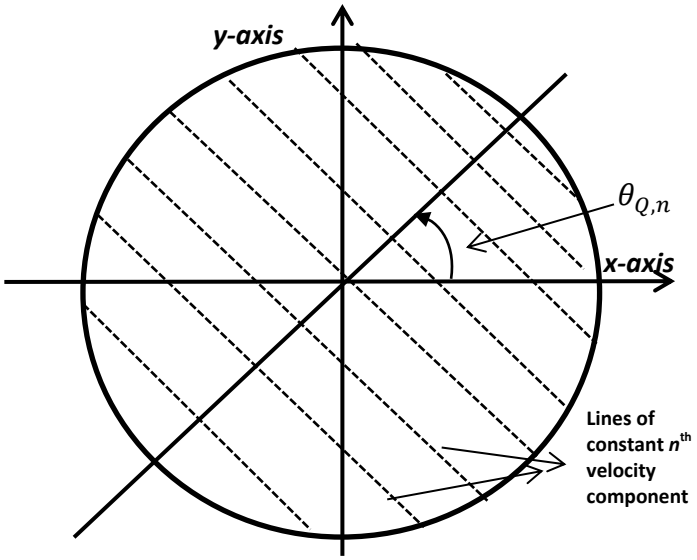

Fig. 3-21 Definition of the direction angle $\theta_{Q,n}$ [96]

From Equation 3-43, the appearance of $\cos(n-2k+1)\theta$ and $\sin(n-2k+1)\theta$ and the fact that the summation is for *k*=0 to *n*/2, shows that the multiple frequency components in the boundary potential distribution are present for the n^{th} velocity component.

3.6.1.1 Determining coefficient of n^{th} order velocity profile

In the last section we defined the basic form of the n^{th} order velocity component and associated boundary potential distribution $U_n(\theta)$. For all of the velocity components, v_n, the overall boundary potential distribution $\tilde{U}(\theta)$ is defined and calculated by adding the values of $U_n(\theta)$ for all *n*. However, because this reconstruction algorithm is based on the Discrete Fourier Transform (DFT) of the boundary potential, a given component of the DFT of the boundary potential distribution $\tilde{U}(\theta)$ relates to multiple individual velocity components. So, in order to obtain information on the n^{th} order velocity component from a single DFT component of $\tilde{U}(\theta)$, a velocity profile expression is proposed such that the $(n+1)^{th}$ component in the DFT of $\tilde{U}(\theta)$ relates only to the n^{th} order velocity component. If *n* is odd, the n^{th} velocity component can be written in the form [93, 96]:

$$v_n = a_{n,n}\frac{(x\cos\theta_{Q,n}+y\sin\theta_{Q,n})^n}{R^n}+a_{n,n-2}\frac{(x\cos\theta_{Q,n}+y\sin\theta_{\backslash Q,n})^{n-2}}{R^{n-2}}+\cdots+a_{n,1}\frac{x\cos\theta_{Q,n}+y\sin\theta_{Q,n}}{R}$$

Equation 3-44

Or, if n is even:

$$v_n(x;y) = a_{n,n}\frac{(x\cos\theta_{Q,n}+y\sin\theta_{Q,n})^n}{R^n}+a_{n,n-2}\frac{(x\cos\theta_{Q,n}+y\sin\theta_{Q,n})^{n-2}}{R^{n-2}}+\cdots+a_{n,0}$$

Equation 3-45

The coefficients used in Equation 3-44 and Equation 3-45 can be defined as:

$$a_{n,n-2} = -\frac{n-1}{4}a_{n,n}$$

Equation 3-46

$$a_{n,n-4} = -\frac{n-3}{(n+1)2^4}\binom{n+1}{2}a_{n,n}-\frac{n-3}{2^2}a_{n,n-2}$$

Equation 3-47

…

$$a_{n,n-2m} = -\frac{(n+1-2m)}{(n+1)2^{2m}}\binom{n+1}{m}a_{n,n}-\frac{(n+1-2m)}{(n-1)2^{2m-2}}\binom{n-1}{m-1}a_{n,n-2}-\frac{(n+1-2m)}{(n-3)2^{2m-4}}\binom{n-3}{m-2}a_{n,n-4}-\ldots$$

$$\ldots\frac{(n+1-2m)}{(n+1-2(m-1))2^2}\times\binom{n+1-2(m-1)}{1}a_{n,n-2(m-1)}$$

where $m = \begin{cases}\frac{n}{2} & \text{for } n \text{ is even}\\ \frac{n-1}{2} & \text{for } n \text{ is odd}\end{cases}$

Equation 3-48

As mentioned earlier, we actually expect the n^{th} order velocity profile to relate only to the $(n+1)^{th}$ DFT component of $\tilde{U}(\theta)$. The unwanted trigonometric terms can be eliminated by using the

coefficient as shown in Equation 3-48. With this condition, from the given form of the potential distribution associated with n^{th} velocity component Equation 3-43, it is possible to write [93, 96]:

$$U_n(\theta) = K_n[\cos n\theta_{Q,n} \cos(n+1)\theta + \sin n\theta_{Q,n} \sin(n+1)\theta] \quad \text{Equation 3-49}$$

where

$$K_n = \frac{1}{(n+1)2^n} a_{n,n} BR \quad \text{Equation 3-50}$$

It is apparent by inspection of Equation 3-49 that the $\cos(n+1)\theta$ and $\sin(n+1)\theta$ are only terms in the simple form of potential distribution related to the *n*th velocity component.

As an example, consider the 3rd order polynomial velocity profile; it contains cubic, quadratic, linear and uniform velocity profiles, which can be written in the form:

$$v(x;y) = v_3(x;y) + v_2(x;y) + v_1(x;y) + v_0 \quad \text{Equation 3-51}$$

From Equation 3-44 and Equation 3-45, the velocity expression can be written as:

$$v_3(x;y) = a_{3,3} \frac{(x\cos\theta_{Q,3} + y\sin\theta_{Q,3})^3}{R^3} + a_{3,1} \frac{x\cos\theta_{Q,3} + y\sin\theta_{Q,3}}{R} \quad \text{Equation 3-52}$$

$$v_2(x;y) = a_{2,2} \frac{(x\cos\theta_{Q,2} + y\sin\theta_{Q,2})^2}{R^2} + a_{2,0} \quad \text{Equation 3-53}$$

$$v_1(x;y) = a_{1,1} \frac{x\cos\theta_{Q,1} + y\sin\theta_{Q,1}}{R} \quad \text{Equation 3-54}$$

$$v_0 = a_{0,0} \quad \text{Equation 3-55}$$

In this case, the overall boundary potential distribution $\tilde{U}(\theta)$ is given by summing $U_3(\theta), U_2(\theta), U_1(\theta)$ and $U_0(\theta)$ which respectively represent the boundary potentials for the cubic, quadratic, linear and uniform velocity components.

(i) The potential distribution for the cubic (3rd) velocity component is written in the form:

$$U_3(\theta) = K_3(\cos 3\theta_{Q,3} \cos 4\theta + \sin 3\theta_{Q,3} \sin 4\theta)$$

where $K_3 = \dfrac{a_{3,3}BR}{32}$ Equation 3-56

Equation 3-56 contains terms in $\cos 4\theta$ and $\sin 4\theta$. Thus, the potential distribution $U_3(\theta)$ is related to the third velocity component and relates only to the fourth DFT component of $\tilde{U}(\theta)$. It is convenient to determine $v_3(x;y)$ by obtaining the coefficient $a_{3,3}$ and the angle $\theta_{Q,3}$ from the fourth DFT component of $\tilde{U}(\theta)$. More detail will be given in the next section.

(ii) The potential distribution associated with the quadratic (2nd) velocity component can be found as follows:

$$U_2(\theta) = K_2(\cos 2\theta_{Q,2} \cos 3\theta + \sin 2\theta_{Q,2} \sin 3\theta)$$

where $K_2 = \dfrac{a_{2,2}BR}{12}$ Equation 3-57

In the same way, from the form of potential distribution $U_2(\theta)$ (Equation 3-57), it is clear that the quadratic (2nd) velocity component only relates to the third component in the DFT of $\tilde{U}(\theta)$.

(iii) The potential distribution for the linear (1st) velocity component is:

$$U_1(\theta) = K_1(\cos \theta_{Q,1} \cos 2\theta + \sin \theta_{Q,1} \sin 2\theta)$$

where $K_1 = \dfrac{a_{1,1}BR}{4}$ Equation 3-58

For the above potential distribution, as shown in where Equation 3-58, the linear (1st) velocity component can only be determined by using the second component in the DFT of $\tilde{U}(\theta)$

(iv) The potential distribution for the uniform (0^{th}) velocity component is:

$$U_0(\theta) = K_0 \cos\theta$$

where $K_0 = a_{0,0} BR$ Equation 3-59

The uniform (0th) velocity component only depends upon the first component in the DFT of $\tilde{U}(\theta)$

From these expressions of potential distribution for all individual velocity components we may state that, if the coefficient $a_{n,n}$ and $\theta_{Q,n}$ can be determined from the associated DFT components, then this 3^{rd} order velocity profile can be reconstructed by using Equation 3-51.

Thus, this section demonstrates how to evaluate $a_{n,n}$ by applying the DFT method to the overall boundary potential distribution $\tilde{U}(\theta)$. In the present study, the potential distribution is considered as being discretised and expressed as $U_p (p = 0,...N-1)$. Note that N denotes the number of potential measurements, which is equal to sixteen, the number of electrodes (see Fig. 3-19). Applying the DFT to the discretised potential U_p , a number of DFT output components are obtained as shown below:

$$X_n = \frac{1}{N} \sum_{p=0}^{N-1} U_p \exp(-2\pi mp / N)$$

$$n = 0,1,...,N-1$$ Equation 3-60

It is worth noting that X_n is associated with the $(n\text{-}1)^{th}$ boundary potential component $U_{n-1}(\theta)$, which is, in turn, associated with $(n\text{-}1)^{th}$ velocity component $v_{n-1}(x;y)$.

With reference to the application of DFT, the output magnitude of the DFT for that particular sinewave gives:

$$|X_n| = \frac{A_0}{2}$$ Equation 3-61

where A_0 is the peak amplitude of the sinewave component of the input signal.

As stated earlier, the term $\tilde{U}(\theta)$ is the sum of a series of boundary potential distributions $U_n(\theta)$. So, it is now possible to determine the coefficient K_n by using the following form:

$$K_n = \pm 2|X_{n+1}|$$ Equation 3-62

The coefficient K_n can be calculated from the output magnitude of the $(n+1)^{th}$ DFT component obtained from the boundary potential $\tilde{U}(\theta)$. The coefficient $a_{n,n}$ and $|X_{n+1}|$ can be related by combining Equation 3-49 and Equation 3-61, thus:

$$a_{n,n} = \pm \frac{(n+1)2^{n+1}}{BR}|X_{n+1}|$$ Equation 3-63

For the uniform velocity profile, the coefficient $a_{0,0}$ can be determined as:

$$a_{0,0} = \text{sgn}(\text{Re}\, X_1)\frac{2|X_1|}{BR}$$ Equation 3-64

For the linear condition ($n = 1$):

$$a_{1,1} = \frac{8}{BR}|X_2|$$ Equation 3-65

For quadratic and higher orders ($n \geq 2$), Equation 3-63 applies with n having the appropriate value.

According to the characteristic of DFT , the unique values of X_n exist only from 0Hz to the Nyquist frequency (the Nyquisty frequency is half the sampling freqnecy $N/2$). In addition, as the first DFT component X_0 and the last DFT component $X_{N/2}$ are real numbers, the n^{th} velocity component can only be determined by using DFT component X_1 to $X_{N/2-1}$. Therefore, the polynomial velocity profile can contain only the 0^{th} to $N/2$-2 components.

Let us now return to the example in regards to 3rd order velocity profile. After applying the above equations Equation 3-63 to Equation 3-65, into four velocity components (Equation 3-52 to Equation 3-55), all individual velocity components are rearranged to give:

$$v_3(x;y) = \pm\frac{64|X_4|}{BR}\frac{(x\cos\theta_{Q,3} + y\sin\theta_{Q,3})^3}{R^3} \mp \frac{32|X_4|}{BR}\frac{x\cos\theta_{Q,3} + y\sin\theta_{Q,3}}{R} \quad \text{Equation 3-66}$$

$$v_2(x;y) = \pm\frac{24|X_3|}{BR}\frac{(x\cos\theta_{Q,2} + y\sin\theta_{Q,2})^2}{R^2} \mp \frac{6|X_3|}{BR} \quad \text{Equation 3-67}$$

$$v_1(x;y) = \frac{8|X_2|}{BR}\frac{x\cos\theta_{Q,1} + y\sin\theta_{Q,1}}{R} \quad \text{Equation 3-68}$$

$$v_0 = \text{sgn}(\text{Re } X_1)\frac{2}{BR}|X_1| \quad \text{Equation 3-69}$$

We can see that, from Equation 3-66 to Equation 3-69, in order to obtain each velocity component, the angle $\theta_{Q,n}$ is also needed to be determined from the information of the associated $n+1^{\text{th}}$ DFT component. This will be described in the following section.

3.6.1.2 Determination of angle of direction of velocity profile

As mentioned earlier, (see section 3.6.1.1), the angle $\theta_{Q,n}$ needs to be determined. This section describes how the direction $\theta_{Q,n}$ of the n^{th} order velocity component (n=1 to 6) is obtained from the argument ψ_{n+1} of the $(n+1)^{\text{th}}$ DFT component, X_{n+1}, associated with the n^{th} order velocity component. For this purpose, there is a need to investigate the relationship between ψ_{n+1} and $\theta_{Q,n}$ for the velocity component from linear to 6th order.

Let us start now by considering the argument ψ_{n+1} associated with the DFT component X_{n+1}. Due to the component X_n being a complex number (see Equation 3-60), it can be seen that the argument (i.e. phase angle) of a DFT component X_n is the inverse tangent of the quotient formed by dividing the imaginary part by the real part. Thus, the argument ψ_{n+1} associated with the DFT component X_{n+1} is determined using

$$\psi_{n+1} = \arctan\frac{\mathrm{Im}(X_{n+1})}{\mathrm{Re}(X_{n+1})}$$ Equation 3-70

It is essential to state that the quadrant in which the complex number X_{n+1} lies must be taken into account when determining ψ_{n+1}. By using this method in conjunction with the form of potential distribution (see Equation 3-49 and Equation 3-50), it is possible to create a plot of the direction $\theta_{Q,n}$ versus the argument ψ_{n+1} for the given velocity component. After repeating this process six times with six individual velocity components, then an analytical function is proposed for determining the direction $\theta_{Q,n}$ from the argument ψ_{n+1} of the complex number X_{n+1}.

(i) Linear velocity component

In order to investigate the relationship of angle ψ_{n+1} and $\theta_{Q,n}$ in the case of the linear velocity component, the linear velocity component is defined in the form:

$$v_1(x;y) = a_{1,1}\frac{x\cos\theta_{Q,1} + y\sin\theta_{Q,1}}{R}$$ Equation 3-71

For the linear velocity component, the potential distribution can be written in terms of Equation 3-72:

$$U_1(\theta) = \frac{a_{1,1}BR}{4}\left(\cos\theta_{Q,1}\cos 2\theta + \sin\theta_{Q,1}\sin 2\theta\right)$$ Equation 3-72

where the angle $\theta_{Q,1}$ lies between 0 to $360°$.

By applying the DFT to the potential distribution (Equation 3-72), the resulting argument ψ_2 can be plotted in the form of $\theta_{Q,1}$ and ψ_2, as shown in Fig. 3-22. The argument ψ_2 is presented in two different forms, because $a_{1,1}$ can be positive ($a_{1,1} > 0$) or negative ($a_{1,1} < 0$).

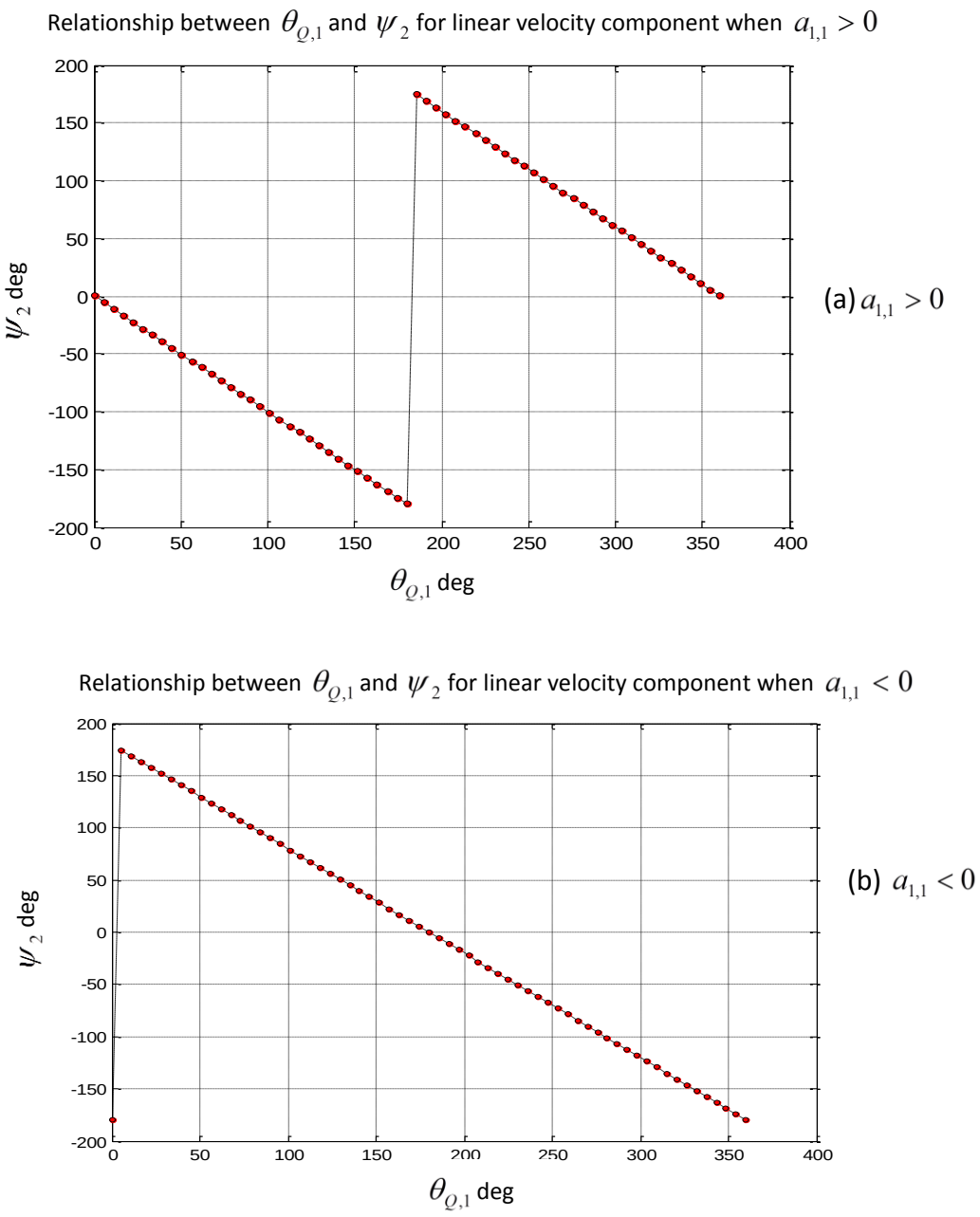

Fig. 3-22 Relationship between $\theta_{Q,1}$ and ψ_2 for linear velocity profile

From Fig. 3-22 (a), when $a_{1,1} > 0$:

$$\begin{cases} \psi_2 = -\theta_{Q,1} & \text{for } \theta_{Q,1} \in [-180°, 180°) \\ \psi_2 = -\theta_{Q,1} + 360° & \text{for } \theta_{Q,1} \in [180°, 540°) \end{cases}$$ Equation 3-73

See Fig. 3-22 (b), if $a_{1,1} < 0$

$$\psi_2 = -\theta_{Q,1} + 180° \quad \text{for } \theta_{Q,1} \in [0, 360°)$$ Equation 3-74

Inspection of Equation 3-73 and Equation 3-74 allows the inverse relationships to be presented.

If $a_{1,1} > 0$:

$$\begin{cases} \theta_{Q,1} = -\psi_2 & \text{for } \psi_2 \in [-180°, 180°) \\ \theta_{Q,1} = -\psi_2 + 360° & \text{for } \psi_2 \in [-180°, 180°) \end{cases}$$ Equation 3-75

If $a_{1,1} < 0$:

$$\theta_{Q,1} = -\psi_2 + 180° \quad \text{for } \psi_2 \in [-180°, 180°)$$ Equation 3-76

(ii) Quadratic velocity profile

Assuming the velocity component is quadratic (see Equation 3-53), the potential distribution of the quadratic velocity component can be expressed as shown in Equation 3-57. The relationship between $\theta_{Q,2}$ and ψ_3 for a quadratic velocity component is shown in Fig. 3-23.

The results shown in Fig. 3-23 (a) for $a_{2,2} > 0$ can be represented by Equation 3-77

$$\begin{cases} \psi_3 = -2\theta_{Q,2} + 360° & \text{for } \theta_{Q,2} \in [90°, 270°) \\ \psi_3 = -2\theta_{Q,2} & \text{for } \theta_{Q,2} \in [-90°, 90°) \end{cases}$$ Equation 3-77

The inverse relationship can be expressed as:

$$\begin{cases} \theta_{Q,2} = -\dfrac{\psi_3}{2} + 180° & \text{for } \psi_3 \in [-180°, 180°) \\ \theta_{Q,2} = -\dfrac{\psi_3}{2} & \text{for } \psi_3 \in [-180°, 180°) \end{cases}$$

Equation 3-78

Fig. 3-23 (b) shows the variation of ψ_3 with $\theta_{Q,2}$ for $a_{2,2} < 0$

$$\psi_3 = -2\theta_{Q,2} + 180° \quad \text{for } \theta_{Q,2} \in [0, 180°)$$

Equation 3-79

The inverse relationship can be written as:

$$\theta_{Q,2} = -\frac{\psi_3}{2} + 90° \quad \text{for } \psi_3 \in [-180°, 180°)$$

Equation 3-80

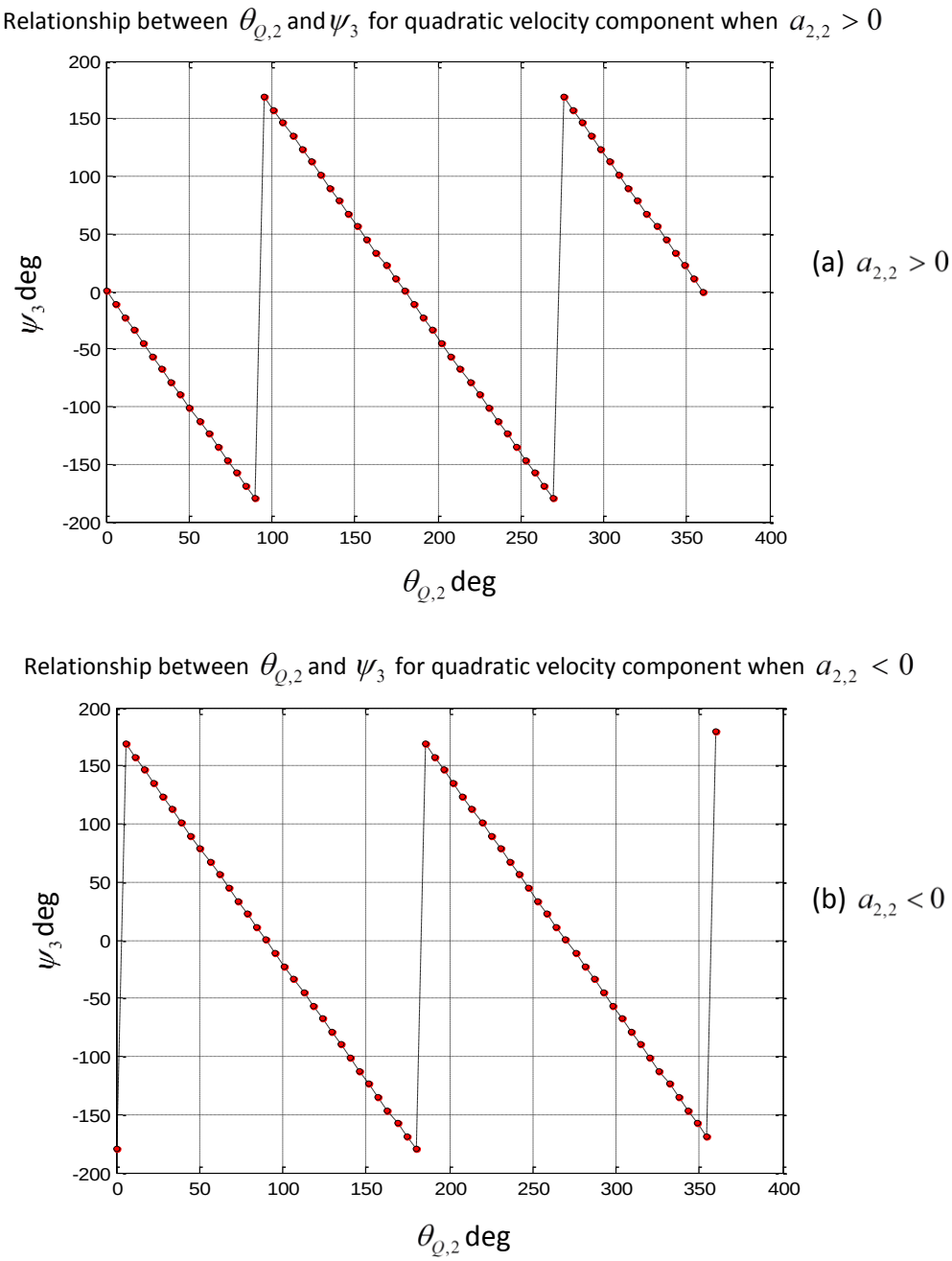

Fig. 3-23 Relationship between $\theta_{Q,2}$ and ψ_3 for quadratic velocity profile

The procedure described above was repeated for the remaining velocity profiles (cubic, quartic, quintic and 6th order). The resulting relationships between the argument ψ_{n+1} and $\theta_{Q,n}$ are shown in Fig. 3-24 to Fig. 3-27.

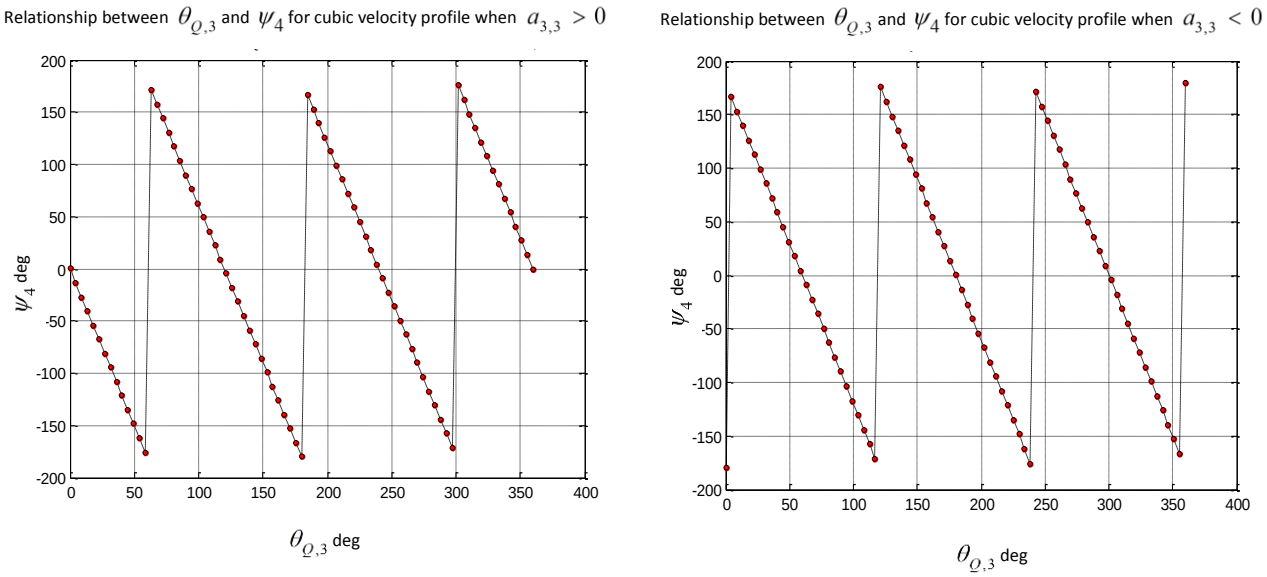

Fig. 3-24 Relationship between $\theta_{Q,3}$ and ψ_4 for cubic velocity profile

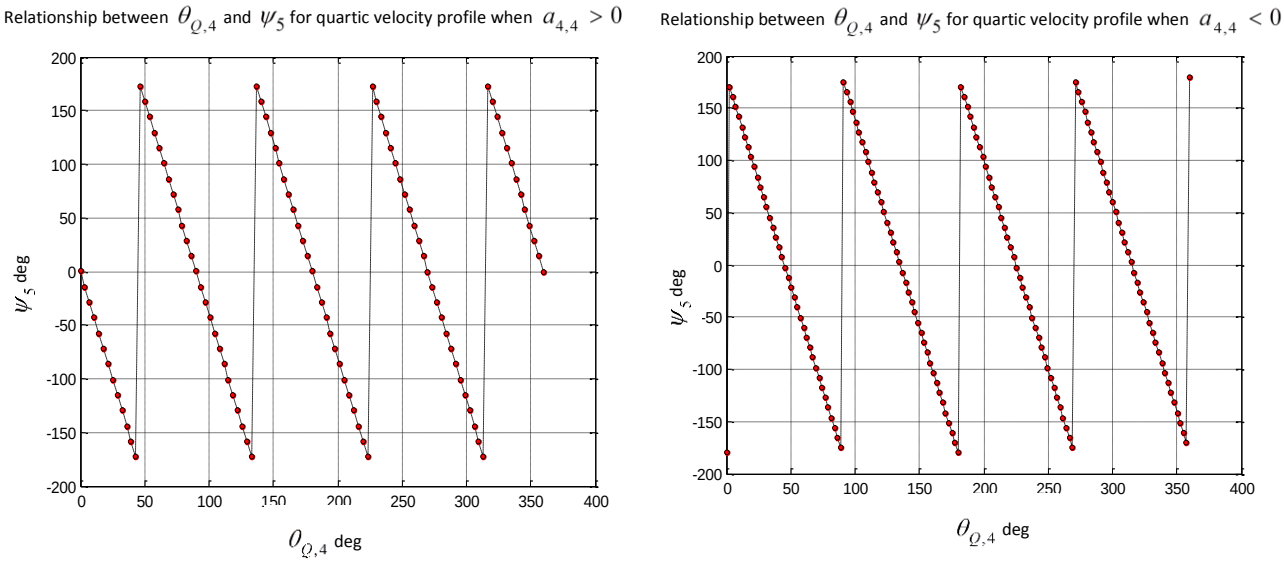

Fig. 3-25 Relationship between $\theta_{Q,4}$ and ψ_5 for quartic velocity profile

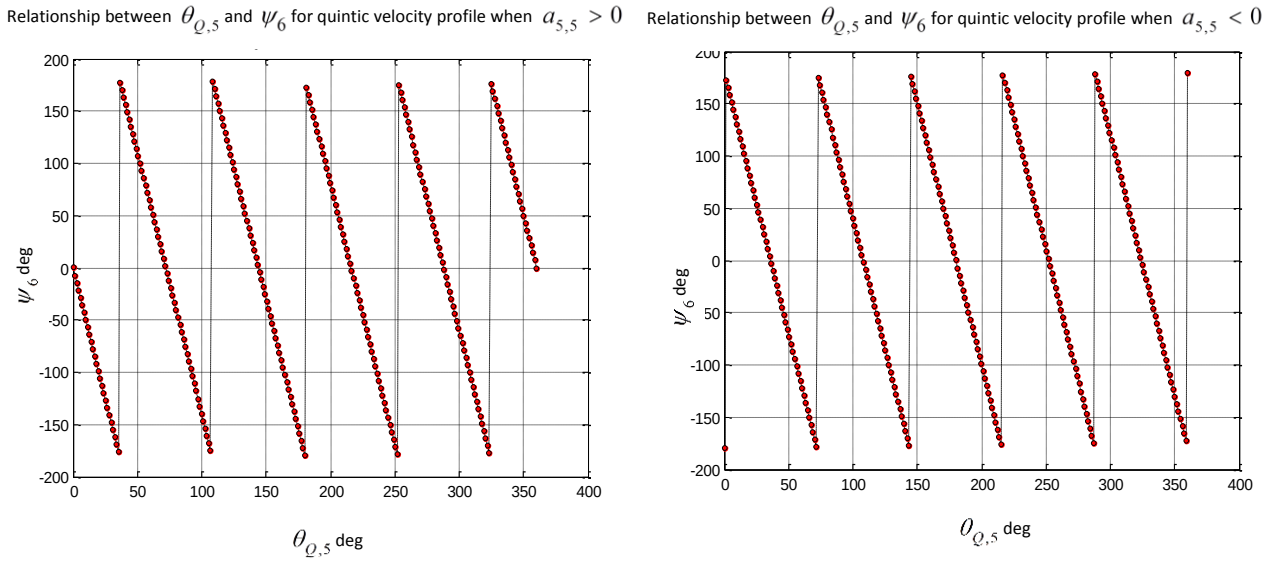

Fig. 3-26 Relationship between $\theta_{Q,5}$ and ψ_6 for quintic velocity profile

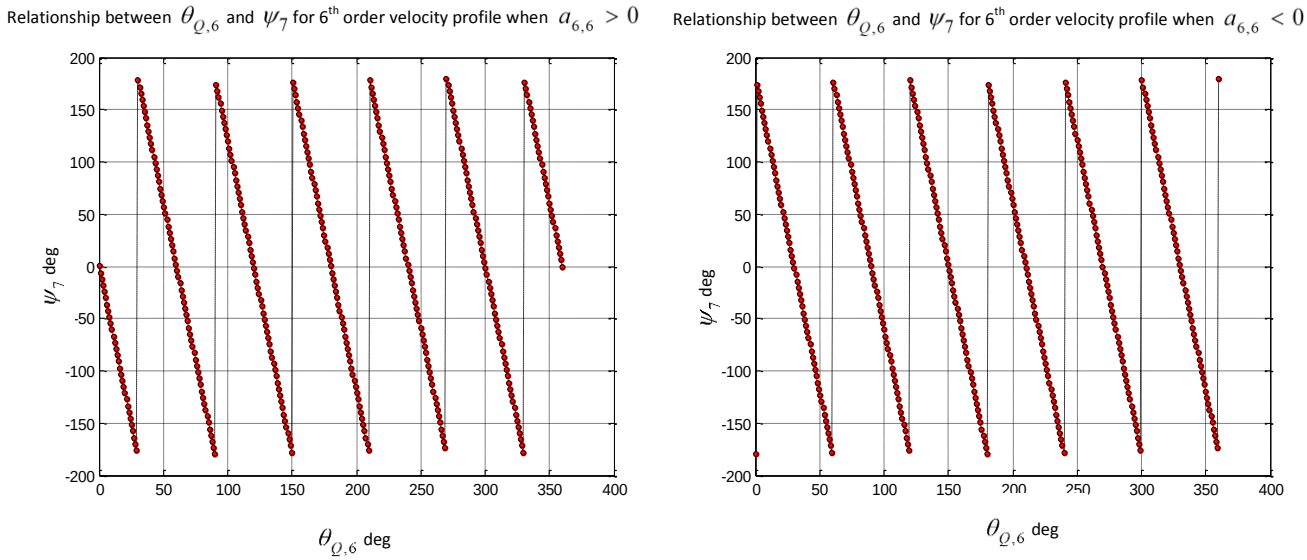

Fig. 3-27 Relationship between $\theta_{Q,6}$ and ψ_7 for 6th order velocity profile

For the relationships between ψ_{n+1} and $\theta_{Q,n}$ shown above, the angle of direction $\theta_{Q,n}$ of the n^{th}-order velocity profile can be written in a general form. When the order n is odd (n=1, 3, and 5), it can be seen from Fig. 3-22, Fig. 3-24 and Fig. 3-26 that, whether the coefficient $a_{n,n}$ is positive or negative, the angle $\theta_{Q,n}$ can be written in the same form:

$$\theta_{Q,n} = -\frac{\psi_{n+1}}{n} + \frac{2k\pi}{n}$$

$$\theta_{Q,n} \in \left[\frac{(2k-1)\pi}{n}, \frac{(2k+1)\pi}{n} \right) \qquad k = 0,1,2...,n-1 \qquad \text{Equation 3-81}$$

In the case when the order n is even, (n=2, 4, and 6), the angle $\theta_{Q,n}$ will depend on whether $a_{n,n} > 0$ or $a_{n,n} < 0$.

When $a_{n,n} > 0$, angle $\theta_{Q,n}$ can be written as:

$$\theta_{Q,n} = -\frac{\psi_{n+1}}{n} + \frac{2k\pi}{n}$$

$$\theta_{Q,n} \in \left[\frac{(2k-1)\pi}{n}, \frac{(2k+1)\pi}{n} \right) \qquad k = 0,1,2...,n/2-1 \qquad \text{Equation 3-82}$$

When $a_{n,n} < 0$, angle $\theta_{Q,n}$ can be written as:

$$\theta_{Q,n} = -\frac{\psi_{n+1}}{n} + \frac{(2k+1)\pi}{n}$$

$$\theta_{Q,n} \in \left[\frac{k2\pi}{n}, \frac{(k+1)2\pi}{n} \right) \qquad k = 0,1,2...,n/2-1 \qquad \text{Equation 3-83}$$

By using the value of angle $\theta_{Q,n}$ calculated from the above equation, in conjunction with the coefficient calculation method described in Section 3.6.1.1, it is possible to reconstruct the velocity profile (see Equation 3-42). However, because there are n possible values of angle $\theta_{Q,n}$ for a given velocity component, there will be $n!$ possible velocity profiles. Choosing the optimum velocity profile is described in the next chapter.

3.7 Extending the reconstruction algorithm to include axisymmetric velocity components

The reconstruction algorithm described in Section 3.6 can only used for determining the local water velocity distribution for non-uniform flow profiles, such as stratified flows which do not include an axisymmetric velocity component. Referring to the defined velocity profile expression in Equation 3-44 and Equation 3-45, this velocity reconstruction algorithm is not suitable for axisymmetric velocity components (see Section 3.5). It was, therefore, decided to perform the following analysis to develop an extended velocity reconstruction technique, which can be used with flows which may contain an axisymmetric velocity component, as well as non-axisymmetric components.

In the extended reconstruction algorithm, the overall velocity profile still includes a superposition of polynomials up to the 6th order, but the 0th order velocity component is replaced by an axisymmetric velocity component. This technique is based upon the method described in Section 3.5, from which it is apparent that the axisymmetric velocity component cannot be determined by simply assuming that the velocity profile associated with the 0th order component is uniform (q=0). Furthermore, in order to distinguish different axisymmetric velocity components, it is necessary to calculate the value of A_q from the electrical potential difference measurements $\hat{U}_j$ in a non-uniform (anti-Helmholtz) magnetic field. It is worth noting that the symbol '^' appearing over a quantity means that that quantity was obtained in a non-uniform magnetic field. This section will focus on two aspects:

i) Using the theory developed in Section 3.5 in conjunction with use of the DFT, it is possible to develop an alternative method to determine the value of A_q and mean velocity $\bar{v}_z$.

ii) Investigating the effects of n^{th} order velocity components on the components of the DFT of the boundary potential distribution obtained in the non-uniform magnetic field and how these DFT components affect the calculation of A_q.

3.7.1 Applying an axisymmetric velocity component into a polynomial velocity profile

With reference to Equation 3-23 and to the discussion in Section 3.5.3, it can be seen that the mean velocity $\bar{v}_z$ and exponent q need to be determined in order to provide the axisymmetric power law velocity profile. Through the study of the three different axisymmetric velocity profiles, q = 0, 1 and 5, it was seen that the parameter A_q was calculated from boundary potential measurements in a non-uniform magnetic field to evaluate the exponent q by using the curve of A_q vs. q (see Fig. 3-19 (a)). The purpose of this section is to predict the mean velocity $\bar{v}_z$ and the parameter A_q using the DFT method described in Section 3.6.1.1.

With reference to Lucas and Zhang [92], from Equation 3-64 and Equation 3-69, it can be shown that for n equal to zero, the mean velocity $\bar{v}_z$ will be equal to $a_{0,0}$. The value of $a_{0,0}$ can be readily determined from the magnitude of the DFT component $|X_1|$, as shown in Equation 3-64. Note that the DFT component X_1 is determined by applying the DFT to the boundary potential distribution in a uniform magnetic field. Fig. 3-28 shows the magnitude of the DFT component $|X_1|$ for the three axisymmetric velocity profiles with the same mean velocity, $\bar{v}_z$ =5m/s (see Section 3.5.2), which are respectively equal to 3.2065×10^{-3}, 3.2060×10^{-3} and 3.2063×10^{-3} for q = 0, 1 and 5, respectively. According to Equation 3-64, the calculated mean velocities are respectively equal to 5.00039m/s, 4.99961m/s and 5.00015m/s. Note that the magnetic flux density is B=5.13 T. By inspection of the results, it can be found that the maximum value of relative error is 0.065%, too small to be considered significant. Therefore, the above results have proven that the mean flow velocity $\bar{v}_z$ is equal to $a_{0,0} = \mathrm{sgn}(\mathrm{Re}\, X_1)\dfrac{2|X_1|}{BR}$ for any axisymmetric velocity profile.

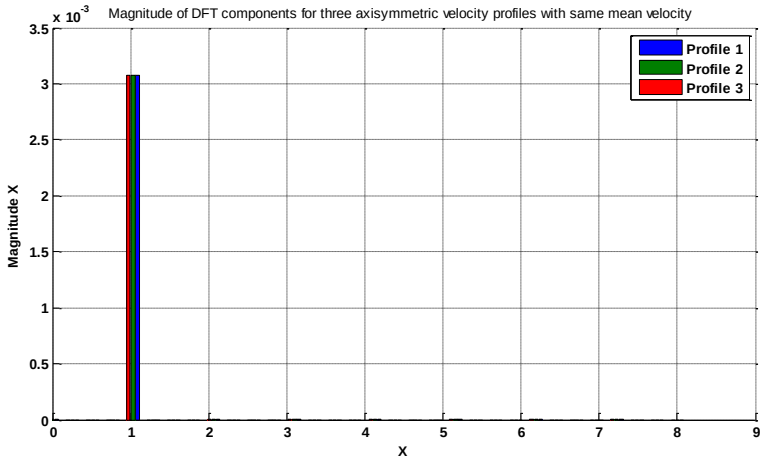

Fig. 3-28 Magnitude of DFT components for three axisymmetric velocity profiles with mean velocity 5m/s and *q* = 0, 1, 5 (see Section 3.5.2) in a uniform magnetic field

The next stage is to consider the form of the A_q function associated with the DFT components.

In order to determine the value of A_q, the potential difference measurement $\varphi_3 - \varphi_5$ in a non-uniform magnetic field has to be found, which is the maximum value of boundary potential distribution in the magnetic field. From Fig. 3-16, it can be seen that for an axisymmetric velocity component the boundary potential distribution is a sine waveform with amplitude $\varphi_3 - \varphi_5$ and wavelength (around the inner pipe boundary) equal to πR. By applying the DFT to the 'sine wave' boundary potential distribution, the amplitude of the sine wave is equal to $2\left|\mathrm{Im}\,\widehat{X}_2\right|$, which is identical to the $\varphi_3 - \varphi_5$.

Fig. 3-29 shows the imaginary parts and real parts of the DFT components for the three velocity profiles (see Section 3.5.2). From inspection of the results shown in Fig. 3-29 (a), the values of $2\left|\mathrm{Im}\,\widehat{X}_2\right|$ are respectively equal to 16.2×10^{-4}, 9.8×10^{-4} and 2.8×10^{-4}, which are the same as the potential measurement $\varphi_3 - \varphi_5$ results shown in Fig. 3-16. The real parts of the DFT components are shown in Fig. 3-29 (b) and it can be seen that the value of $\left|\mathrm{Re}\,\widehat{X}_2\right|$ is approximately equal to 1×10^{-7}, which is negligible compared to the $\left|\mathrm{Im}\,\widehat{X}_2\right|$. Thus, the term A_q can also be defined by [96]:

$$A_q = \frac{2\left|\mathrm{Im}\,\hat{X}_2\right|}{B_{op}R\bar{v}_z}$$ Equation 3-84

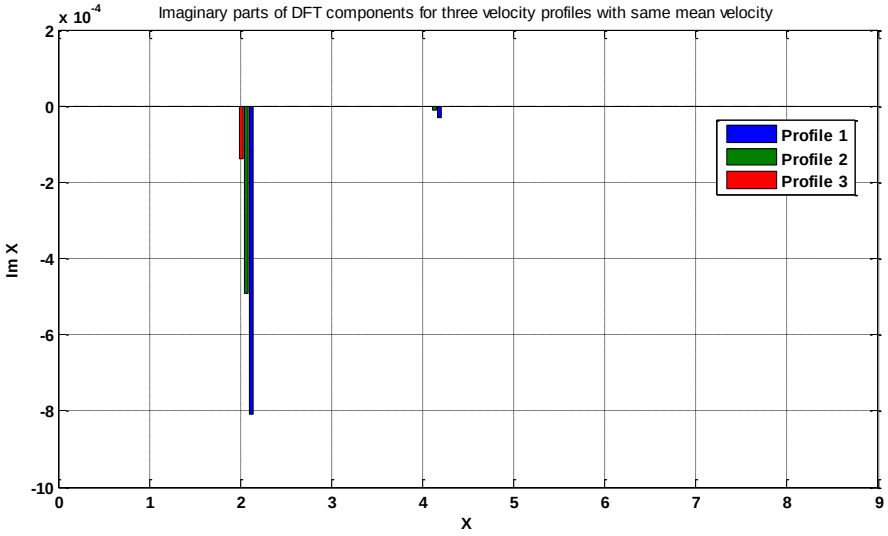

(a)

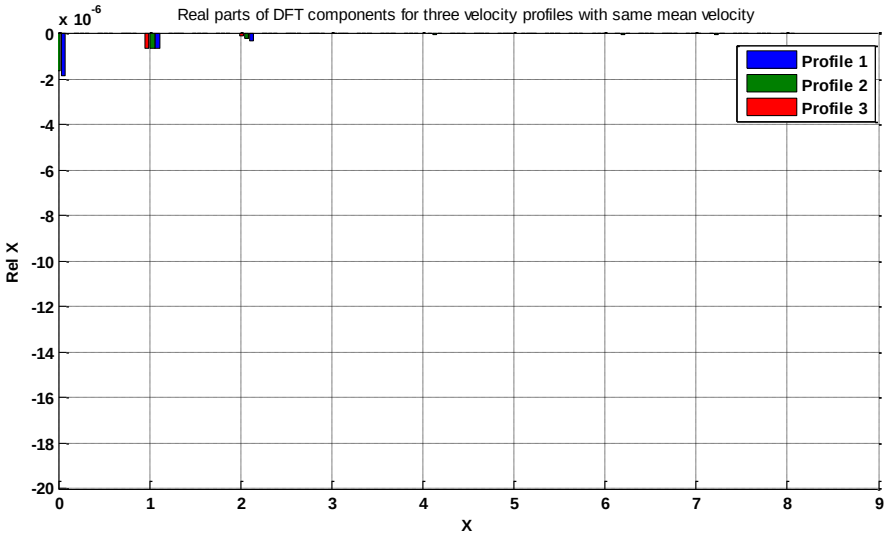

(b)

Fig. 3-29 Applying DFT into boundary potential distribution in a non-uniform magnetic field (a) imaginary parts of DFT components for three axisymmetric velocity profiles; (b) real parts of DFT components for three velocity profiles (see Section 3.5.2)

It is worth noting that, by using Fig. 3-19 (a), q can be determined from the value of A_q given in Equation 3-84 only when the velocity profile is purely axisymmetric. When the velocity profile contains additional polynomial components, the value of $\left|\mathrm{Im}\,\hat{X}_2\right|$ will be affected. This is addressed in the next section.

3.7.2 Study of the effects of polynomial velocity components on DFT component $Im\hat{X}_2$

Section 3.7.1 clearly showed that axisymmetric velocity components with different values of q gave different values of $\mathrm{Im}\,\hat{X}_2$, and this $\mathrm{Im}\,\hat{X}_2$ can be considered as a unique signature of the individual axisymmetric velocity component and can be used to determine the value of A_q. This section will discuss the influence of the polynomial velocity components (1st to 6th order) on the imaginary part of the DFT component, $\mathrm{Im}\,\hat{X}_2$.

Using Equation 3-44 and Equation 3-45, six polynomial velocity components (1st to 6th order) were defined and respectively applied to the COMSOL simulation model. It should be noted that the coefficients $a_{1,1}, a_{2,2}, ..., a_{6,6}$ were set to be a constant value 10, and the angle $\theta_{Q,n}$ was varied from 0 to 360°. With velocity components of different orders, and using a non-uniform magnetic field, the electrical potential differences $\hat{U}_j$ were obtained. The DFT component $\mathrm{Im}\,\hat{X}_2$ can be determined by applying the DFT to the electrical potential differences $\hat{U}_j$. The relationships between $\mathrm{Im}\,\hat{X}_2$ and angle $\theta_{Q,n}$ for each polynomial velocity component are shown in Fig. 3-30.

By inspection of Fig. 3-30, it can be seen that the influence of the quadratic (2nd order) velocity component on the value of $\mathrm{Im}\,\hat{X}_2$ is much greater than the effects of any of the other polynomial velocity components (1st, 3rd, 4th, 5th and 6th). Note that the value of $\mathrm{Im}\,\hat{X}_2$ for polynomial velocity components other than the 2nd order were in the range of 10^{-7} to 10^{-8}, which were too small to be considered significant.

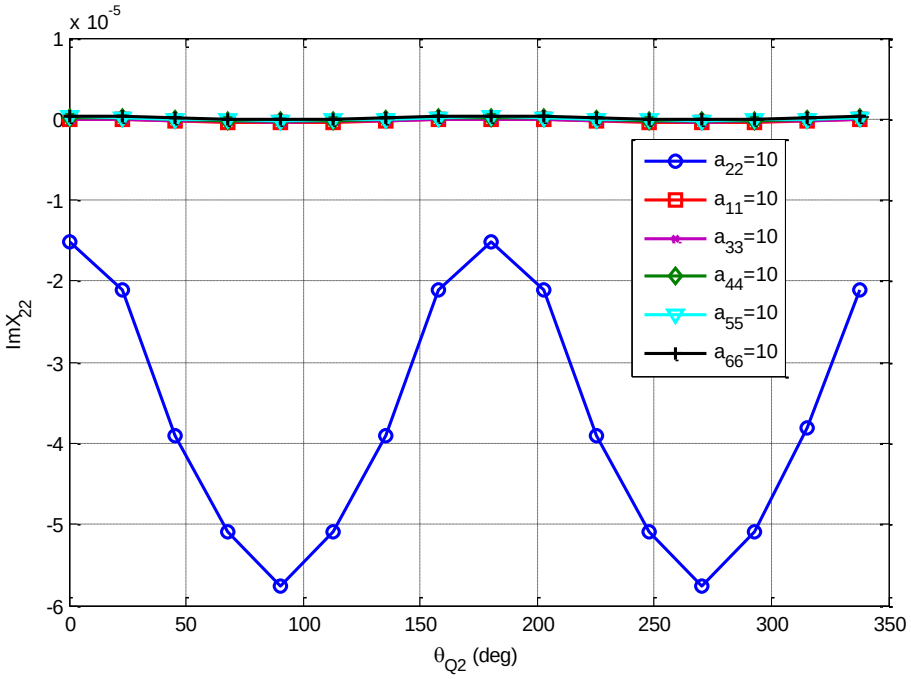

Fig. 3-30 The imaginary part $Im\hat{X}_2$ for polynomial velocity components 1st to 6th order with varying angle

From the results presented in Fig. 3-30, the value of A_q cannot be readily determined from the DFT component $\hat{X}_2$, because $\mathrm{Im}\,\hat{X}_2$ will not only be affected by the axisymmetric velocity component, but will also be affected by the quadratic velocity component. It is necessary to remove the contribution of the quadratic velocity component $\mathrm{Im}\,\hat{X}_2$ before A_q, as defined by Equation 3-84, can be used in conjunction with Fig. 3-19 (a) to give the power law exponent q associated with the axisymmetric velocity component. Once the contribution of the quadratic velocity component to $\mathrm{Im}\,\hat{X}_2$ has been determined, then this contribution to $\mathrm{Im}\,\hat{X}_2$ can be removed using [96]:

$$(\mathrm{Im}\,\hat{X}_2)_0 = \mathrm{Im}\,\hat{X}_2 - \mathrm{Im}(\hat{X}_2)_2 \qquad \text{Equation 3-85}$$

where $(\mathrm{Im}\,\hat{X}_2)_0$ and $\mathrm{Im}(\hat{X}_2)_2$ refer to the contributions of the axisymmetric and quadratic velocity components to $\mathrm{Im}\,\hat{X}_2$, respectively.

Let us now consider the possible factors which can influence the value of $\mathrm{Im}(\hat{X}_2)_2$. With reference to Equation 3-53, the coefficient $a_{2,0}$ can be calculated from $a_{2,2}$ according to Equation 3-46. Thus, the effects of coefficient $a_{2,2}$ and angle $\theta_{Q,2}$ on $\mathrm{Im}(\hat{X}_2)_2$ should be investigated. Moreover, as mentioned earlier, $\mathrm{Im}\,\hat{X}_2$ is determined by applying the DFT to the potential difference measurements $\hat{U}_j$. Thus, the magnetic flux density B_{op} (i.e. non-uniform magnetic field) and pipe radius *R* should also be considered.

Based on these concerns, three quadratic velocity profiles can be defined and used in the COMSOL simulation model. The differences between the three quadratic velocity profiles are as follows:

In the first instance, *R* was set to be 0.025m, the magnetic flux density B_{op} = 0.0052 T and $a_{2,2}$ =10.

In the second instance, *R* was kept as 0.025m, the magnetic flux density B_{op} =0.0052 T and $a_{2,2}$ =100.

In the last instance, *R* was kept as 0.025m, the magnetic flux density B_{op} =0.052 T and $a_{2,2}$ =100.

After applying the DFT to the measured potential difference distribution $\hat{U}_j$, the imaginary parts of the DFT components $\mathrm{Im}(\hat{X}_2)_2$ were found with different values of $\theta_{Q,2}$ for each of the three different quadratic velocity profiles and are shown in Fig. 3-31.

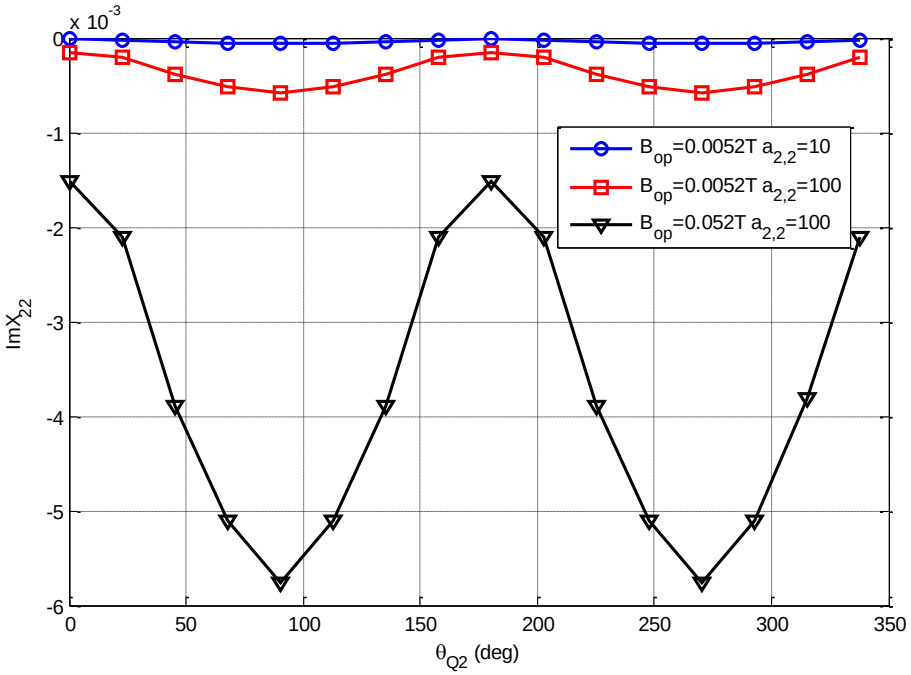

Fig. 3-31 Effects of different quadratic velocity profiles on ImX_{22}

Detailed analysis of the data given in Fig. 3-31 reveals that the quantity of $\mathrm{Im}(\hat{X}_2)_2$ not only varies with angle $\theta_{Q,2}$, but is also proportional to coefficient $a_{2,2}$, the magnetic flux density B_{op} and the pipe radius R. Consequently, a new parameter $A_{2,\theta}$ can be defined as [96]:

$$A_{2,\theta} = \frac{\mathrm{Im}(\hat{X}_2)_2}{B_{op} a_{2,2} R} \qquad \text{Equation 3-86}$$

By substituting $\mathrm{Im}(\hat{X}_2)_2$ and associated parameters B_{op}, $a_{2,2}$ and R from Fig. 3-31 into Equation 3-86, the relationship between value of $A_{2,\theta}$ and angle $\theta_{Q,2}$ can be written in the form:

$$A_{2,\theta} = 0.009653 \cos 2\theta_{Q,2} - 0.01665 \qquad \text{Equation 3-87}$$

$A_{2,\theta}$ as a function of angle $\theta_{Q,2}$ can be seen in Fig. 3-32.

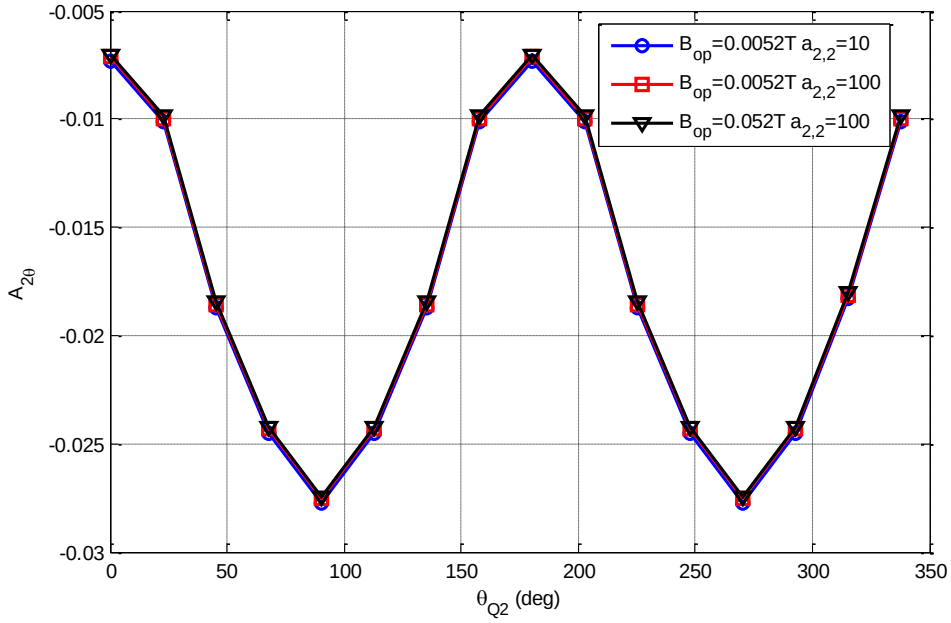

Fig. 3-32 $A_{2,\theta}$ as a function of $\theta_{Q,2}$

Using Equation 3-86 and Equation 3-87, in conjunction with the relevant values of B_{op}, $a_{2,2}$ and R, the contribution of $\mathrm{Im}(\hat{X}_2)_2$ to $\mathrm{Im}\,\hat{X}_2$ can be determined. By subtracting $\mathrm{Im}(\hat{X}_2)_2$ from $\mathrm{Im}\,\hat{X}_2$, the remainder $(\mathrm{Im}\,\hat{X}_2)_0$ is found (Equation 3-85) which can then be used to calculate the parameter A_q, with Equation 3-84 rewritten as:

$$A_q = \frac{2\left|(\mathrm{Im}\,\hat{X}_2)_0\right|}{B_{op}R\bar{v}_z} \qquad \text{Equation 3-88}$$

With reference to the method for determining angle $\theta_{Q,n}$ described in Section 3.6.1.2, it can be seen that the angle $\theta_{Q,2}$ for a quadratic velocity component has two possible solutions, which are:

If $a_{2,2} = \frac{24}{BR}\left|X_2\right|$, which means $a_{2,2} > 0$

$$\theta_{Q,2} = -\frac{\psi_3}{2} \quad \text{Equation 3-89}$$

$$\theta_{Q,2} \in \left[-\frac{\pi}{2}, \frac{\pi}{2}\right) \quad \text{Equation 3-90}$$

If $a_{2,2} = -\frac{24}{BR}|X_2|$ it means $a_{2,2} < 0$

$$\theta_{Q,2} = -\frac{\psi_3}{2} + \frac{\pi}{2} \quad \text{Equation 3-91}$$

$$\theta_{Q,2} \in [0, \pi) \quad \text{Equation 3-92}$$

Because of the two solutions of $\theta_{Q,2}$ shown in Equation 3-89 and Equation 3-91, two possible solutions of $A_{2,\theta}$ can be determined by using Equation 3-87. In this case, by substituting each solution of $A_{2,\theta}$ and corresponding $a_{2,2}$ into Equation 3-86, respectively, the imaginary parts of the DFT components $\mathrm{Im}(\hat{X}_2)_2$ were determined. After this process was completed, using Equation 3-85 and Equation 3-88, in conjunction with the value of $\bar{v}_z$, it was possible to obtain the parameter A_q for each value of $\mathrm{Im}(\hat{X}_2)_2$. It is worth noting that the value of $\bar{v}_z$ is determined by using $a_{0,0} = \mathrm{sgn}(\mathrm{Re}\, X_1)\frac{2|X_1|}{BR}$ (see Section 3.7.1). These two values of A_q would then be respectively substituted in the fitting function shown in Fig. 3-19 (a). So, there are two values of the exponent q calculated. Thus, we can now have two different axisymmetric velocity components as given by Equation 3-23. For the purposes of the present investigation, the overall velocity profile can be determined by combining the appropriate axisymmetric velocity component with the n^{th} order polynomial velocity components (n=1 to 6). Therefore, with two axisymmetric velocity components, if the polynomial components number up to two, there exist two possible velocity profile solutions. Consequently, with reference to Section 3.6.1.2, it is apparent that, with an overall velocity profile comprising an axisymmetric component and polynomial components up to n (1 to 6), there exist n! possible velocity profile solutions. In order to find the correct velocity profile, a method to find an optimum solution from the n! possible velocity profile solutions is required and this is described in Section 4.2.

3.8 Summary

Section 3.2 presented a brief historical review and described the principle of the conventional electromagnetic flowmeter. In Section 3.3, an analysis of the magnetic flux density distribution for a non-uniform magnetic (anti-Helmholtz) field was demonstrated, which is useful for determining the axisymmetric velocity component and selection of the optimum possible velocity solutions. (The method of selecting optimum velocity solution will be detailed in the next chapter.) In Section 3.4, COMSOL software was used to create the simulation model for the IFT flowmeter, which is able to investigate the potential distribution with varying physical parameters, such as magnetic flux density distribution and imposed velocity profiles. In Section 3.5, numerical analysis based on COMSOL simulation results demonstrated the effects of different axisymmetric velocity profiles on the boundary potential distribution under a non-uniform (anti-Helmholtz) magnetic field. It also showed that, based on the numerical simulation results, the boundary potential difference distribution in the non-uniform magnetic field can be used to find a unique term A_q , which is capable of determining the exponent q for different axisymmetric velocity profiles.

Section 3.6 describes a DFT-based method for reconstruction of the local velocity distribution of the conducting continuous phase from fifteen potential differences, U_j. Because the reconstruction algorithm is based on polynomial velocity components, this section demonstrated the mathematical analysis required to determine a generalised equation for the polynomial expression and angles of direction of these components.

The drawback of the original DFT-based velocity reconstruction algorithm is that it cannot distinguish between different axisymmetric velocity profiles components, because the velocity profile is assumed to be uniform when the order n is equal to 0. By using a DFT-based method in conjunction with the 'power law' theorem, it was possible to develop an improved velocity reconstruction algorithm (which was presented in Section 3.7.), which enabled the reconstructed velocity profile to be expressed as the sum of an axisymmetric velocity component and the polynomial velocity components of order 1 to 6. Because $n!$ possible velocity profile solutions exist using this technique, a method for selection of the optimum velocity profile solution will be explained in the next chapter.

4 Implementation of the velocity profile reconstruction algorithms

4.1 Introduction

Referring to the theoretical work developed in Chapter 3, the improved velocity reconstruction algorithm provides $n!$ possible velocity profile solutions. Section 4.2 will introduce a method based on a weight value technique, which can be applied to choose the optimum solution by measuring the boundary potential distribution in a non-uniform magnetic field.

Section 4.3 demonstrates the procedure of the velocity profile reconstruction algorithm. Because the mathematical model is implemented by using a MATLAB program, this section also shows the explanations of the MATLAB program corresponding to each stage of the reconstruction procedure.

In the final section, the optimum velocity results for two imposed velocity profiles are discussed.

4.2 Determining an optimum velocity profile solution

In Section 3.7, a method for reconstructing velocity profile containing both axisymmetric and non-uniform velocity components was described. Referring to the theoretical work described in Section 3.6 and Section 3.7, the overall reconstructed velocity profile is obtained by summing all the individual velocity components, and can be shown in the following form:

$$v(x;y) = v_n(x;y) + v_{n-1}(x;y)... + v_{axi}(x;y) \qquad \text{Equation 4-1}$$

where n is the order of the polynomial equation ($1 \leq n \leq 6$) chosen to fit the given velocity profile. Note that $v_{axi}(x;y)$ represents the axisymmetric velocity component that is used to replace the uniform velocity component $v_0(x;y)$ described in Section 3.6. Because for each velocity component there are n possible values of $\theta_{Q,n}$ (see Equation 3-81, Equation 3-82 and Equation 3-83), the number of possible solutions for $v(x;y)$ is $n!$. Thus, it is necessary to develop a method, which can be used to choose the optimum of these $n!$ solutions. A proposed technique is to select the optimum reconstructed velocity profile using the weight function theory described in this section.

Because this technique is based on the use of the principle of weight functions to predict the boundary potential distribution in a non-uniform magnetic field for a given velocity profile (i.e. one of the possible solutions for $v(x;y)$), weight values for the present investigation need to be determined. In the present investigation, the pipe cross-section is divided into 30 regimes with areas $A_i (i = 1,2,...,30)$ (see Fig. 4-1). The procedure for calculating the weight value $w_{i,j}$ was that the pixel under consideration was imposed with a given axial velocity $v_{wt,i}$ in the non-uniform (anti-Helmholtz) magnetic field for which the magnetic flux density at electrode e_{13} was B_{op} ; fifteen electrical potential difference measurements $\widehat{U}_{wt,j}$ were then obtained between the 15 electrode pairs (see Table 3-2). It is worth noting that in each of the COMSOL simulations, only one fluid region under consideration had a flow velocity of $v_{wt,i}$ while the remaining regions had zero velocity. The weight values $w_{i,j}$ associated with the chosen region with index i were calculated from the potential differences using the following equation:

$$w_{i,j} = \frac{\pi R}{2B_{op}} \cdot \frac{\hat{U}_{wt,j}}{A_i v_{wt,i}} \qquad i=1,\ldots 30; \quad j=1,\ldots.,15 \qquad \text{Equation 4-2}$$

After repeating this procedure for the remaining regions, the calculated values $w_{i,j}$ constitute a matrix with 450 weight value elements. It is worth noting that the reason for using a 30 region geometry was because the COMSOL simulation work for each given region demands quite a lengthy computing time. Therefore, the number of regions in the present research was limited to 30.

The technique to choose the optimum velocity profile followed the steps given below:

- Once all the weight values were calculated and stored, the electrical potential difference in a non-uniform magnetic field could be calculated by successively substituting each possible velocity profile and the weight values into Equation 4-3.

$$\hat{U}_j = \frac{2B_{op}}{\pi R} \sum_{i=1}^{M} v_i w_{i,j} A_i \qquad \text{where} \quad j = 1,\ldots, N-1 \qquad \text{Equation 4-3}$$

where $\hat{U}_j$ is the calculated potential difference between the j^{th} electrode pair (see Table 3-2), M is the total number of regions v_i is the mean axial velocity in the i^{th} pixel as known from the relevant velocity profile under consideration and R is the internal pipe radius. Note that the value of B_{op} used in the simulations described in this chapter was taken as the y component of the magnetic flux density at electrode e_{13} (see Fig. 3-20) and set to 5.019×10^{-3} T.

- After the calculated potential differences $\hat{U}_j$ were obtained, the reference potential differences, $\hat{U}_{j,ref}$, for the imposed velocity profile had to be determined. In the simulations described in this chapter, by imposing the velocity profile into the COMSOL simulation model, fifteen reference potential differences, $\hat{U}_{j,ref}$, (j =1 to 15), were calculated between the j^{th} electrode pair (see Table 3-2). These potential differences, $\hat{U}_{j,ref}$, were obtained by using COMSOL to calculate the boundary potential distribution in the non-uniform magnetic field. It is worth noting that the reference potential differences, $\hat{U}_{j,ref}$, used when the physical IFT device

made velocity profile measurements in real flows, were obtained from real potential difference measurements made between the 15 electrode pairs.

- From the statements above, we can see that the optimum velocity profile is the one for which the calculated potential differences, $\hat{U}_j$ (j= 1 to 15) correspond most closely to the measured potential differences, $\hat{U}_{j,ref}$ (j= 1 to 15). In order to evaluate a measure of the closeness between the calculated potential difference $\hat{U}_j$ and the reference potential differences $\hat{U}_{j,ref}$ for each of the n! possible velocity profiles, a parameter S_U was introduced and defined as:

$$S_U = \sum_{j=1}^{15} (\hat{U}_{j,ref} - \hat{U}_j)^2 \qquad \text{Equation 4-4}$$

It is clear from inspection of Equation 4-4 that the optimum velocity profile from the n! possible solutions occurs when the value of S_U is a minimum.

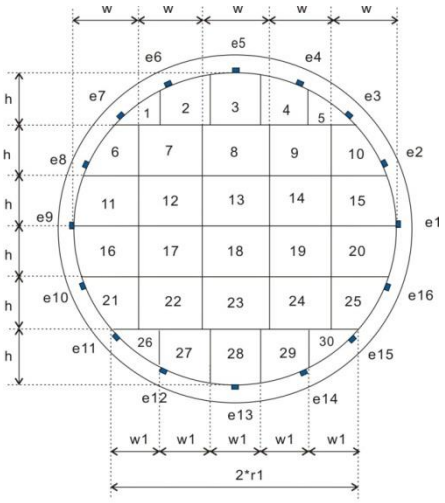

Fig. 4-1 Schematic diagram of the flow regions [93]

4.3 Application of the velocity profile reconstruction algorithm

In the last chapter it was described how the IFT flowmeter device provides fifteen electrical potential difference measurements when a conductive fluid is passed through a uniform or non-uniform magnetic field. In particular, the boundary potential measurements in a non-uniform magnetic field show different behaviour for the different axisymmetric velocity profiles. With this feature, an IFT flowmeter can use the boundary potential measurements from uniform and non-uniform magnetic fields to reconstruct an axisymmetric velocity profile based on the power law reconstruction method.

In Sections 3.6 and 3.7, two analytical velocity profile reconstruction algorithms were introduced. These included consideration of a uniform velocity component (i.e. axisymmetric velocity with exponent q=0) or an axisymmetric velocity with non-zero exponent (q>0). In this section, the local axial velocity distribution is obtained from the potential difference measurements with the aid of the two velocity profile reconstruction algorithms using COMSOL. In order to validate the two reconstruction algorithms, two different velocity profiles were reconstructed and compared with their reference velocity profiles. Furthermore, because the algorithms were implemented using MATLAB software, it is necessary to present some explanation of the MATLAB code for each stage of the velocity reconstruction procedures.

4.3.1 Simulation velocity profile

For the purpose of the present research, the simulation velocity profiles were defined as non-uniform. Referring to the experimental results obtained by Lucas [28] for two phase oil-in-water flow in an inclined circular pipe, as shown in Fig. 4-2, the velocity profile in Fig. 4-2 arose from solving the Navier-stokes equation for an upward inclined flow with continuously varying density. The lower density of the oil-water mixture which occurs towards the upper side of the pipe gives rise to a higher upward velocity than the higher density mixture towards the lower side of the inclined pipe. Indeed, for the data shown in Fig. 4-2, the fluid at the lower side of the inclined pipe actually has a negative axial velocity (i.e. in the downward direction).

The analytical function of the first imposed velocity profile, as shown in Equation 4-5, was obtained with the aid of a 4^{th} order polynomial fitted to the experimental data from Fig. 4-2.

$$v_{1st}(x;y) = 0.2237\left(\frac{x\cos 90° + y\sin 90°}{R}\right)^4 - 0.3745\left(\frac{x\cos 90° + y\sin 90°}{R}\right)^3 - 0.5797\left(\frac{x\cos 90° + y\sin 90°}{R}\right)^2 + 0.4537\left(\frac{x\cos 90° + y\sin 90°}{R}\right) + 0.3462$$

Equation 4-5

where R is the radius of the pipe.

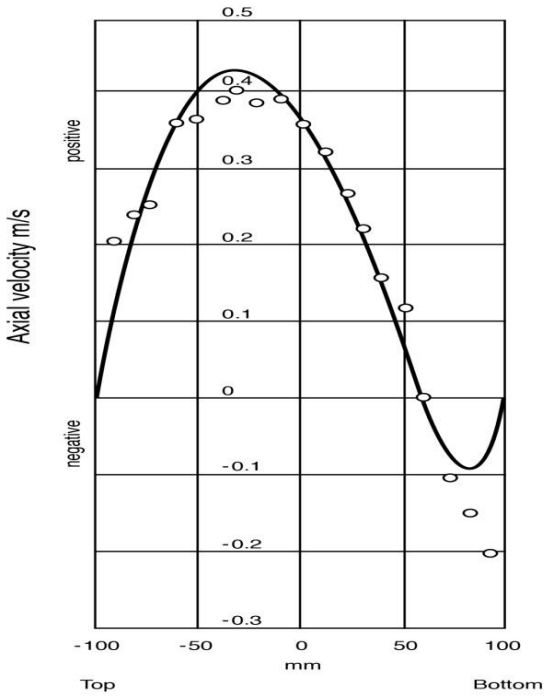

Fig. 4-2 Axial velocity profile in two phase oil-in-water flow in a pipe with inclination of 25 °to vertical (solid line is predicted velocity profile and circles represent experimental velocity profiles) [28]

The imposed velocity profile according to Equation 4-5 has been plotted in Fig. 4-3 (a). Comparing Fig. 4-3 (a) with Fig. 4-2, the defined velocity profile has good agreement with the velocity profile measured by Lucas [28].

The second imposed velocity profile also consists of polynomial velocity components up to the 4th order, and is expressed in Equation 4-7. This velocity profile is shown in Fig. 4-3 (b). By

inspection of Equation 4-5 and Equation 4-7, it can be seen that the form of the second velocity profile is similar to the first, with the difference being that the uniform component in the first velocity profile is replaced by an axisymmetric velocity component with non-zero *q*. The axisymmetric velocity component in the second velocity profile is defined by using the following equation:

$$v_{axi}(x;y) = v_{\max}\left(1-\frac{\sqrt{x^2+y^2}}{R}\right)^q \qquad \text{Equation 4-6}$$

where $v_{\max}$ is the maximum velocity at the centre of the axisymmetric velocity profile and is set equal to 0.9139, and q is a power law exponent, which is set to be 0.2. Note that these values are arbitrarily selected.

$$v_{2nd}(x;y) = 0.2237\left(\frac{x\cos 90° + y\sin 90°}{R}\right)^4 - 0.3745\left(\frac{x\cos 90° + y\sin 90°}{R}\right)^3 - 0.5797\left(\frac{x\cos 90° + y\sin 90°}{R}\right)^2 + 0.4537\left(\frac{x\cos 90° + y\sin 90°}{R}\right) + 0.9139\left(1-\frac{\sqrt{x^2+y^2}}{R}\right)^{0.2} \qquad \text{Equation 4-7}$$

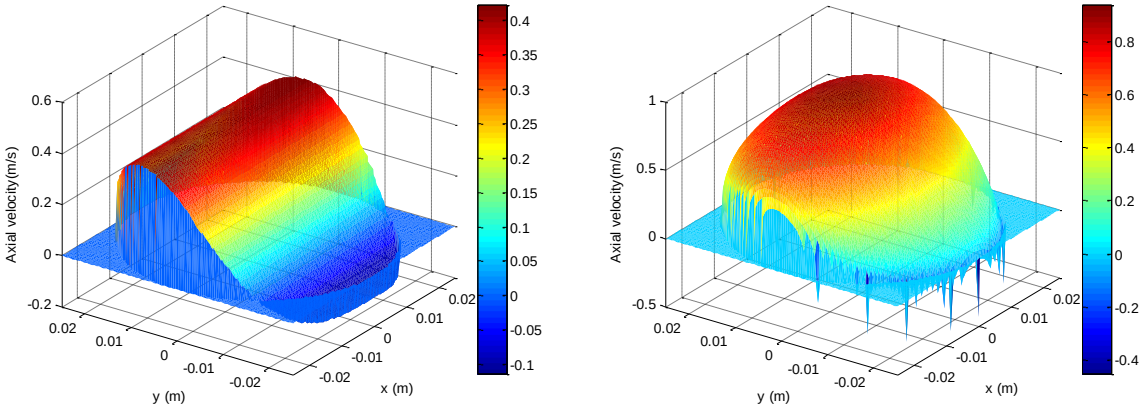

(a) (b)

Fig. 4-3 Imposed velocity as defined by Equation 4-6 and Equation 4-7: (a) the imposed asymmetric "first" velocity profile is defined by Equation 4-6 (b) the imposed axisymmetric "second" velocity profile is defined by Equation 4-7

4.3.2 Software prototype of velocity reconstruction procedure in MATLAB

This section describes the practical procedures for reconstruction of the velocity profile in the flow cross-section of the IFT meter from the boundary potential difference measurements using the mathematical models and theory given in Section 3.6 to Section 3.7. It also gives an explanation of the associated MATLAB-based software program developed to implement the reconstruction.

The entire MATLAB program for the velocity reconstruction algorithm is given in Appendix A.

Input data for the velocity reconstruction algorithm

To illustrate the practical reconstruction procedure, boundary potential distributions in uniform and non-uniform (anti-Helmholtz) magnetic fields were obtained in COMSOL simulations for the reference velocity profiles shown in Fig. 4-3 and defined by Equation 4-5 and Equation 4-7. Note that in these simulations, the potential at electrode e5 was set to zero for both the uniform and non-uniform magnetic fields. This corresponds with the way that potential difference measurements were made using the practical EMFM, described in Chapter 5. For this practical EMFM electrical potential difference measurements were always made using e5 as a reference electrode. Consequently, for both the COMSOL simulations and the practical EMFM described in Chapter 5, for a given velocity profile, boundary potential distributions were obtained for both the uniform and non-uniform magnetic fields with the potential at electrode e5 equal to zero. These boundary potential distributions were required as inputs to the velocity profile reconstruction procedures. The potential distributions in the uniform and non-uniform magnetic fields are stored in data files named ‘potdistr_unif.dat’ and ‘potdistr_nonu.dat’, respectively. These potential distributions for both imposed velocity profiles in the uniform and non-uniform magnetic fields are respectively plotted as shown in Fig. 4-4. Furthermore, referring to Section 3.6 and 3.7, there are several parameters that also must be defined before starting to determine the velocity profile. These are shown as follows.

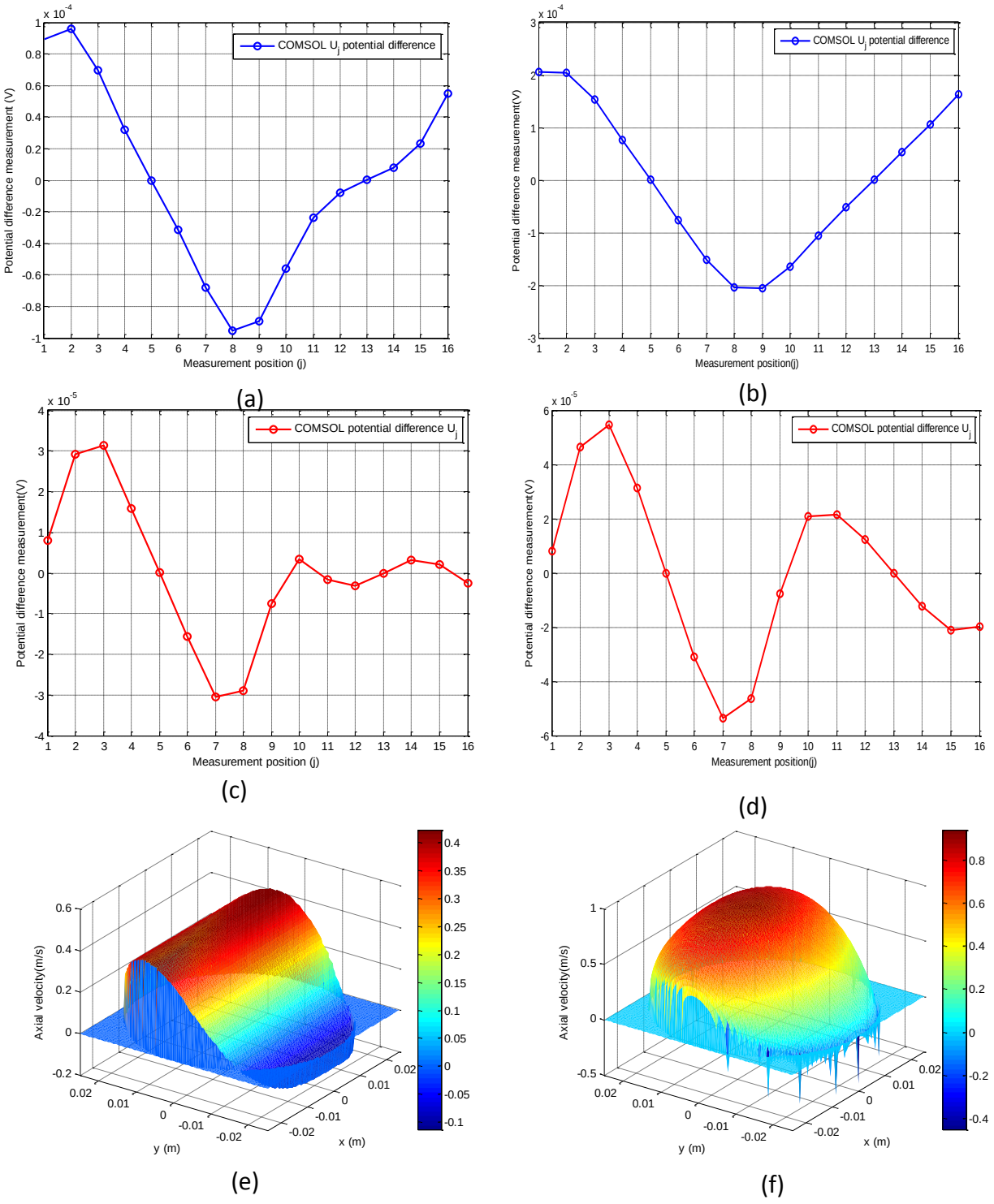

Fig. 4-4 (a) potential difference distribution for the first imposed velocity profile in the uniform magnetic field (see Equation 4-5); (b) potential differences distribution for the second imposed velocity profile in the uniform magnetic field (see Equation 4-7); (c) potential difference distribution for the first imposed velocity profile in the non-uniform magnetic field ; (d) potential difference distribution for the second imposed velocity profile in the non-uniform magnetic field; (e) asymmetric velocity profile(first velocity profile) Equation 4-5; and (f) axisymmetric velocity profile(second velocity profile) Equation 4-7

- The number of electrodes on the boundary wall of the pipe is 'ne'; in the present study, this number is sixteen.
- The magnetic flux density for the uniform magnetic field is denoted Bm and is an important parameter for determining the coefficient $a_{n,n}$ (see Equation 3-63, Equation 3-64 and Equation 3-65**)**. Bm can be obtained from simulation results or practical measurement. In this case, the magnetic flux density for the uniform magnetic field is calculated by the COMSOL software and equals 8.358 $\times 10^{-3}$ T. The unit of magnetic flux density is the Tesla. Note that a relatively high magnetic flux density is used to improve the accuracy of the potential distribution calculation.
- The magnetic flux density at electrode e_{13} in the non-uniform magnetic field B_{op} is denoted as 'Bmnu'. For the simulation described above, the value of 'Bmnu' is equal to 5.019 $\times 10^{-3}$ T.
- For the IFT model geometry, the pipe radius *R* is 0.025m. In the MATLAB program, it is written as 'Rp=0.025'.
- 'nmax': the maximum order of the polynomial velocity profile *n* can be defined from 0 to 6, according to Equation 3-42.
- 'm' represents the number of sub-regions into which the pipe cross-section is divided.
- As described in Section 4.2, the calculated weight value matrix with 450 weight value elements used to determine the optimum velocity solution, is saved into a file named 'wei.dat.' Once the *n*! possible velocity solutions have been calculated, the file 'wei.dat' will be loaded for this further analysis.

With reference to Section 3.7, the axisymmetric velocity component is used to replace the uniform velocity component from the polynomial velocity profile. To determine the axisymmetric velocity component, there are two important expressions which must be used; these are:

1) The relationship between *q* and A_q is shown in Fig. 3-19 (a), which can be used to determine the exponent *q* by interpolation.
2) Another important expression is described in Section 3.7.2, which shows the relationship between $\mathrm{Im}(\widehat{X}_2)_2$ and $\theta_{Q,2}$ (see Fig. 3-30). By using Equation 3-86 and Equation 3-87,

the contribution of $\mathrm{Im}(\widehat{X}_2)_2$ to $\mathrm{Im}\,\widehat{X}_2$ can be found and, by further analysis, it is possible to determine the contribution of $(\mathrm{Im}\,\widehat{X}_2)_0$ to $\mathrm{Im}\,\widehat{X}_2$ (see Equation 3-85). The value of $(\mathrm{Im}\,\widehat{X}_2)_0$ is then used to calculate A_q.

The following constant parameters are used to form two relationship expressions as described above.

```
ac2v = [0.0099 0.009653];
b2v = [-0.0172 -0.01665];
curvx2 = 2;        % curvx2=1: 80mm model
ac2 = ac2v(curvx2);    % curvx2=2: 50mm model -
b2 = b2v(curvx2);

curv = 3;         % curv=1: 80mm model
qaq3 = qaq3v(curv);
qaq2 = qaq2v(curv);    % curv=3: 50mm model
qaq1 = qaq1v(curv);
qaq0 = qaq0v(curv);
```

It is worth noting that the constants for both relationships, q vs. A_q, and $\mathrm{Im}(\widehat{X}_2)_2$ vs. $\theta_{Q,2}$, depend upon the simulation model geometry (i.e. pipe diameter 50mm or 80mm). In the present study, only the 50mm model geometry is considered. It should be noted that the reason the program includes results for the 80mm model was to enable it to reconstruct the velocity profile if an 80mm flowmeter device was used.

- 'ac2' and'b2' are the coefficients of Equation 3-87. The values of 'ac2' and 'b2' are defined by selecting a suitable value from the numerical arrays'ac2v' and 'b2v'. In the present study, the second values of the numerical array 'ac2v' and 'b2v' relevant to the 50mm device were selected. With reference to Equation 3-87, the function of $A_{2,\theta}$ can be rewritten as:

$$A_{2,\theta} = \mathrm{ac2}\cos 2\theta_{Q,2} + \mathrm{b2} \qquad \text{Equation 4-8}$$

- 'qaq3' 'qaq2' 'qaq1' 'qaq0': are the coefficients of the 3rd order equation as shown in Fig. 3-19 (a). Their values can be defined by choosing the index number 'curv' corresponding to different model geometries. The values used in the current investigation are the third

elements of the numerical arrays ‘qaq3v’, ‘qaq2v’, ‘qaq1v’ and ‘qaq0v’ shown above(see also Appendix A). The 3rd order polynomial fitting function shown in Fig. 3-19 (a) can be rewritten as:

$$q=\text{qaq3}\,(A_q)^3+\text{qaq2}\,(A_q)^2+\text{qaq1}\,(A_q)+\text{qaq0} \qquad \text{Equation 4-9}$$

Applying the DFT method to the potential difference measurements

Once the data files and constant parameters were defined, the velocity reconstruction procedure was started. In the first stage, it was required to apply Equation 3-60 to determine the DFT components of the boundary potential difference distributions in uniform and non-uniform magnetic fields. It should be noted that Equation 3-60 is the common DFT definition expression.

To calculate the DFT components for the potential differences in the uniform magnetic field, the relevant parameters and MATLAB built-in functions are used, and are demonstrated in the following commands:

```
fs = ne;  % sampling frequency
N = length(Uu);
fn = fs/2; % Nyquist frequency
f = linspace(0,fn-fn/(N/2),N/2);
% DFT
X = fft(Uu)/N;
XA = X(1:N/2+1);
XAR = real(XA);
XAI = imag(XA);
```

- ‘fs’ is the sampling frequency. In this case, ‘fs’ is equal to the number of potential difference measurements (i.e. sixteen).
- It is well known that a unique value of X exists only from 0 Hz to the Nyquist frequency ‘fn’. Note that the Nyquist frequency is equal to half the sampling frequency ‘fs’ (i.e. fn=8).
- By reading data file ‘potdistr_unif.dat’, sixteen potential difference measurements for the uniform magnetic field are inserted into the matrix ‘Uu’. In other words, the matrix ‘Uu’ is the input data, U_p , of Equation 3-60.
- Both real parts and imaginary parts for the DFT components X_n are also determined and saved into matrices ‘XAR’ and ‘XAI’, respectively.

Similarly, the potential difference measurements in a non-uniform magnetic field can also be analysed using a DFT. The following code finds the DFT components of the input potential data 'Unu'. It should be noted that the file 'potdistr_nonu.dat' is read into a new matrix, 'Unu'. Referring to the mathematical model developed in Section 3.6, it is known that the imaginary part of the DFT component $\mathrm{Im}\,\widehat{X}_2$ can be used to determine the value of $\mathrm{Im}(\widehat{X}_2)_2$, which is a key factor in the calculation of A_q. A detailed explanation of the corresponding program is given in the following section.

```
Xnu = fft(Unu)/N;
XAnu = Xnu(1:N/2+1);
Xnuout = [real(XAnu.') imag(XAnu.') abs(XAnu.')];
imx2 = imag(XAnu(3));
```

- The imaginary part of the DFT component $\mathrm{Im}\,\widehat{X}_2$ is denoted as 'imx2', which is associated with the third element of the matrix 'XAnu'. The matrix 'XAnu' contains nine complex numbers, 'Xnu'. It is worth noting that the first value of 'Xnu' is a 'DC component', which is not used in the present study.

Determining coefficient $a_{n,n}$ and angle $\theta_{Q,n}$

The next stage is to consider the determination of the coefficient $a_{n,n}$ and angle $\theta_{Q,n}$ for the polynomial velocity profile (see Equation 3-44 and Equation 3-45).

The order of n is from 0 to 6, and the first coefficient considered is $a_{0,0}$, which corresponds to the uniform velocity component (i.e. 0^{th} order) or the axisymmetric velocity component. The value of $a_{0,0}$ can be calculated by using Equation 3-64. The following MATLAB code can be used to find one solution of $a_{0,0}$ by determining the sign of the real part of X_1. It is worth noting that the uniform velocity component contains only $a_{0,0}$ and has no directional angle $\theta_{Q,n}$ associated with it (see Fig. 3-21).

```
% Uniform (0th order) term
if XAR(N/fs+1) > 0
  a00 = 2*abs(XA(N/fs+1))/(Bm*Rp);
else
  a00 = -2*abs(XA(N/fs+1))/(Bm*Rp);
end
```

For the linear velocity component (i.e. n=1), the corresponding coefficient $a_{1,1}$ can be calculated by using Equation 3-65. It can be implemented by using the second line of the following MATLAB code. In order to calculate the angle $\theta_{Q,1}$, the arctan function 'atan' gives the value of ψ_2. Referring to Equation 3-82, $\theta_{Q,1}$ is equal to $-\psi_2$,which is shown in the last line of the following program. There is an issue with function 'atan' used to determine ψ_2. If both real and imaginary parts are negative, the 'atan' function gives the same value as if they were both positive. In other words, if the real part is positive and the imaginary part is negative, the 'atan' function gives the same answer as it does for the real part being negative and the imaginary part positive. To overcome this issue, π is added to ψ_2 when the real part is negative and the imaginary part is positive. If both the real and imaginary parts are negative, the π is subtracted from ψ_2. Similarly for the terms ψ_{n+1} for the remaining velocity components, a similar method was used.

```
% Linear (1st order) term
a11 = 2*abs(XA(2*N/fs+1))*4/(Bm*Rp);
if XAR(2*N/fs+1)>=0
  psi = atan(XAI(2*N/fs+1)/XAR(2*N/fs+1))*180/pi;
elseif XAI(2*N/fs+1)>=0
  psi = (atan(XAI(2*N/fs+1)/XAR(2*N/fs+1))+pi)*180/pi;
else
  psi = (atan(XAI(2*N/fs+1)/XAR(2*N/fs+1))-pi)*180/pi;
end
theta1 = -psi;
```

Inspection of Equation 3-53 shows that the quadratic velocity profile contains two coefficients, $a_{2,2}$ and $a_{2,0}$. The value of $a_{2,0}$ can be calculated by using Equation 3-46. The calculation of both coefficients $a_{2,2}$ and $a_{2,0}$, can be performed by using the second and third lines of the following MATLAB code. Referring to Equation 3-82 and Equation 3-83, the quadratic velocity component should have two possible solutions.

```
% Quadratic (2nd order) term
a22 = 2*abs(XA(3*N/fs+1))*12/(Bm*Rp);
a20 = -a22/4;
if XAR(3*N/fs+1)>=0
  psi = atan(XAI(3*N/fs+1)/XAR(3*N/fs+1))*180/pi;
elseif XAI(3*N/fs+1)>=0
  psi = (atan(XAI(3*N/fs+1)/XAR(3*N/fs+1))+pi)*180/pi;
else
  psi = (atan(XAI(3*N/fs+1)/XAR(3*N/fs+1))-pi)*180/pi;
end
theta2 = -psi/2;
```

Thus, referring to Equation 3-48, Equation 3-81, and using the same MATLAB function, the coefficients $a_{n,n}$ and angles $\theta_{Q,n}$ for the remaining velocity components (i.e. cubic, quartic, quintic and 6th order) can be determined.

Finding the axisymmetric component

The MATLAB program for the determination of the axisymmetric velocity components is described below. By inspection of the program code in the red dashed rectangle, it can be seen that, if the order *n* is greater than 1, there are two $\mathrm{Im}(\widehat{X}_2)_2$ values calculated using Equation 3-86 and Equation 3-87. As described above, the quadratic velocity component has two possible solutions, so that the contribution of the axisymmetric velocity component 'imx20' also has two possible values. With the matrix 'imx20', the parameter A_q for each of the two different values of $(\mathrm{Im}\,\widehat{X}_2)_0$ is determined.

It should be noted that the term $\mathrm{Im}\,\widehat{X}_2$ is also used to calculate A_q according to Equation 3-84 when n<2. In the case of the order n2, the matrix 'Aq' should have three elements. The MATLAB code for the calculation of the parameter A_q is shown in the green dashed rectangle.

Once the parameter A_q is determined, the exponent q for the power law expression can be determined by using a curve fitting function (see Fig. 3-19 a). The MATLAB code of this function is shown in the purple dashed rectangle.

```
imx20(1) = imx2;
ixmax = 1;
if nmax >= 2
  imx221 = (ac2*cosd(2*theta2)+b2)*a22*Bmnu*Rp;
  imx20(2) = imx2 - imx221;
  imx222 = (ac2*cosd(2*(theta2+180/2))+b2)*(-a22)*Bmnu*Rp;
  imx20(3) = imx2 - imx222;
  ixmax = 3;
end
```

```
for ix = 1:3
  if imx20(ix) >= 0
    if a00 >= 0
      qaxi(ix) = 0;
    else
      Aq(ix) = abs(2*imx20(ix)/(a00*Bmnu*Rp));
    end
  else
    if a00 < 0
      qaxi(ix) = 0;
    else
      Aq(ix) = abs(2*imx20(ix)/(a00*Bmnu*Rp));
    end
  end
  if Aq(ix) > Aqmax
    qaxi(ix) = 0;
  else
    qaxi(ix) = qaq3*Aq(ix)^3+qaq2*Aq(ix)^2+qaq1*Aq(ix)+qaq0;
  end
end
```

For the benefit of the reader, it is import to give an explanation for those parameters shown in each 'dashed rectangle'.

- Red dashed rectangle

Referring to Section 3.7.2, it clearly shows that, if the maximum order of polynomial component 'nmax' is ≥ 2, there are two solutions of $A_{2,\theta}$ as shown in Equation 4-8 due to two solutions of $\theta_{Q,2}$ which is denoted as 'theta2'. Note that $\cos 2\theta_{Q,2}$ is denoted as 'cosd(2*theta2)' which provides the cosine of the '2*theta2' in degrees. As described in section 3.7.2, once the value of $A_{2,\theta}$ was determined, two solutions of $\mathrm{Im}(\hat{X}_2)_2$ were calculated by using Equation 3-86. Note that the two solutions of $\mathrm{Im}(\hat{X}_2)_2$ are denoted as 'imx221'and 'imx222', respectively. Then, by

using Equation 3-85, two solutions of $(\mathrm{Im}\,\hat{X}_2)_0$ were determined. Both solutions of $(\mathrm{Im}\,\hat{X}_2)_0$ were saved in the second and third column of matrix 'imx20'. It is worth noting that, if the term 'nmax'<2, then $\mathrm{Im}\,\hat{X}_2$ only has the contribution of the axisymmetric velocity component without considering the effects of the quadratic velocity component. Thus, this value of $\mathrm{Im}\,\hat{X}_2$ is saved in the first column of matrix 'imx20'.

- Green dashed rectangle

In this part of the program, the elements of matrix 'imx20' (i.e. $(\mathrm{Im}\,\hat{X}_2)_0$ or $\mathrm{Im}\,\hat{X}_2$) were respectively substituted into Equation 3-88, which is used to determine the parameter A_q. These values of A_q are saved in matrix 'Aq'.

- Purple dashed rectangle

With reference to the Equation 4-9, in conjunction with 'Aq(ix)', it can be seen that the exponent q, which is denoted as 'qaxi', is calculated.

Choosing the optimum solution

As mentioned in Section 4.2, there exist *n*! possible velocity profile solutions. In the present study, the order *n* is set to be 4 and the possible velocity solutions would be expected to be 4! = 24. It is worth noting that the reason for using the 4^{th} order polynomial component is because the higher order velocity components (5^{th} and 6^{th}) will be considered as noise, due to the imposed velocity profile consisting of polynomial components only up to the 4^{th} order (see Equation 4-5 and Equation 4-7).

At the start of this stage, the calculated coefficients and angles for each velocity component must be saved and organised. Thus, the relevant program code is as shown below:

```
if kn == 1
  A0 = [a00 qaxi(1); 0 0];
end
if kn == 2
  A1 = [a11 theta1];
end
if kn == 3
  A0 = [a00 qaxi(2); a00 qaxi(3)];
  A2 = [a22 a20 theta2; -a22 -a20 theta2+180/2];
```

```
end
if kn == 4
  A3 = [a33 a31 theta3; a33 a31 theta3+360/3; a33 a31 theta3+2*360/3];
end
if kn == 5
  A4 = [a44 a42 a40 theta4; a44 a42 a40 theta4+360/4; -a44 -a42 -a40
theta4+180/4; -a44 -a42 -a40 theta4+3*180/4];
```

In order to give reader a better understanding of this program, the terms in the above program are defined as:

- 'kn': With reference to Appendix A, it is clear that this term is the 'for-loop' variable. The above program is executed with this value of 'kn', which is set equal to $n+1$.
- 'qaxi': a matrix including three possible solutions of exponent *q*.
- 'a11': coefficient $a_{1,1}$ for the linear velocity component (see Equation 3-65).
- 'a22': coefficient $a_{2,2}$ for the quadratic velocity component. The value of $a_{2,2}$ is determined by using Equation 3-63.
- 'a20': coefficient $a_{2,0}$ for the quadratic velocity component (see Equation 3-46).
- 'a33': coefficient $a_{3,3}$ for the cubic velocity component. The value of $a_{3,3}$ is determined by using Equation 3-63.
- 'a31': coefficient $a_{3,1}$ for the cubic velocity component. (see Equation 3-46).
- 'a44':coefficient $a_{4,4}$ for the quartic velocity component . The value of $a_{4,4}$ is determined by using Equation 3-63.
- 'a42': coefficient $a_{4,2}$ for the quartic velocity component.(see Equation 3-46).
- 'a40': coefficient $a_{4,0}$ for the quartic velocity component(see Equation 3-47).
- 'theta1': angle of direction $\theta_{Q,1}$ (see Equation 3-81).
- 'theta2' and 'theta2 +180/2': angle of direction $\theta_{Q,2}$ (refer to Equation 3-82); angle of direction $\theta_{Q,2}$ +90 º(see Equation 3-83).
- 'theta3','theta3+360/3' and 'theta3+2*360/3' : angle of direction $\theta_{Q,3}$, $\theta_{Q,3}$ +120 º and $\theta_{Q,3}$ +240 º(see Equation 3-81).

- ‘theta4’, ‘theta4+360/4’, ‘theta4+180/4’and ‘theta+3*180/4’: angle of direction $\theta_{Q,4}$, $\theta_{Q,4}$ +90 º; $\theta_{Q,4}$ +45 ºand $\theta_{Q,4}$ +135 º.

The coefficients $a_{n,n}$ and angle $\theta_{Q,n}$ for each velocity component are saved into the matrices ‘A0, A1…A4’, respectively (see Equation 4-10 to Equation 4-14). The matrix ‘A0’ is associated with the possible axisymmetric velocity component and would be expected to be a 2×2 square matrix with four elements. As described in Section 3.7.1, if the polynomial order is smaller than two, there is only one solution of exponent *q*, which is determined directly from $\mathrm{Im}\,\widehat{X}_2$ (see Equation 3-84). So, the coefficient $a_{0,0}$ and exponent q are inserted into the matrix A0, as shown in Equation 4-10. Referring to Section 3.7.2 and earlier in this section, it is shown that there exist two possible solutions of exponent q when the order $n\geq2$.Thus, in the matrix A0 (see Equation 4-11), the first row includes $a_{0,0}$ and the calculated exponent q associated with the first solution of ‘imx20’; the second row includes $a_{0,0}$ and the calculated exponent q associated with the second solution of ‘imx20’. The matrix ‘A1’ is associated with the linear velocity component; there is only one row which includes the coefficient $a_{1,1}$ and $\theta_{Q,1}$. Similarly, referring to Equation 3-81, Equation 3-82 and Equation 3-83, the matrices ‘A2’, ‘A3’ and ‘A4’ are shown in Equation 4-13, Equation 4-14 and Equation 4-15, respectively.

$$A0=\begin{bmatrix} a_{0,0} & q(1) \\ 0 & 0 \end{bmatrix} \text{ for order } n<2 \qquad \text{Equation 4-10}$$

$$A0=\begin{bmatrix} a_{0,0} & q(2) \\ a_{0,0} & q(3) \end{bmatrix} \text{ for order } n\geq2 \qquad \text{Equation 4-11}$$

$$A1=\begin{bmatrix} a_{1,1} & \theta_{Q,1} \end{bmatrix} \qquad \text{Equation 4-12}$$

$$A2=\begin{bmatrix} a_{2,2} & a_{2,0} & \theta_{Q,2} \\ -a_{2,2} & -a_{2,0} & \theta_{Q,2}+90° \end{bmatrix} \qquad \text{Equation 4-13}$$

$$A3=\begin{bmatrix} a_{3,3} & a_{3,1} & \theta_{Q,3} \\ a_{3,3} & a_{3,1} & \theta_{Q,3}+120° \\ a_{3,3} & a_{3,1} & \theta_{Q,3}+240° \end{bmatrix} \qquad \text{Equation 4-14}$$

$$A4=\begin{bmatrix} a_{4,4} & a_{4,2} & a_{4,0} & \theta_{Q,4} \\ a_{4,4} & a_{4,2} & a_{4,0} & \theta_{Q,4}+90° \\ -a_{4,4} & -a_{4,2} & -a_{4,0} & \theta_{Q,4}+45° \\ -a_{4,4} & -a_{4,2} & -a_{4,0} & \theta_{Q,4}+135° \end{bmatrix} \qquad \text{Equation 4-15}$$

With the matrices 'A0, A1,…, A4', one of the possible velocity profiles can be determined using the following program:

```
for i=1:(m+1)*(m+1)
if x(i)^2+y(i)^2 > Rp^2
  v(i) = 0;
else
v0(i)=A0(n2,1)/2*(1-
sqrt(x(i)^2+y(i)^2)/Rp)^A0(n2,2)*(A0(n2,2)+1)*(A0(n2,2)+2);
v1(i) = A1(1)*(x(i)*cosd(A1(2))+y(i)*sind(A1(2)))/Rp;
v2(i)=A2(n2,1)*(x(i)*cosd(A2(n2,3))+y(i)*sind(A2(n2,3)))^2/Rp^2 + A2(n2,2);
v3(i) = A3(n3,1)*(x(i)*cosd(A3(n3,3))+y(i)*sind(A3(n3,3)))^3/Rp^3 ...
   + A3(n3,2)*(x(i)*cosd(A3(n3,3))+y(i)*sind(A3(n3,3)))/Rp;
v4(i) = A4(n4,1)*(x(i)*cosd(A4(n4,4))+y(i)*sind(A4(n4,4)))^4/Rp^4 ...
    +A4(n4,2)*(x(i)*cosd(A4(n4,4))+y(i)*sind(A4(n4,4)))^2/Rp^2 ...
    + A4(n4,3);
v(i) = v0(i)+v1(i)+v2(i)+v3(i)+v4(i);
end
end
```

- 'x(i)' and 'y(i)': as mentioned earlier, the rectangular section including the pipe, is divided into m×m points, on which the velocity calculations are made. The corresponding x and y coordinates are saved in two matrices, "x" and "y".
- 'v0(i) , v1(i)….v4(i)': for each velocity component, the velocity values are calculated at each point 'x(i) and y(i)' and saved into the matrices 'v0, v1,…v4'.

  'v0' is the axisymmetric velocity component or uniform velocity component (q=0). The relevant expression is in Equation 3-23 or Equation 3-55.

'v1' is the linear velocity component and is shown in Equation 3-54. 'v2' is the quadratic velocity component and is shown in Equation 3-53. 'v3' is the cubic velocity component and is shown in Equation 3-52. For the quartic velocity component, 'v4', it can be written as shown in Equation 4-16 by using Equation 3-45

$$v_4(x;y) = a_{4,4}\frac{(x\cos\theta_{Q,4} + y\sin\theta_{Q,4})^4}{R^4} + a_{4,2}\frac{(x\cos\theta_{Q,4} + y\sin\theta_{Q,4})^2}{R^2} + a_{4,0}$$

Equation 4-16

- 'n2, n3, … n4': these values represent index numbers for each matrix 'A0, A1, … A4', which are used to locate the coefficient and angle for each possible velocity solution, (see Appendix A). Terms 'n2, n3,…n4' can take several different values, depending upon which velocity profile solution we have chosen at this stage (e.g. n4 can take four different values, relating to the four different possible 4th order velocity components.)
- 'v(i)': this term represents the overall velocity at the i^{th} point in the flow cross section. Referring to Section 3.6.1.1, a possible overall velocity profile is written in this form:

$$v(x;y) = v_4(x;y) + v_3(x;y) + v_2(x;y) + v_1(x;y) + v_{axis}(x;y) \qquad \text{Equation 4-17}$$

where $v_{axis}(x;y)$ represents the axisymmetric velocity component (see Equation 3-23), which can also be replaced by the uniform velocity component $v_0(x;y)$ (q=0)

Referring to the method proposed in Section 4.2, it is clear that the optimum velocity profile solution is determined by obtaining the best agreement between calculated potential differences $\widehat{U}_j$ and the measured electrical potential difference $\widehat{U}_{j,ref}$ obtained in the non-uniform (anti-Helmholtz) magnetic field. For a given velocity profile, $v(x;y)$, fifteen potential differences, $\widehat{U}_j$, between the electrode pairs (see Table 3-2) are calculated using Equation 4-2. The resultant values of $\widehat{U}_j$ are then compared with the fifteen measured potential differences, $\widehat{U}_{j,ref}$ .The process is repeated for all n ! possible velocity profiles.

The program code for calculating the values of $\widehat{U}_j$ is shown in the following blue dashed rectangle. Note that the matrix 'vmA' is determined according to the sub-program 'vmean30', which is used for estimating the mean velocity in 30 regions shown in Fig. 4-1 from the possible velocity solution, 'v'.

```
delU = zeros(1,ne-1);
for j=1:ne-1
for i=1:30
  delU(j) = delU(j) + 2*Bmnu/(pi*Rp)*vmA(i,1)*wei(j,i)*vmA(i,2);
end
end
```

```
for j=1:4
  U(k,j) = delU(ne-5+j);
end
for j=1:ne-5
  U(k,j+5) = delU(j);
end
```

In the black dashed rectangle, this section reorganises the data $\widehat{U}_j$, for the 'kth' velocity profile solution, so the value 'U(k,j)' now represents the potential on the j^{th} electrode with the potential on the 5th electrode set to zero(i.e. U(k,1) represents potential on e1, U(k,2) represents potential on e2 …U(k,16) potential on e16).

In the final stage, as described in Section 4.2, the difference between calculated potential differences $\widehat{U}_j$ and measured electrical potential differences $\widehat{U}_{j,ref}$ can be calculated according to Equation 4-4, which can be achieved using the following program code.

```
del(k) = 0;
for i=1:ne
  del(k) = del(k) + (U(k,i)-Unu(i))^2;
end
```

Referring to Equation 4-4 , we can see that 'del(k)' is equivalent to S_U . 'U(k,i)' is equivalent to $\widehat{U}_j$ and 'Unu(i)' is equivalent to $\widehat{U}_{j,ref}$. Although in the lines of code (for a sixteen electrode

system ‘ne’=16), ‘del (k)’ is obtained from sixteen values, note that ‘U (k, 5)’ =0 and ‘Unu(5)’=0, so the contribution from electrode 5 to ‘del(k)’ is zero. By finding the lowest value of S_U for all possible velocity profiles, the optimum velocity profile can be determined.

4.3.3 Reconstruction results for simulation velocity profiles

As described earlier in Section 4.3, two different velocity profiles have been chosen for the COMSOL simulation as shown in Equation 4-5 and Equation 4-7, respectively. With the first imposed velocity profile v_{1st} flowing through a uniform and non-uniform magnetic field, the potential distribution U_p and potential difference distribution $\widehat{U}_{j,ref}$ were obtained. In this case, the U_p and $\widehat{U}_{j,ref}$ terms can be used to reconstruct the velocity profile according to two reconstruction algorithms (i.e. with and without the use of an axisymmetric velocity component, see Section 3.6 and 3.7). After this process, there are $n!$ possible velocity profiles. By using the method shown in Section 4.2, the chosen optimum velocity profiles for two reconstruction algorithms (i.e. with and without the use of an axisymmetric velocity component) were determined, as shown below in Fig. 4-5 (a) and (b). Fig. 4-5 (c) clearly indicates the electrical potential difference distribution for the non-uniform magnetic field: the red curve represents the potential difference distribution obtained using COMSOL in a non-uniform magnetic field, the black curve (closest calculated) represents potential difference distribution of optimum velocity profile when the value of S_U is minimum (refer to Equation 4-4), and the potential difference distribution for the value of S_U is maximum is shown by green curve (farthest calculated). It is readily apparent from Fig. 4-5 that the chosen optimum velocity profile is the same for both velocity profile reconstruction algorithms. This is because the parameter A_q was calculated to be 0.4005, which means the exponent q is equal to 0. Thus, the reconstructed velocity profile does not contain the axisymmetric velocity component, which shows good agreements with the defined velocity profile (see Equation 4-5).

To evaluate the reliability of the reconstruction algorithm, the mean deviance of local velocities was defined as follows:

$$\delta v = \frac{\sum_{i=1}^{\tilde{M}} \left| v_i - v_{in,i} \right|}{\tilde{M}\left(v_{in,\max} - v_{in,\min}\right)} \times 100\% \qquad \text{Equation 4-18}$$

where term δv is the mean deviance of local velocities; $\tilde{M}$ is a number of sub-regions into which the cross-section can be divided and where the velocity is calculated; $v_{in,i}$ is the imposed velocity in the i^{th} sub-region; v_i is the velocity obtained from the optimum velocity profile in the i^{th} sub-region; $v_{in,\max}$ and $v_{in,\min}$ are, respectively, the maximum and minimum velocities in the imposed velocity profile.

The local error between velocities can be calculated by:

$$\delta v_i = \frac{v_i - v_{in,i}}{v_{in,\max} - v_{in,\min}} \times 100\% \qquad \text{Equation 4-19}$$

where δv_i represents the error in the i^{th} sub-region

When analysing the velocity results presented in Fig. 4-5, the mean deviance in the reconstructed velocity was found to be 0.96%, which is an acceptable level of error in multiphase flow measurement applications. Furthermore, the local error between the imposed velocity and the reconstructed velocity is shown in Fig. 4-6. Inspection of Fig. 4-6 shows that the absolute local error δv_i in most of the cross-section is in the range of approximately 0~1%. The highest value of δv_i occurs in the region close to the pipe wall and is ≈ 3.7%. This percentage level is also acceptable. Therefore, it is reasonable to conclude that the reconstruction algorithm developed in Section 3.6 is applicable to reconstruct highly non-uniform velocity profiles.

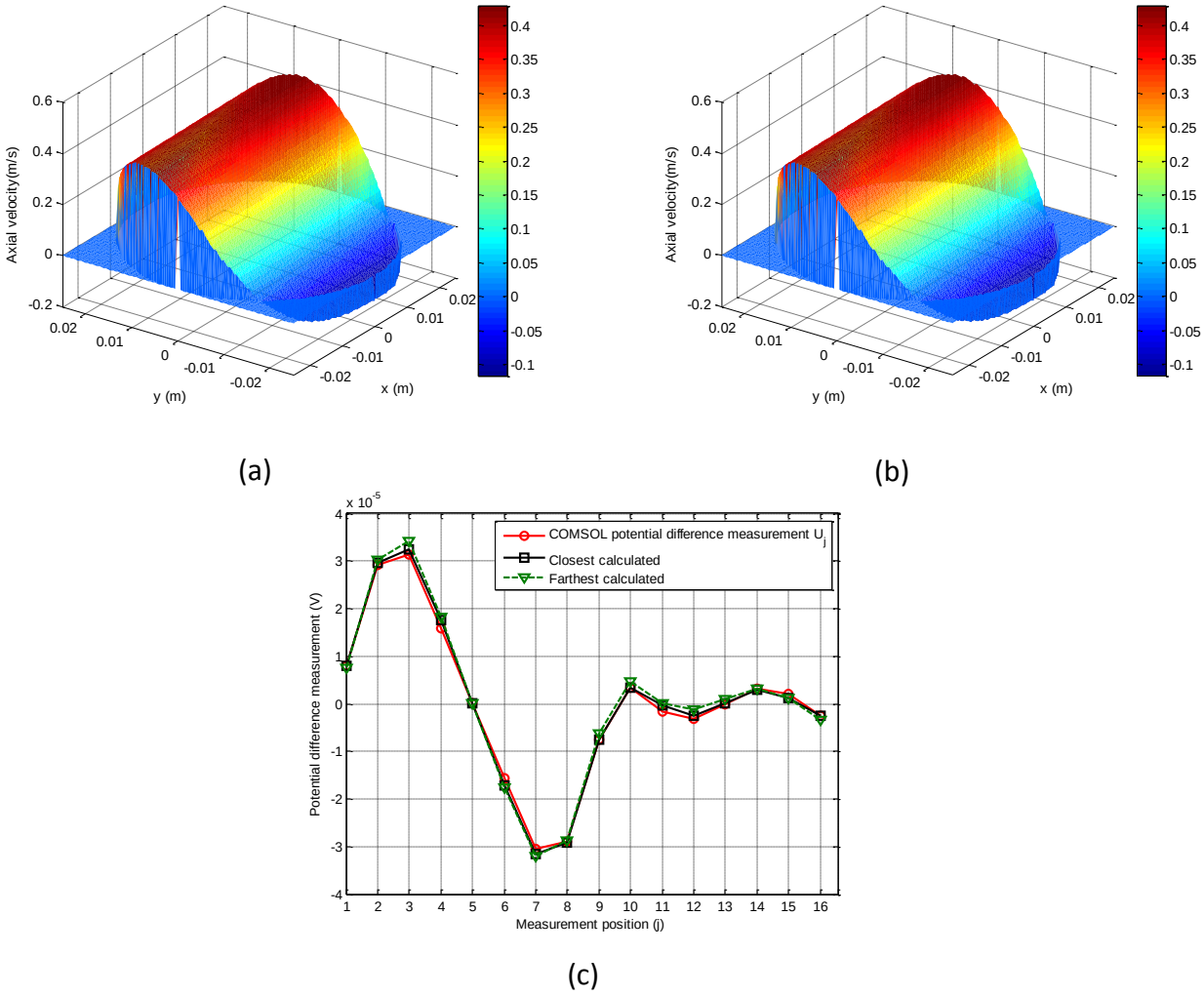

Fig. 4-5 The chosen optimum velocity profile: (a) reconstructed by using the method without use of an axisymmetric component referring to Section3.6; (b) reconstructed by using the method with use of an axisymmetric component referring to Section 3.7; and (c) potential difference distribution for imposed and reconstructed velocity profiles in the non-uniform(anti-Helmholtz) magnetic field

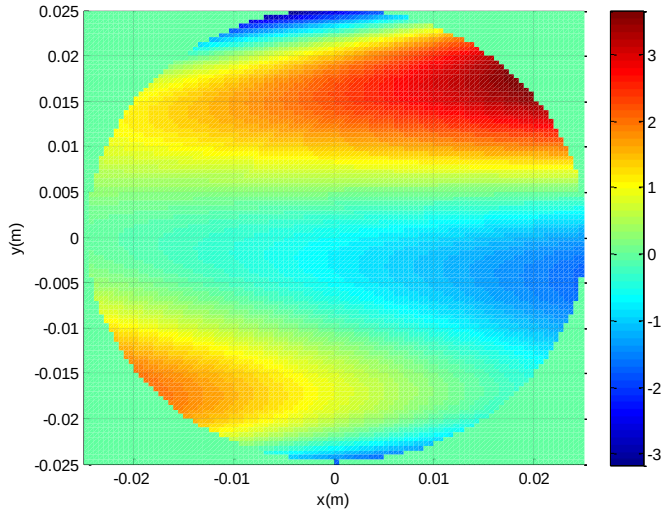

Fig. 4-6 Local percentage error between imposed velocity and reconstructed velocity; colour bar is in %

Using a similar procedure to that described above, the optimum reconstructed velocity profile corresponding to the second imposed velocity profile (see Equation 4-7) was obtained and is shown in Fig. 4-7. From Fig. 4-7 (a) it is clear that the reconstructed velocity, which is determined from the reconstruction algorithm without the use of an axisymmetric velocity component, does not give accurate local velocity results for the top of the pipe, though it does show the highest velocity close to the top of the pipe and the lowest velocity at the bottom of the pipe. By inspection of Fig. 4-7 (b), it can be seen that the reconstructed velocity profile obtained using the reconstruction algorithm with the use of an axisymmetric component is similar to the imposed velocity profile Fig. 4-3 (b). This is because the calculated exponent q = 0.21 is close to the defined value of q = 0.2 (see Equation 4-7). The mean deviance between the imposed velocity profile, Fig. 4-3 (b), and reconstructed velocity profile, Fig. 4-7 (b), is calculated to be 1.10%, which is small enough to be acceptable. Using Equation 4-19, the local error distribution between the two velocities was calculated and is shown in Fig. 4-8. It can be seen that the local error δv_i is in the range of 2~4 %, which is still less than the minimum level acceptable in most industrial applications.

Therefore, from the analysis and discussion above, it is clear that the velocity reconstruction algorithm with the use of an axisymmetric velocity component can be applied to conductive fluids with both non-uniform and axisymmetric velocity profiles.

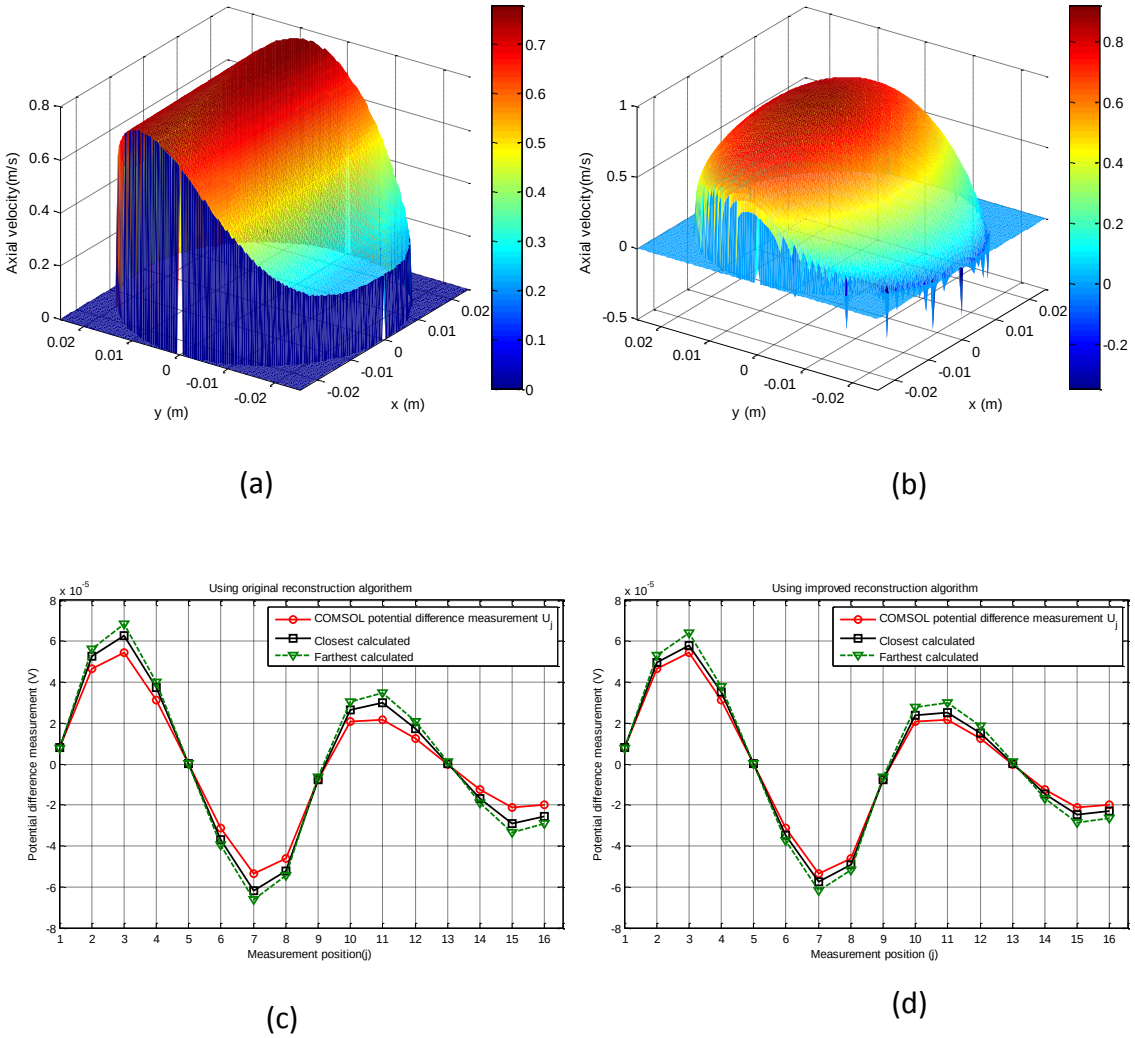

Fig. 4-7 Reconstructed velocities for imposed velocity profile defined by Equation 4-7: (a) optimum velocity profile obtained using reconstruction algorithm without use of an axisymmetric component; (b) optimum velocity profile obtained using reconstruction algorithm with use of an axisymmetric component; (c) potential difference distributions in the non-uniform magnetic field of simulated and reconstructed velocity profiles for reconstruction algorithm without use of an axisymmetric velocity component; and (d) potential difference distributions in the non-uniform magnetic field of simulated and reconstructed velocity profiles for reconstruction algorithm with the use of an axisymmetric velocity component.

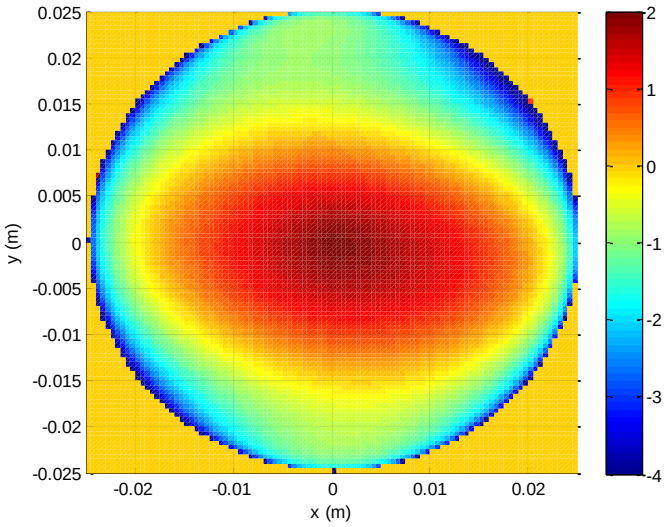

Fig. 4-8 Local percentage error between reference velocity defined by Equation 4-7 **and reconstructed velocity in Fig. 4-7(b); colour bar is in%**

4.4 Summary

Chapter 3 described a DFT-based reconstruction algorithm which is able to provide *n*! possible velocity profiles using measured electrical potential differences in uniform and non-uniform magnetic field. For this reason, the method for choosing the optimum velocity solution was proposed and described in this chapter. This method is based on determining the differences between the calculated potential differences, $\widehat{U}_j$, and measured potential difference, $\widehat{U}_{j,ref}$, in a non-uniform magnetic field for a given velocity profile. The calculated potential differences are obtained by using a technique which, foreach of the *n*! possible velocity solutions, determines the values of $\widehat{U}_j$ using weight values and the mean velocity in each of 30 regions (Fig. 4-1) for the relevant velocity profile solution.

The flow velocity reconstruction algorithm and the above method for choosing the optimum solution have been implemented in MATLAB. The program corresponding to the main procedure of reconstruction was explained. The complete program is shown in Appendix A.

Finally, both velocity profile reconstruction algorithms (with and without the use of an axisymmetric velocity component) were applied to reconstruct two quartic velocity profiles with

different axisymmetric velocity components. The results are presented in Fig. 4-5 and Fig. 4-6 and show that the reconstructed velocity profiles for both reconstruction algorithms have a good agreement with the first imposed velocity profile (see Equation 4-5). The mean deviation is 0.96% and the maximum local velocity error is 3.7%.

From the results presented in Fig. 4-7 and Fig. 4-8, it appears that the velocity profile obtained from the improved velocity reconstruction algorithm, which enables the reconstruction of axisymmetric velocity components, coincides closely with the second imposed velocity profile. The mean deviation in velocity is 1.10% and the maximum local velocity error is 4%, which is in the acceptable level of industrial multiphase flow applications.

5 Experimental apparatus

5.1 Introduction

A theoretical study of Inductive Flow Tomography (IFT) (analytical/numerical) has been made and a local axial velocity distribution reconstruction method developed. This was presented in Chapters 3 and 4. To validate the reconstruction velocity results produced by the simulation, a real IFT device was constructed based on the geometry of the simulation model (see Section 3.4).

This chapter comprises:

(i) an introduction to the construction of the IFT device, including the Helmholtz coil, electrodes and flow conduit design, and

(ii) a description of the potential difference measurement and coil excitation circuitry.

5.2 The Inductive Flow Tomography flow meter

A schematic drawing of a fully-assembled flowmeter body for the IFT device is shown in Fig. 5-1. By inspection of the figure, it can be seen that the flowmeter body consists mainly of the Helmholtz coil, coil clamps, non-conducting flow conduit, detection electrodes, aluminium casing and cable holder. Details of these components are given in the following sections.

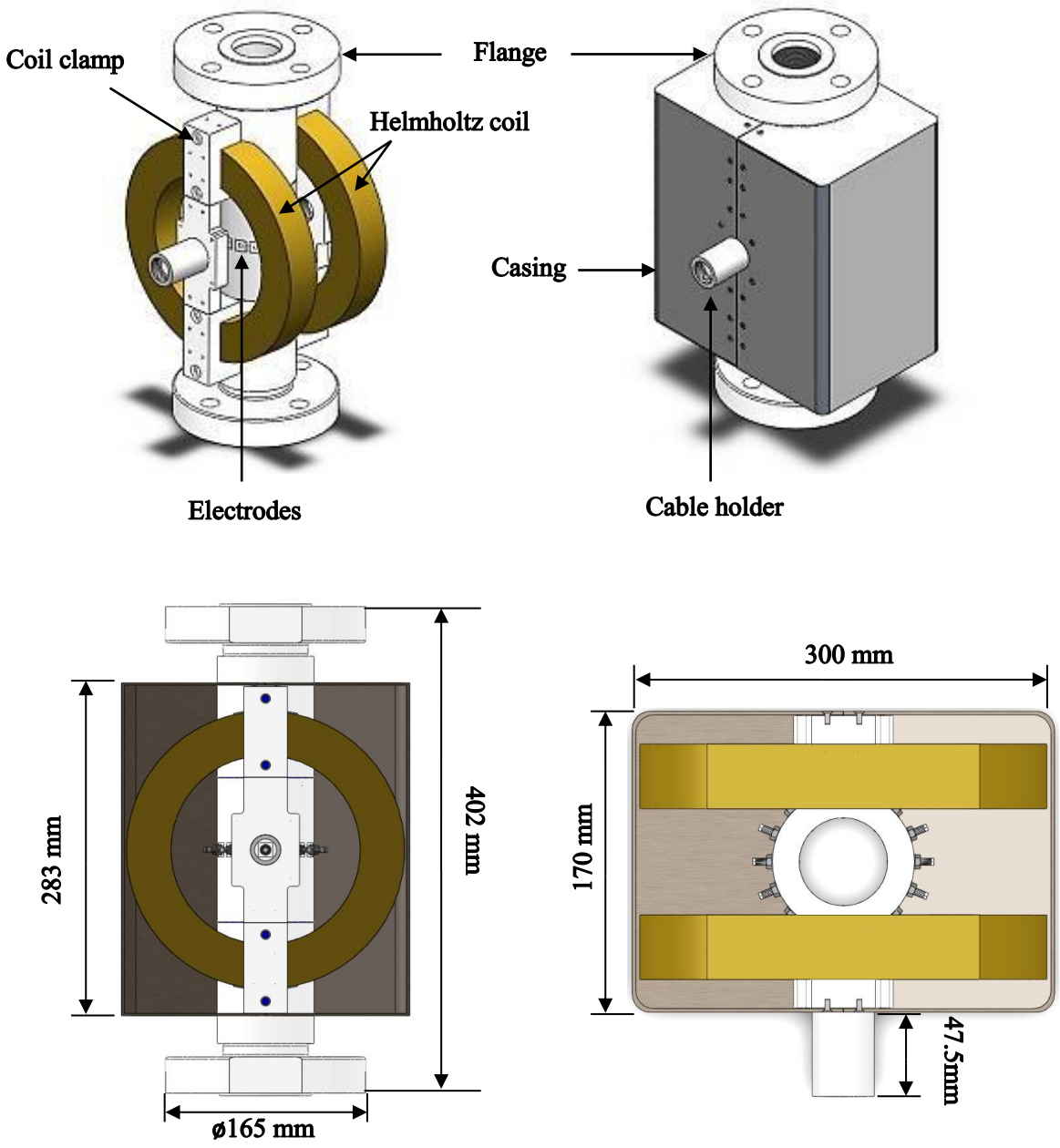

Fig. 5-1 Fully assembled IFT device and overall dimensions

5.2.1 The IFT flow conduit design

The body of the IFT flowmeter was designed and constructed based on the construction of an existing multi-electrode electromagnetic flowmeter [1]. A 50mm internal diameter Delrin pipe of 400mm length was used for the flow conduit of the meter. It is worth noting that the meter body was constructed from Delrin, because it is a non-conducting, non-magnetic material with a relative permeability of 1, which means the meter body does not distort the magnetic fields produced by the Helmholtz coil.

The flow conduit shown in Fig. 5-2 consists of four different elements: two threaded flanges, four 58 × 5.33mm rubber O-Rings, and a central pipe section with sixteen holes bored for the electrodes. There were also two pipe end sections. The flow conduit can be easily assembled (or disassembled) because each part is threaded based on 2" BSP (British Standard Pipe thread). This design allows straightforward replacement if any section is damaged. The grooves (coloured red) near the ends of the two pipes have been accurately machined to hold two circular coils of copper wire which form the Helmholtz coil configuration. Note that the real photo of IFT flow conduit is shown in Appendix B.

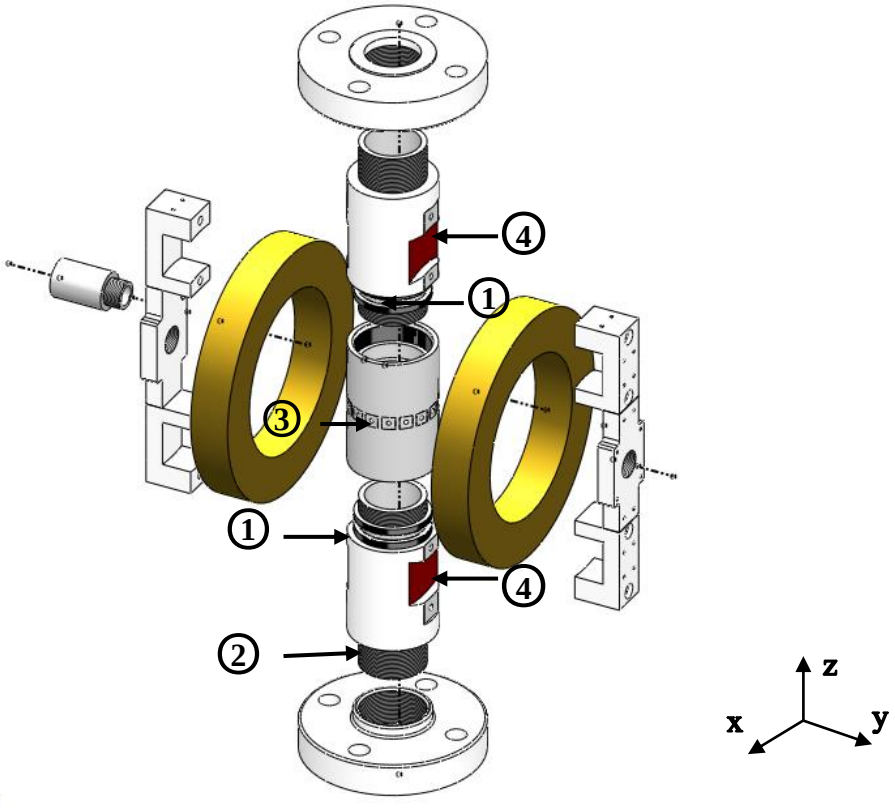

Fig. 5-2 Component parts of the IFT device ① rubber O-Ring ② 2" BSP thread ③ electrodes holes ④ grooves

Referring to the geometry of the simulation model as described in Section 3.4.2, sixteen equi-spaced holes were drilled into the central pipe section in the plane z=0 for the electrodes. More details of the electrode assembly are shown in Fig. 5-4.

5.2.2 Excitation coil specifications

The design and geometry of the excitation coils is based on the required magnetic flux density as predicted by the simulation of magnetic flux density distribution (see Section 3.3).

Referring to the simulation results (see Fig. 3-8), when the current in the two coils is flowing in the same direction, then the magnetic flux density can be considered as uniform over the flow cross-section, which indicates that the Helmholtz coil geometry used in the simulation environment can be made for practical application.

For the uniform magnetic field, the magnetic flux density for the IFT device in multiphase flow (water is the continuous phase) needed to create a measurable flow velocity signal is more than 100 Gauss [1]. Taking into account possible electrical overheating of the coils, the diameter of copper wire was chosen to be 0.766 mm and a current rating of 1.62 amp used for normal operations. In the simulation model, the width and thickness of the coil were chosen to be 35mm $\times$35mm, giving 1400 as the total number of turns.

The resistance of the two coils (denoted 1 and 2) were measured using an Ohmmeter, and were found to be 33.80 and 33.76, respectively. The 0.12% difference between resistances was considered negligible and the two coils could be expected to carry the same current when the excitation power voltage supply was connected.

The coil current is used to predict the component in the y-direction of the magnetic flux density for the uniform and non-uniform magnetic fields. A brief description and calculation of the magnetic flux density B_y is given below.

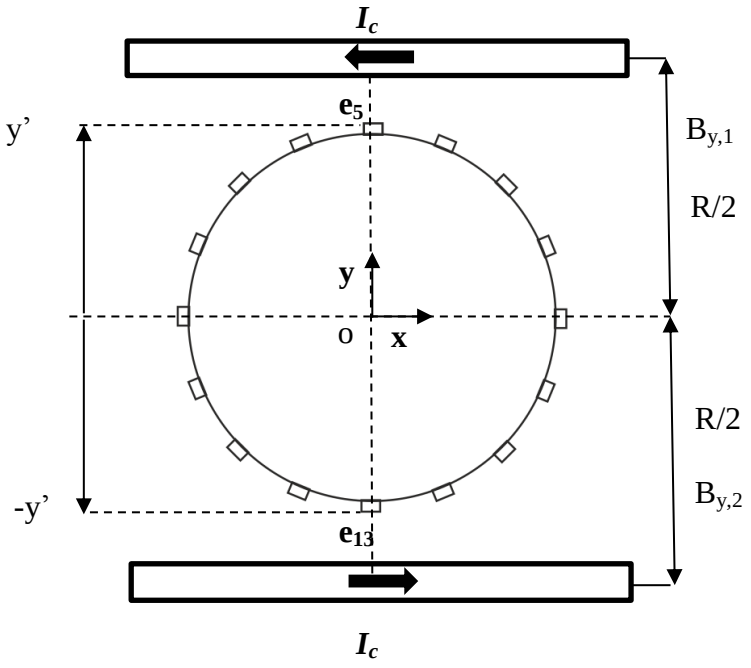

Fig. 5-3 IFT device in anti-Helmholtz configuration.

The Helmholtz coils were fixed to the upper and bottom side of the pipe, as shown in Fig. 5-1; the distance separating the two coils is equal to the mean radius *R* of each coil. The same electrical current flowed in each coil in the same or opposite direction, which can be used to respectively generate a uniform or a non-uniform magnetic field over the pipe's cross-sectional area. In the case of a uniform magnetic field the y component B_y of the magnetic flux density at the centre of the pipe cross-section can be expressed as: [97, 98]

$$B_y = \frac{8}{5\sqrt{5}} \frac{\mu_0 n_c I_c}{R} \qquad \text{Equation 5-1}$$

where $\mu_0 = 4\pi \times 10^{-7}$ H/m is the permeability of free space, n_c is number of turns in each coil, and I_c is the coil current.

When an electrical current flows through the coils in opposite directions(see Fig. 5-3), a non-uniform anti-Helmholtz magnetic field with component in the y direction B_y is established over the pipe cross-sectional area. B_y can be written in the form (see Section 3.3) [97, 98]:

$$B_y = B_{y,1} + B_{y,2} \qquad \text{Equation 5-2}$$

$$B_{y,1} = \frac{\mu_0 n_c I_c}{2} \cdot \frac{R^2}{[R^2 + (\frac{R}{2} + y)^2]^{3/2}} \qquad \text{Equation 5-3}$$

$$B_{y,2} = -\frac{\mu_0 n_c I_c}{2} \cdot \frac{R^2}{[R^2 + (\frac{R}{2} - y)^2]^{3/2}} \qquad \text{Equation 5-4}$$

Equation 5-2 can be re-written as

$$B_y = \frac{R^2 \mu_0 n_c I_c}{2} \cdot \left\{ \frac{1}{[R^2 + (\frac{R}{2} + y)^2]^{3/2}} - \frac{1}{[R^2 + (\frac{R}{2} - y)^2]^{3/2}} \right\} \qquad \text{Equation 5-5}$$

where y is the displacement from the origin O, which is at the centre of the pipe cross-section.

The magnetic flux density in the y-direction varies with the value of y. When $y = 0$, the magnitude B_y of the y component of the non-uniform magnetic flux density is equal to zero. [Note that in the plane z=0, the components of the magnetic flux density in the x and z directions are negligible.]

The radius R of each coil was 114mm, the current in each coil was 1.42A (the reasons for this are explained in Section 5.3.2) and the number of turns n_c for each coil was 1400. Thus, referring to Equation 5-1, the mean magnetic flux density, B_y, at the centre point of the magnetic field between the two coils, was calculated to be 157 G when the coil currents were flowing in same direction, which shows a agreement with the measurement made using a Gauss meter. Note that the value of magnetic flux density in the uniform magnetic field is used to reconstruct velocity profile. For the anti-Helmholtz coil configuration (coil currents flowing in opposite directions), the magnetic flux density B_y is a function of the position, y. Referring to the distribution of the y components of magnetic flux density, as described in Section 3.3, the maximum and minimum magnitude of B_y occurs at the position of electrode 13 (e_{13}) and electrode 5 (e_5) (see Fig. 3-4 (a) and Fig. 5-3). With reference to the Section 3.5.3 and Fig. 5-3, it is clear that the value of magnetic flux density B_{op} is equal to the maximum magnitude of B_y at position y=-y'. Referring to Equation 5-5, the magnetic flux density B_{op} in a non-uniform magnetic field can be expressed as:

$$B_{op} = \frac{R^2 \mu_0 n_c I_c}{2} \cdot \left\{ \frac{1}{[R^2 + (\frac{R}{2} - y')^2]^{3/2}} - \frac{1}{[R^2 + (\frac{R}{2} + y')^2]^{3/2}} \right\} \qquad \text{Equation 5-6}$$

According to Equation 5-6, the calculated value of B_{op} was equal to 42G, which was similar to a practical measurement (45G) made using a Gauss meter. Note that the practical measurement 45G was used to reconstruct velocity profiles for the experiments – this will be shown later in Chapter 7.

The operation of the Helmholtz coil can be modelled as a simple resistance-inductance (RL) circuit, which means the current does not rise immediately to its maximum value when a voltage

is applied to each coil. The current reached its maximum value at approximately 5τ, where τ is the time constant of the circuit. The rise time of the magnetic field can be determined from Equation 5-7. The magnetic flux density is then stable if the current remains constant. Note that Equation 5-7 can also be used for calculating the decay time of the magnetic field. Time constant,

$$\tau = \frac{L_{t,c}}{R_{t,c}} \qquad \text{Equation 5-7}$$

where the $L_{t,c}$ and $R_{t,c}$ is the total inductance and resistance of the Helmholtz coil.

Given the values of resistance and inductance of the coils, the time constant was calculated to be 0.012s. More details of the coil excitation method are discussed in the following section. In the present study, hybrid pulsed-DC excitation was chosen to avoid the electrode polarisation effect (see Section 5.3.1). The flow induced potential difference signals could be accurately measured after 5τ, when the magnetic field had stabilised.

5.2.3 The electrode array

Electrodes to measure flow induced electrical potential differences in multiphase flow were inserted into the flow conduit, as shown in Fig. 5-4. It can be seen that the electrode geometry is compatible with the electrical potential difference measurement circuits described in Section 5.3. Each electrode was manufactured from stainless steel (a non-magnetic material) and was 5 mm in diameter. As illustrated in Fig. 5-4 , the top surface of the electrode was mounted flush with the inside surface of the flow conduit. The sixteen electrodes formed an array, so that the flow induced electrical potential distribution could be measured around the periphery of the flow cross-sectional area.

To prevent leakage of fluid from the electrode bores, an ‘O’ ring was used and a rubber washer was fixed between the hex nut and outside pipe wall (see Fig. 5-4). Note that the a signal cable with crimp connector was clamped under an M2 screw enabling an electrical connection to be made between each electrode and the measurement circuitry. As stated above, an O-ring meeting ISO 3601-1:2012 was placed between the electrode and the pipe wall to prevent any leaks (see Fig. 5-4).

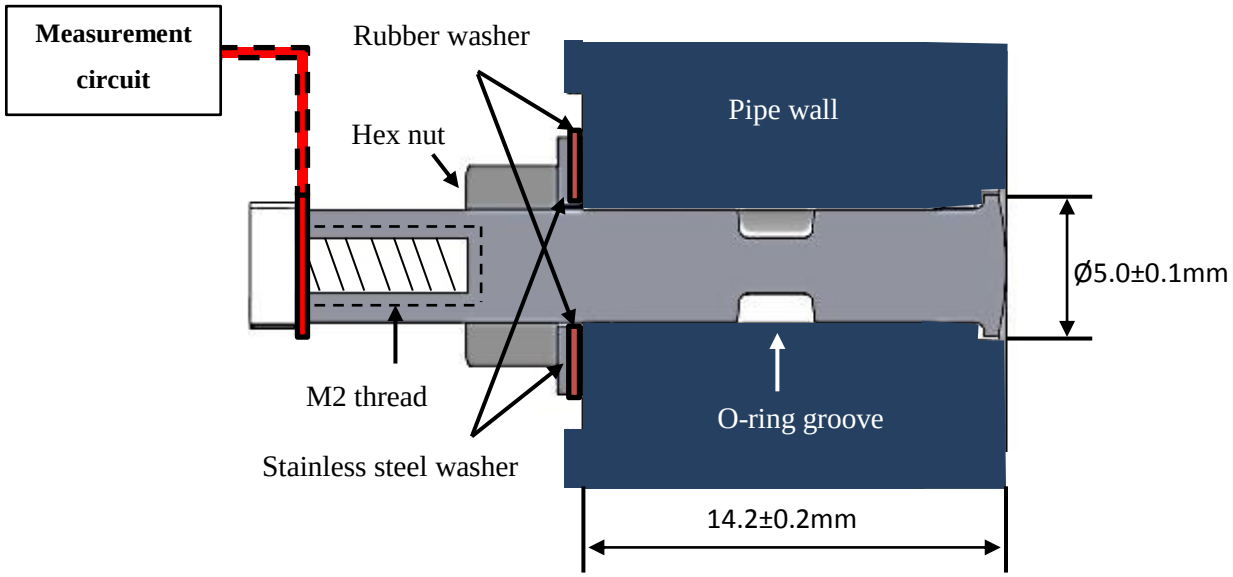

Fig. 5-4 Electrode assembly inside the flow conduit ("inside" or "in the side of")

5.3 The electronic systems for IFT

The IFT flow measurement device uses an off-line processing system based on a PC control system platform. As can be seen from the block diagram in Fig. 5-5, the IFT device comprises the following main parts: (i) multi-channel potential difference measurement circuitry; (ii) coil excitation system; (iii) data acquisition system; and (iv) host computer. The data acquisition system was also used to generate the digital control signals to the coil excitation circuit, which supplies voltages to the Helmholtz coil to create magnetic fields in the pipe cross-section. Because the coil temperature affected the coil current, a coil current monitoring circuit was used to obtain a voltage signal U_r which was proportional to the coil current (see Section 5.3.2 (iv)). The flow induced electrical potential difference signals U_j were measured between the j^{th} electrode e_j (j =1 to 4 and 6 to 16) and the reference electrode e_5 by using 'high gain voltage measurement circuitry'. The output signal from each channel was then measured via the data acquisition system. All measurements, including U_j and U_r, were sent back to the host computer and saved as a text file.

As stated above, in order to operate this system effectively, it was necessary to design and build two sets of electronic circuitry, i.e. coil excitation circuitry and potential difference measurement circuitry. Both electronic circuitries are explained in the following sections.

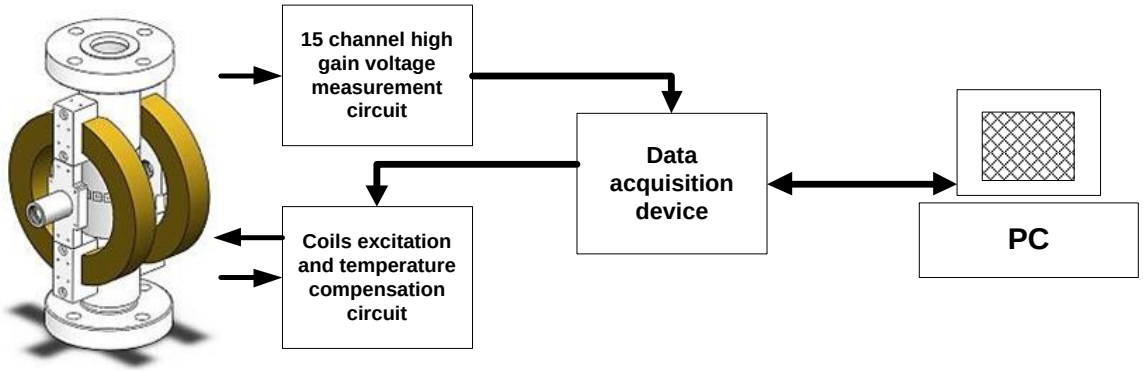

Fig. 5-5 The structure of IFT flow measurement system

5.3.1 Coil excitation

A careful approach is required when selecting the type of coil excitation because this will have a significant effect on the accuracy of the potential difference measurements for IFT. The appropriate excitation can not only help to overcome the polarisation effects at the electrode /water interface, which cause baseline drift in the potential difference measurement circuitry, but must also generate sufficiently large uniform and non-uniform magnetic flux densities in the flow cross-section.

Previous methods used for driving the coils of a conventional electromagnetic flowmeter have been DC, AC and Hybrid pulsed DC excitation [99], as described below.

- DC excitation

A common method for driving the coils of a conventional electromagnetic flowmeter is DC coil excitation, whereby the magnetic field in the pipe cross-section is constant. Because the angular frequency of the DC signal is zero this eliminates the common-mode magnetically-induced noise, which appears on the flow induced signals when non-DC excitation is used. However, a

significant problem associated with this method is the so-called 'electrochemical effect' between the metal electrodes and the ion-conducting fluid, which can cause unpredictable low frequency voltages to be added to the flow induced signal [100].

- AC excitation design

In order to prevent the electrochemical voltage, some researchers have excited the coils using an AC signal source. With AC excitation, the amplitude of the flow induced voltage signal measured at the electrodes can be proportional to the fluid velocity [101], but this approach also introduces magnetically-induced quadrature voltages as noise into the flow induced signal. It is possible to eliminate this noise and separate the phases of quadrature and flow induced signals, though this requires the design of a special phase-sensitive filter to match the phase of the quadrature signal and filter it out. The AC excitation design-based EMFM is generally used for detecting rapid changes in flow velocity, because its response time is much quicker than the pulsed DC excitation method, as described below. However, the pulsed DC excitation method is commonly used in industry applications, since it can prevent most of the unwanted signals encountered with the AC excitation design (as described below).

- Hybrid pulsed DC design

Another excitation method which has been extensively used is based on a low frequency square wave (a pulsed DC signal). With this excitation design, the flow velocity is proportional to the amplitude of the pulse [99, 101]. This approach can be effective in coping with many undesirable issues, such as baseline drift, quadrature voltages and the electrochemical effect. Although the flow induced signal includes stray noise, the latter can be simply separated by detecting the difference between signals with the pulses ON and then OFF [102]. Another benefit of using hybrid pulsed DC excitation is that the power requirement of the system is much lower than for conventional sinusoidal AC excitation. The reason is that the coils are only energised for part of the cycle. As mentioned above (AC excitation design), the hybrid pulsed DC excitation is not suitable for measuring rapidly varying flow velocity because the flow velocity information would be lost while the magnetic field is off.

In the present study, the hybrid pulsed DC excitation method has been selected for use with the coil excitation circuitry for the IFT. Fig. 5-6 illustrates a 'hybrid square wave' magnetic field generated by the ON and OFF sequence of the DC excitation. One cycle of excitation signal

contains four stages (S1, S2, S3 and S4). When the DC pulse is ON (S1 and S3), the electrical potential difference signal U_j rapidly increases until it reaches a constant level. As mentioned in Section 5.2.2, the magnitude of magnetic flux density B_y (y component) reaches a maximum value B_{max} after a time equal to five times the time constant of the coil. The measured flow induced potential differences U_j also reach a maximum value at this time. In a similar manner, the electrical potential differences U_j and the magnetic flux density B_y decrease from a constant level to zero when the DC pulse is OFF (S2 and S4). From the characteristics of the hybrid pulsed-DC excitation sequence, it can be seen that both the flow induced voltage and the DC off-set are measured during the period of maximum magnetic flux density. When the magnetic field is off (S2 and S4) only the DC offset voltage (i.e. caused by polarisztion at the electrode) is measured. Subtracting this measured non-flow induced voltage from the voltage measured when the magnetic field is ON gives the flow induced voltage without any DC offset. Note that by reversing the magnetic field (stage S1 and S3), the flow induced potentials at the electrodes are periodically reversed. This reduces electrode erosion due to electrolysis effects. More details of the coil excitation signal for the IFT flow measurement will be described in the next chapter.

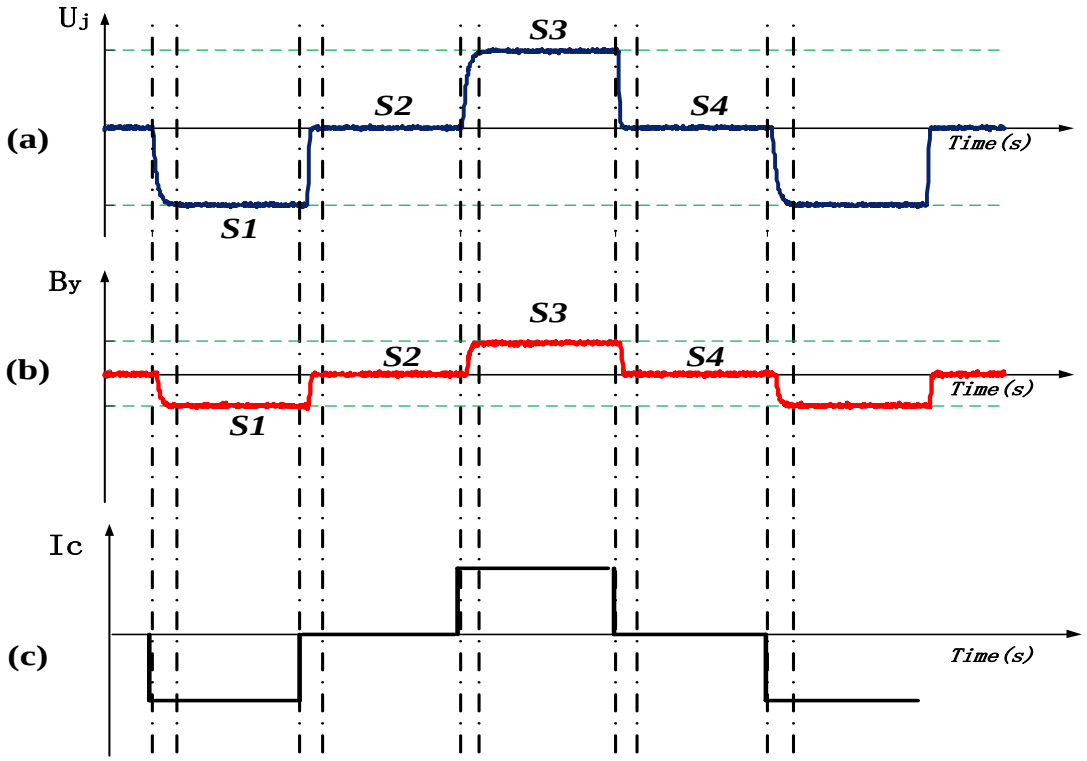

Fig. 5-6 (a) electrical potential difference Uj, (b) magnetic flux density B_y, and (c) the hybrid pulsed DC excitation signal

5.3.2 Coil excitation control circuitry

This section is concerned with achieving the required coil excitation currents. The design of the electronic circuitry for coil excitation was based around a H bridge configuration of solid state relays. This design has been described by Leeungculsatien and Lucas [1]. In this research, a new feature was introduced into the electronic circuitry which can be used to impose coil currents flowing in opposite directions. Fig. 5-7 is a schematic diagram showing the major units of this circuitry.

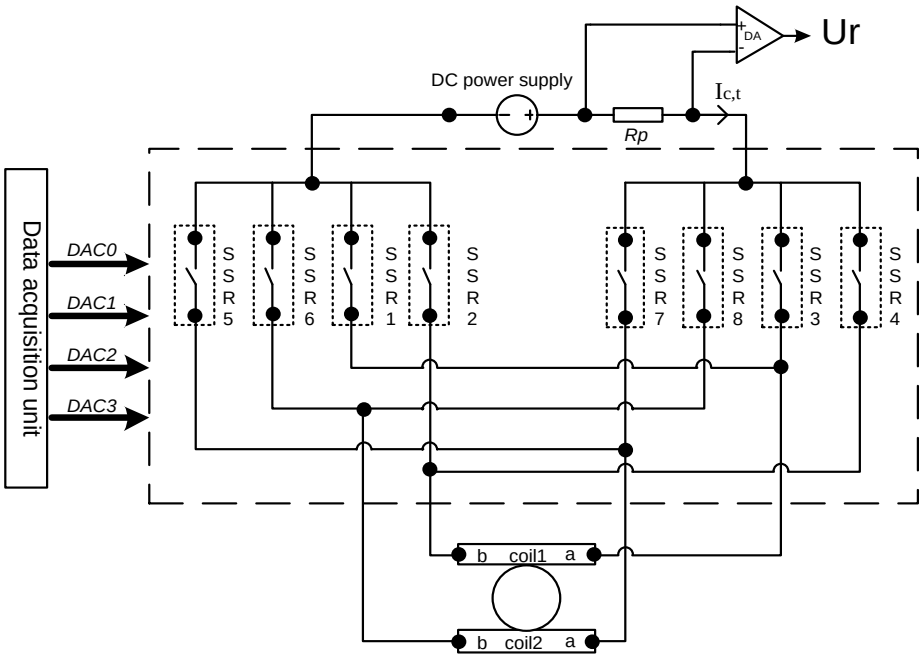

Fig. 5-7 Overview of Helmholtz coil circuit and coil current monitoring circuit

(i) DC power supply

In order to simplify the circuitry design, and improve its reliability, an industrial AC-to-DC power supply, TRACO POWER TXH Series 240W, was used to provide a maximum voltage, U_{DC}, of approximately 48 volts at upto 5 amps. The total resistance of the two coils in parallel is 16.89 (see Section 5.2.2), thus the total coil current $I_{c,t}$ was calculated to be 2.84A, according to Ohm's law. The current through each coil is 1.42A, half of $I_{c,t}$. Note that each coil current is still equal to 1.42A for the anti-Helmholtz coil configuration.

(ii) H-bridge configuration of solid-state relays

The voltage (48V) from the DC power supply was fed into the H bridge of the solids-state relays (SSR), which were configured as a switching circuit. These circuits ensure the currents pass through the coils in the required directions. To control the SSRs, a reference voltage unit was used as shown in Fig. 5-8. Referring to the schematic diagram of the H bridge of SSRs coil excitation circuitry, as shown in Fig. 5-9, the +5V voltage is fed into the solid-state relay (SSR) and a simple voltage divider is generated by using a voltage regulator (L7805C, see Fig. 5-8).

The output of the voltage divider is 1V and gives a reference signal to comparators labelled LM393. By comparing this reference signal (1V) with the digital control signal (DAC), the output signal of comparator can be used to turn the SSR relays on/off. The controlling routines for the digital control signal (DAC) are shown in Table 5-1, corresponding to Fig. 5-7 and Fig. 5-9. It is worth noting that the digital control signals (DAC) are sent from a multifunction NI USB-6255 DAQ board (see Section 6.2).

Consider the uniform magnetic field as an example (see Fig. 5-9); when the solid-relays SSR 3, 2, 7 and 6 were switched on and SSR 4, 1, 8 and 5 were off, the voltage 'U_{DC}' was created at position 'a', and position 'b' was connected to the ground (i.e. voltage at 'b' is zero). This implies that a uniform magnetic field with magnetic flux density $-B_y$ (S1 in Fig. 5-6 (b)) was established between the two coils, while the coil current $-I_c$ (S1 in Fig. 5-6 (c)) was flowing through the coils from 'a' to 'b'. According to the hybrid pulsed-DC excitation method described in section 5.3.1, the magnetic field would then be turned off so that the voltage at 'a' and 'b' were both connected to the ground (zero) (S2 in Fig. 5-6 (b) and Fig. 5-6 (c)). Next, in stage S3 (see Fig. 5-6), the solid-relays SSR 4, 1, 8 and 5 were switched on and SSR 3, 2, 7 and 6 were off and a uniform magnetic field with magnetic flux density B_y (S3 in Fig. 5-6 (b)) was established. It can be easily seen from Fig. 5-7 that the voltage at 'a' was zero and the voltage at 'b' was 'U_{DC}' and that the coil current I_c flowed from 'b' to 'a'. Finally in S4 (Fig. 5-6) the voltage at 'a' and 'b' were both connected to ground again so that the magnetic field was again turned off.

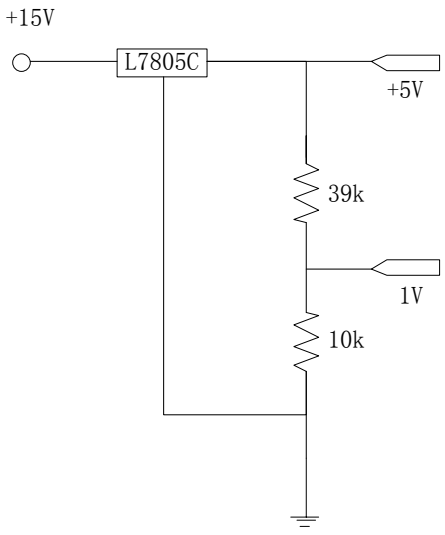

Fig. 5-8 Schematic diagram of reference voltage unit

DAC				Coil 1		Coil 2		Relay number (SSR)				Magnetic flux density	Magnetic Field status
0	1	2	3	Voltage at 'a'	Voltage at 'b'	Voltage at 'a'	Voltage at 'b'	3 & 2	7 & 6	4 & 1	8 & 5		
high	low	high	low	U_{dc}	0	U_{dc}	0	on	on	off	off	$-B_y$	Uniform
low	high	low	high	0	U_{dc}	0	U_{dc}	off	off	on	on	B_y	
high	low	low	high	U_{dc}	0	0	U_{dc}	on	off	off	on	$-B_y$	Non-uniform
low	high	high	low	0	U_{dc}	U_{dc}	0	off	on	on	off	B_y	
low	low	low	low	0	0	0	0	off	off	off	off	Zero	None

Table 5-1 the working state of relays and voltages across Helmholtz coil for uniform and non-uniform magnetic fields

Fig. 5-9 can also show how to use the solids-state relay switching circuit to inject current into two coils (coil 1 and coil 2) in order to generate a non-uniform magnetic field. Note that the non-uniform magnetic flux density distribution is produced by injecting coil currents in opposite directions. Referring to the example shown in Fig. 5-9, by using the output signal of the LM393 comparators, the solids-state pairs of relays SSRs 2 and 3 and SSRs 5 and 8 are activated, and, simultaneously, the pairs of relays SSRs 1 and 4 and SSRs 6 and 7 are switched off. Thus, it is seen that the DC voltage (48V) is connected to 'a' of coil 1, and the other end, 'b', of coil 1 has been connected to 0V. DC current flows from 'a' to 'b'. Similarly, the current through coil 2 flows from 'b' to 'a'.

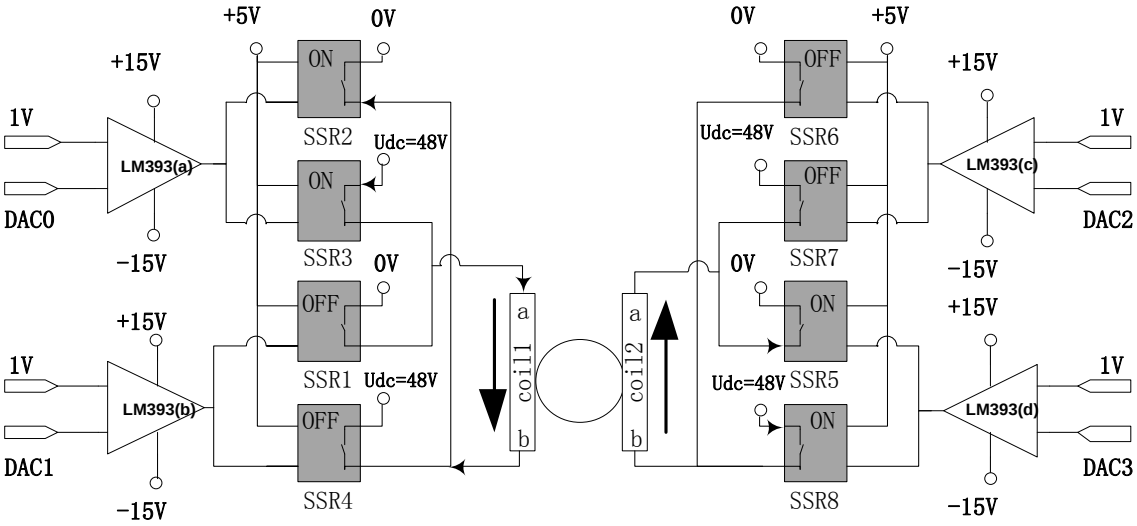

Fig. 5-9 H bridge of SSRs coil excitation circuitry

A photo of real coil excitation control circuitry of IFT system is shown in Fig. 5-10.

Fig. 5-10 coil excitation control circuitry of IFT system

(iii) Coil current monitoring unit

Referring to the general equation governing the EMFM (see Equation 3-1), the flow induced voltage would change if either or both the conducting fluid velocity or magnetic flux density varied. It can be seen that, for a varying magnetic field the measured induced voltage cannot accurately reflect the variation of the conducting fluid velocity.

The magnitude of the magnetic flux density in the IFT device depends upon the ampere-turns within the coil. The number of turns of the Helmholtz coils is constant, so the magnetic flux density is proportional to the current passing through the coil. Furthermore, according to Ohm's law, the DC coil current is calculated from the applied voltage and resistance of the coil. It is apparent that, if the coil resistance increases, the value of the ampere-turns decreases, and that reduces the magnetic field strength. The supply voltage is fixed at 48V by the power supply unit; thus, increasing the resistance of the coil decreases the magnetic field strength.

When the cross-sectional area and length of the wire remain constant, the resistance of the wire can change with its temperature (see Equation 5-8) [103, 104], according to the following equation.

$$R_p = R_{ini} \times \left(\frac{T_p + 234.5}{T_{ini} + 234.5} \right) \qquad \text{Equation 5-8}$$

where R_p is coil resistance at coil temperature T_p (℃), R_{ini} is coil resistance at initial temperature, T_{ini}; -234.5℃ is the effective absolute zero temperature of copper [103, 104]. Equation 5-8 shows that, if the temperature of the coil T_p increases, then the resistance R_p of the coil will increase by $R_{ini} \times (T_p + 234.5 / T_{ini} + 234.5) - R_{ini}$. According to Ohm's law, the coil current will reduce proportionately, which will cause a reduction in the magnetic flux density. When the Helmholtz coil is powered on, the relationship between mean magnetic flux density and coil current can be represented as:

$$\frac{I_{p,c}}{I_{\max,c}} = \frac{\overline{B}_p}{\overline{B}_{\max}}$$ Equation 5-9

where $I_{p,c}$ is the coil current at actual coil operating temperature, $I_{\max,c}$ is the coil current at the initial coil temperature, $\overline{B}_p$ is the mean magnetic flux density at the actual coil operating temperature, and $\overline{B}_{\max}$ is mean magnetic flux density at the initial coil temperature. Leeungculsatien [1] practically proved that when the Helmholtz coil was constantly energised, the temperature of the coil was increased (see Fig. 5-11 (a)). The magnetic flux density starts decreasing from the maximum magnitude of $\overline{B}_{\max}$ as soon as the coils start to operate (see Fig. 5-11 (b)). Thus, it can be seen that $I_{\max,c}$ and $\overline{B}_{\max}$ were considered as maximum values when the coil temperature was the same as room temperature [1].

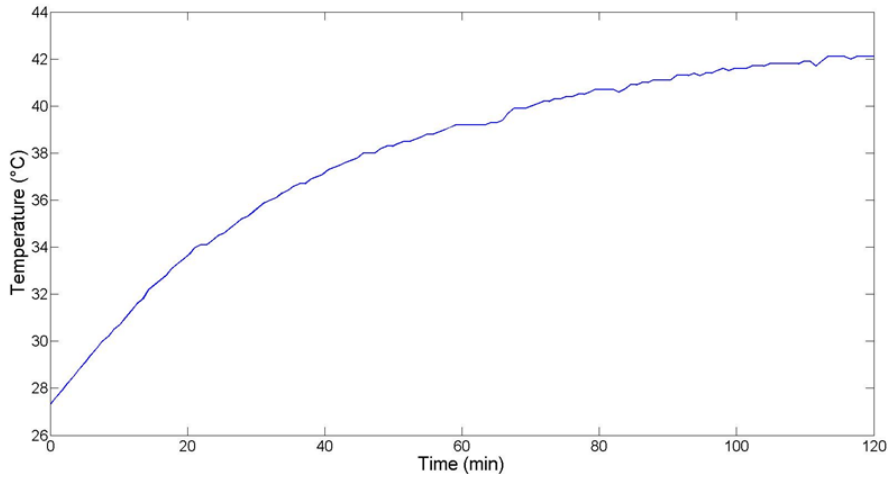

(a)

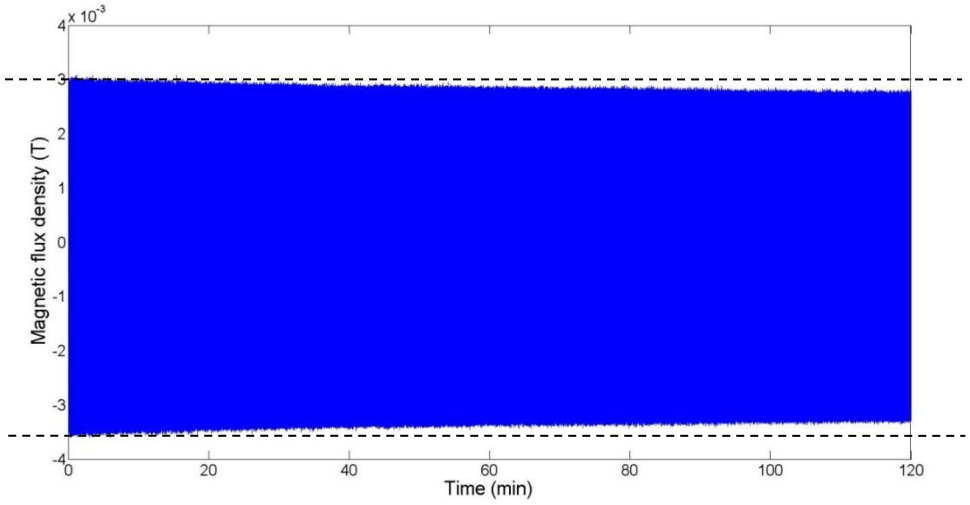

(b)

Fig. 5-11 (a) Measured temperature on the coil surface, (b) dynamic measurement of the magnetic flux density [1]

In order to compensate for the effects of coil resistance on the magnetic flux density, a coil current monitoring circuit was used as shown in Fig. 5-12 and as 'DA' in Fig. 5-7. The major stages of this circuit are described and explained below.

In the first stage, a differential amplifier was used to obtain a voltage drop across a precision resistor R_{ref} of 0.1, which was connected in series between the Helmholtz coil and the DC power

supply unit (see Fig. 5-7). Note that the resistance of 0.1 does not significantly affect the voltage drop across the Helmholtz coil because the resistor is only 0.58% of the total resistance in the circuit. The output voltage from the differential amplifier is $U_{ref,1}$

where:

$$U_{ref,1} = (U_+ - U_-) \times \frac{R_{fb}}{R_1} \qquad \text{Equation 5-10}$$

In Equation 5-10, R_2 and R_1 are the resistances shown in Fig. 5-12, U_+ is the non-inverting input voltage signal and U_- is the inverting input voltage signal.

In the next stage, the output voltage $U_{ref,1}$ is smoothed using a Butterworth low-pass filter with a cut-off frequency, f_{ct} of approximately 6Hz (see Fig. 5-12). The output from the Butterworth low-pase filter stage is U_r, we may write,

$$I_c = \frac{U_{R,ref}}{0.1\Omega} \qquad \text{Equation 5-11}$$

where I_c is the sum of the magnitudes of the currents in the two coils and where $U_{R,ref}$ is the voltage drop across the precision reference resistor R_{ref} (i.e. $U_{R,ref} = U_+ - U_-$). Since the gain of the differential amplifier is equal to 10 and the gain of the Butterworth low-pass filter is 1 we may now write:

$$U_{R,ref} = \frac{U_r}{10} \qquad \text{Equation 5-12}$$

Thus, the voltage drop across the precision resistor $U_{R,ref}$ is proportional to the sum of the magnitudes of the currents in the two coils I_c. According to Equation 5-11 and Equation 5-12, we may write $U_r = I_c$ (i.e. U_r and I_c are numerically equal). Since the magnetic flux density for both the uniform and non-uniform fields is proportional to I_c, the measured voltage U_r can be used to compensate for the effects of coil temperature on magnetic field strength as explained in Section 6.3.

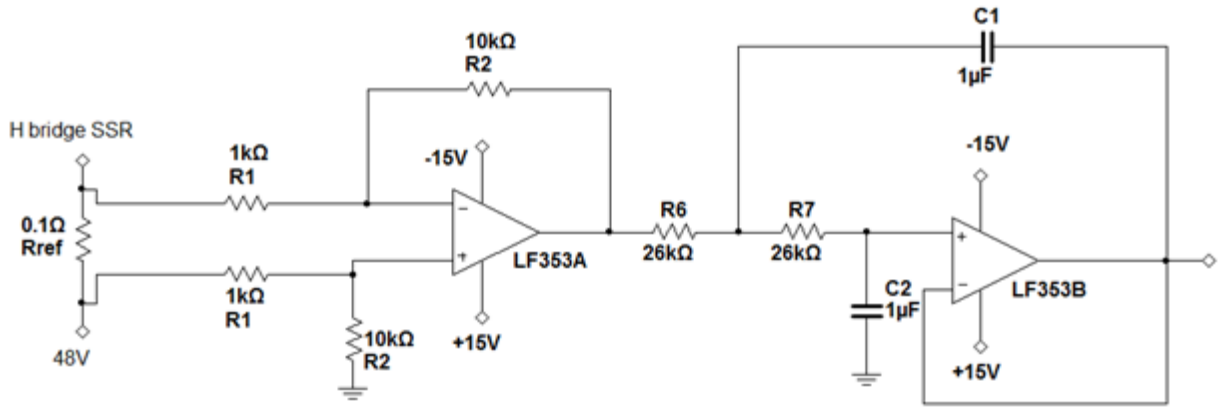

Fig. 5-12 Coil current monitor circuitry

5.3.3 Potential difference measurement circuitry

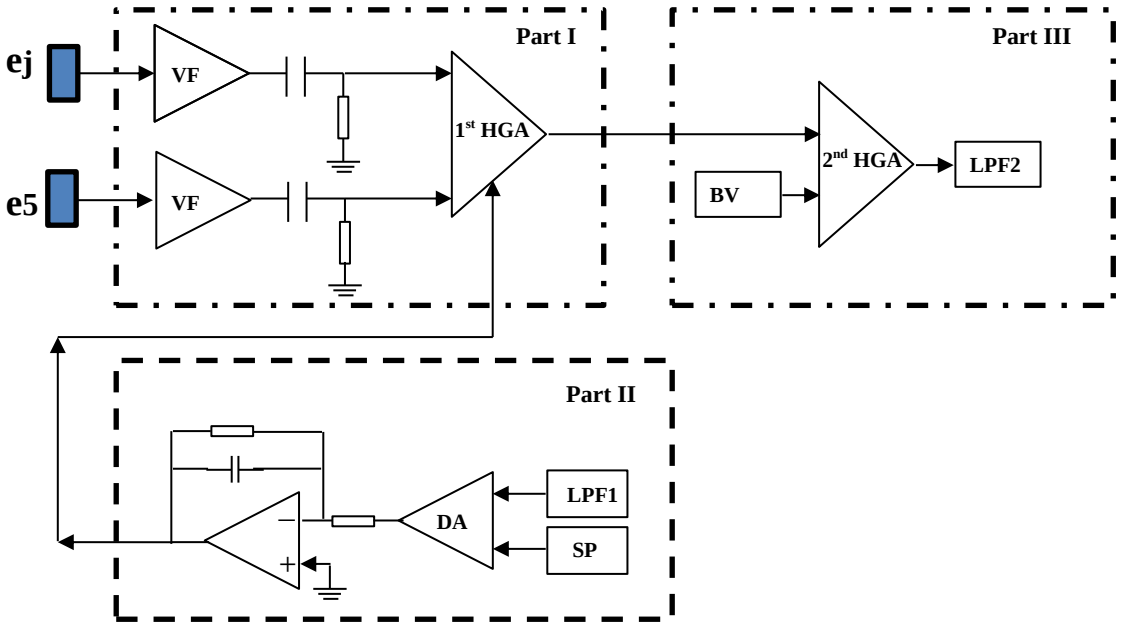

Fig. 5-13 Overview of potential difference measurement circuitry

As described in Chapter 3, it was required to measure the flow induced potential differences U_j between the j^{th} electrode and the 5^{th} electrode e_5 (i.e. the reference electrode). Since it was

required to measure 15 potential differences U_j (j = 1 to 4 and 6 to 16) 15 separate potential difference measurement circuits were designed and build. The following describes the operation of one of these circuits (measuring the potential differences between e_j and e_5). The difference between the potential on the j^{th} electrode and the 5^{th} electrode e_5.

However, the physical signal, $\varphi_j - \varphi_5$ (j= 1to 4 and 6 to 16), is only a few millivolts, which is outside the range of most commonly used data acquisition devices. In order to detect these relatively small signals, it is necessary to amplify them. This is done by using a well-designed high-gain differential amplifier. In addition, any unwanted DC offset mixed with the electrode potential signal is amplified by the gain, and would result in background voltage drift. Unwanted DC offsets come from many sources, such as those listed below:

- Electrochemical effects between the electrodes and conducting fluid.
- Leakage current from the AC coupling and high pass filter.
- Static charge on non-conducting pipe walls, such as a PVC pipe.

The potential difference measurement circuitry is grouped into three parts (see Fig. 5-13).

Part I Signal detection and amplification

The flow induced potential signals from the electrodes are fed into the non-inverting input of a unity gain buffer (LF353) (see Fig. 5-15). The reason for using a voltage buffers is because they have high input impedance.

With a low offset of 10, a very low input bias current of 50pA and high input impedance 10^{12} , it can be stated that the LF353 has the appropriate characteristics for the required purpose. The two output signals from the voltage buffers were then filtered using high pass filters (see Fig. 5-15). The high pass filters were used to remove low frequency signals, such as DC currents due to electrochemical effects on the electrodes and static electric charge on the non-conducting pipe wall. The cut-off frequency f_{ct} of the high pass filters depends on the excitation frequency. If the cut-off frequency was set too close to the excitation frequency, the potential signal with the hybrid pulsed DC waveform would be converted into 'spiky' waveform, as shown in Fig. 5-14, which could affect the accuracy of potential difference measurements. In this design, the cut-off frequency f_{ct} was set to 0.001693Hz. How the cut-off frequency was determined is explained in

Chapter 6. However, the DC offset U_{dc} was not entirely removed by the high pass filters because of mismatches arising from component tolerances. In Fig. 5-15, $U_j + U_{dc}$ denotes the overall input signal before it passes to the high gain amplifier (INA129). As mentioned earlier, the flow induced potential difference signal U_j should be amplified with a gain of 1000, because the amplitude of U_j is in the millivolt range. By considering the effects of the DC offset, a two-stage amplification unit was used, which effectively prevents the circuit saturating. Referring to Fig. 5-15, the signal $U_j + U_{dc}$ was amplified by the first amplification unit INA1 with a gain A_1 =50.4. The output from this first amplification stage can be written as $A_1(U_j + U_{dc})$ (see Fig. 5-15). It is worth noting that, by using the DC offset control circuit (as shown in Fig. 5-16), $A_1 U_{dc}$ effectively becomes zero.

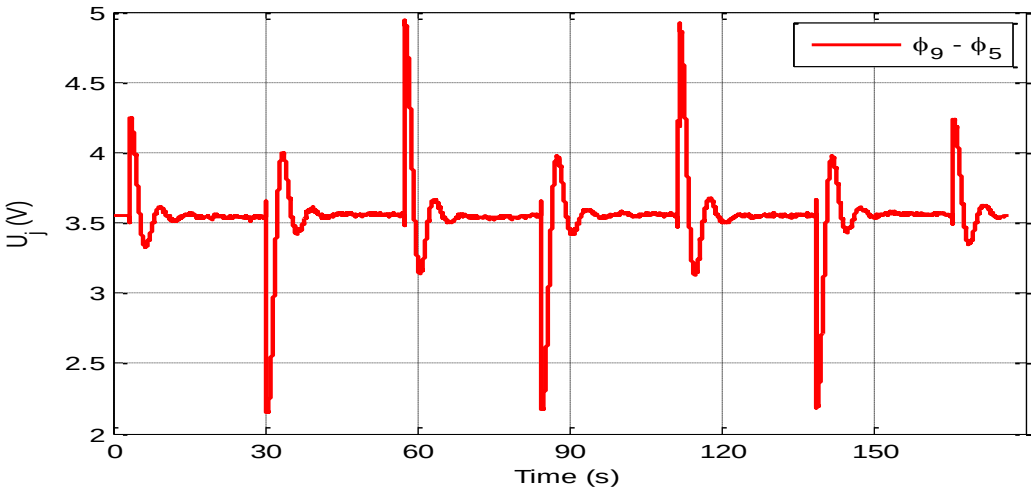

Fig. 5-14 Physical potential signal U_9 with excitation frequency of 0.0167Hz

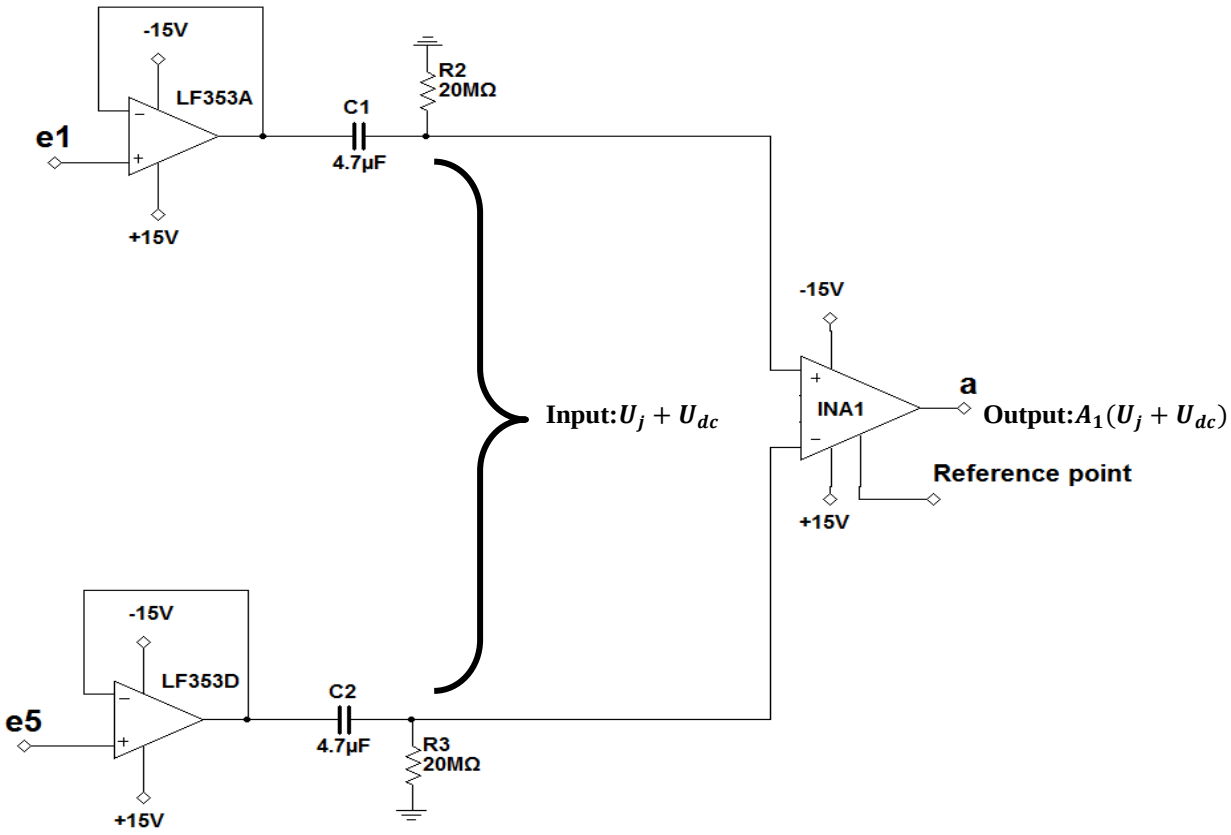

Fig. 5-15 Part I Signal detection and amplifier[note that signal at 'a' is fed into the circuit shown in Fig. 5-16 and that the signal at 'Reference point' is the output from the circuit in Fig. 5-16]

Part Ⅱ DC offset control circuit

In order to extract the flow induced voltage signal U_j from the amplified voltage signal $A_1(U_j + U_{dc})$ a control circuit is required, which continually delivers a compensating voltage to the reference input of INA1 (see Fig. 5-16). The compensating voltage contains only the inverted amplified DC offset $-A_1U_{dc}$. It can be seen from Equation 5-13 that, when the DC component A_1U_{dc} is removed from the output signal, we obtain:

$$V_{o,INA1} = A_1(U_j + U_{dc}) - A_1U_{dc}$$

$$V_{o,INA1} = A_1 U_j$$

Equation 5-13

where $V_{o,INA1}$ is the output from amplifier INA1.

There are two features of the DC offset control:

(i) Firstly, the output signal $A_1(U_j + U_{dc})$ of the first amplification unit INA1 was fed into the first stage of the DC offset control circuit and the signal was low-pass filtered by a Butterworth low-pass filter with a lower frequency limit of 0.28Hz. Then the flow induced potential signal $A_1 U_j$ was removed leaving only the DC component, $A_1 U_{dc}$

(ii) The DC voltage, $A_1 U_{dc}$, was then fed into the integrator (see Fig. 5-16) with an RC time constant of 1 second. The output of the integrator can be written as:

$$U_{com} = \frac{-1}{RC} \int_0^t A_1 U_{dc} dt \qquad \text{Equation 5-14}$$

From Equation 5-14 , it is now possible to define the resultant compensating voltage U_{com} as:

$$U_{com} = -\int_0^t A_1 U_{dc} dt \qquad \text{Equation 5-15}$$

The output of the integrator U_{com} was then fed back into the reference input of INA1 to compensate the flow induced potential signal. It should be noted that the integrator configuration does not contain a feedback resistor, allowing the capacitor to be fully charged to the inverted DC offset value in such a way as to ensure that the absolute compensated voltage $|U_{com}|$ is equal to $A_1 U_{dc}$ [106].

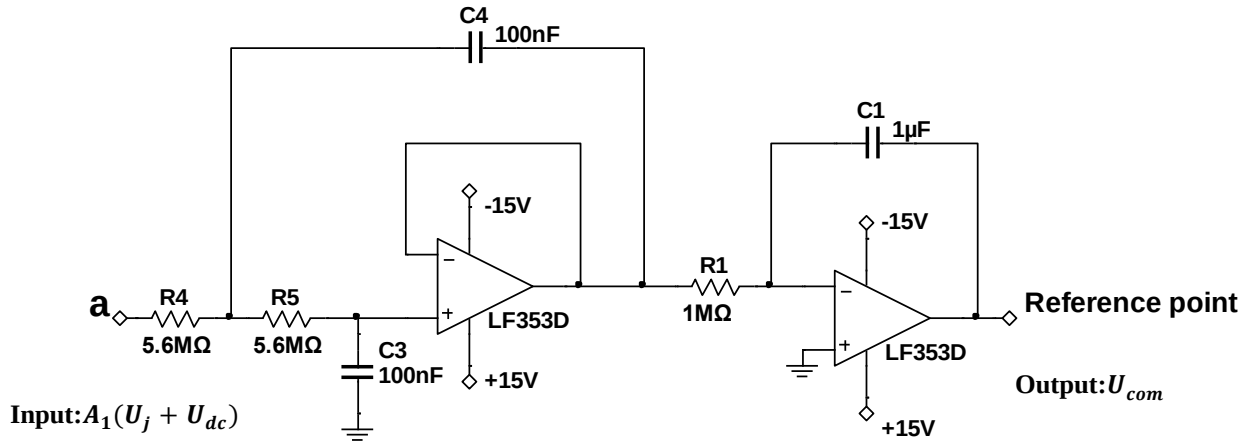

Fig. 5-16 Part Ⅱ DC offset control circuit [Note that signal at 'a' is the output from the circuit in Fig. 5-15 and the signal at ' Reference point' is fed into the circuit shown in Fig. 5-15]

Part Ⅲ second amplification within bias voltage control circuit and Butterworth low pass filter

The third signal detection stage is the application of the second amplifier INA2 to amplify the flow induced potential signal with a gain A_2 of 19.92. Referring to Fig. 5-17, a bias voltage signal U_{BV} is continuously generated by a voltage divider. Note that the output range of the voltage divider is from 1.67V to 5.00V. By setting an appropriate bias voltage U_{BV} the amplified flow induced potential difference signal $A_2A_1U_j$ can be maintained within the required input range of the analogue to digital converters (ADC). The output of the final stage, $V_{o,INA2}$, is given by:

$$V_{o,INA2} = A_2A_1U_j + U_{BV} \qquad \text{Equation 5-16}$$

$V_{o,INA2}$ can also be expressed as:

$$U_{j,a} = V_{o,INA2} \qquad \text{Equation 5-17}$$

Further processing of the signals $U_{j,a}$ is described in the next chapter.

Before the flow induced potential signals were collected by the data acquisition unit or ADC of the microcontroller, another Butterworth low-pass filter was used to remove high frequency noise, such as the well-known 50Hz 'mains' noise. Through practical testing, the cut-off frequency f_{ct} of this Butterworth filter was set to 15.9 Hz.

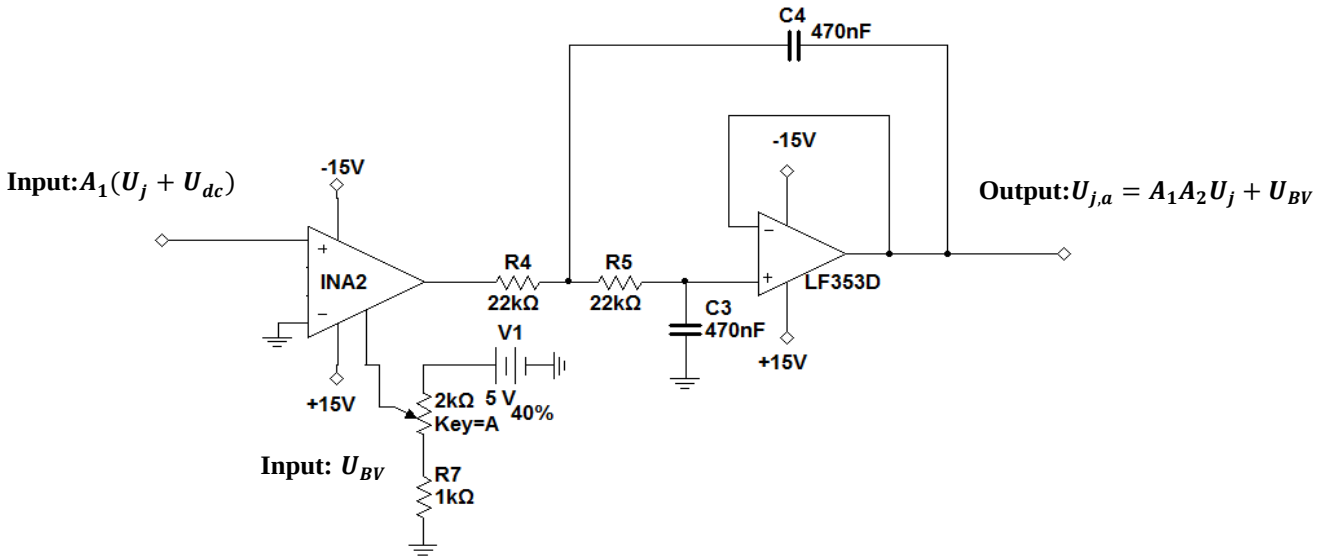

Fig. 5-17 Part Ⅲ second amplification within bias voltage control circuit and Butterworth low pass filter [note that the input is effectively equal to zero duo to the action of the DC offset control circuit (see Fig. 5-16)]

Fig. 5-18 shows photograph of the 15 channels potential difference measurements circuit described in this section.

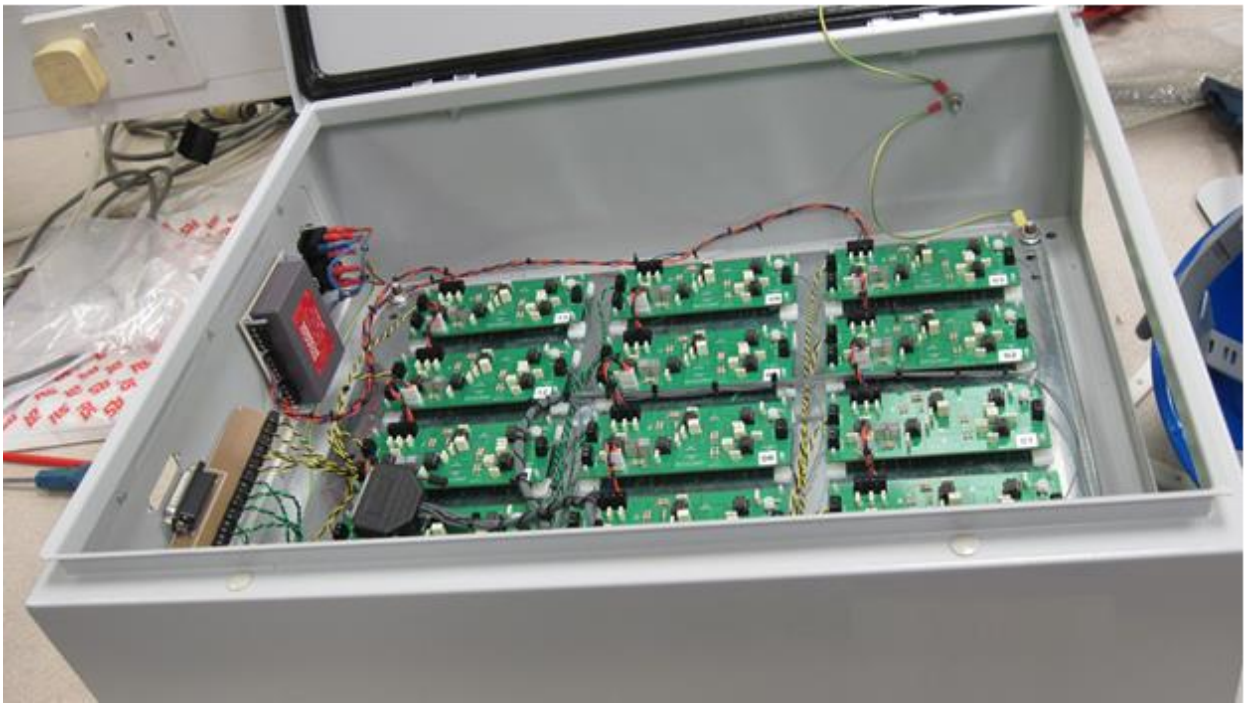

Fig. 5-18 Photograph of the 15 channels potential differences measurement circuit

5.4 Summary

A non-intrusive IFT flowmeter has been designed and constructed based on a design determined by the simulation model, and which can be used to determine the local water velocity distribution in either water continuous multiphase flow or single phase flow of a conducting fluid.

The IFT flowmeter consists of a non-conducting flow conduit constructed from Delrin with an internal diameter of 50mm. To ensure that the two circular coils were rigidly attached to the flow conduit, four grooves were machined on the outside surface of the flow conduit, into which the coils fitted. The flow conduit can be easily assembled from three different sections (central section, and two end sections). The two ends of each section were threaded for easy removal or replacement.

Section 5.2.2 explains that the two excitation coils were designed and manufactured with 1400 turns on each coil. The width and thickness of the individual coils was 35mm × 35mm. The radius of each coil was 114mm, which is the same as the coil separation distance. The resistance of each coil was equal to 33.78 Ω ± 0.02 Ω

The IFT flowmeter comprises sixteen electrodes arranged around a circular pipe. The angular separation was 22.5 º. To prevent leakage of fluid, an O-ring was used to seal any gap between the electrode and pipe wall.

Section 5.3, describes the electronic circuits which were designed to control the magnetic field and to obtain the electrical potential difference signals from the electrode pairs. Based on all the advantages of the different approaches described in Section 5.3.1, hybrid pulsed DC excitation was used in this research. Using hybrid pulsed-DC excitation, both electrochemical effects and quadrature noise can be eliminated. This type of excitation combines the advantages of AC and DC excitation.

In order to generate a hybrid pulsed magnetic flux density excitation signal, control circuitry was designed and constructed. This comprised a DC power supply and an H bridge configuration of solid state relays. Because the coil current will decrease as the coil temperature increases, coil current monitoring circuitry was designed and built, which was used to continuously obtain a voltage U_r, which was numerically equal to the sum of the magnitude of the current flowing in the two coils

To obtain the electrical potential difference signals U_j from the electrodes pairs, a voltage signal measurement and control circuitry was designed. 15 electronic circuits were constructed to measure the potential differences between electrode e_j (j= 1 to 4 and 6 to 16) and electrode e_5.

6 IFT system control and signal processing

6.1 Introduction

The previous chapter described how the IFT flowmeter and electronic circuitry were designed and built. Referring to the block diagram shown in Fig. 5-5, the IFT system has a PC to control a data acquisition unit which continuously collects the measured potential difference signals. The data acquisition unit is also used to feed signals to the relays which control the current in the Helmholtz coil.

This chapter describes the software design of the IFT measurement and control systems. With reference to the characteristics of the electronic hardware and coil excitation system used with the IFT flowmeter, a controlling and processing program for the measurement and control system was developed using MATLAB and LabVIEW software. The measurement and control hardware is based around an NI multi-function data acquisition board which has digital I/O and 16-bit analogue to digital conversion resolution.

In Section 6.2, due to the fact that the coil excitation control, data acquisition and storage of data must be performed in parallel, a multiple task program based on the LabVIEW software platform is described.

In Section 6.3 , the MATLAB technique used for analysing the electrical potential differences U_j and U_r, is discussed.

6.2 Signal acquisition and control software design

Referring to Fig. 5-9, the control signals for the coil excitation circuitry (i.e. DAC0, DAC1, DAC2 and DAC3) were connected to the digital output pins DI/O0, DI/O1, DI/O2 and DI/O3, respectively, on the data acquisition device. This data acquisition device was controlled using a host computer with a LabVIEW-based software program. It was also used to collect amplified induced voltage signals $U_{j,a}$ from the potential difference measurement circuits (see Equation

5-17) and coil current monitoring signals U_r via seventeen analogue inputs (i.e. fifteen induced voltage signals $U_{j,a}$ one control signal and the coil current monitoring signal U_r). To provide a controlling digital signal with an accurate frequency while obtaining accurate readings from the multi-channel analogue inputs, a multifunction NI USB-6255 DAQ board was used. The NI USB-6255 DAQ board has eighty 16-bit analogue inputs with a maximum scanning rate of 1.25MS/s and twenty-four digital I/O channels, which satisfies the requirement of the IFT system.

6.2.1 Parallel processing of signal acquisition and data storage based on a graphical program

LabVIEW is a graphical programming platform which provides many built-in functions, making it easier for programmers to develop stand-alone applications. Specifically, LabVIEW uses so-called dataflow programming that appears as a circuit wiring diagram. The results of wiring the required function blocks together can be seen immediately. It can be considerably quicker and more efficient for multi-task parallel execution than using conventional program languages such as C or C++. The program developed in this way for the IFT system comprised three modules: data acquisition, data storing and coil excitation, labelled A to C, respectively, in Fig. 6-1.

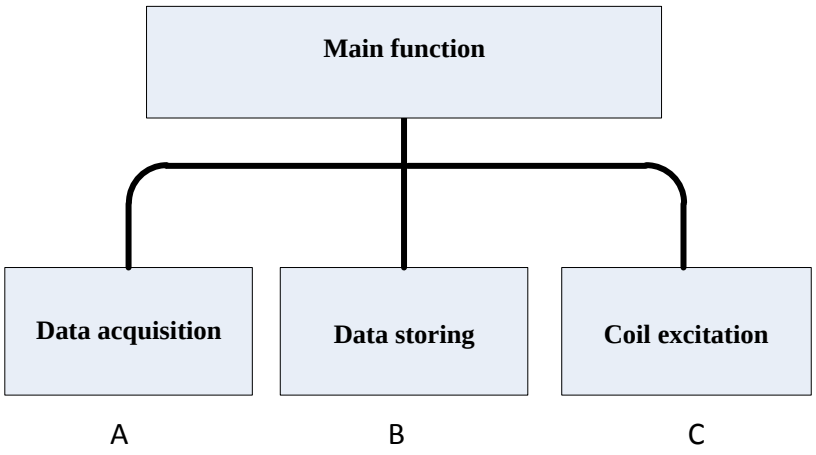

Fig. 6-1 Framework of IFT LabVIEW based software

To collect and record the signals simultaneously, it was necessary to produce a general structure which contained multiple parallel loops. In this case, a basic programming pattern, the so-called 'producer and consumer' method, was used to generate functions A and B (data acquisition and storage). The major advantage of the 'producer/consumer loop' pattern design is that all data collected in the producer loop could be queued in a buffer until the data were processed in the consumer loops. This pattern is capable of not only capturing data, but also ensuring no data were lost. For applications where a rapidly varying flow velocity measurement is required, it is important that the electrical potential signal can be obtained without losing any samples. Note that this can be achieved only if the computer has an adequately sized buffer. However, in such applications, size of buffer is not the only factor of concern, the efficiency of the program also depends upon how the logic loops and sub-functions are used.

In the present investigation, the producer loop was used to acquire electrical potential signals at a rate of 1000 samples/sec. Because the accuracy of data collected from seventeen analogue input signals might be affected by the execution time of the data acquisition function, the DAQmx sub-functions were configured as a data acquisition module (see Fig. 6-2), as this provided greater efficiency of data acquisition than the general application, because it did not have to initialise after every cycle of the loop.

The data collected from the data acquisition module were continuously placed in a queue in the same order as the actual signals. Referring to the setting shown in Fig. 6-2, the producer loop placed two seconds' worth of data (about 2000 samples) in the buffer, which contained fifteen electrical potential difference measurements $U_{j,a}$, one control signal from the DAC output of NI DAQ board and the voltage U_r across the precision resistor.These data samples were then fed into a built-in function, 'Write To Measurement File.vi', in the consumer loop. This function saved the data samples as a text-based measurement file which contained data acquisition information such as sampling frequency, time interval of samples and analogue input channel number. From the saved data files, the stored signals were used for further analysis, using MATLAB, to investigate the boundary potential distribution on the 16 electrodes. The way in which the voltage signals $U_{j,a}$ output from potential difference measurement circuits and the coil current monitoring signals through the precision resistor U_r could be used together to produce

sixteen compensated potential difference measurements $U_{j,cp}$ is discussed in Section 6.3. Note that the electrical potential difference measurements requires only fifteen analogue inputs because the value of U_5 is by definition equal to zero.

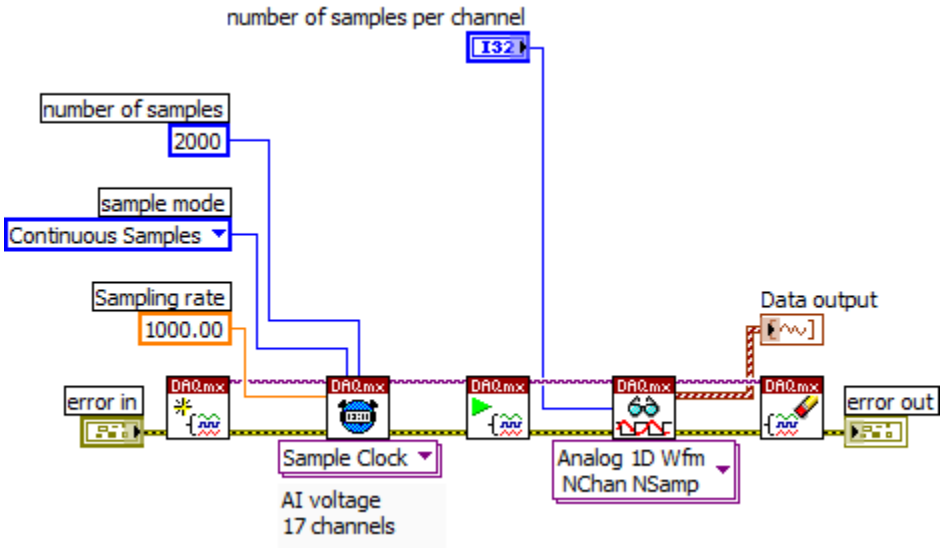

Fig. 6-2 Signal acquisition block diagram with DAQmx code

6.2.2 Coil excitation signal control program

As mentioned in Section 5.3.1, the Helmholtz coil configuration used to generate a magnetic flux density in the flow cross-section used the hybrid pulsed-DC excitation method. The excitation frequency is extremely important for the IFT system. Before explaining the software design for coil excitation, the choice of excitation frequency needs to be discussed. This depends upon the following considerations:

- *Displacement current*

When the conductive fluid passes through a magnetic field, the electric current density in the pipe cross-section can be expressed as:

$$J_{total} = J_D + J_C \qquad \text{Equation 6-1}$$

where J_C is called the conduction current density, and J_D is the displacement current density.

In practice, the displacement current is difficult to detect and, to avoid adverse effects on the measurements, the conduction current density J_C must be much greater than J_D. The expression for this is given in Equation 6-2 and Equation 6-3.

$$J_D << J_C \qquad \text{Equation 6-2}$$

Equation 6-2 can be re-written as:

$$\varepsilon_0 \varepsilon_r \omega E << \sigma_w E \qquad \text{Equation 6-3}$$

where E is the electric field, σ_w is the conductivity of water, ε_0 is the permittivity of vacuum and ε_r is the relative permittivity of the water [107]. Given, ω is the angular frequency of the excitation signal ($2\pi f$), we obtain from Equation 6-3:

$$f << \frac{\sigma_w}{2\pi\varepsilon_0\varepsilon_r} \qquad \text{Equation 6-4}$$

In Equation 6-4, the conductivity of pure water σ_w is 5×10^{-6} S/m, [108] ε_0 =8.855×10^{-12} F/m and $\varepsilon_r = 78.3$ [109]. Thus, Equation 6-4 can be rewritten as:

$$f << 1147.7\,\text{Hz} \qquad \text{Equation 6-5}$$

From the result of this computation, the excitation frequency must be much smaller than 1147.7 Hz. In the present study, the effective coil excitation frequency of the hybrid pulse DC excitation technique that was employed was set equal to 0.5Hz, which is much smaller than 1147.7Hz. Furthermore, the water conductivity used in the experiments was 1.5×10^{-2} S/m, which is much greater than the conductivity of pure water, 5×10^{-6} S/m, as shown in Equation 6-4. Consequently, the displacement current density J_D can be totally ignored in the present investigation.

- *Counter-electromotive force interference*

As seen in Fig. 5-6, when the magnetic field is turned on or off (S1 to S2 or S3 to S4), there is a noise-induced voltage signal called a counter-emf present in the measured flow signal, and this noise is generated in the direction opposite to the original magnetic field. The major reason why this noise is generated by the IFT system is that the electrode cable loops cannot be perfectly

parallel to the local direction of the magnetic field. According to Lenz's law, this noise can be expressed as:

$$e_w = -\frac{\partial B}{\partial t} \qquad \text{Equation 6-6}$$

It is apparent by inspection of Equation 6-6 that the magnitude of the counter-emf noise can be reduced by lowering the rate of change of the time varying magnetic field.

Another factor that needs to be considered is that the electrical potential difference measurements should not be measured or analysed until after the magnetic flux density reaches its constant value. Generally, the transient time of signal is approximately 5τ where τ is the Helmholtz coil time constant (see Section 5.2.2). To ensure that the signals are of sufficient length to take an adequate number of samples when the magnetic field is turned on or off, the time of each segment (S1, S2, S3 and S4) needs to be longer than 5τ. Note that the counter-emf noise occurs during the transient periods. It was found to be necessary to increase the duration of the ON time of the magnetic field to 0.5 seconds to ensure a steady signal for an adequate time. Note that this value of duration of ON or OFF time is used in the experimental investigation.

As a result of these considerations, and with the experience of taking observations, it was decided that the excitation frequency would be 0.5Hz (periodicity 2sec) (see Equation 6-5). It was decided that the time the magnetic field was ON (S1 and S3) and OFF (S2 and S4) should be four intervals, each of 0.5sec, which gives sufficient data points for accurate electrical potential difference measurements during the periods of constant magnetic flux density.

As mentioned in Section 6.2.1, with the sampling frequency of 1000Hz there are about 2000 data points collected in any one complete cycle (S1 to S4) of the signal. By removing the data collected during the transient times, there are 375 data points for each ON-time and OFF-time, which is much higher than for the previous electromagnetic flowmeter (i.e. the seven pixels EMFM device) [1].

Knowing the excitation frequency and duration of each segment, the program for the Helmholtz coil excitation was developed based on a while-loop structure. The programming flow chart for the coil excitation routine is shown in Fig. 6-3.

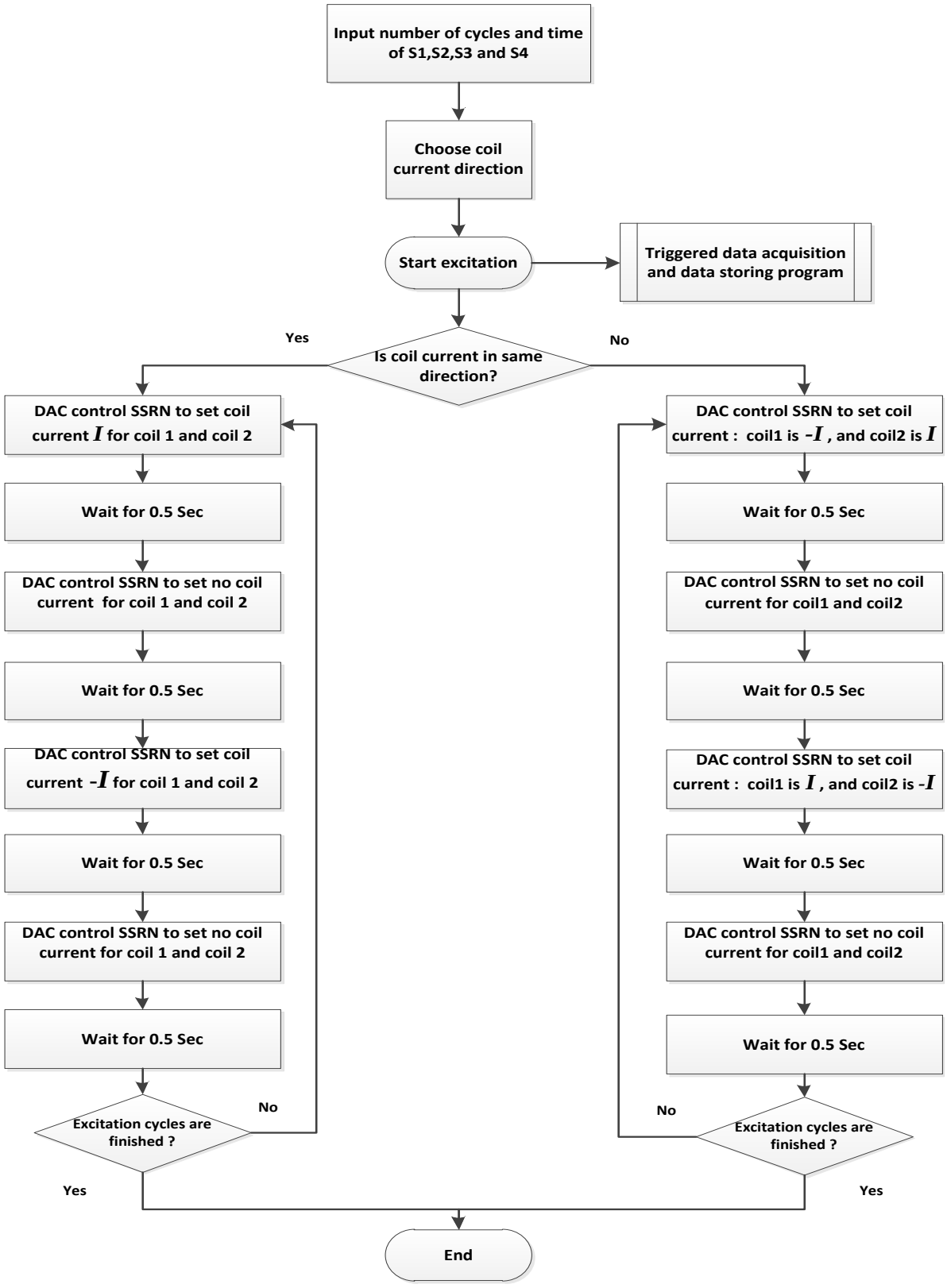

Fig. 6-3 Coil excitation routine

Before the program is executed, the number of complete excitation cycles (each cycle consisting of stages S1 to S4), which represents the total period of coil excitation, is entered into the control panel of the main interface. In addition, by using ‘case structure’, the program will decide to run either configuration 1 or configuration 2, which represents coil currents in the ‘same direction’ or in ‘opposite directions’, respectively. Once the ‘start excitation’ button is pressed, the coil excitation program starts running, and also triggers other subsidiary programs, such as data acquisition and storage.

As mentioned earlier, each excitation cycle contains four segments (S1 to S4). In order to construct a full hybrid pulsed DC excitation signal, the coil excitation program needs to change the status of the digital outputs in a certain order. In this case, a flat sequence structure was used to execute the digital output sub-program according to truth Table 5-1. The LabVIEW program for the routine is shown in Fig. 6-4. Note that the time delay function was used to achieve the time of 0.5sec for each segment.

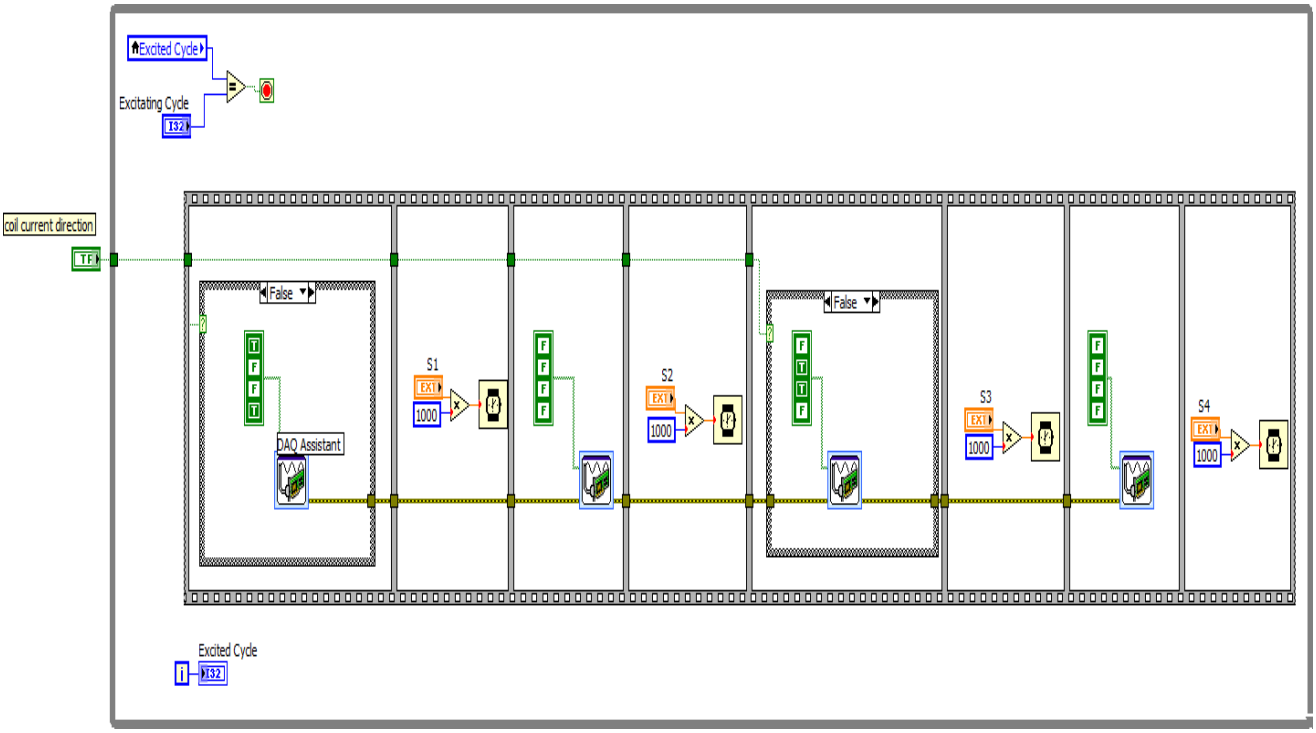

Fig. 6-4 LabVIEW program for coil excitation routine

6.3 Procedures for processing the measured IFT data

From the description of the data storage program given in Section 6.2.1, it is clear that a saved data file contains seventeen analogue signals, including the fifteen amplified electrical potential differences $U_{j,a}$ one control signal and one coil current monitoring signal U_r (see Section 5.3). In the present study, MATLAB-based signal processing software was developed which was used to determine averaged flow induced electrical potential difference U_j from the saved data files. Chapters 3 and 4 describe how these sixteen electrical potential differences U_j (including $U_5 = 0$) are used for further analysis to reconstruct the local velocity distribution. The analysis of the measured electrical potential differences and the coil current monitoring signal U_r is described below.

The first stage of the signal analysis was to divide one cycle of each measured electrical potential difference signal $U_{j,a}$ into four segments, denoted S1 to S4, as shown in Fig. 6-5. Note that τ_t is the transient time. As mentioned earlier, the transient portions of the signal are not included in the analysis. Thus, associated with each segment *Sm* (where m = 1, 2, 3 or 4) was a time period t_m (m=1, 2, 3, or 4) which represents the time over which useful (non-transient) data can be sampled. The value of $U_{j,a}$ during the times t_m in segments 1, 2, 3, and 4 is denoted $(U_{j,a})_1$, $(U_{j,a})_2$, $(U_{j,a})_3$ and $(U_{j,a})_4$ respectively. Because the output signal from the potential difference measurement circuit has a bias voltage, which was described in Section 5.3.3, the value of $(U_{j,a})_1$ is given by:

$$(U_{j,a})_1 = A_2 A_1 U_j^+ + U_{BV} \qquad \text{Equation 6-7}$$

where U_j^+ the maximum is the value of the potential difference between electrode e_j and e_5 during the time period t_1 and $A_2 A_1$ is the total gain of the potential difference measurement circuit.

By taking the average of $(U_{j,a})_1$ for time period t_1, the averaged measured electrical potential difference for the first segment S1 can be expressed as:

$$(\overline{U}_{j,a})_1 = A_2 A_1 \overline{U}_j^+ + \overline{U}_{BV} \quad \text{Equation 6-8}$$

where $\overline{U}_j^+$ is the averaged value of U_j^+ for the time period t_1 and $\overline{U}_{BV}$ is the average value of U_{BV} during the time period t_1 .

Note that this process is repeated fifteen times (i.e.= 1 to 4 and 6 to 16). The measured potential differences during segments S2 and S4 are both equal to the bias voltage experienced when the magnetic field is off. The respective expressions are shown in Equation 6-9 and Equation 6-10.

$$(U_{j,a})_2 = U_{BV} \quad \text{Equation 6-9}$$

$$(U_{j,a})_4 = U_{BV} \quad \text{Equation 6-10}$$

The average potential difference measurement for the second segment $(\overline{U}_{j,a})_2$ is determined by averaging a number of samples of $(U_{j,a})_2$ over time period t_2. In the same manner, the average potential difference measurement for the fourth segment $(\overline{U}_{j,a})_4$ is determined by averaging a number of samples $(U_{j,a})_4$ over time period t_4. These can be written as:

$$(\overline{U}_{j,a})_2 = \overline{U}_{BV} \quad \text{Equation 6-11}$$

$$(\overline{U}_{j,a})_4 = \overline{U}_{BV} \quad \text{Equation 6-12}$$

$(U_{j,a})_3$ is the electrical potential difference, at segment S3, while the magnetic field is in a negative direction. Thus, $(U_{j,a})_3$ is given by:

$$(U_{j,a})_3 = A_2 A_1 U_j^- + U_{BV} \quad \text{Equation 6-13}$$

where U_j^- is the minimum value of the electrical potential difference during the time period t_3. The average potential difference, $(\overline{U}_{j,a})_3$, is calculated by:

$$(\overline{U}_{j,a})_3 = A_2 A_1 \overline{U}_j^- + \overline{U}_{BV} \qquad \text{Equation 6-14}$$

where $\overline{U}_j^-$ is the averaged value of U_j^- for the time period t_3 and $\overline{U}_{BV}$ is the average value of U_{BV} during the time period t_3.

In order to evaluate the flow induced electrical potential difference U_j between e_j and e_5 for a given cycle, the bias voltage $\overline{U}_{BV}$ must be removed. This can be achieved by ensuring that $(\overline{U}_{j,a})_2$ and $(\overline{U}_{j,a})_4$ are subtracted respectively from $(\overline{U}_{j,a})_1$ and $(\overline{U}_{j,a})_3$, as:

$$(\overline{U}_{j,a})_1 - (\overline{U}_{j,a})_2 = A_2 A_1 \overline{U}_j^+ \qquad \text{Equation 6-15}$$

$$(\overline{U}_{j,a})_3 - (\overline{U}_{j,a})_4 = A_2 A_1 \overline{U}_j^- \qquad \text{Equation 6-16}$$

The final required electrical potential difference U_j is given by:

$$U_j = \frac{\left|(\overline{U}_{j,a})_1 - (\overline{U}_{j,a})_2\right| + \left|(\overline{U}_{j,a})_3 - (\overline{U}_{j,a})_4\right|}{2A_2 A_1}$$

Equation 6-17

From Equation 6-15 and Equation 6-16 it is clear that the value of U_j given by Equation 6-17 can also be written as:

$$U_j = \frac{\left(\left|U_j^+\right| + \left|U_j^-\right|\right)}{2} \qquad \text{Equation 6-18}$$

Consequently, the value of U_j obtained from the potential difference measurements, and calculated according to Equation 6-17, represents the mean flow induced potential difference between electrodes e_j and e_5 over the relevant excitation cycle.

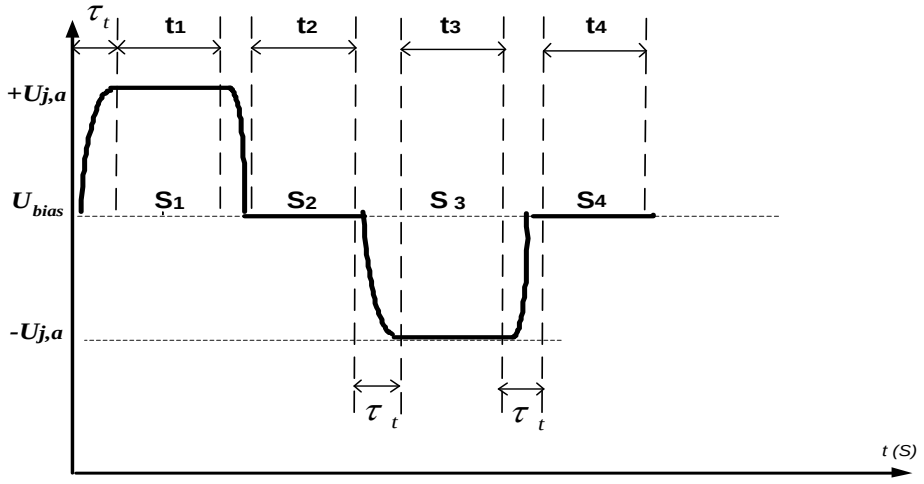

Fig. 6-5 One cycle of averaged electrical potential difference signal, $U_{j,a}$

Once all the U_j values (= 1 to 4, 5 to 16) for a given cycle have been calculated, these values have to be compensated by the corresponding value of U_r to take into account the effects of coil temperature on the magnetic flux density as described in Section 5.3.2. The next step is to perform an analysis of U_r for a given cycle.

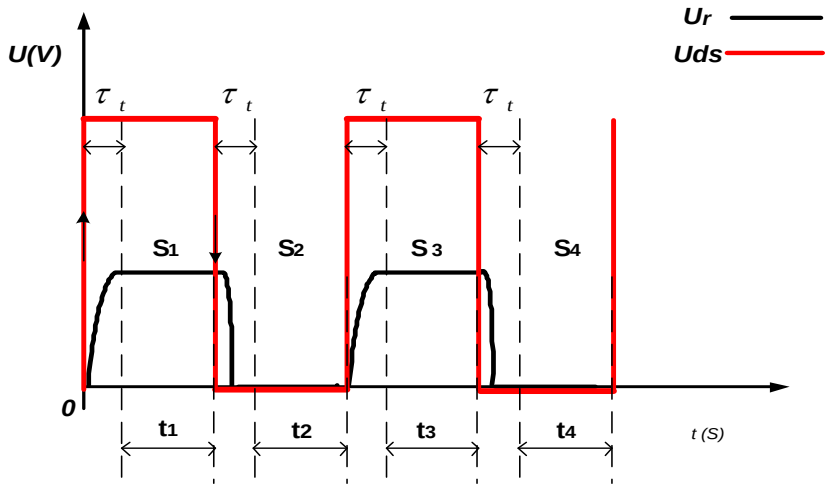

Fig. 6-6 Coil current signal U_r and 'square wave' digital control signal for one cycle

Referring to Section 5.3.2, the output signal U_r from the coil current monitoring circuitry can also be considered as being divided into four segments, S1, S2, S3 and S4, as shown in Fig. 6-6. As explained in Section 5.3.2, it is known that the coil current value of I_c is numerically equal to the value of U_r. In Fig. 6-6, the combined digital control signal, DAC0 + DAC1, is considered as a simple square wave, denoted 'U_{ds}' and can be measured for each cycle. By taking the gradient of the square wave signal, U_{ds}, the rising edge of the excitation signal can be located at the point where the value of $\frac{dU_{ds}}{dt}$ is much greater than the previous value. The gradient of U_{ds} is effectively zero while U_{ds} maintains a constant level. The decreasing edge of the excitation signal will be located at the point where the value of $\frac{dU_{ds}}{dt}$ suddenly becomes negative. Note that the amplitude of the square wave signal U_{ds} alternates at a fixed frequency (i.e. 0.5Hz) between zero and five volts.

The gradient of U_{ds} can be described by the equation:

$$\frac{dU_{ds}}{dt} \approx \frac{U_{ds,N+1} - U_{ds,N}}{\Delta t} \qquad \text{Equation 6-19}$$

where is the N^{th} data sample, and Δt is the sampling interval between consecutive data samples.

Once the time index of the rising and decreasing edges of the excitation signal is established, then the time intervals t_1, t_2, t_3 and t_4 shown in Fig. 6-6 can be determined. During the signal processing, the transient time τ_t of the signal was defined as 0.125sec.

After the time index values for each segment, t_1, t_2, t_3 and t_4 of the excitation cycle are established, the averaged coil current value U_r can be obtained by using Equation 6-20.

$$U_r = \frac{\left|(\overline{U}_r)_1 - (\overline{U}_r)_2\right| + \left|(\overline{U}_r)_3 - (\overline{U}_r)_4\right|}{2} \qquad \text{Equation 6-20}$$

where $(\overline{U}_r)_m$ represents the mean value of U_r during the time t_m associated with the m^{th} stage of the excitation cycle..

Referring to Equation 5-9 in Section 5.3.2, since the coil current U_r is proportional to magnetic flux density $\overline{B}$ it is apparent that the potential difference U_j given in Equation 6-18 is also proportional to the coil current U_r. Thus, the relationship between U_j and U_r can be expressed as:

$$\frac{U_{r,ref}}{U_r} = \frac{U_{j,cp}}{U_j} \qquad \text{Equation 6-21}$$

where $U_{r,ref}$ is the coil current signal at the initial coil temperature, U_r is the measured coil current for a given cycle, U_j is measured electrical potential difference for a given cycle and $U_{j,cp}$ is the compensated electrical potential difference which would occur at the reference magnetic flux density at the initial temperature. The compensated electrical potential difference U_j can be expressed as:

$$U_{j,cp} = \frac{U_{r,ref}}{U_r} U_j \qquad \text{Equation 6-22}$$

After the analysis described above, the compensated electrical potential difference measurements $U_{j,cp}$ for a given cycle are obtained. The procedure described above is then repeated for all G cycles. This gives a $16 \times G$ square matrix (i.e. includes $U_5 = 0$).

From reviews of previous research into EVP results [1], it was seen that, for vertical single phase water-only flow, the potential difference measurements for each cycle have small variations due to white noise produced by the analogue electronic circuitry. It was also found that the accuracy of the reconstructed water velocity profiles could be adversely affected if this noise significantly contaminated the main signals. In order to improve the accuracy of the velocity reconstruction results, the compensated electrical potential difference $U_{j,cp}$ was averaged over G cycles to reduce the effects of the random noise. During the present investigation, the appropriate number of excitation cycles was found to be 30. Thus, the total excitation time period was 60 seconds. The j^{th} compensated potential difference averaged over 30 cycles is given by:

$$\overline{U}_{j,cp} = \frac{1}{G}\sum_{g=1}^{g=G}(U_{j,cp})_g \qquad \text{Equation 6-23}$$

where G=30

These values of $\overline{U}_{j,cp}$ were used in the reconstruction algorithms given in Chapter 3 and 4 to reconstruct the velocity profile of the conducting continuous phase, averaged over a time period of 60 seconds.

The flow chart of the signal processing software for the procedures given above is shown in Fig. 6-7.

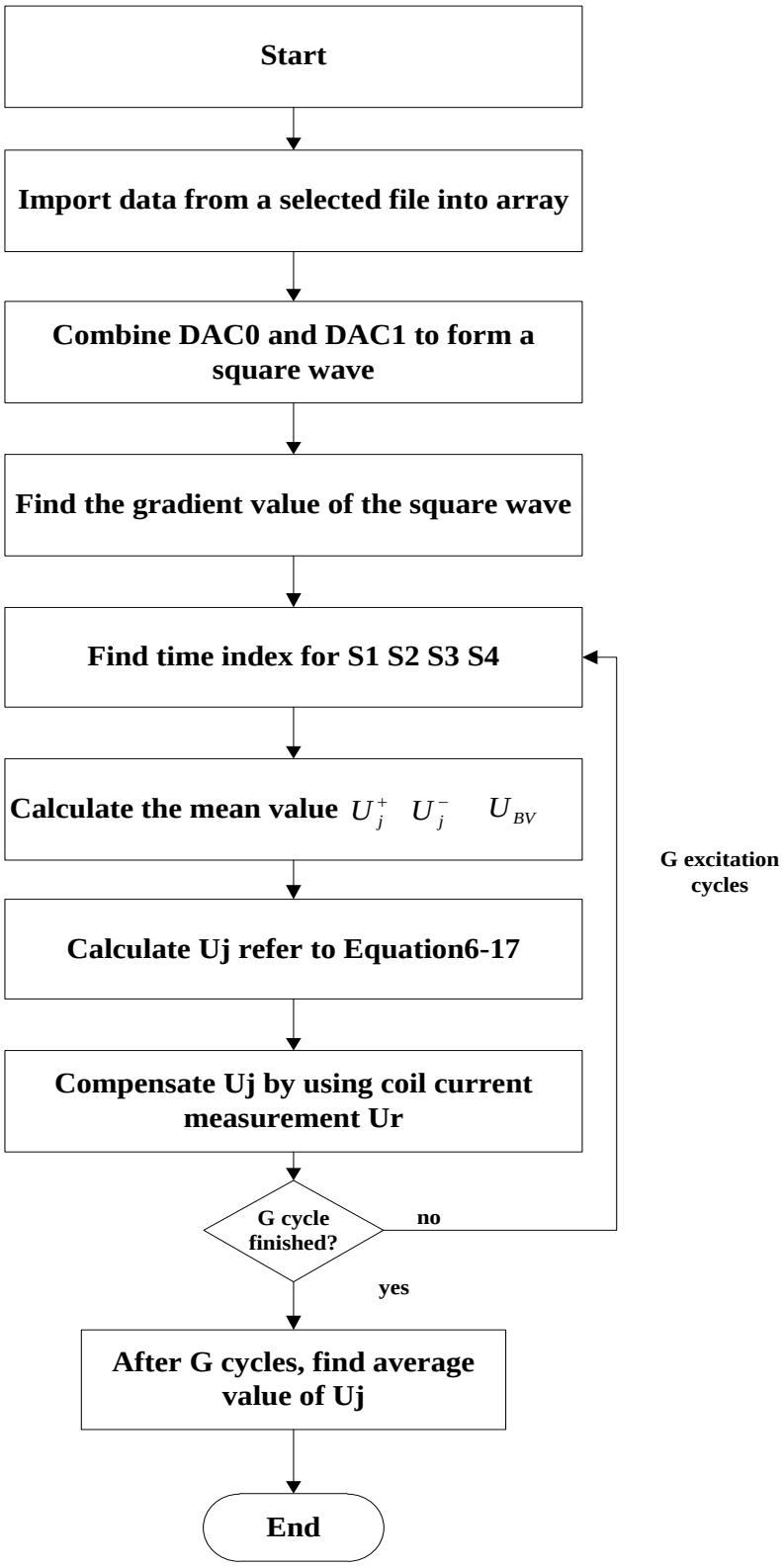

Fig. 6-7 Flow chart of signal processing software

6.4 Summary

To collect and measure the electrical potential differences $U_{j,a}$ the data acquisition and data storing programs were designed in a LabVIEW software environment. The programs were capable of continuously collecting the voltage signals $U_{j,a}$ and U_r with a 1000Hz sampling frequency and saving all the data points into a text file for further offline analysis.

This chapter has described the coil excitation program routine, also written in the LabVIEW programming language, and the procedures for selecting the excitation frequency for the IFT system. The coil excitation routine was constructed by using several built-in functions, such as 'case structure' and 'while loop'. The coil excitation program is capable of generating a sequential digital signal which controls the 'H' bridge solid-state relays to create a hybrid pulsed DC magnetic flux density in the flow cross-section.

To analyse the acquired data in the text file, a signal processing program was developed in MATLAB. The compensated electrical potential differences $U_{j,cp}$ were calculated from the original measured signals $U_{j,a}$ and the coil current monitoring signal U_r. In order to improve the accuracy of the results for further velocity reconstruction, the final result of the electrical potential difference was calculated by averaging 30 cycles of compensated electrical potential differences $U_{j,cp}$. It should be noted that the analysis program described above was used for all the experiments described in Chapter 7.

7 Experimental tests of IFT and analysis of results

7.1 Introduction

After the construction of the IFT system (see Chapters 5 and 6), it was necessary to verify the IFT multiphase velocity measurement technique via a series of multiphase flow experiments, including axisymmetric and non-uniform velocity profiles of air-in-water two phase, and oil-gas-water three phase flows. In order to satisfy such requirements, the flow loops used in the investigation must have certain features. For example, each flow loop must be able to provide three phase or two phase flows with the desired flow rates and with a working section that can be inclined at different angles to vertical in order to achieve highly non-uniform continuous phase velocity profiles in multiphase flows. To evaluate measurement accuracy, several reference flowmeters were used as a means of producing reference measurements, including a commercial EMFM flowmeter, a turbine flowmeter and a thermal mass flowmeter.

To estimate the accuracy of local water velocity distributions, as measured by the IFT flowmeter, a further set of experiments was performed using the "flow magnetic resonance imaging" (MRI) technique to provide a reference measurement of the local water velocity distribution for air-in-water two phase flow. However, there were limitations of the Flow MRI experimental apparatus, so that both the IFT and MRI flow metering techniques could be compared only for vertical flow (see Fig. 7-3). Because the MRI and ERT flow measurement techniques were developed at different universities, their working principles will be briefly described separately in Sections 7.3.2 and 7.3.3, respectively.

The objective of the first series of experiments described below was to determine the accuracy with which the IFT flowmeter can practically determine the local water velocity distribution in vertical and inclined oil-gas-water three phase flow.

The second series of experiments compared the local water velocity distributions obtained using MRI measurements and with the IFT system in vertical flows.

7.2 Multiphase flow loop facility

7.2.1 Multiphase flow loop in the Schlumberger Gould Research (SGR) Centre

The first set of experiments described in the present investigation was performed using the multiphase flow loop at the laboratories of Schlumberger Gould Research Centre in Cambridge. One of the features for this flow loop is that the working section can be inclined through various angles θ from the vertical ($0^0 \leq \theta \leq 90^0$) (see Fig. 7-1), allowing vertically upward and upward-inclined flows to be established.

With reference to the schematic diagram of this flow loop shown in Fig. 7-1, it can be seen that the flow loop is capable of generating oil-gas-water three phase flows. The working section is 10 meters long with a 50mm diameter bore. To ensure that the flow velocity profile was fully developed, the flowmeter devices relevant to this study were installed at least 10 pipe diameters downstream of the working section inlet. Degassed kerosene (oil) with an average density of 800kg/m^3 was pumped into the base of the working section through two turbine meters (measurement ranges 2.3-23.3m^3/hr and 20-201m^3/hr, respectively), which were used to determine the oil flow rate. The oil flow rate could be set to specific values by adjusting the appropriate control valve or varying the appropriate pump speed.

Similarly, the water flow rate could be controlled using the appropriate water pump and/or adjusting the appropriate control valve. The water flow rate was measured using one of two conventional EMFM flowmeters with measurement ranges 2.4-24m^3/hr and 14-141m^3/hr, respectively, after which the water flowed into the working section. The conductivity of the water used in the present investigation was 1.5×10^{-2} S/m.

Nitrogen gas with density of 1.25kg/m^3 was supplied from a gas tank and piped into the working section via a thermal mass flowmeter and control valve. This allowed the gas mass flow rate in the working section to be determined. By means of a PID control valve, the gas flow rate could be set to an appropriate value. Note that the measurement range of the thermal mass flowmeter is 0-250scfm (standard cubic feet per minute).

After the mixed fluids passed through the working section, the three phase flow was piped into a separator, which separated the flow into individual components and the Nitrogen gas was vented to atmosphere. Once the oil and water were separated in the separator tank, they again become available for pumping around the flow loop, as described above.

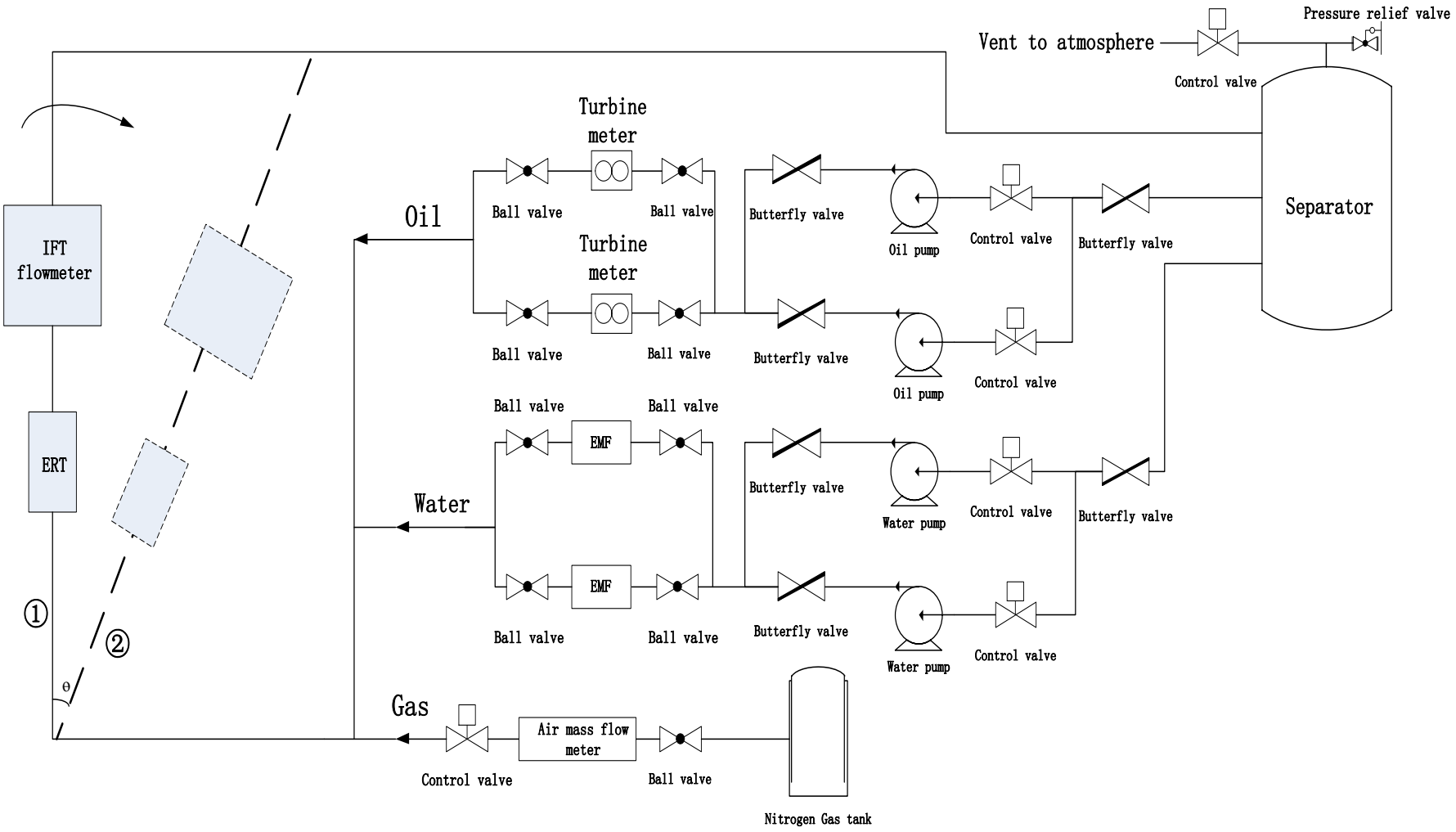

Fig. 7-1 Diagram showing the features of the multiphase flow loop in SGR [110]. Note that: ① represents flow loop working section in vertical position. ② represents flow loop working section inclined at an angle ɵ to the vertical

(a) IFT system at vertical position

(b) IFT system inclined at 30 º to vertical

Fig. 7-2 Photographs of the Schlumberger Gould Research (SGR) multiphase flow loop. ①Mounting position of the IFT flowmeter ② working section with 50mm diameter bore

7.2.2 Vertical two phase flow loop in the Magnetic Resonance Research Centre (MRRC) of the University of Cambridge

The University of Cambridge flow loop is shown in Fig. 7-3 and Fig. 7-4 and is capable of delivering water-only single phase flow and gas-in-water two phase flows with water as the continuous phase. In the present study, only vertical upward two phase flows were investigated. Fig. 7-4 shows the flow loop with its vertical working section with the IFT device and the Flow MRI installed (see Section 2.3.2). The working section of the pipe is approximately 4 meters long with an internal diameter of 50mm.

The water is stored in a portable tank and fed to the flow loop using a centrifugal pump. The water flow rate is measured using a turbine flowmeter prior to mixing with the gas phase. However in practice, because there was not a sufficient number of straight pipe lengths upstream of the turbine meter to ensure a fully developed turbulent flow profile, the accuracy of the water volumetric flow rate readings obtained from the turbine flowmeter could have been affected.

The gas is supplied by the laboratory air supply using a regulator with an outlet pressure of 0.5 bar gauge pressure. The air flow rate is measured with a rotameter before being mixed with the water via a vertical section of capped brass tube with a number of 1mm holes drilled into it. Fig. 7-3 shows that the water and air flow rates could be varied by adjusting the position of valves 1 and 2, respectively.

Two pressure tappings are included in the flow loop working section, 1.5m apart, to measure the pressure differential across the imaging region to enable a reference measurement of the mean gas volume fraction $\overline{\alpha}_g$ of the air-water mixture to be obtained (see Section 7.3.1). A clear section of pipe was also incorporated to allow for visual observation of the regime of the flowing air-water mixture.

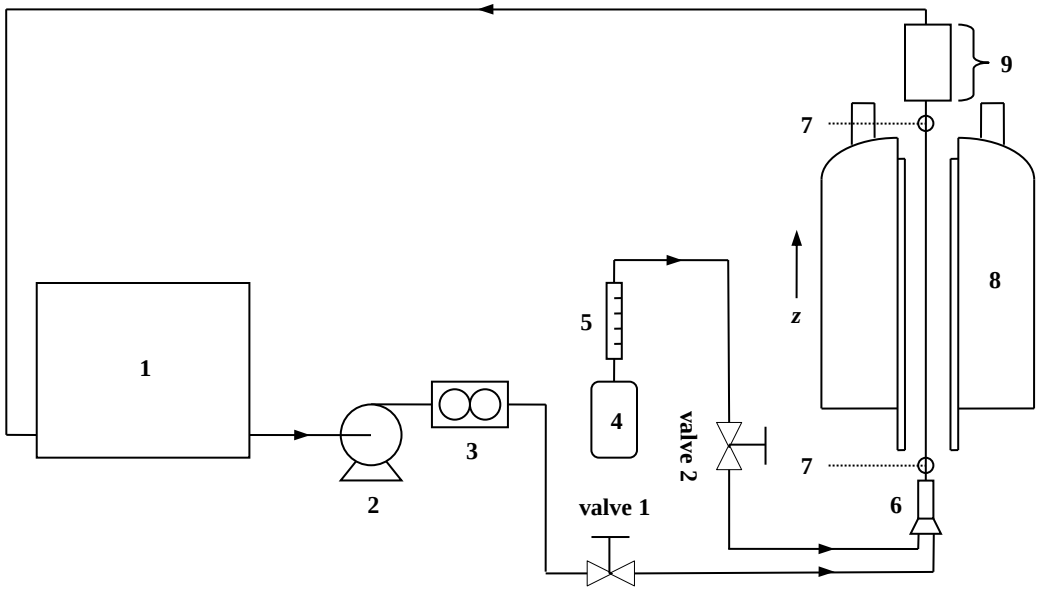

Fig. 7-3. Schematic of MRRC flow loop at the University of Cambridge. 1) storage tank; 2) pump; 3) liquid flowmeter; 4) compressed air feed; 5) gas rotameter; 6) mixing section; 7) differential pressure tapping; 8) MRI system; 9) IFT sensor with clear section of pipe for visual observation.

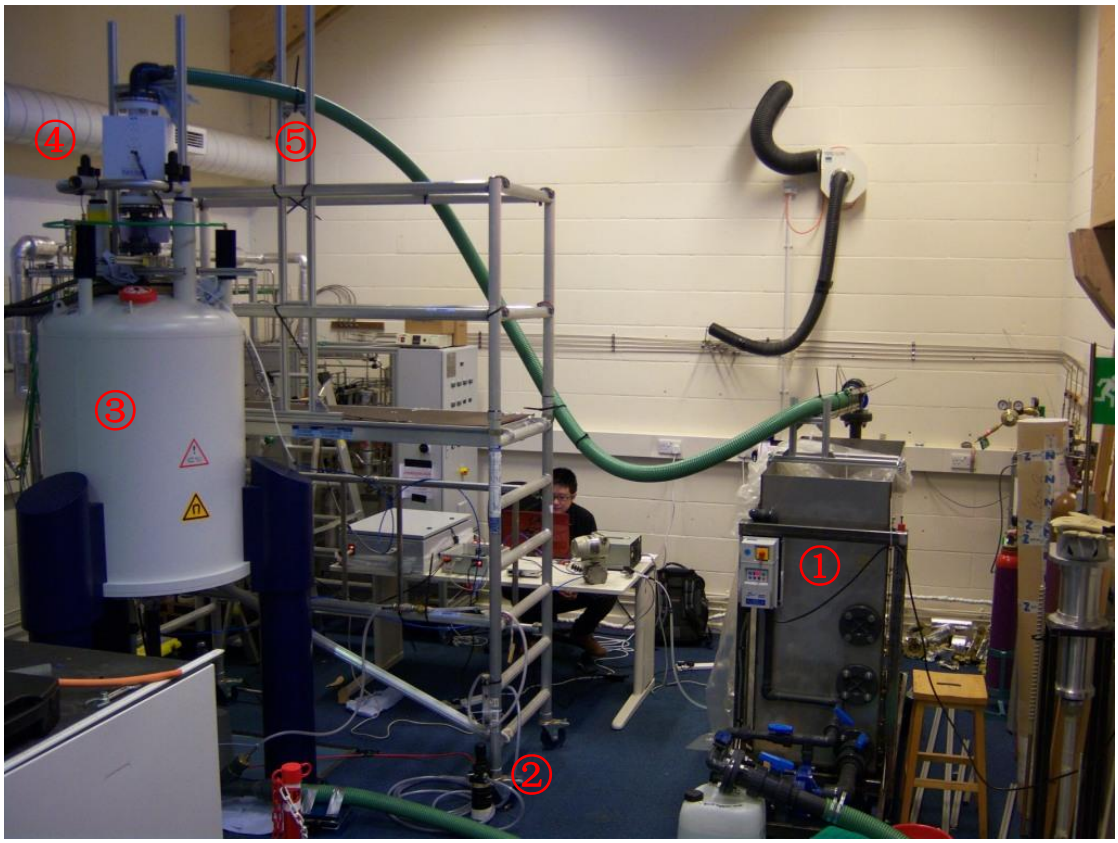

Fig. 7-4 The modular flow loop with vertical working section and with IFT and MRI installed. 1) storage tank, 2) compressed air feed, 3) MRI system, 4) IFT flowmeter, 5) return line to tank.

7.3 Reference flow measurement techniques used in the present experimental investigation

This section describes the reference flow measurement techniques used in this investigation. These techniques comprised:

1) Differential pressure measurement for determining the mean volume fraction of the dispersed gas in the air-water two phase flows. This technique was used only for determining gas volume fraction in gas-in-water two phase vertical flows (see Section 7.2.2).

2) Electrical Resistance Tomography (ERT) was used to determine the local volume faction distribution of the dispersed phases (oil and gas). Note that this technique was used only in the experiment undertaken at SGR (see Section 7.2.1).

3) As mentioned earlier, MRI was used for determining the local axial velocity distribution in the experiments at the UoC(University of Cambridge) flow loop. The obtained results are compared with the results obtained from the IFT system.

7.3.1 Differential pressure technique

For the experimental investigation undertaken at UoC, the differential pressure technique was used to determine the mean gas volume fraction $\overline{\alpha}_g$ in gas-in-water two phase flows. As described in the previous section, there were two pressure tappings sited in the wall of the pipe and separated by a vertical distance L of 1.5 meter (see Fig. 7-5). These pressure tappings were connected to a Honeywell differential pressure transducer through water-filled lines (coloured purple in Fig. 7-5). Note that the output signal of the DP transducer was 4-20 mA. By using a current-to-voltage converter circuit, the voltage output was from 1-5 V.

In this part of the investigation, the working section was vertical only. With reference to Fig. 7-5, it is possible to write that the differential pressure ΔP measured by the DP cell is given by:

$$\Delta P = P_2 - P_1 + \rho_w g L \qquad \text{Equation 7-1}$$

where P_1 and P_2 are the static pressures at the upstream and downstream pressure tappings, respectively, ρ_w is the density of water and g is the acceleration due to gravity.

The relationship between P_1 and P_2 can be written as:

$$P_1 = P_2 + \rho_m g L + F_m \qquad \text{Equation 7-2}$$

where ρ_m is the mean density of the flowing fluid and F_m is the frictional pressure loss over the measurement length.

Combining Equation 7-1 and Equation 7-2 gives:

$$\Delta P = \rho_m g L - \rho_w g L - F_m \qquad \text{Equation 7-3}$$

The density of the water is much greater than the density of the gas (air), and so an approximate expression for the mixture density is:

$$\rho_m = (1 - \bar{\alpha}_g)\rho_w \qquad \text{Equation 7-4}$$

where $\bar{\alpha}_g$ is the mean gas volume fraction.

Substituting Equation 7-4 into Equation 7-3 gives:

$$\bar{\alpha}_g = \frac{\Delta P + F_m}{\rho_w g L} \qquad \text{Equation 7-5}$$

By inspection of Equation 7-5, it can be seen that it was necessary to determine the value of the frictional pressure drop F_m before calculating the volume fraction of the gas α_g. The following procedure shows how to determine the value of F_m. Following Cory [55] and Al-Hinai [13], the assumption is made that a single phase friction factor f could be used to calculate the frictional pressure loss in the present study. Based on the work of Cory and Al-Hinai, the frictional pressure loss for a circular pipe in a two phase flow, over an axial distance *L* can be written as:

$$F_m = \frac{2\rho_w L f U_h^2}{D} \qquad \text{Equation 7-6}$$

where U_h is the mixture superficial velocity, f is the friction factor and D is the pipe diameter.

The mixture superficial velocity can be expressed as:

$$U_h = \frac{Q_w + Q_g}{A}$$ Equation 7-7

where Q_w and Q_g are the water and gas volumetric flow rates, respectively, and A is the flow cross-sectional area.

In the present study, U_h was determined from measurements of Q_w and Q_g made using a turbine flowmeter and a rotameter. With reference to Cory [55], for the type of pipe used in these experiments a friction factor f equal to 0.0075 was assumed. Thus, the mean gas volume fraction $\overline{\alpha}_g$ was calculated from Equation 7-5, Equation 7-6 and Equation 7-7. The mean water volume fraction $\overline{\alpha}_w$ is given by $\overline{\alpha}_w = 1 - \overline{\alpha}_g$.

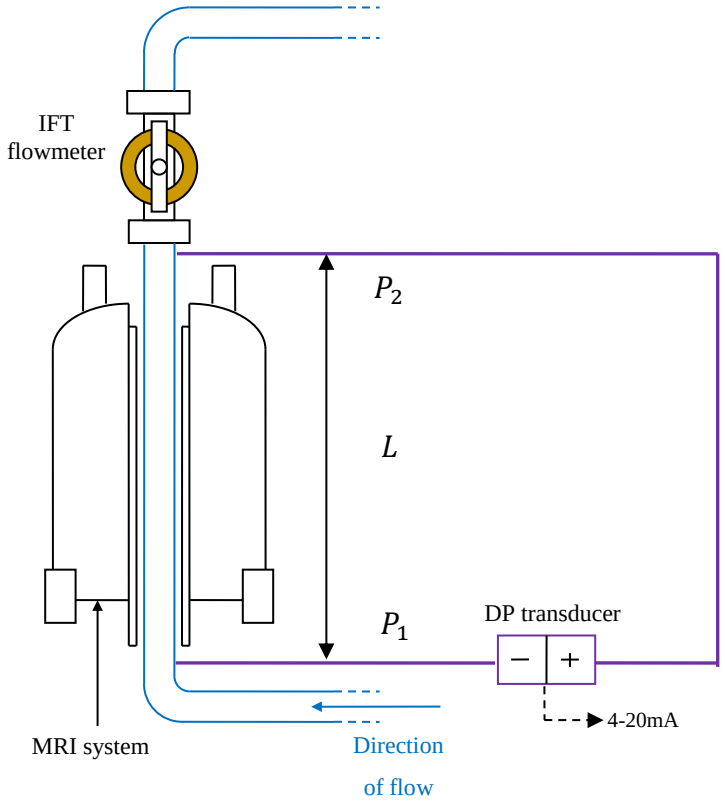

Fig. 7-5 Schematic of the differential pressure connections for measuring $\overline{\alpha}_g$ (see also item "7" in Fig. 7-3)

7.3.2 Electrical resistance tomography

The differential pressure technique described above can only be used to determine the mean volume fraction of each phase in two phase flow. However, referring to Equation 1-3, because the local water velocity distribution can be measured using inductive flow tomography (IFT), it is also necessary to determine the local volume fraction distribution of the continuous phase. In the present study, a dual-plane Electrical Resistance Tomography (ERT) system with a 50mm internal diameter was used to determine the local volume fraction of the dispersed phase. The local volume fraction of the continuous phase is given by $\alpha_{c,i} = 1-\alpha_{d,i}$ where $\alpha_{d,i}$ and $\alpha_{c,i}$ respectively represent the local dispersed phase and continuous phase volume fractions in the i^{th} subregion of the pipe cross-section. (note that i is the index of the sub-regions in the pipe cross-section), as shown in Section 1.2. By using the measurement of the local volume fraction distribution of the continuous phase $\alpha_{c,i}$ in conjunction with the reconstructed local water velocity profile, the volumetric flow rate of water Q_w can be obtained (see Equation 1-3).

The dual-plane ERT system used in the experiments at SGR consisted of sixteen wall-mounted electrodes on each plane (see Fig. 7-6a). One adjacent pair of electrodes was connected to an excitation source (15mA) and then the remaining electrodes were used to obtain the potential differences between every remaining electrode pair of adjacent electrodes or opposite electrodes (see Section 2.2.3). This procedure was repeated until a full rotation was completed, which formed a set of measurements. Using the related reconstruction algorithm [60], the electrical conductivity distribution in the flow cross-section was obtained. The local volume fraction distribution of the dispersed phase was then obtained from the conductivity distribution results based on Equation 2-1. In the present investigation, each individual local dispersed phase (gas and oil) volume fraction image result consisted of a 20×20 pixel array. The circular image was formed from 316 of the 400 pixels, forming a squared grid (see Fig. 7-6 (b)).

As mentioned in Section 1.4 and at the beginning of this section, the principle of a feasible multiphase flow measurement system comprises the dual plane ERT system in conjunction with the IFT system. The IFT system is used to obtain the local axial velocity distribution of the electrically conducting continuous phase. The local volume fraction distribution of the dispersed

phase obtained using the dual plane ERT system is used with the measured continuous phase velocity distribution to obtain the continuous phase volumetric flow rate, as shown in:

$$Q_w = \int_A (1-\alpha_{d,i}) v_{w,i} A_i \qquad \text{Equation 7-8}$$

where $\alpha_{d,i}$ and $v_{w,i}$ respectively represent the dispersed phase (oil and gas) volume fraction for the i^{th} region and the water velocity for the i^{th} region and A_i is the area of the i^{th} region. In order to integrate the $\alpha_{d,i}$ and $v_{w,i}$ measurements from the two devices, the sub-region arrangement of the ERT device, as shown in Fig. 7-6 (b), was adopted and was also used for results from the IFT device when ERT and IFT were used together. In Fig. 7-6 (b), the cross section is divided into 316 regions and so Equation 7-8 can be written in the terms of the 316 regions as:

$$Q_w = \sum_{i=1}^{316} (1-\alpha_{d,i}) v_{w,i} A_i \qquad \text{Equation 7-9}$$

As should be clear from above, in the experimental results shown in Section 7.5, the local water velocity profiles were reconstructed based on the ERT grid map given in Fig. 7-6 (b) (see also Fig. 7-22, Fig. 7-27).

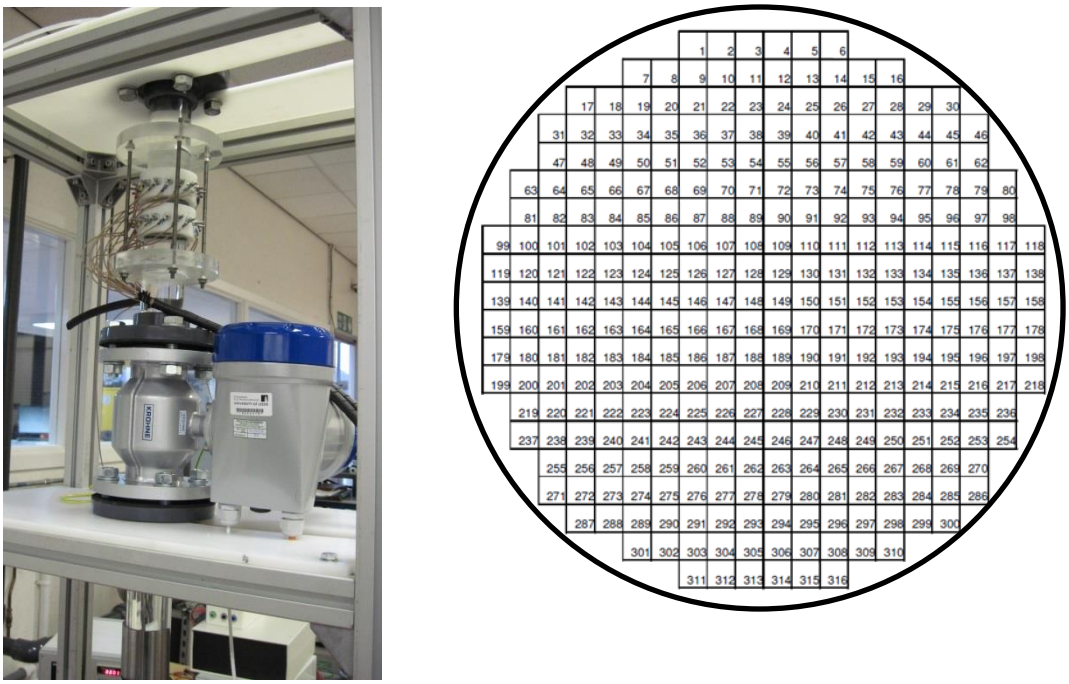

(a) (b)

Fig. 7-6 The dual-plane ERT flowmeter device used in the present study (developed and constructed by University of Leeds) (a) photograph of the ERT system, and (b) circular image with 316 pixels

7.3.3 Magnetic resonance imaging technique

This section briefly describes the magnetic resonance imaging (MRI) system used for the experimental tests at UoC. The working-section installed was as shown in Fig. 7-3, with the MRI system placed under the IFT system. The distance between the IFT and MRI imaging region was approximately equal to 1.3m, which meant the measurement plane of the MRI would have been slightly different to the measurement plane of the IFT system.

In the experimental testing, all MRI measurements were performed using a SWB-300 spectrometer (Bruker Instruments) operating at a ^{1}H frequency of 300MHz and a probe with an internal bore diameter of 65mm. Referring to Section 2.3.2, the technique by which the MRI velocimeter reconstructed the water's velocity profile is based on the phase-shift method [75, 77]. After some discussion with Magnetic Resonance Group (MRG) in UoC, it was decided that an appropriate method for obtaining the local water velocity image in multiphase flow would be

based on a time-averaged method, such as single-point imaging (SPI). More detail about this flow imaging method can be found in a paper by Gladden [77].

For the experimental investigation at UoC, the Flow MRI system can be used to obtain the local water velocity distribution in the flow cross-section for gas-in-water two phase flow. The measured local axial velocity distribution obtained by Flow MRI can be used to validate the reconstructed local axial velocity obtained by the IFT system.

For this experiment, the majority of the reconstructed MRI velocity images had a resolution of 16 ×16 pixels; a field-of-view of 60mm in both the *x* and *y* axis directions and a 10mm slice thickness in the *z* axis direction. Only small sets of images were acquired with the higher resolution of 32×32 pixels.

7.4 Correction of electrical potentials measurement, φ_j

Referring to Chapter 5, the body of the IFT flowmeter included three different removable parts (see Fig. 5-2). The sixteen electrode housings were placed at angular intervals of 22.5 º on the second part of the flow pipe and the line joining electrodes e_{13} and e_5 was intended to be perpendicular to coils 1 and 2 (see Fig. 3-20). However, in practical operation, as it was fitted, the central portion of the IFT was unexpectedly rotated through a small angle η (see Fig. 7-7), which resulted in the positions of the electrodes all moving through the same angle about the line (*y*-axis) joining the centres of the coils.

For some initial experiments with single phase flow (water-only) using the IFT system with this rotation angle η present, the electrical potential distribution φ_j on the pipe inner boundary obtained for four flow conditions f1 to f4 (in a uniform magnetic field) is shown in Fig. 7-8. It is worth noting that, for the convenience of investigation in this section, the compensated potential differences measurements $U_{j,cp}$ (see Section 6.3) were expressed as electrical potentials φ_j (j = 1 to 16) due to the electrical potential on e_5 being defined as equal to zero. Comparing Fig. 7-8 with Fig. 3-14 showing the potential difference distribution that is expected for an axisymmetric

velocity distribution, it is apparent that the minimum value of φ_j has moved from $j = 9$ to a new position near $j = 10$.

Referring to the conclusion made in the final section of Chapter 3, if the water velocity profile is axisymmetric, the mean water velocity $\bar{v}_z$ can be calculated using Equation 3-32 which assumed symmetry around electrode $j = 9$. If this assumption is not correct due to the rotation of the electrode array with respect to the y-axis as shown in Fig. 7-7 there can be significant inaccuracy in the calculated mean flow velocity which will lead to an incorrect reconstruction of the velocity profile. In the same way, the electrical potential measurements obtained for a rotated tube with the non-uniform magnetic field are shown on Fig. 7-9. Again the sixteen measurement points have shifted. The next section explains how this problem was overcome during the data processing stage.

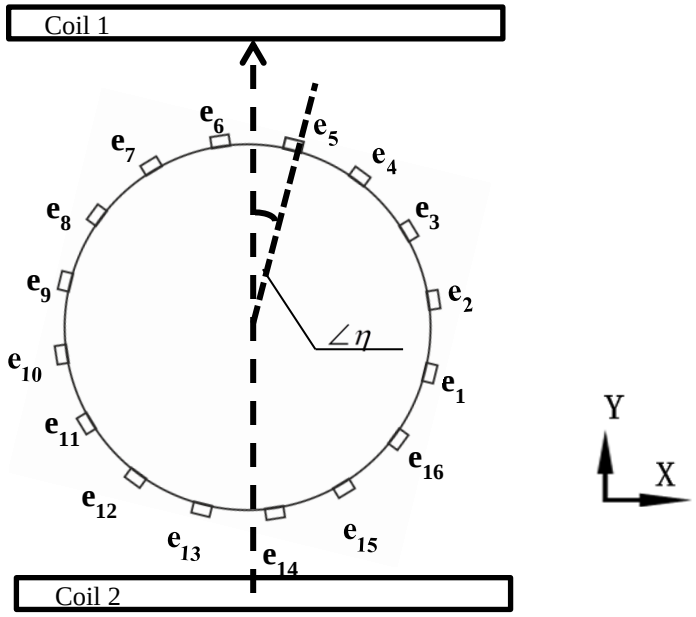

Fig. 7-7 Sixteen electrodes on pipe wall rotated by angle η relative to the *y*-axis

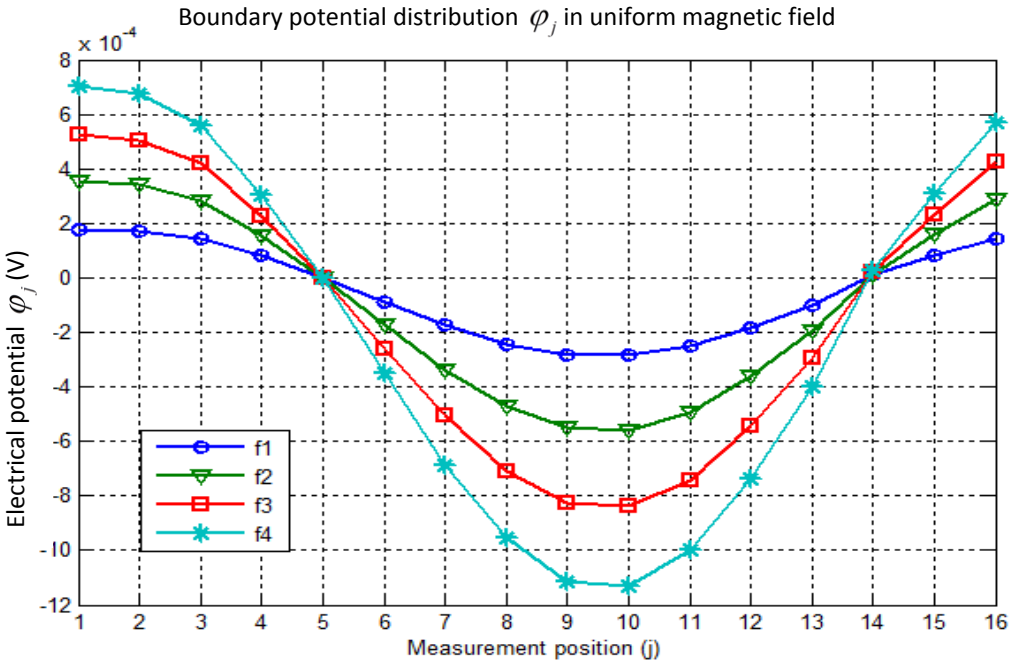

Fig. 7-8 Electrical potential distribution on pipe boundary for vertical water-only single phase flow conditions (uniform magnetic field) with electrodes rotated by angle η

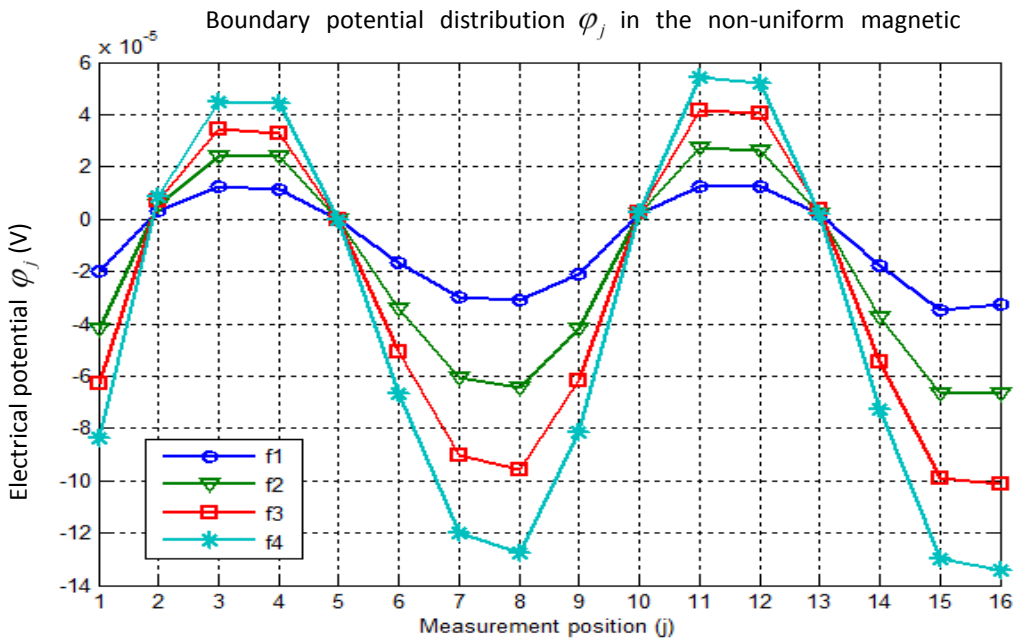

Fig. 7-9 Potential difference distribution on the pipe boundary for vertical water-only single phase flow conditions (non-uniform magnetic field) with electrodes rotated by angle η

7.4.1 Procedure for correction of electrical potential

From the statements above, we can see that, if the electrical potential distribution φ_j, as shown in Fig. 7-8 and Fig. 7-9, is applied into both reconstruction algorithms (see Section 3.6 and 3.7), the reconstructed local water velocity distribution will have errors. Therefore, it is necessary to apply an appropriate data correction into the inaccurate potential distributions φ_j. The main objective of this data correction is to find a new potential distribution φ_j'' corresponding to "virtual electrode" position j', where the virtual electrodes occupy the positions that the real electrodes would have occupied had angular shift η not occured (see Fig. 7-10). The data correction method used in this study is based on linear and polynomial interpolation methods. Calculations of the new potential distribution, φ_j'' vs., were obtained as demonstrated in this section.

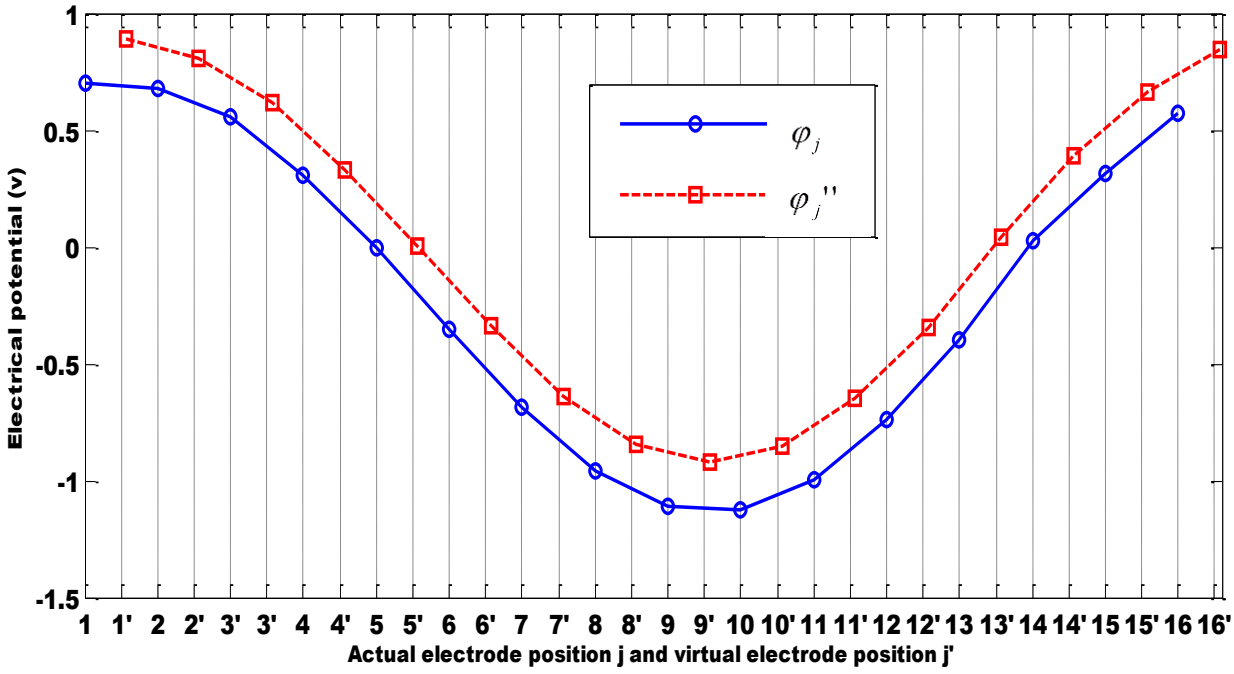

(a)

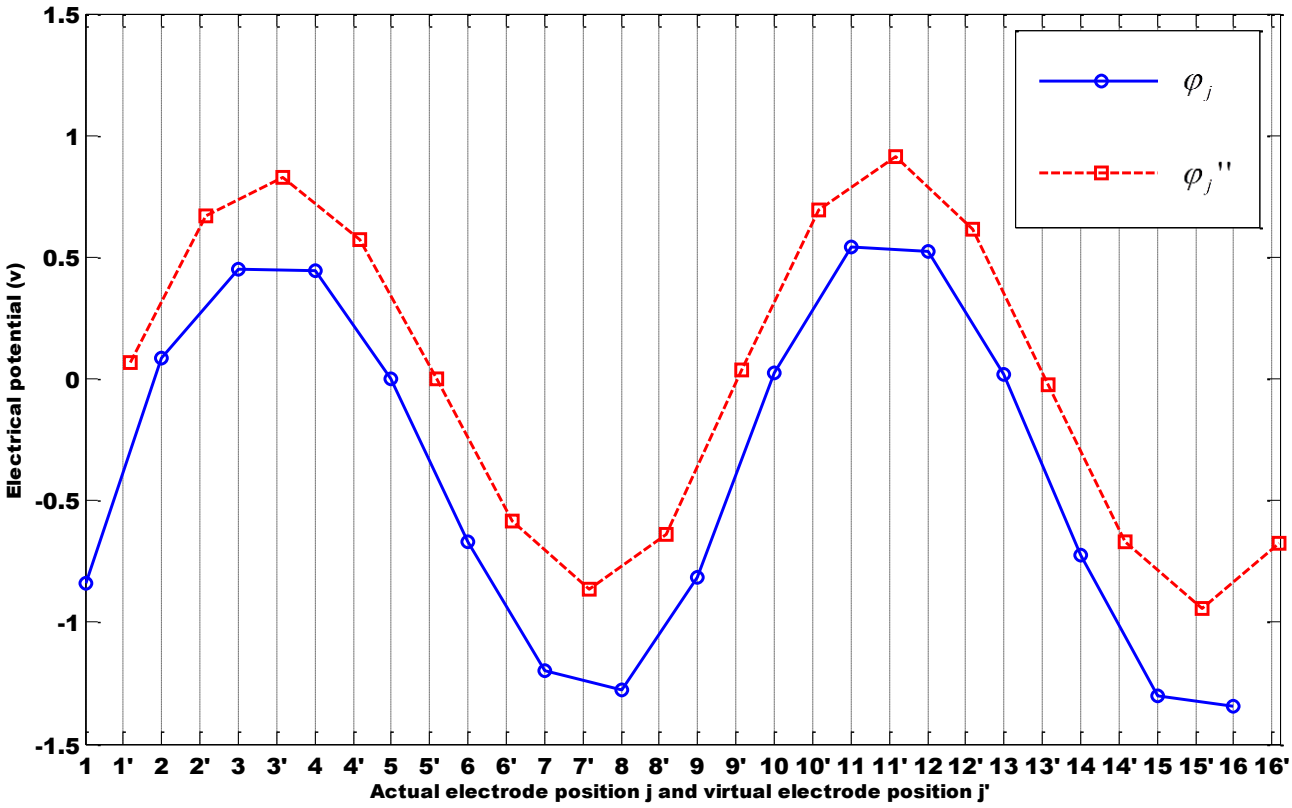

(b)

Fig. 7-10 Measured potential distribution φ_j vs. actual electrode position j ; corrected potential distribution φ_j'' vs. virtual electrode position j' ; (a) uniform magnetic field, (b) non-uniform magnetic field

One of the effects of the rotation angle η was to introduce a DC offset U_{dc} into the measured potential distribution φ_j vs. j (see Fig. 7-10). By applying the DFT to the potential distribution obtained in the uniform magnetic field, the magnitude of U_{dc} could be obtained as shown in Fig. 7-11. The DFT signal processing method was chosen to remove this DC offset from the results for the potential distribution φ_j, because it can show the component *X* of the DFT of the boundary potential distribution. The DC offset value, the zero frequency component of the DFT, is found in the real part of the DFT, as shown in Fig. 7-11.

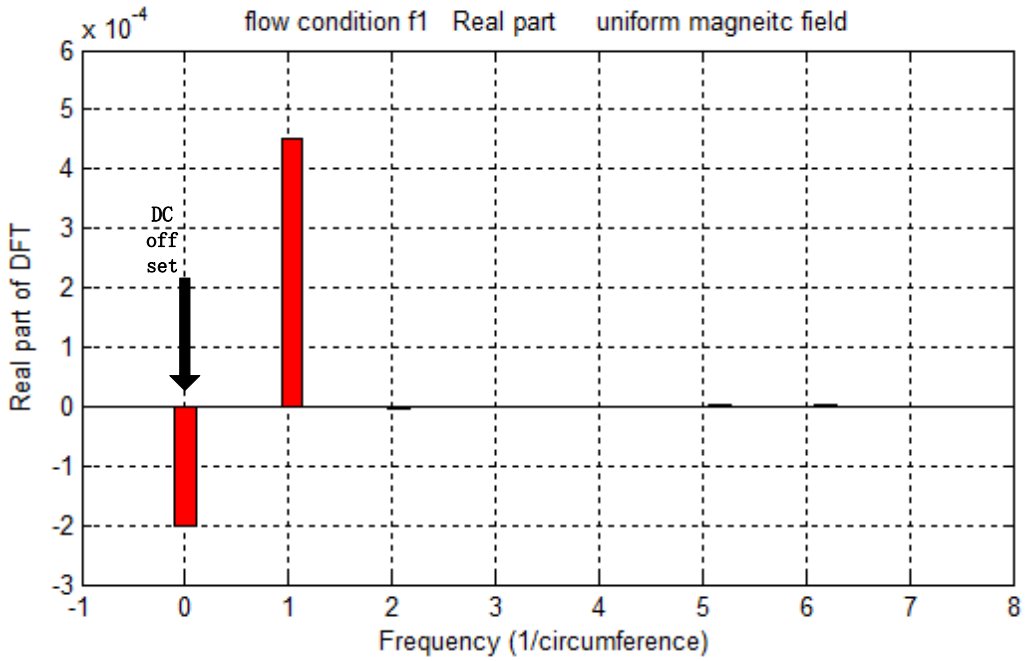

Fig. 7-11 DC offset value is found in the real part of the DFT

The measured experimental electrical potential φ_j can be modified by removing the value of the zero frequency component, as:

$$\varphi_j' = \varphi_j - U_{dc} \qquad \text{Equation 7-10}$$

where U_{dc} is the DC offset. The difference between φ_j and φ_j' is shown in Fig. 7-12. It is obvious that the value of potential measurements for each measurement position φ_j is changed by removing the DC offset.

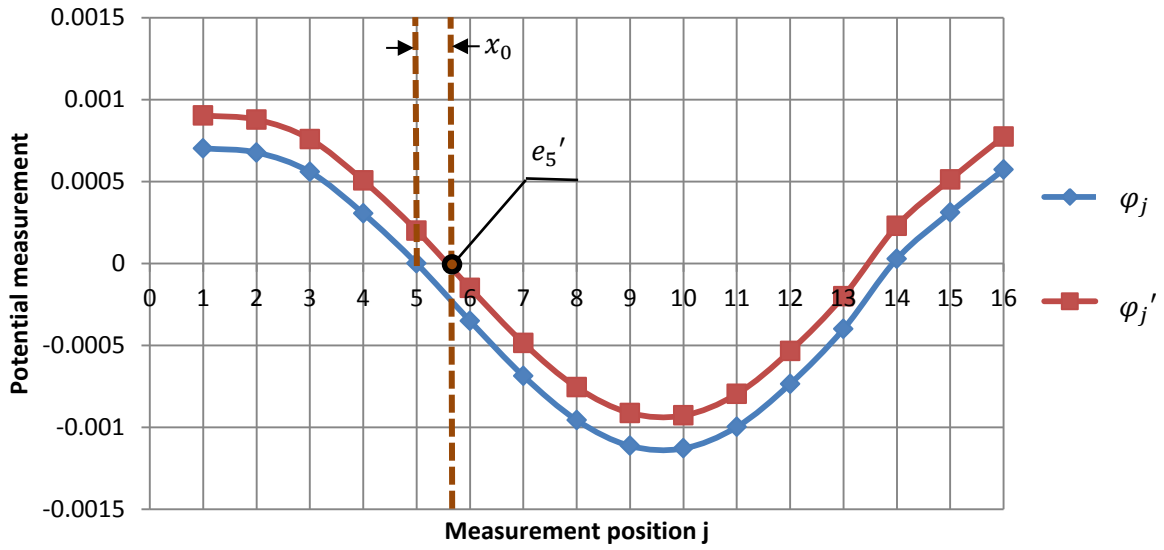

Fig. 7-12 Comparison of potential measurement values of φ_j and φ_j' (uniform magnetic field)

It is now essential to find the position of the virtual electrode (e_5') where the potential φ_j' is equal to zero (see Fig. 7-12). The offset x_0, as shown in Fig. 7-12, is the difference between the virtual electrode position $5'$ (i.e. e_5') and the actual position of electrode 5 (i.e. e_5). For this purpose, firstly, a polynomial curve of order 15 was selected to fit the data points (i.e. φ_j') using the least squares technique, as shown in Fig. 7-13. Then, from a solution of the polynomial equation $a_{15}x^{15}+a_{14}x^{14}+a_{13}x^{13}+\ldots+a_0 = 0$ and by inspection of Fig. 7-13, the root of this equation is equal to 5.56 (i.e. $\varphi_5' = 0$). Thus, the offset x_0 of electrode position j on the x-axis (in Fig. 7-12 and Fig. 7-13) is written in the form:

$$x_0 = x - 5 = 5.56 - 5 = 0.56 \qquad \text{Equation 7-11}$$

where x is the root of the 15th order polynomial equation when $\varphi_5' = 0$. It is worth noting that, by combining two series of sixteen electrical potentials φ_j', the data points used for determining the polynomial fitting curve were extended to thirty-two. The reason for this was to minimise the difference between the polynomial equation model and the data.

Once the offset x_0 was calculated, the next step was to determine the value of electrical potential for the virtual electrode positions i.e. $x = 1 + x_0$, $2 + x_0$,…, $16 + x_0$. The value of electrical potential is denoted as φ_j'', which corresponds to the virtual electrode position j' .

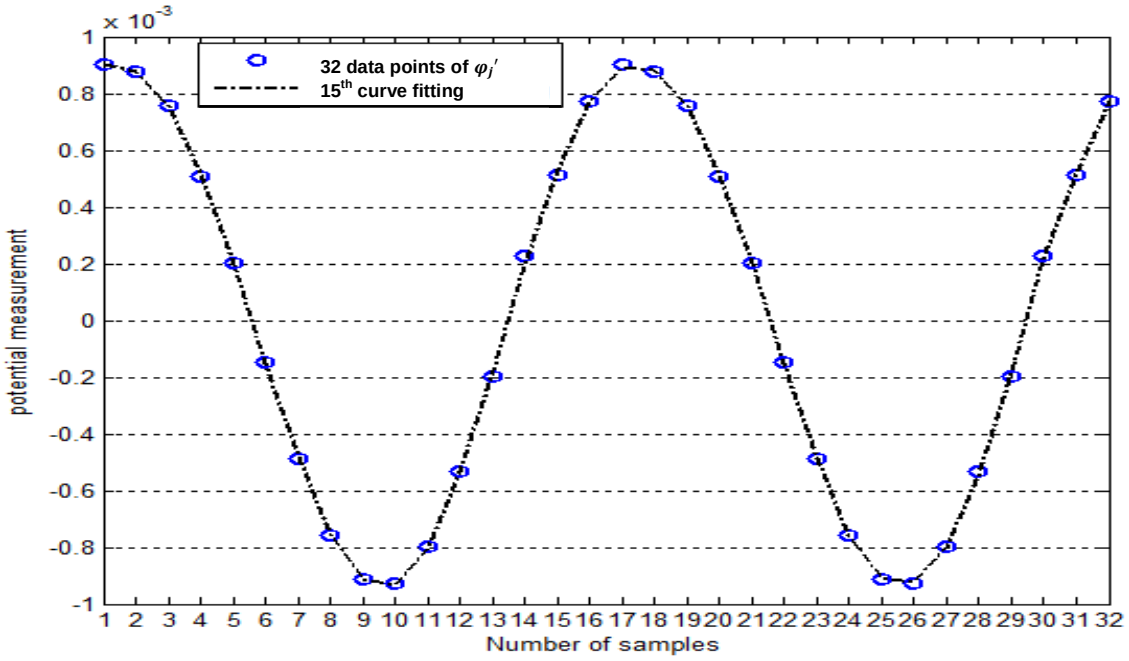

Fig. 7-13 Polynomial curve fitting for φ_j' order 15

To determine the corrected value of electrical potential measurement φ_j'' at the virtual electrode positions, two methods were used, polynomial and linear interpolation.

- ***Polynomial interpolation method***

With regards to the polynomial interpolation analysis, the potential φ_j'' for the virtual electrode position j' could be determined by substituting the $x = 1 + x_0$, $2 + x_0$,…, $16 + x_0$ into the 15th order polynomial equation (see Fig. 7-13) as shown in Fig. 7-15.

It is apparent from Fig. 7-15, that the distribution of φ_j'' has been translated along the *x*-axis by an amount 0.56. Note that j' represents the virtual electrode position of the potential distribution measurement (j' = 1 to16). From Fig. 7-16, it should be readily apparent to the reader how much difference there is between φ_j'' and φ_j.

- ***Linear interpolation***

The second method of finding the new potential distribution φ_j'' is the linear interpolation technique, which assumes a linear relationship between potentials φ_j' and φ_j''.

With reference to the sixteen electrical potentials φ_j', we can define *u'*(*x*) as a continuous function of *x* (where *x* is the horizontal axis of Fig. 7-12). When *x* is integer from 1 to 16, the values of *u'* correspond to φ_1' to φ_{16}'. As mentioned earlier, there is an offset x_0 between actual electrode position *j* and virtual electrode position j'. By substituting $x = x_{j'} = x_j + x_0$ (i.e. x_j = 1 to 16) into *u'* (*x*), the value of φ_j'' can be calculated (see Fig. 7-14).

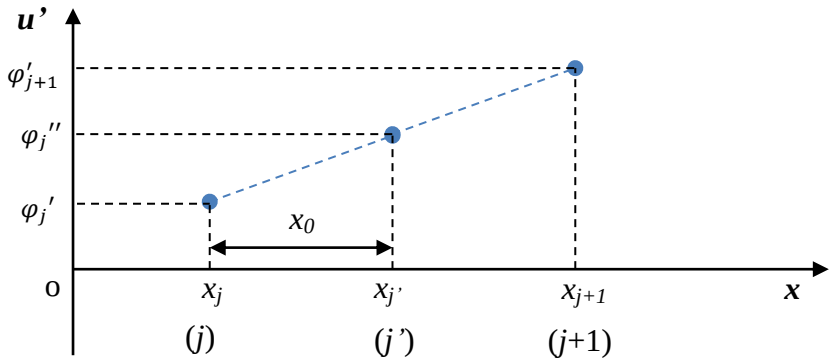

Fig. 7-14 Electrical potential φ_j'' was determined by using the linear interpolation technique.

Referring to Fig. 7-14, it can be seen that the value of $x_{j'}$ is in between x_j and x_{j+1}. Two adjacent potential measurements, φ_j' and φ_{j+1}', can be used to find the correct potential value φ_j'' at an intermediate value of $x_{j'}$. According to the linear interpolation technique, we have:

$$\varphi_j''-\varphi_j'=\left[\frac{x_{j'}-x_j}{x_{j+1}-x_j}\right](\varphi'_{j+1}-\varphi'_j) \qquad \text{Equation 7-12}$$

where $x_{j'}-x_j$ is offset x_0 and $x_{j+1}-x_j$ is equal to 1.

Equation 7-12 can be re-arranged as:

$$\varphi_j''=\varphi_j'+(\varphi_{j+1}'-\varphi_j')x_0 \qquad \text{Equation 7-13}$$

The values of the potentials φ_j', as shown in Fig. 7-12, were substituted into Equation 7-13. The corrected potentials φ_j'' on the inner pipe wall versus virtual electrode position j' are shown in Fig. 7-17. Now, from Fig. 7-15 and Fig. 7-17, it is easy to see that the new corrected potentials φ_j'' using the two interpolation methods are much the same.

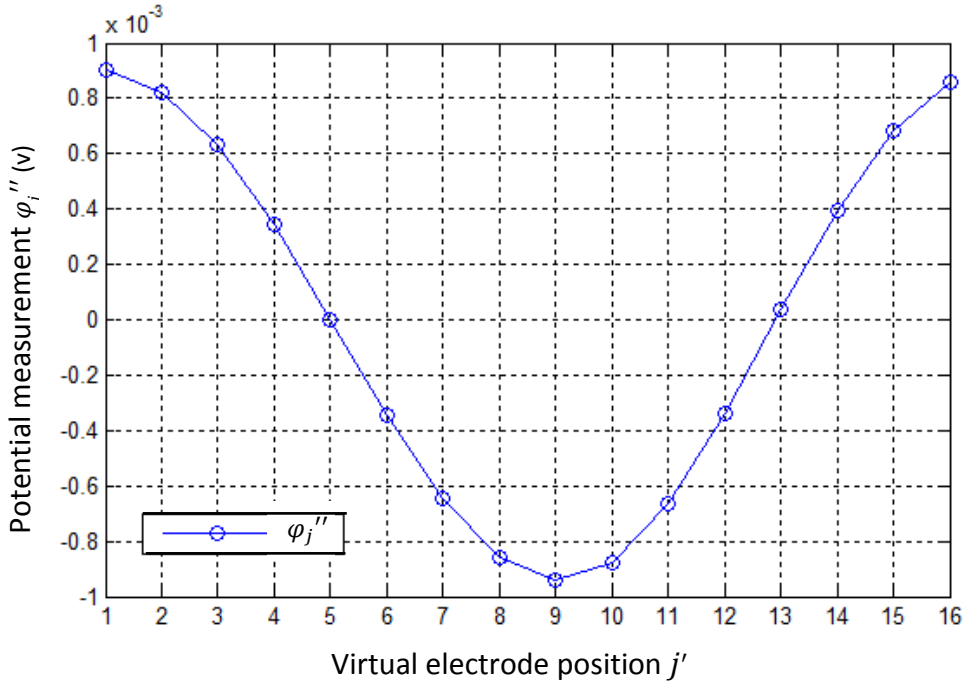

Fig. 7-15 Corrected potential measurement distribution φ_j'' using the polynomial interpolation method

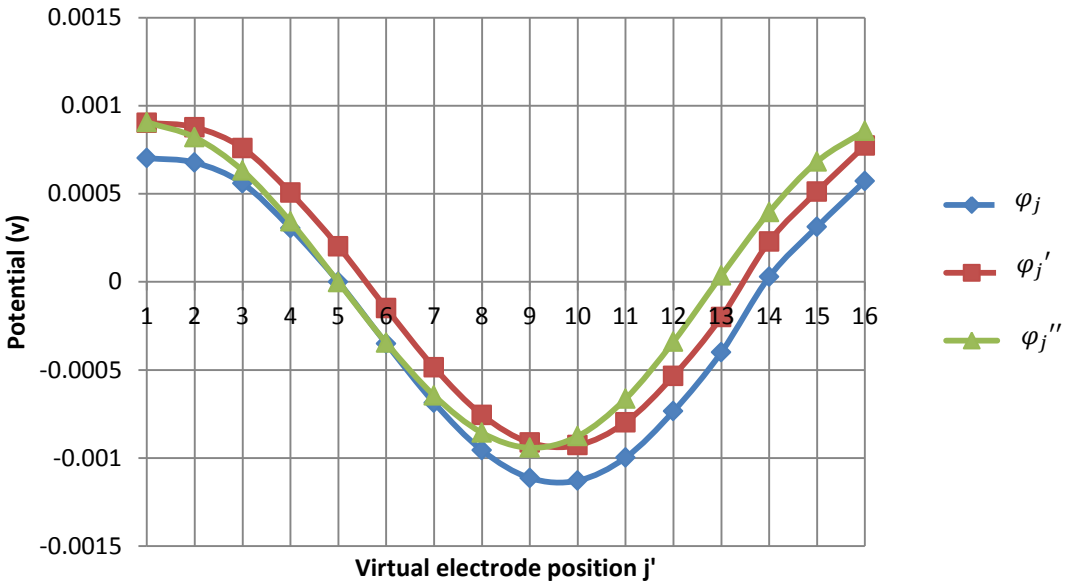

Fig. 7-16 Comparison of φ_j, φ_j' and φ_j''

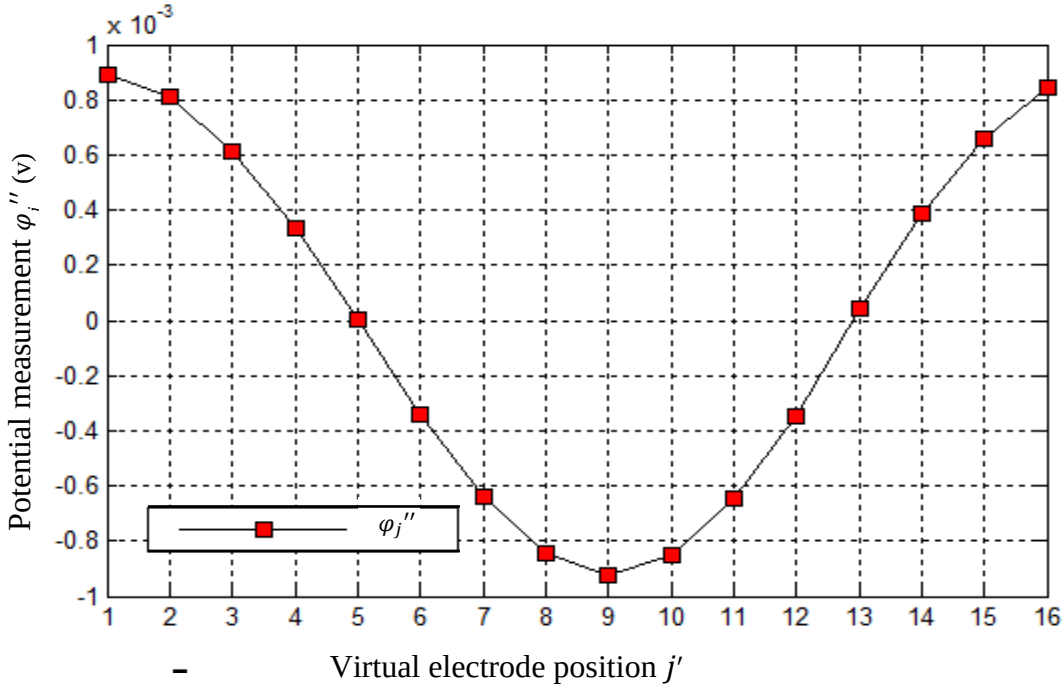

Fig. 7-17 Corrected potential measurement distribution φ_j'' against j' using the linear interpolation method

A similar technique to that decribed above was used to derive the corrected φ_j'' at virtual electrode positions j' for the potential distribution obtained in the non-uniform magnetic field. Polynomial interpolation has the disadvantage that it will fluctuate severely near the end points of the data range. This was found to be the case for the potentials for the non-uniform magnetic field (see Fig. 7-18). To achieve a more accurate result, the linear interpolation technique was used to calculate the new potentials φ_j''. Fig. 7-19 shows that, after the interpolation using Equation 7-13, the potential distribution φ_j'' in the pipe cross-section with measurement position was more symmetrical.

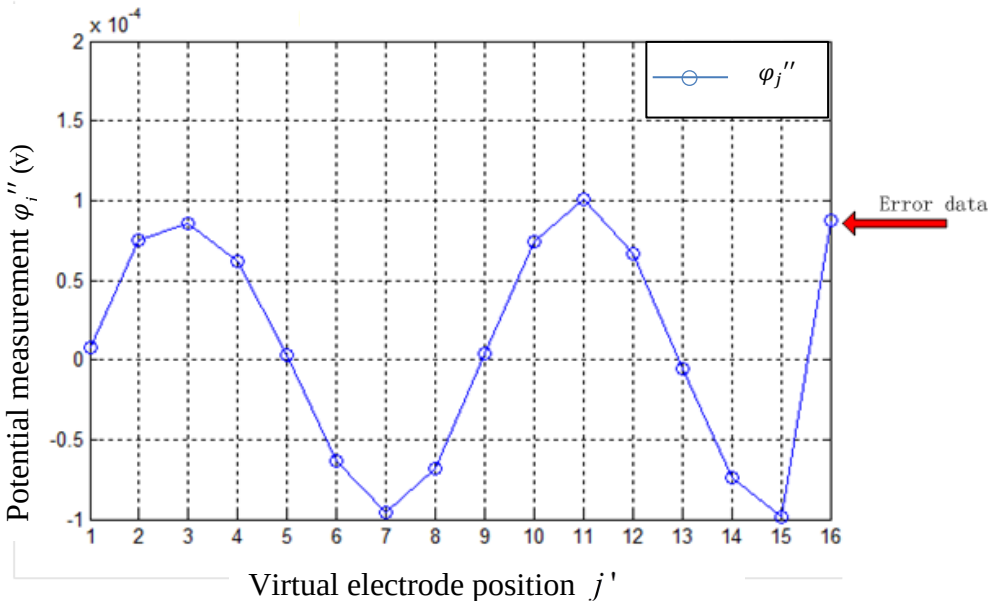

Fig. 7-18 φ_j'' against j' (corrected using the polynomial interpolation method) in a non-uniform magnetic field

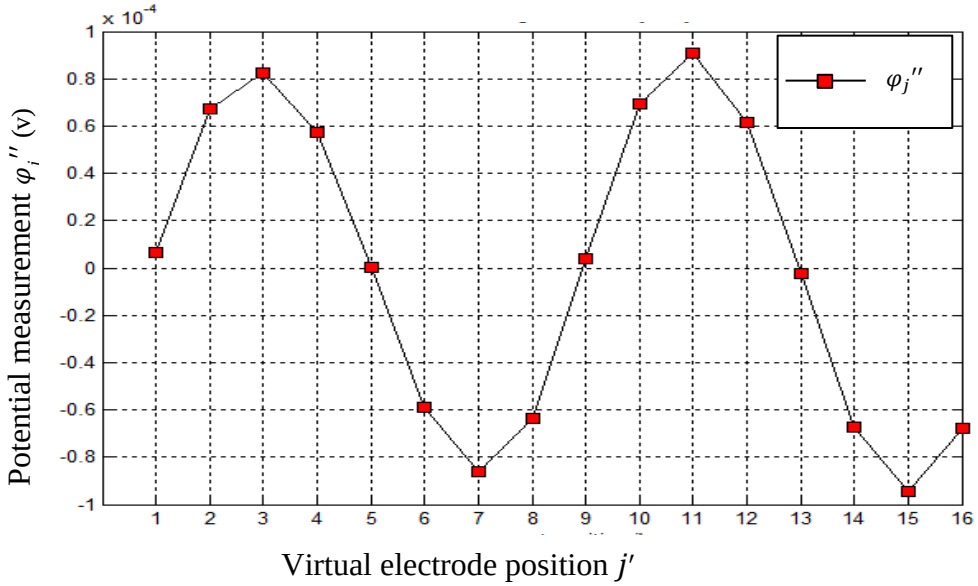

Fig. 7-19 φ_j'' against j' (corrected using the linear interpolation method) in a non-uniform magnetic field

7.5 Testing the performance of the IFT system in inclined and vertical flows

To determine the accuracy of measurements obtained from the IFT system in oil-gas-water three phase flows, four reference measurement techniques were used (see Table 7-1). This research is concerned only with the measurement of the conductive phase. The local water velocities and local water volume fraction distributions were compared with the global measurement of water volumetric flow rate by integrating the product of the local water velocity and the local water volume fraction over the flow cross-section (see Equation 7-9).

7.5.1 Reference measurement parameters and experimental flow conditions

Referring to Section 7.2.1 and Fig. 7-1, the reference measurement parameters obtained from the reference measurement techniques are shown in Table 7-1

Reference measurement parameter	Measurement technique
Oil volumetric flow rate, $Q_{o,ref}$	The reference for the oil volumetric flow rate was obtained by the turbine flowmeter from the SGR laboratory (see Fig. 7-1)
Gas volumetric flow rate, $Q_{g,ref}$	The global reading of gas volumetric flow rate was obtained using a thermal mass flowmeter from the SGR laboratory (see Fig. 7-1)
Water volumetric flow rate, $Q_{w,ref}$	The global reading of water volumetric flow rate was obtained by using a commercial EMFM flowmeter from the SGR laboratory (see Fig. 7-1)
Local volume fraction distribution of dispersed phase (oil and gas) $\alpha_{o+g,i}$ for the i^{th} region (see Section 7.3.2).	The combined local volume fraction of both the oil and gas phase were determined by using an ERT device, as described in Section 7.3.2. This measurement also can be used to determine the local water volume fraction by using $\alpha_{w,i} = 1 - \alpha_{o+g,i}$

Table 7-1 Flow measurement techniques and related reference measurement parameters

In the oil-gas-water three phase flow experiment, several flow conditions were used with the working section inclined at 30° 45° and 60° to the vertical. The flow conditions investigated are presented in Table 7-2.

Flow condition	Angle of inclination of the working-section	Water volumetric flow rate (m^3/hr)	Oil volumetric flow rate (m^3/hr)	Gas volumetric flow rate (m^3/hr)
fm1	30 °	5	2	3.4
fm2	30 °	10	2	3.4
fm3	30 °	10	2	8.5
fm4	45 °	5	2	3.4
fm5	60 °	5	2	3.4

Table 7-2 Flow conditions used in the oil-gas-water three phase flow in non-vertical pipe experiments

In addition to the experiments in inclined oil-gas-water three phase flows using the IFT system, a series of vertical flows, which included water-only single phase, oil-in-water two phase and oil-gas-water three phase flow, were also investigated. For each of these conditions, the reference water, oil and gas volumetric flow rates were measured using the methods described in Table 7-1. These flow conditions investigated are shown in Table 7-3.

Flow condition	Angle of inclination of the working-section	Water volumetric flow rate (m^3/hr)	Oil volumetric flow rate (m^3/hr)	Gas volumetric flow rate (m^3/hr)
fv1	0 °	4	0	0
fv2	0 °	8	0	0
fv3	0 °	16	0	0
fv4	0 º	12	0	0
fv5	0 º	8	4	0
fv6	0 º	10	2	8.5
fv7	0 º	15	2	8.5
fv8	0 º	15	2	17

Table 7-3 Flow conditions used in the water only single phase, oil-in-water two phase , oil-gas-water three phase flows in vertical pipe experiments

7.5.2 Reconstructed local water velocity distribution for non-vertical oil-gas-water three phase flows using IFT

In non-vertical three phase flow experiments, the electrical potential differences U_j for both uniform and non-uniform magnetic field were measured (as described in Section 4.3). By applying the methods as described in Section 7.4, the corrected electrical potential difference measurements $U_j^{''}$ vs. j' are shown in Fig. 7-20 for flows fm1 to fm5 (see Table 7-2). It should be noted that, since the potential at virtual electrode e_5' is defined as being equal to zero, the corrected potential distribution φ_j'' vs j' defined in Section 7.4, is identical to corrected the

potential difference distribution $U_j^{"}$ vs. j' used here,where $U_j^{"}$ is the corrected potential difference at the virtual electrode e_j' relative to virtual electrode e_5'.

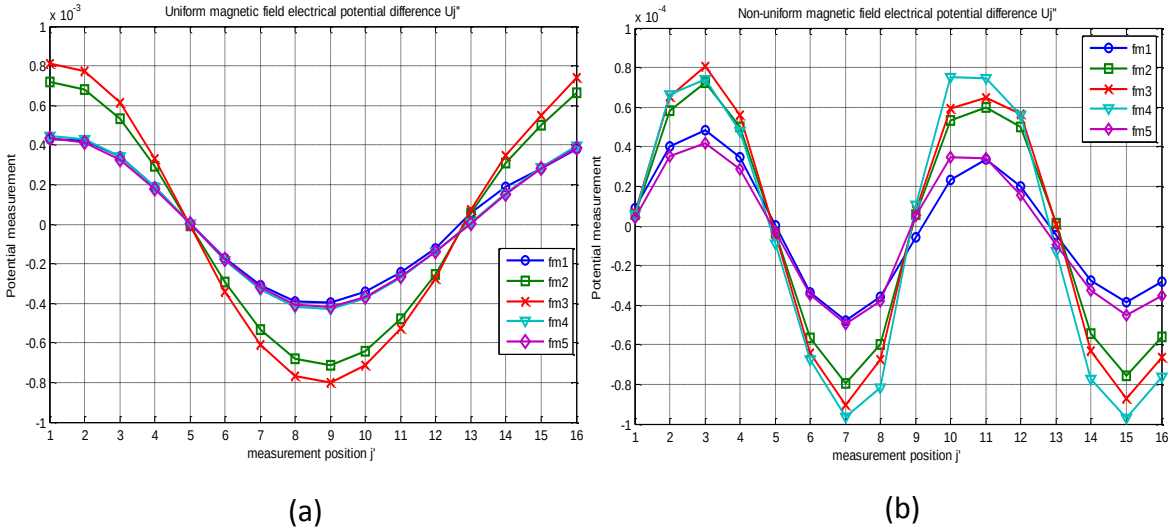

Fig. 7-20 Corrected potential difference measurements Uj''vs j' for non-vertical oil-gas-water three phase flows (a) uniform magnetic field (b) non-uniform magnetic field

Inspection of Fig. 7-20 (b) shows that the corrected electrical potential $U_j^{"}$ distribution has noticeable and significant differences to the pure sinusoid shown in Fig. 3-16. This is because the water velocity profile for these five flow conditions had a non-axisymmetric velocity distribution across the pipe cross-section.

The corrected measured potential difference distribution $U_j^{"}$ vs. j' for the uniform magnetic field shown in Fig. 7-20 (a) is also different from that which could be expected for a uniform or axisymmetric velocity distribution (see Fig. 3-13), though this variation is much less than that of the corrected measured potential difference in the non-uniform magnetic field in Fig. 7-20 (b). Because $U_5^{"}$ is set equal to zero, the data shown in Fig. 7-20 (a) and (b) also represent the potential distribution data required as inputs to the reconstruction technique as described in Section 4.3. After applying the DFT to these data, the magnitude of the DFT components in the uniform magnetic field for each flow condition are as shown in Fig. 7-21. From the bar plots in

Fig. 7-21, it is apparent that the magnitudes of the DFT component $|X_1|$ for fm2 (green) and fm3 (red) are greater than for the other flow conditions. This is because the water flow rates for both flow condition fm2 and fm3 were twice as large as for fm1, fm4 and fm5. It can also be seen that the values of the magnitude of the remaining DFT components were not negligible. In particular, the values of $|X_2|$ for fm1 (blue) and fm5 (purple) are approximately 10% of the value of $|X_1|$. This indicates that the reconstructed velocity profiles contain not only uniform and linear components, but also quadratic and cubic velocity components.

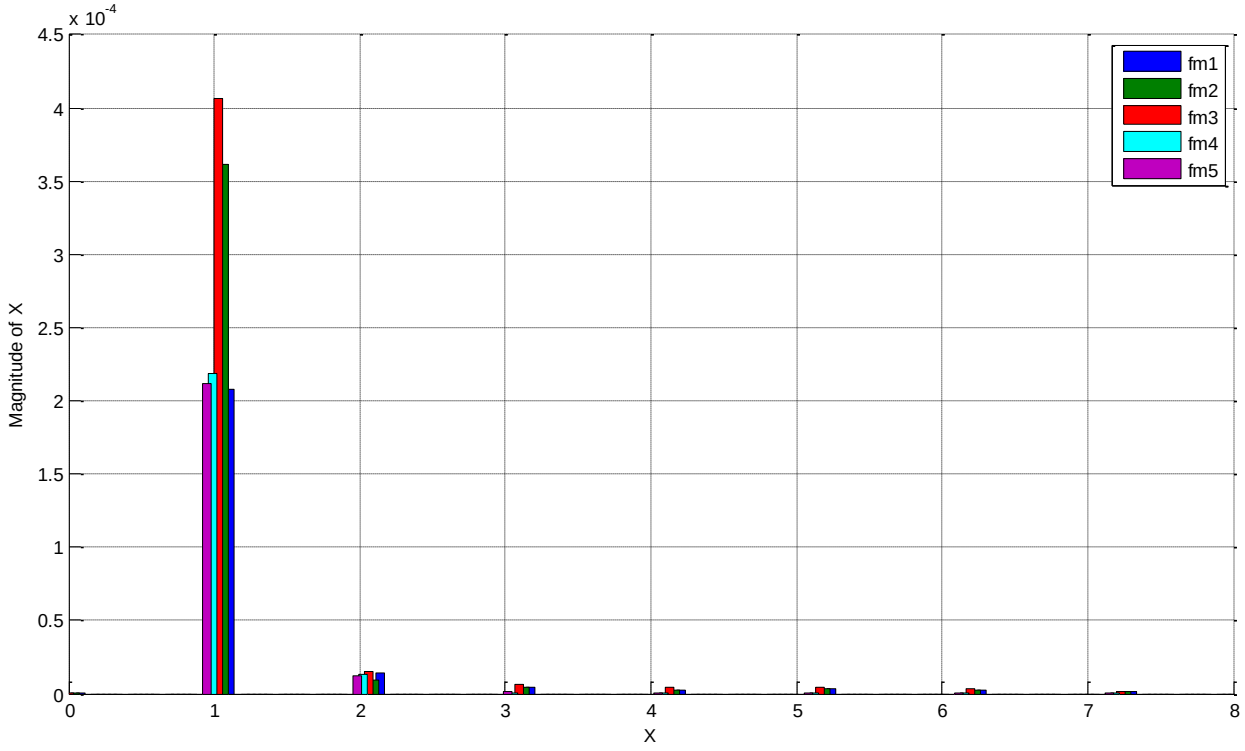

Fig. 7-21 Magnitude of DFT components for potential distributions U_j'' for uniform magnetic field, for experimental conditions fm1 to fm5

7.5.2.1 Reconstructed local water velocity distribution by using the reconstruction algorithm without the use of an axisymmetric velocity component

The corrected potential difference distributions, $U_j^{"}$ vs. j ' for both uniform and non-uniform magnetic fields shown in Fig. 7-20 for flow conditions fm1 to fm5 were used with the velocity

reconstruction algorithm, as described in Section 3.6 assuming a uniform velocity component (exponent q = 0) (i.e. an axisymmetric velocity component was not assumed).

The reconstructed local water velocity distributions for each oil-gas-water flow are shown in Fig. 7-22. These results are plotted with both a high resolution 100×100 grid (see Fig. 7-6 on the left of the figures) and a relatively low resolution 20×20 ERT grid (on the right). The local water velocity distributions with the ERT grid will be used in conjunction with local volume fraction results obtained by the ERT device for further analysis.

For the convenience of comparison between each water velocity profile, the mean water volume fraction $\overline{\alpha}_w$ and dispersed phase (oil and gas) volume fraction $\overline{\alpha}_{o+g}$ are shown at the bottom of each figure. Note that the mean volume fraction of the conductive continuous phase (water) $\overline{\alpha}_w$ was calculated by using Equation 7-14

$$\overline{\alpha}_w = \frac{1}{N}\sum_{i=1}^{N}(1-\alpha_{o+g,i}) \qquad \text{Equation 7-14}$$

where $\alpha_{o+g,i}$ is the local non-conducting dispersed phase (oil and gas) volume fraction in the i^{th} sub-region (obtained from ERT). With reference to the pixel arrangement of the ERT system, as described in Section 7.3.2, Equation 7-14 can be rewritten as:

$$\overline{\alpha}_w = \frac{1}{316}\sum_{i=1}^{316}(1-\alpha_{o+g,i}) \qquad \text{Equation 7-15}$$

Here, 316 is total number of sub-regions in the flow cross-section.

Flow conditions fm1, fm2 and fm3 are reconstructed using velocity components up to order n=2 (quadratic) – see Section 3.6.1.1. Flow conditions fm4 and fm5 are reconstructed using velocity components up to order n=3 (cubic). If higer order components were used, the reconstructed velocity profiles became " noisy" and this is reflected in the fact that the term S_U becomes larger for the higher order velocity profiles. In fact, for all of the velocity profiles presented in this thesis, the profile selected is that for which S_U has the minimum possible value.

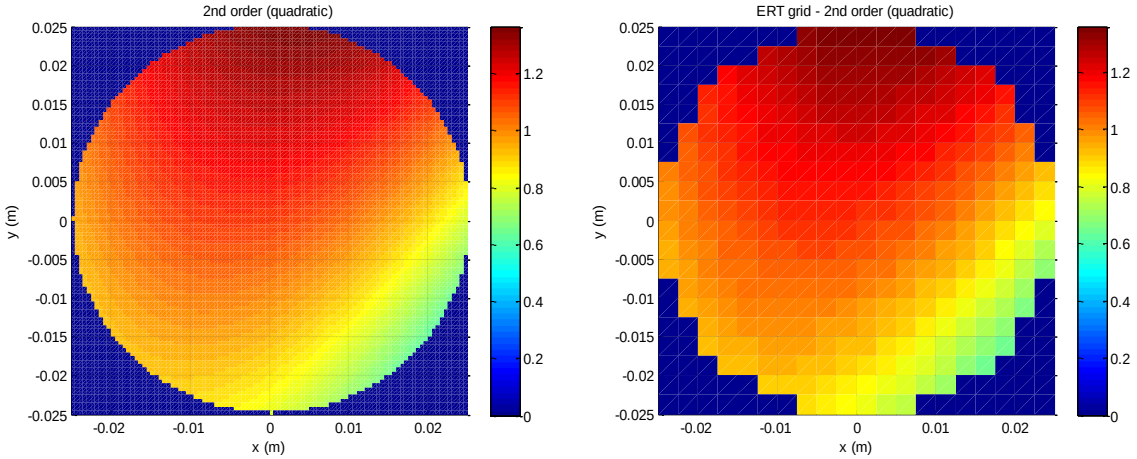

(a) Flow condition fm1 $\bar{\alpha}_w$=0.705 $\bar{\alpha}_{o+g}$=0.295

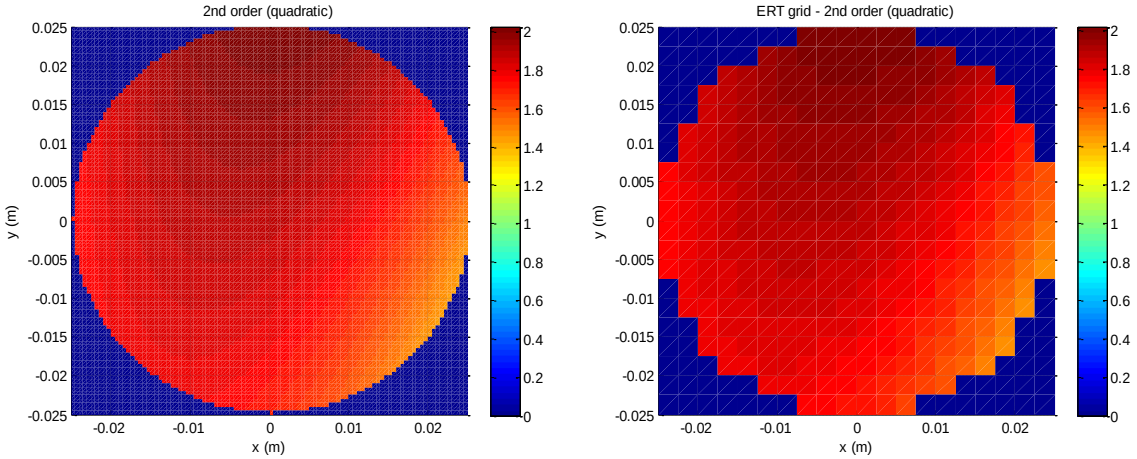

(b) Flow condition fm2 $\bar{\alpha}_w$=0.8128 $\bar{\alpha}_{o+g}$=0.1872

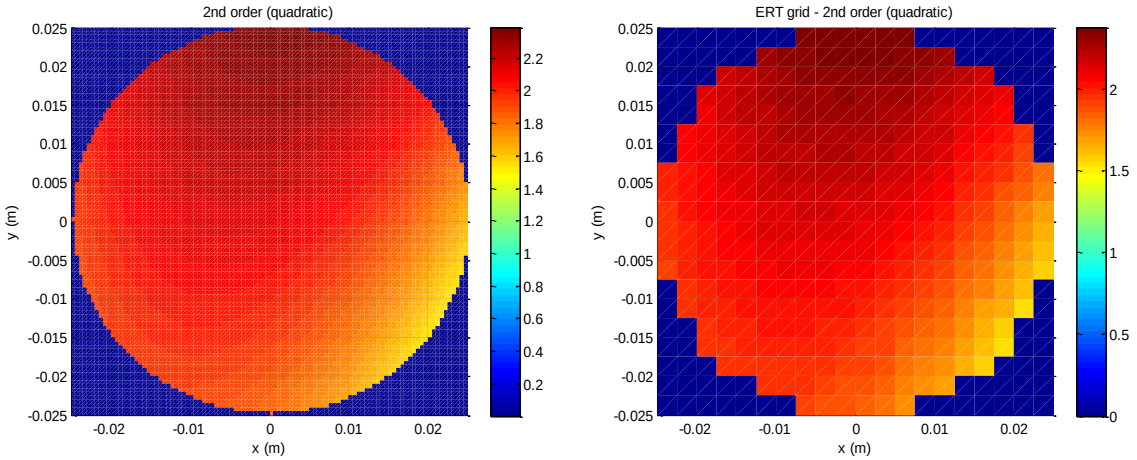

(c) Flow condition fm3 $\bar{\alpha}_w$=0.6744 $\bar{\alpha}_{o+g}$=0.3256

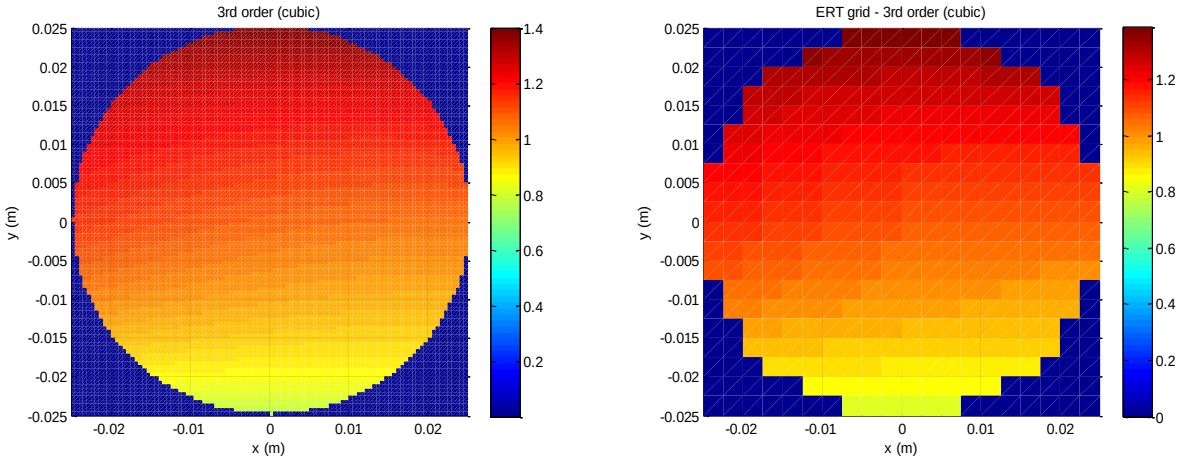

(d) Flow condition fm4 $\bar{\alpha}_w$=0.7013 $\bar{\alpha}_{o+g}$=0.2987

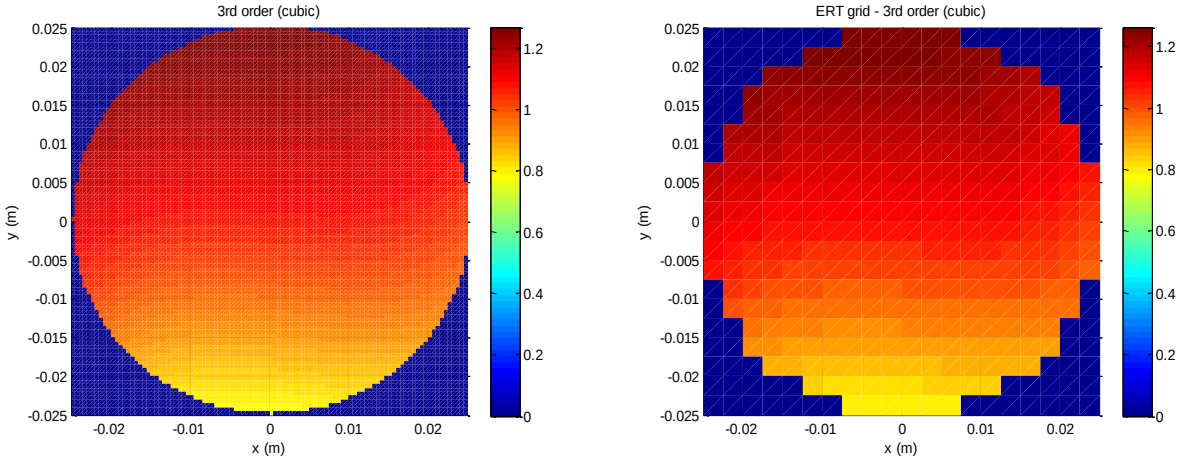

(e) Flow condition fm5 $\bar{\alpha}_w$=0.6945 $\bar{\alpha}_{o+g}$=0.3055

Fig. 7-22 Reconstructed velocity profiles in non-vertical oil-gas-water three phase flows. The water velocity in this colour bar is in ms^{-1}

The velocity profiles for all five flow conditions are shown in Fig. 7-22 (a) to (e), where the colour red represents a relatively high value of local water velocity and yellow/green represents a relatively low value of local water velocity. By inspection of Fig. 7-22, these results are reasonably close to the results of gas-in-water and oil-in-water non-vertical flows achieved by Lucas [28, 111]. In particular, the water velocity attained a maximum value at the upper side of the inclined pipe (from 0.015m to 0.025m *y*-axis) and a relatively lower velocity occurred at the bottom of pipe (from -0.015m to -0.025m *y*-axis).

The figure also shows the effect of angle of deviation from the vertical on the water velocity at the upper side of the pipe. This phenomenon can be observed by comparing the velocity results, as shown in Fig. 7-22 (a) (d) and (e). It can be seen that, for the same phase flow rates, when the deviation angle θ is increased from 30 °to 45 °to 60 °(fm1 to fm4 to fm5), a relatively higher velocity occurs over a larger region at the top of the pipe. In addition, it is also apparent that the water velocity distribution has more variation along the *y*-axis. Lucas [111] explained that as the angle of deviation increases, buoyancy forces cause more bubbles (oil and gas) to congregate along the top of the working section. The lower density of the fluids towards the upper side of the inclined pipe causes them to move faster than the higher density fluid (water) at the lower side of the inclined pipe(see Fig. 7-23).

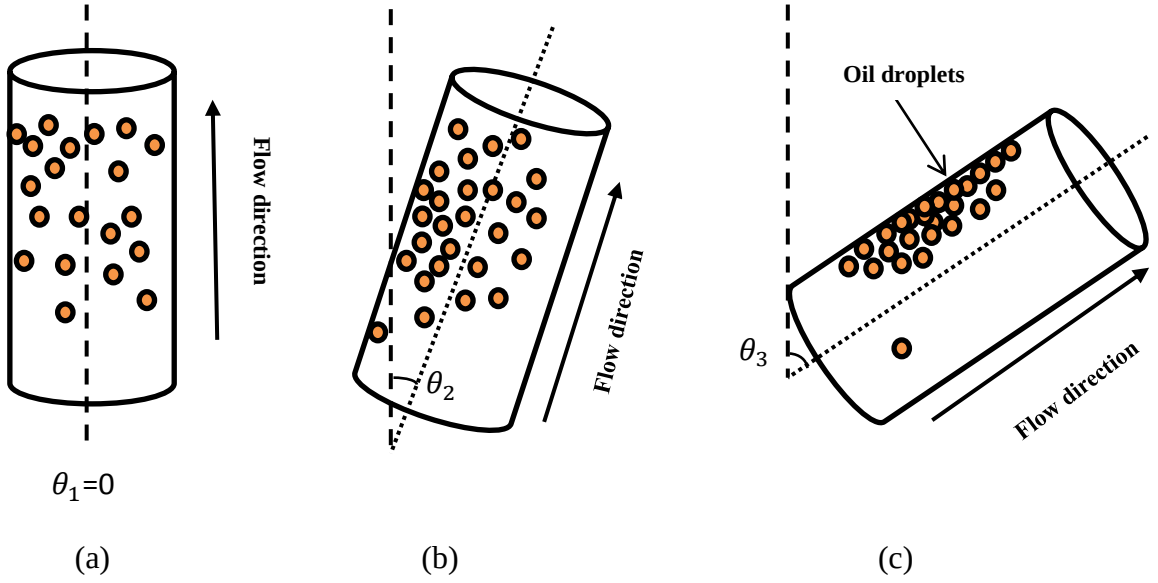

Fig. 7-23 Flow characteristics observed in vertical and non-vertical oil-in-water two phase flows. As the angle of deviation θ increases, buoyancy forces cause more bubbles (oil and gas) to congregate along the upperside of the inclined working section (Vigneaux [112])

Lucas [111] and Oddie [11] stated that, with increasing angle of deviation θ more gas bubbles congregate along the upper side of the pipe and can coalesce to form larger bubbles. In the case of the flow condition fm5 it is therefore to be expected that with θ = 60 °elongated gas bubbles would occupy the upper side of the pipe cross-section. This can be observed by inspecting Fig.

7-24, which shows a photograph of one such elongated bubble (slug) that appeared in the working section. Because the continuous phase (water) was accelerated by these slugs, the measured local water velocity was a maximum near the upper side of the inclined pipe (coloured dark red in Fig. 7-22).

Zuber and Findlay [113], Vedapuri [114] and Vigneaux [112] have described the behaviour of oil-in-water two phase flows. They demonstrated that, with an increase in angle of deviation, the oil phase flow gradually separated from the water layer and moved towards to the upper side of the pipe cross-section due to the effects of gravity, as shown in Fig. 7-23.

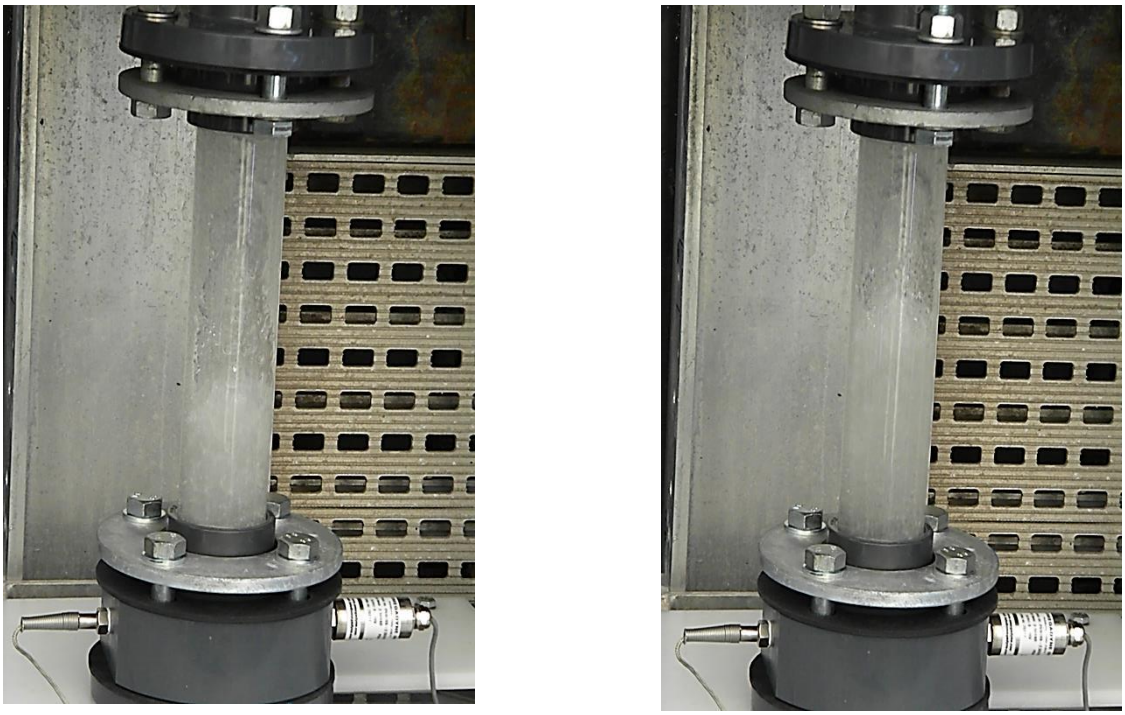

Fig. 7-24 Flow patterns for flow condition fm5; note elongated bubble along upper side of inclined pipe in this flow condition :Q_w=5m^3/hr Q_o=2m^3/hr Q_g=3.4m^3/hr inclination angle θ=60 ٩.

Referring to Fig. 7-25, if we compare the local volume fraction distribution of the dispersed phases (oil and gas) for fm1 and fm4, corresponding to (a) and (d) in the figure, it is to be

expected that, at the upper side of the pipe, the volume fraction of the dispersed phases is increased, and the peak value of $\alpha_{o+g,i}$ (see Equation 7-14) moves closer to the top side of the pipe. This is because the phase flow rates are the same for fm1 and fm4 (Table 7-2) but the inclination angle is changed from 30 ºto 45 º. In addition, for the flow conditions fm1 and fm4, when the angle θ is increased from 30 º to 45 º, there is greater variation in the local water velocity at the upper side of the pipe for fm4 than is the case for in fm1 (see Fig. 7-22). However, when the angle of deviation from the vertical was increased to 60 º (see Fig. 7-22 (e)) it is interesting to observe that the local water velocity at the upper side of the pipe becomes relatively constant. In order to explain this phenomenon, it is necessary to discuss the behaviour of the water velocity in gas-in-water and oil-in-water two phase flows, respectively.

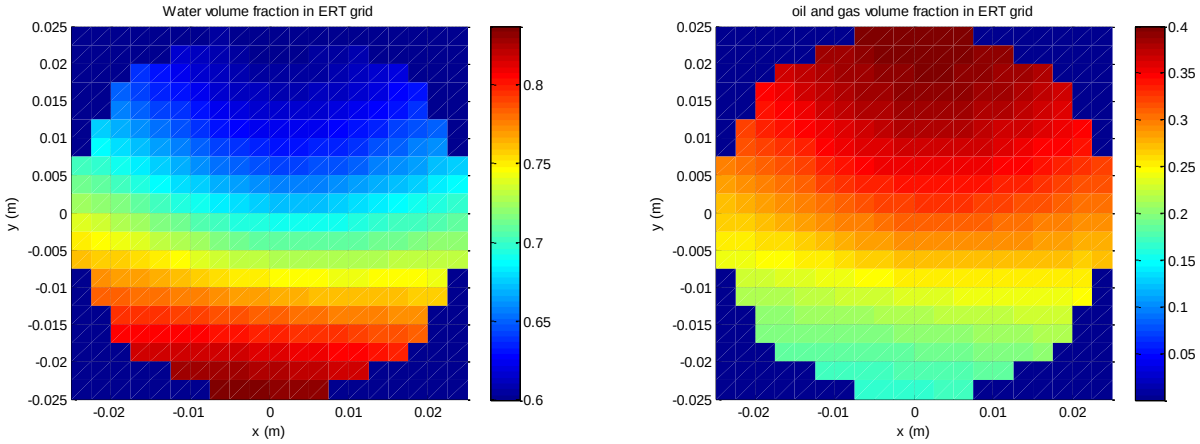

(a) Flow condition fm1 $\bar{\alpha}_w$=0.705 $\bar{\alpha}_{o+g}$=0.295

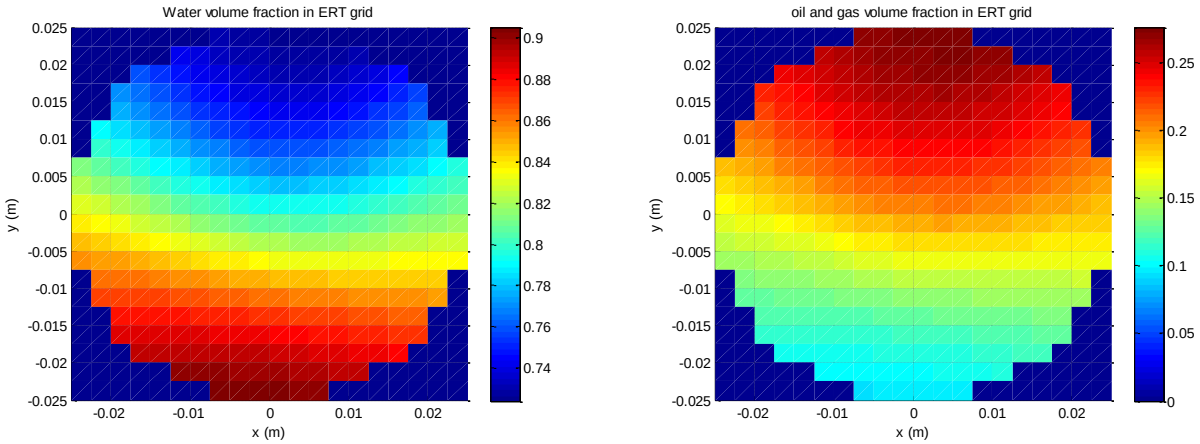

(b) Flow condition fm2 $\bar{\alpha}_w$=0.8128 $\bar{\alpha}_{o+g}$=0.1872

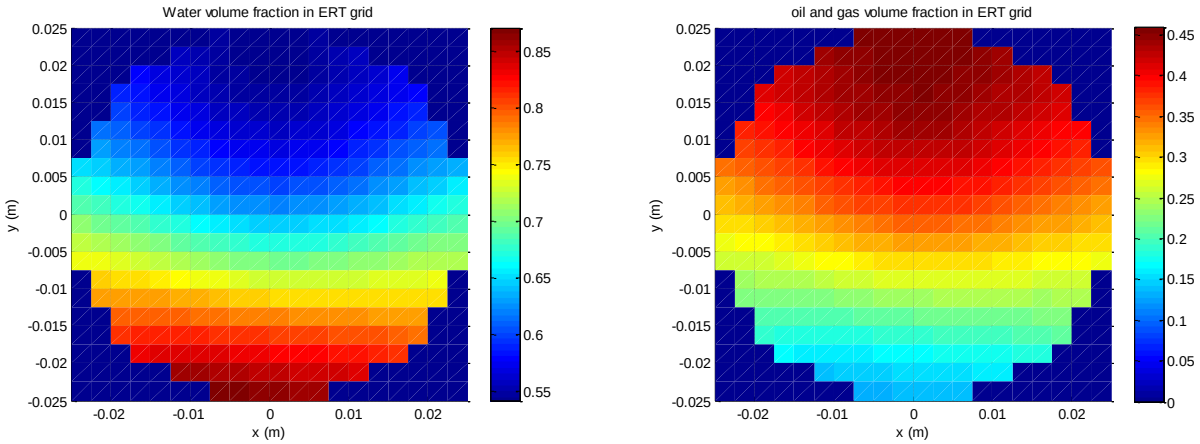

(c) Flow condition fm3 $\bar{\alpha}_w$=0.6744 $\bar{\alpha}_{o+g}$=0.3256

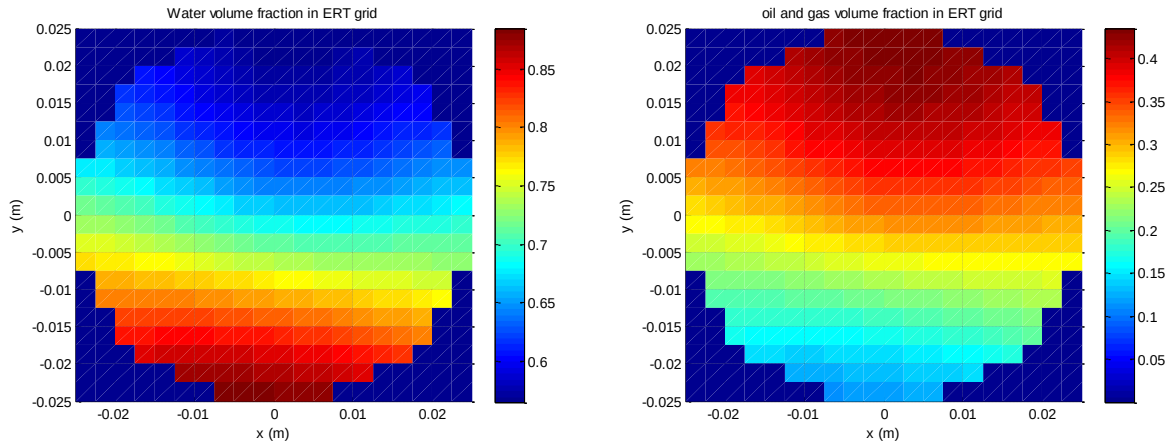

(d) Flow condition fm4 $\bar{\alpha}_w$=0.7013 $\bar{\alpha}_{o+g}$=0.2987

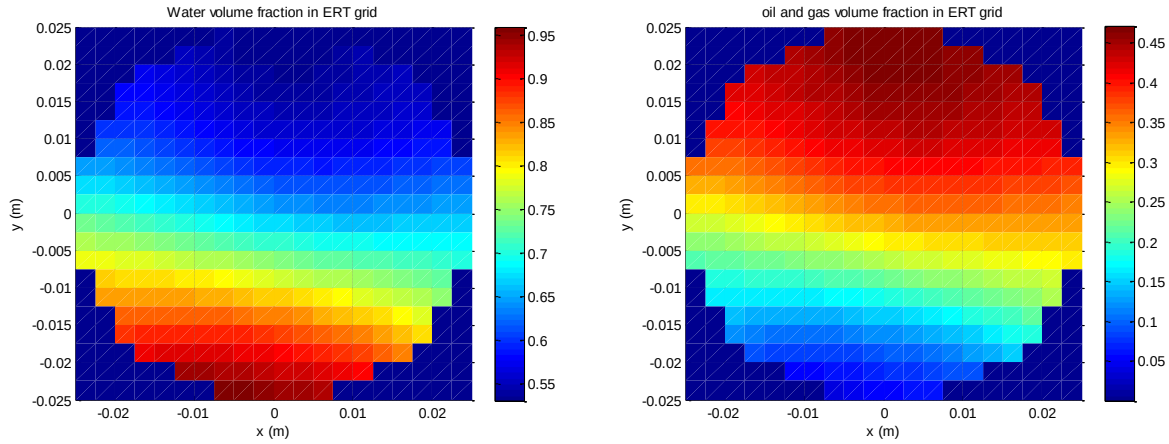

(e) Flow condition fm5 $\bar{\alpha}_w$=0.6945 $\bar{\alpha}_{o+g}$=0.3055

Fig. 7-25 Local water volume fraction distribution and local dispersed phase(oil and gas) volume fraction distribution

The propensity for a larger local oil volume fraction to occur at the upper side of the pipe, where the local velocity of the dispersed phase is highest means that, when the angle of deviation is 60 º, the oil phase will tend to separate from the water phase. This has the consequence that the local oil phase velocity increases towards the upper side of the pipe. Due to local interaction between the phases this will also lead to a greater local water velocity than at the lower side of the pipe. However, by inspection of Fig. 7-22 (e), it can be seen that, at the upper side of the pipe, the local water velocity is lower than for the result shown in Fig. 7-22 (d). Thus, for the same phase flow rates, the local water velocity at the upper side of the inclined pipe is seen to be lower for 60 ºinclination than for 45 ºinclination. The reasons for this can be found from previous research

into oil-in-water two phase flows by Zuber and Findlay [113] who proposed a mathematical model to express the mean dispersed phase flow velocity. This model has been extended by Hasan and Kabir [115], who proposed the following equation:

$$U_d = C_{o\theta} U_h + U_{dj} \qquad \text{Equation 7-16}$$

where U_d is the mean dispersed phase velocity, U_h is the homogeneous velocity of the mixture, U_{dj} is the drift velocity of the dispersed phase and $C_{o\theta}$ is an inclination dependent distribution parameter, which can be defined as:

$$C_{o\theta} = \frac{\overline{\alpha_l j_m}}{\overline{\alpha}_d U_h} \qquad \text{Equation 7-17}$$

where $\overline{\alpha}_d$ is the mean volume fraction of the dispersed phase, α_l is the local volume fraction of the dispersed phase, and j_m is the sum of the local flux densities of the two flow components. Additionally, with reference to Lucas and Jin [116], the drift velocity of the dispersed phase U_{dj} is defined as:

$$U_{dj} = \frac{\overline{\alpha_l (1-\alpha_l) v_r}}{\overline{\alpha}_d} \qquad \text{Equation 7-18}$$

where v_r is the local relative velocity between the phases (i.e. the local slip velocity)

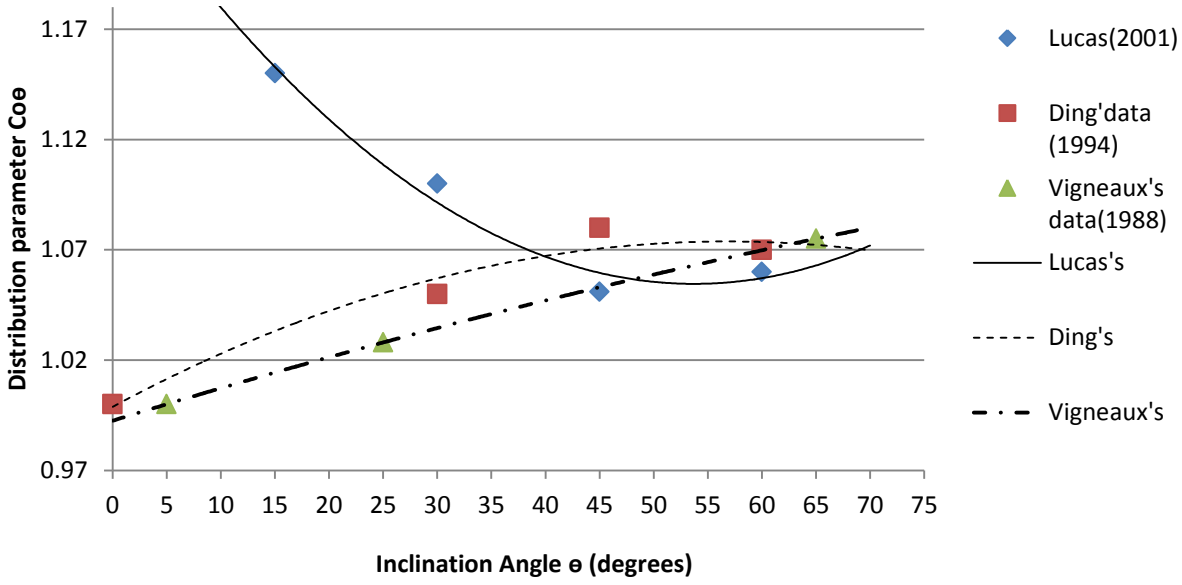

Fig. 7-26 Distribution parameter values $C_{o\theta}$ for various experimental data sets [116]

The values of $C_{o\theta}$ for different angles of deviation are shown in Fig. 7-26 [116]. From inspection of Fig. 7-26, it can be seen that there is some suggestion that, above 45 º $C_{o\theta}$ either remains constant or might even fall with increase in θ. Hence, referring to Equation 7-16 and Equation 7-17, the mean dispersed phase velocity could decrease as θ is increased from 45 º to 60 º. It is, therefore, concluded that the reason the local water velocity at the upper side of the pipe for fm5 is more constant, and relatively smaller, than for fm4 is because the mean oil phase velocity has been reduced, and due to the interaction between the phases this has caused a reduction in the water velocity.

After comparing the velocity results between flow conditions fm1, fm4 and fm5, we may now compare the velocity results obtained for fm2 and fm3 (see Fig. 7-22 (b) and (c), respectively). Referring to Table 7-2, both fm2 and fm3 have the same angle of deviation, θ = 30 º, the only difference is the volume fraction of dispersed phase. The value of $\overline{\alpha}_{o+g}$ increased from 18.72% to 32.56% from fm2 to fm3. With reference to the results obtained by Lucas [111] for a fixed input water volumetric flow rate, the region of higher volume fraction of the dispersed phase should increase when the volume fraction of either gas or oil is increased. In the case of fm3, the gas flow rate was increased relative to fm2 (see Table 7-2). Due to gravity and buoyancy; more

of the gas phase migrates towards the upper side of the pipe, which results in an increase in the region of higher volume fraction of dispersed phase. This could force the water at the upper side of the pipe to move faster than at the lower side of the pipe. In Fig. 7-22 (b), the reconstructed local water velocity at the upper side of the pipe (y=0.015m–0.025m) is approximately in a range of 1.9m/s to 2m/s. From the results shown in Fig. 7-22 (c), in the same region, the reconstructed local water velocity is approximately in a range of 2.2m/s to 2.4m/s, which is in qualitative agreement with the arguments given above. The comparison between fm2 and fm3 presented above has already shown that the reconstructed water velocity profiles using the reconstruction algorithm with use of a uniform component, as opposed to an axisymmetric component, has good agreement with previous research results by Lucas [111]. The next section will discuss the reconstructed local water velocity distribution for the same flow conditions using the reconstruction algorithm with use of an axisymmetric velocity component.

7.5.2.2 Reconstructed local water velocity distribution using reconstruction algorithm with use of an axisymmetric velocity component

The last section showed the local water velocity profiles for different three phase flow conditions reconstructed using the first velocity reconstruction algorithm without use of an axisymmetric component (see Section 3.6). In this section, the same potential differences (see Fig. 7-20) are introduced into the second reconstruction algorithm (see Section 3.7) to obtain local water velocity profiles which contain an axisymmetric velocity component. The results are shown in Fig. 7-27.

Because there is no technique that can be easily used to provide a reference measurement of local water velocity profiles, the results shown in Fig. 7-27 may be close to realistic velocity profiles. An investigation to find the most suitable reconstruction algorithm for the inclined flow conditions is described in a later section. It is worth noting that the reconstructed velocity profile shown in Fig. 7-27 (d) is the same as Fig. 7-22 (d), because the calculated exponent q is equal to zero. In other words, for the flow condition fm4, the local water velocity profile does not appear to contain an axisymmetric velocity component.

By close inspection of Fig. 7-27, one can see that all of the reconstructed velocity profiles have a similar tendency to give a relatively higher velocity at the upper side of the pipe cross-section. However, the peak value of local water velocity for flow conditions fm2 and fm3 appears near to the centre of the pipe, which is different from the reconstructed velocity profiles using the original reconstruction algorithm (see Fig. 7-22 (b) and (c)). Oddie [11] showed that, in three phase flows, particularly at high flow rates, the oil and water are well mixed by the gas slipping and that there is the possibility that the maximum value of the water velocity may appear just above the centreline. It is therefore not unreasonable to assume that the reconstructed velocity profiles containing an axisymmetric component are actually more realistic.

As described earlier, there was no flowmeter device that could be used to independently identify the local water velocity distribution during the experiments at SGR. Therefore, it was necessary to adopt an alternative approach to see which velocity profile reconstruction algorithm was most appropriate. This will be described in the next section.

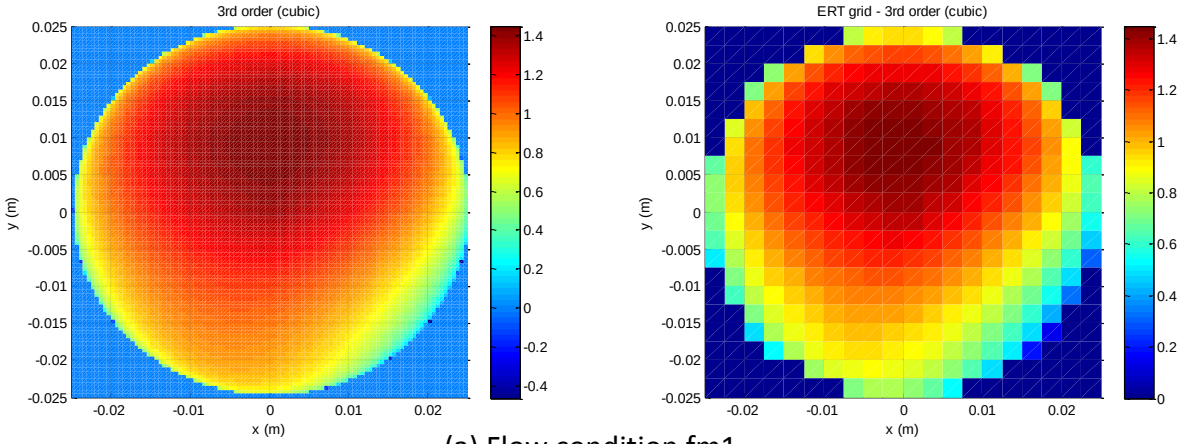

(a) Flow condition fm1

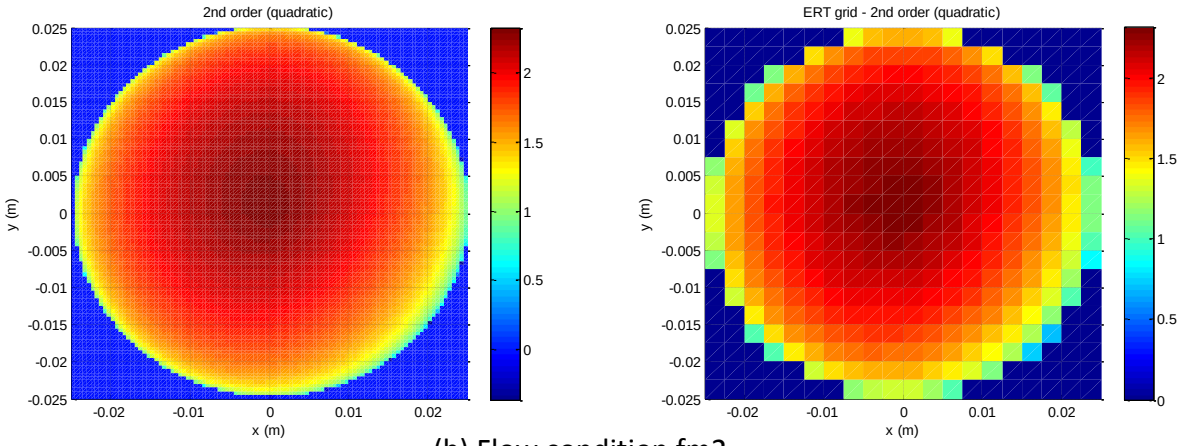

(b) Flow condition fm2

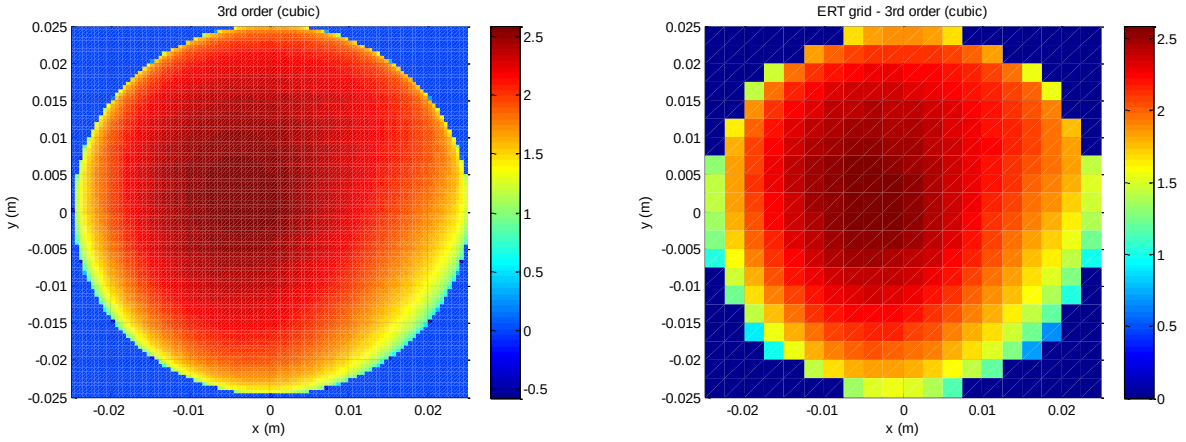

(c) Flow condition fm3

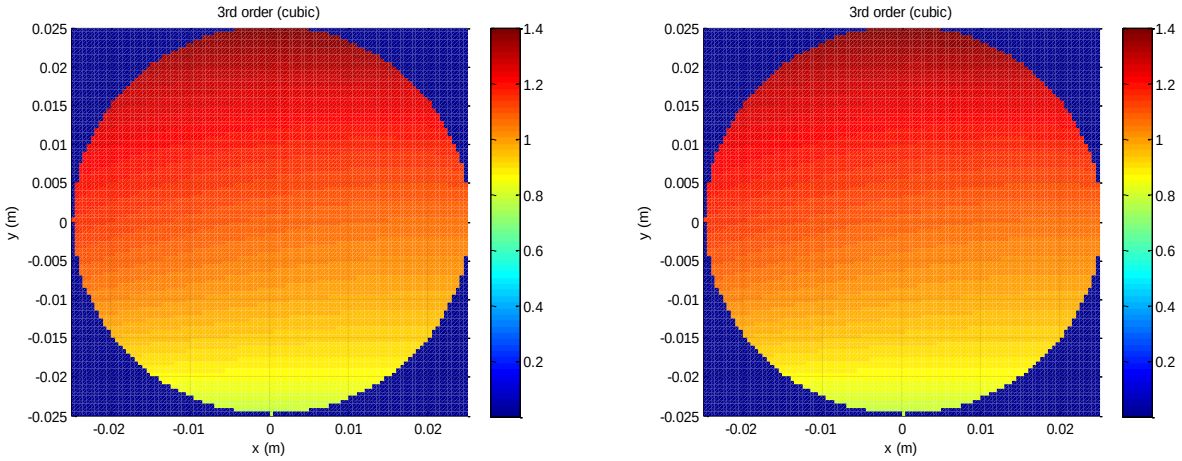

(d) Flow condition fm4

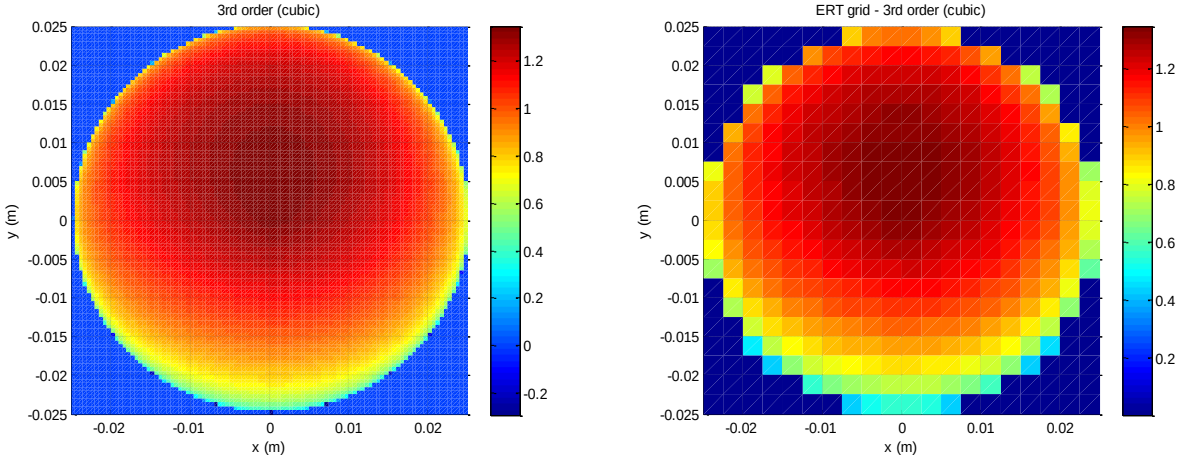

(e) Flow condition fm5

Fig. 7-27 Reconstructed velocity profiles for different velocity flow conditions (fm1 to fm5) by using the improved reconstruction algorithm. The water velocities in the colour bars are in ms-1

7.5.2.3 Comparison of experimental results for both reconstruction algorithms with reference measurement in oil-gas-water three phase flows

In order to quantify the performance of the IFT instrument, an important parameter that can be compared with a reference measurement is the volumetric flow rate of water $Q_{w,IFT}$ measured by the IFT instrument in oil-gas-water three phase flows. Referring to Section 7.3.2 and Equation 7-9, the parameter $Q_{w,IFT}$ is the sum over the cross-section of the product of the local water velocity in the i^{th} pixel $v_{w,i}$, the local water volume fraction flow in the i^{th} pixel $\alpha_{w,i}$ and the area of the i^{th} pixel A_i, which can be expressed as:

$$Q_{w,IFT} = \sum_{i=1}^{316} \alpha_{w,i} v_{w,i} A_i \qquad \text{Equation 7-19}$$

Note that the pixel arrangement is based on the ERT pixel configuration containing 316 pixels and shown in Fig. 7-6(b).

As mentioned in Section 7.5.1, the local dispersed phase volume fraction distribution is obtained using the dual-plane ERT system and can be used to give the local continuous phase volume fraction distribution $\alpha_{w,i}$ in the i^{th} pixel as follows:

$$\alpha_{w,i} = 1 - \frac{\alpha_{o+g,p1,i} + \alpha_{o+g,p2,i}}{2} \qquad \text{Equation 7-20}$$

where $\alpha_{o+g,p1,i}$ and $\alpha_{o+g,p2,i}$ are the dispersed phase volume fraction obtained using ERT at the first and second planes respectively (see Section 2.2.3 and Fig. 2-6).

For the purposes of quantitative comparison, the percentage difference between the measured water flow rate $Q_{w,IFT}$ and the reference water volumetric flow rate $Q_{w,ref}$ is defined as:

$$\varepsilon = \frac{Q_{w,IFT} - Q_{w,ref}}{Q_{w,ref}} \times 100\% \qquad \text{Equation 7-21}$$

The percentage difference in the water volumetric flow rate obtained from the IFT system in inclined oil-gas-water three phase flows are shown in Table 7-4 and Table 7-5 for the original (without use of an axisymmetric component) and improved (with use of an axisymmetric component) reconstruction algorithms respectively. The maximum percentage difference is -5.6% for both reconstruction algorithm results. It is worth noting that the percentage difference shown in Table 7-4 and Table 7-5 are highly reliant on the accuracy of the ERT system, which provides the measurement of local volume fraction of the dispersed phases. However, at present, the ERT system is a developing technique for multiphase flow measurement and has its own measurement error. Thus, it can be seen that the percentage difference in $Q_{w,IFT}$ might be reduced by using a more accurate measurement technique to obtain the local volume fraction of the dispersed phases. In addition, the reference water flow rate measurement, made using a commercial EMFM flowmeter, will have had an uncertainty of about 1% even if this commercial EMFM had been recently calibrated. This uncertainty in the reference measurement may have contributed to the observed differences between $Q_{w,IFT}$ and $Q_{w,ref}$.

Flow condition	Angle of inclination of working section	Reference measurement $Q_{w,ref}$ (m^3/hr)	Calculated $Q_{w,IFT}$ (m^3/hr) using original reconstruction algorithm	Percentage difference ε (%)
fm1	30 º	5	5.04	0.80
fm2	30 º	10	10.19	1.90
fm3	30 º	10	9.44	-5.60
fm4	45 º	5	5.23	4.60
fm5	60 º	5	5.02	0.40

Table 7-4 Percentage difference between reference measurement $Q_{w,ref}$ and water volumetric flow rate $Q_{w,IFT}$ based on velocity results calculated by using the reconstruction algorithm without use of an axisymmetric velocity component (see Section 3.6)

Flow condition	Reference measurement $Q_{w,ref}$(m^3/hr)	Calculated $Q_{w,IFT}$ (m^3/hr) using improved reconstruction algorithm	Percentage difference ε (%)
fm1	5	5.07	1.40
fm2	10	10.27	2.70
fm3	10	9.49	-5.10
fm4	5	5.23	4.60
fm5	5	5.05	1.00

Table 7-5 Percentage difference between reference measurement $Q_{w,ref}$ and water volumetric flow rate $Q_{w,IFT}$ based on velocity results calculated by using the reconstruction algorithm with use of an axisymmetric velocity component(see Section 3.7)

7.5.3 Reconstructed local water velocity distribution for vertical multiphase flow (oil-in-water two phase and oil-gas-water three phase) and water only single phase flow using IFT

In this section, the experiments were carried out with the working section vertical $\theta = 0°$, as described in Section 7.5.1. The IFT system and ERT system were installed in the working section, as shown in Fig. 7-2 (a). The flow conditions used in the experiments were according to Table 7-3. With reference to previous research by Lucas [90, 111, 117] and Zhang and Lucas [92], it is expected that, for either water-only single phase flow or oil-in-water (or gas-in-water) two phase flow, the local flow velocity and volume fraction distributions will be axisymmetric when the working section is vertical. Thus, the flow velocity profiles in the working section are expected to be very similar to the velocity profiles shown in Fig. 3-11. Note that the axisymmetric velocity profile can be described by using power law functions (see Equation 3-23).

In the same way, the corrected potential differences $U_j^{"}$ vs. j' for each flow condition were determined by using the method given in Section 7.4. Fig. 7-28 shows the corrected electrical potential difference distribution $U_j^{"}$ vs. j' in both uniform and non-uniform magnetic fields obtained under the different flow conditions shown in Table 7-3.

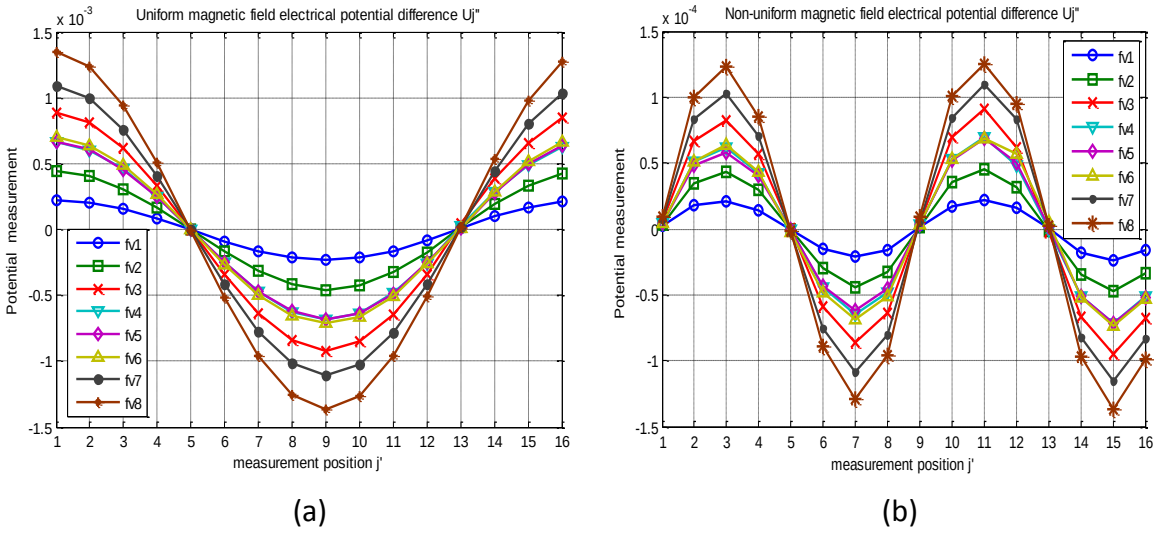

Fig. 7-28 Potential difference distribution U_j'' vs. j′ for all flow conditions shown in Table 7-3: (a) uniform magnetic field, (b) non-uniform magnetic field

It is clear in Fig. 7-28 that the corrected potential difference distribution $U_j^{"}$ vs. j' under the vertical flow condition is proportional to the flow velocity. As would be expected, the corrected potential difference distribution $U_j^{"}$ vs. j' approximates to a sine waveform. This is due to the fact that the flow velocity profiles for all flow conditions are axisymmetric (see Section 3.5). By applying the DFT to the corrected potential differences $U_j^{"}$ for both uniform and non-uniform magnetic fields, we see that the real part of the DFT component X_n (see Equation 3-60) in the uniform magnetic field is plotted in Fig. 7-29 (a) and the imaginary parts of DFT component X_n in the non-uniform magnetic field is plotted Fig. 7-29 (b). From Fig. 7-29 (a), it can be seen that the magnitude of X_1 is much higher than the remaining components. This is because the potential difference distribution $U_j^{"}$ under a uniform magnetic field is a full one cycle cosine waveform when the velocity profile is approximate to axisymmetric. In a non-uniform magnetic field, the potential difference distribution $U_j^{"}$ is a two cycle sine waveform. As shown in Fig. 7-29 (b), the imaginary parts of X_2 are greater than the remaining DFT components.

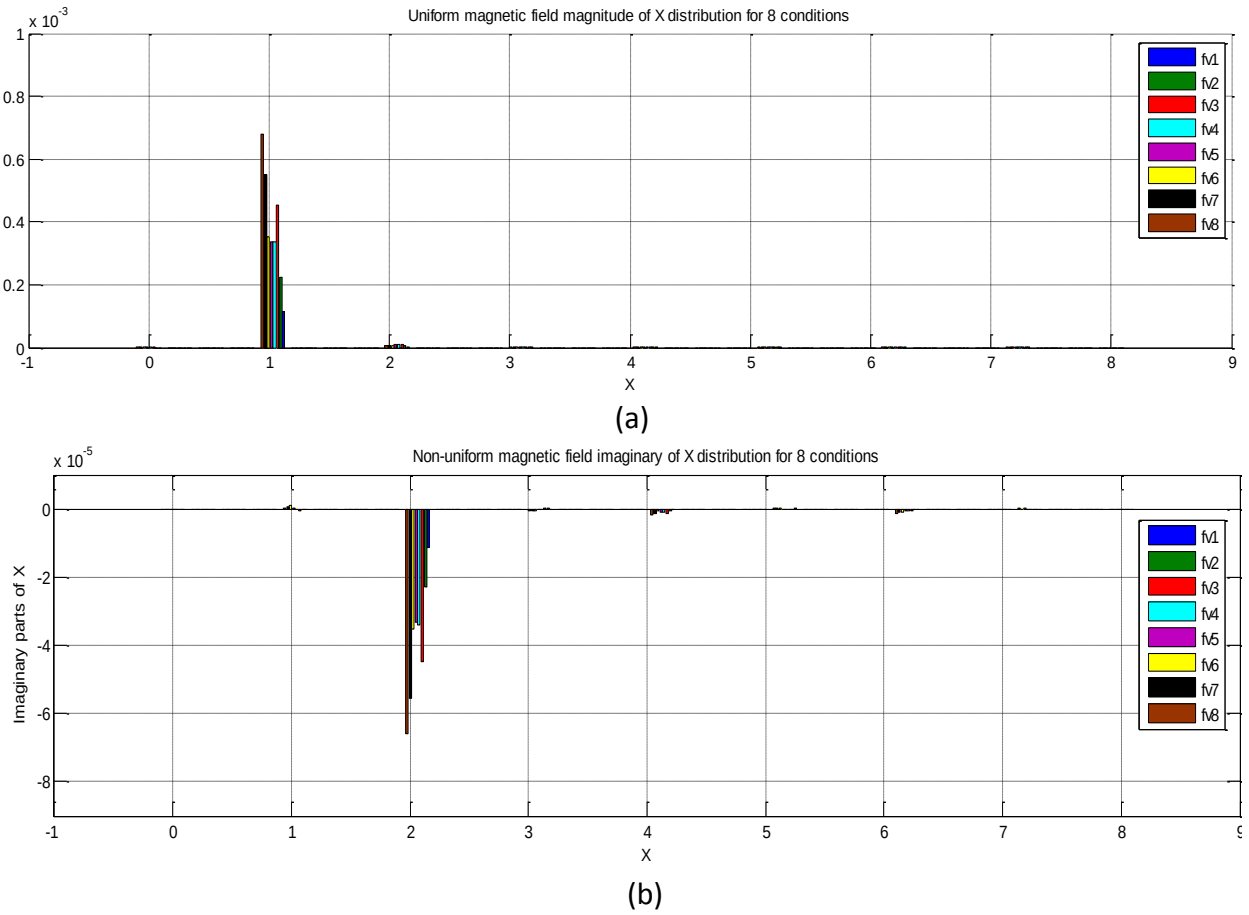

Fig. 7-29 (a) The real parts of the DFT components for a uniform magnetic field, (b) the imaginary parts of the DFT components for a non-uniform magnetic field.

7.5.3.1 Reconstructed velocity profiles for water only single phase flow

In Section 7.5.2, it was shown the local water velocity profiles for inclined three phase flow were reconstructed by using two different reconstruction algorithms (i.e. with and without use of an axisymmetric component). Furthermore, in order to quantify the accuracy of the reconstructed velocity results for both reconstruction algorithms, Section 7.5.2.3 also shows the percentage difference of water volumetric flow rate for all flow conditions and for both reconstruction algorithms. Note that the reference water volumetric flow rate measurements were obtained using the commercial EMFM, as described in Table 7-1.

For the experiments carried out at SGR in vertical flow conditions, the experimental results were investigated using the same procedures as in Section 7.5.2.

Let us now analyse the performance of the IFT system in the water-only single phase flow in vertical flow conditions (fv1 to fv4). The corrected electrical potential difference distribution $U_j^{''}$ vs. j' in Fig. 7-28 for uniform and non-uniform magnetic fields in different flow conditions was used to perform velocity profile reconstruction using the two different algorithms (see Section 3.6 and 3.7). For the convenience of comparison, the reconstructed water velocity profiles using both reconstruction algorithms are presented in the same diagram. Taking flow condition fv1 as an example, the reconstructed water velocity profiles for the two reconstruction algorithms (with and without use of an axisymmetric component) are respectively shown in Fig. 7-31 (a) and (b) using both the high resolution and low resolution grids to present the data. Similar results for fv2 to fv4 are presented in Fig. 7-32 to Fig. 7-34 respectively. From inspection of Fig. 7-31 (b), Fig. 7-33 (b) and Fig. 7-34 (b), it can be seen that, for the reconstruction algorithm without the use of an axisymmetric velocity component, the reconstructed velocity near the bottom side of the pipe wall (i.e. y = -0.02m to -0.025m) is always higher than the velocity in the centre of the pipe. However, with reference to Lucas [90], Zhang and Lucas [92] and Leeungculsatien [1], it is apparent that, in such a vertical water-only single phase flow, the reconstructed velocity profile would be expected to be an axisymmetric velocity profile where the highest local water velocity is at the centre of the pipe and the velocity gradually decreases towards the pipe wall. Thus, the reconstructed velocity profiles shown in Fig. 7-31 (b), Fig. 7-33(b) and Fig. 7-34 (b) are unrealistic. The reason for this is because each velocity component only changes in the direction $\theta_{Q,n}$ (see Fig. 3-21) and is constant along lines orthogonal to this direction (see also Section 3.6). Note that the reconstructed velocity profile shown in Fig. 7-32 (b) is completely uniform, which is also unrealistic.

By applying the reconstruction algorithm with the use of an axisymmetric component (see Section 3.7), the reconstructed velocity profiles for flow condition fv1 to fv4 are presented in Fig. 7-31 (a), Fig. 7-32 (a), Fig. 7-33 (a) and Fig. 7-34 (a).

Similar local water velocity distributions to Fig. 7-31 (a), Fig. 7-32 (a), Fig. 7-33 (a) and Fig. 7-34 (a) obtained from Pitot stati tube have also been reported by Leeungculsatien [1] using the

University of Huddersfield multiphase flow lab facility (see Fig. 7-30). It can therefore be seen that the reconstructed water velocity profiles which were obtained using the reconstruction algorithm which assumes an axisymmetric velocity component are similar to those of Leeungculsatien's [1] work. Note that the velocity profiles shown in Fig. 7-30 were obtained from an 80mm internal diameter pipe and 3m working section.

By substituting the local water velocity $v_{w,i}$ with the sub-region area A_i, according to Equation 7-19, the water volumetric flow rate $Q_{w,IFT}$ was calculated for the water-only single phase flow (fv1 to fv4). From Equation 7-21, the volumetric flow rate percentage difference ε was calculated for each flow condition by using the results from the IFT system and the reference water volumetric flow rates $Q_{w,ref}$ obtained using the commercial EMFM (see Table 7-1). The results are shown in Table 7-6 and Table 7-7, which repectively show results obtained for the reconstruction algorithms without and with the axisymmetric velocity component.

Inspection of Table 7-6 shows that the percentage difference ε of water volumetric flow rate in vertical water-only single phase flow varied from -2.25% to 0.25 %. The standard deviation of this percentage difference ε is 0.97%. From Table 7-7, it can be seen that, by using the reconstruction algorithm with use of an axisymmetric component, the percentage difference ε of water volumetric flow rate in all flow conditions varied from -0.25% to 1.25%. The standard deviation of this percentage difference ε is 0.91%, which is smaller than for the results which do not assume an axisymmetric velocity component. It may therefore be tentatively concluded that for single phase vertical flow, the reconstruction algorithm which assumes an axisymmetric velocity component gives rise to more realistic velocity profiles.

Flow condition	Angle of inclination of working section	Reference measurement $Q_{w,ref}$(m^3/hr)	Calculated $Q_{w,IFT}$ (m^3/hr) using original reconstruction algorithm	Percentage difference ε (%)
fv1	0 º	4	4.01	0.25
fv2	0 º	8	7.84	-2
fv3	0 º	16	15.77	-1.44
fv4	0 º	12	11.73	-2.25

Table 7-6 Percentage difference between reference measurement $Q_{w,ref}$ and water volumetric flow rate $Q_{w,IFT}$ based on velocity results calculated by using the reconstruction algorithm without use of an axisymmetric velocity component (see Section 3.6)

Flow condition	Angle of inclination of working section	Reference measurement $Q_{w,ref}$(m^3/hr)	Calculated $Q_{w,IFT}$ (m^3/hr) using original reconstruction algorithm	Percentage difference ε (%)
fv1	0 º	4	4.05	1.25
fv2	0 º	8	7.94	-0.75
fv3	0 º	16	15.96	-0.25
fv4	0 º	12	11.86	-1.17

Table 7-7 Percentage difference between reference measurement $Q_{w,ref}$ and water volumetric flow rate $Q_{w,IFT}$ based on velocity results calculated by using the reconstruction algorithm with use of an axisymmetric velocity component(see Section 3.7)

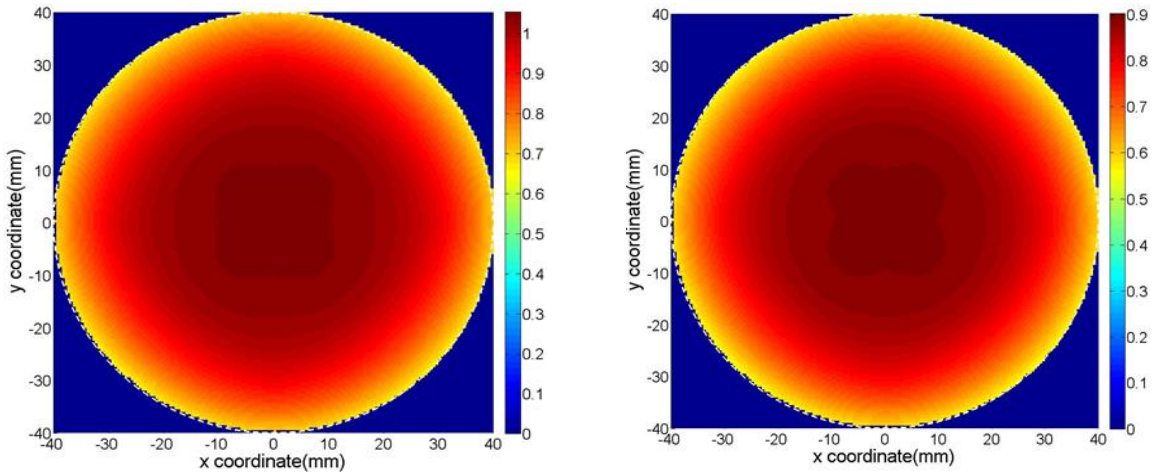

a) Flow condition Q_w=16.17m^3/hr *b*) Flow condition Q_w=13.86m^3/hr

Fig. 7-30 Local water velocity distributions in water only single phase flow in vertical pipe as reported by Leeungculsatien [1]. The water velocity in the colour bar is in ms^{-1}

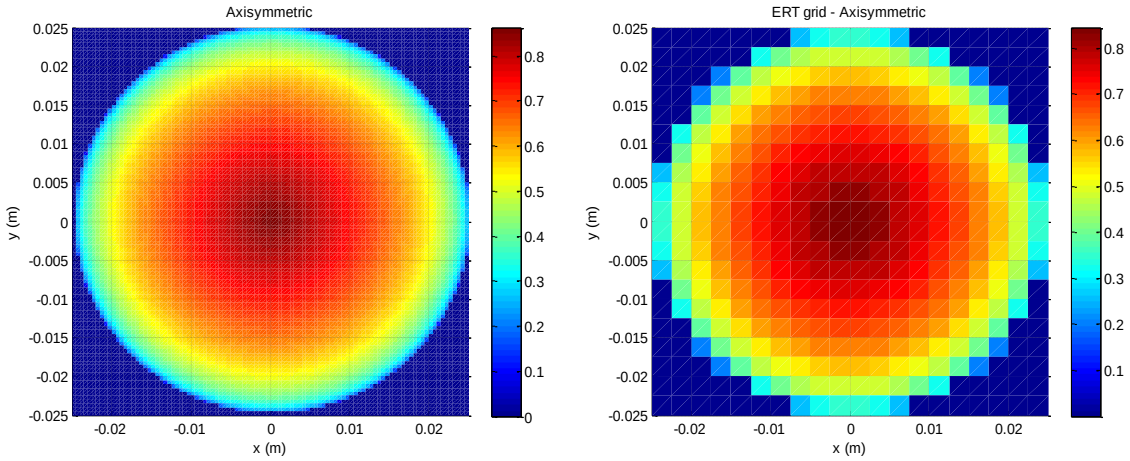

(a) Reconstruction algorithm with use of axisymmetric component

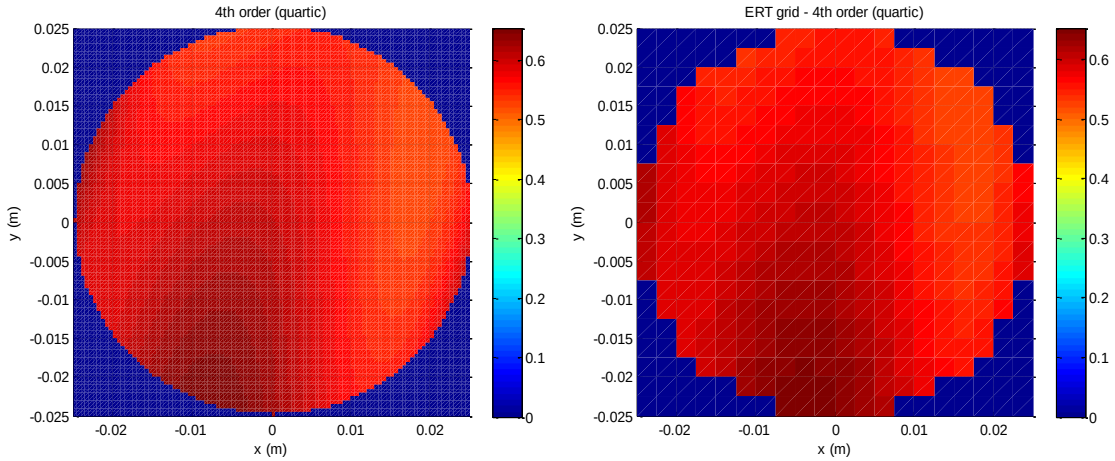

(b) Reconstruction algorithm without use of axisymmetric component

Fig. 7-31 Flow condition fv1: (a) reconstructed velocity profile using the reconstruction algorithm with use of an axisymmetric component; (b) reconstructed velocity profile using the reconstruction algorithm without use of an axisymmetric component. Note that the water velocity profile with higher resolution (100×100) is on the left of the figure, and the water velocity profile with low resolution (20×20 ERT grid) is on the right. The water velocities in the colour bars are in ms^{-1}

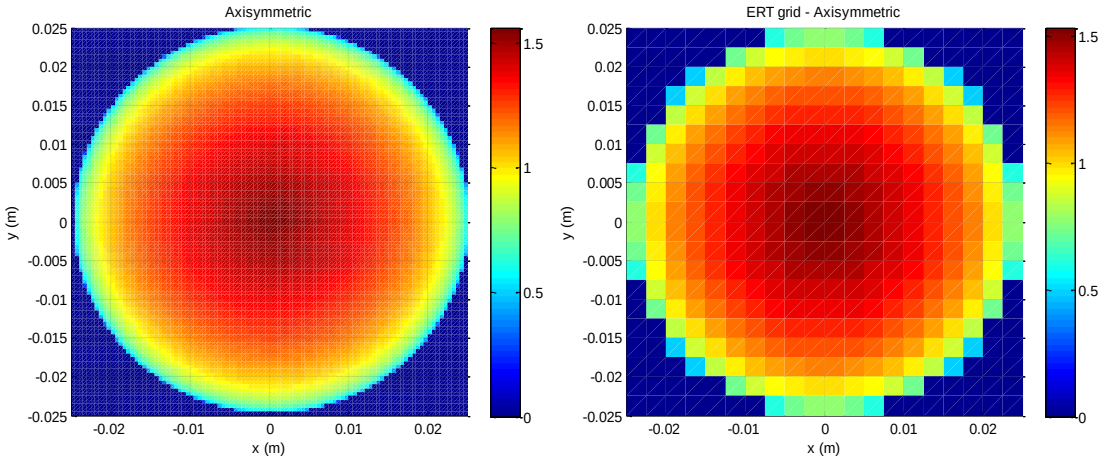

(a) Reconstruction algorithm with use of axisymmetric component

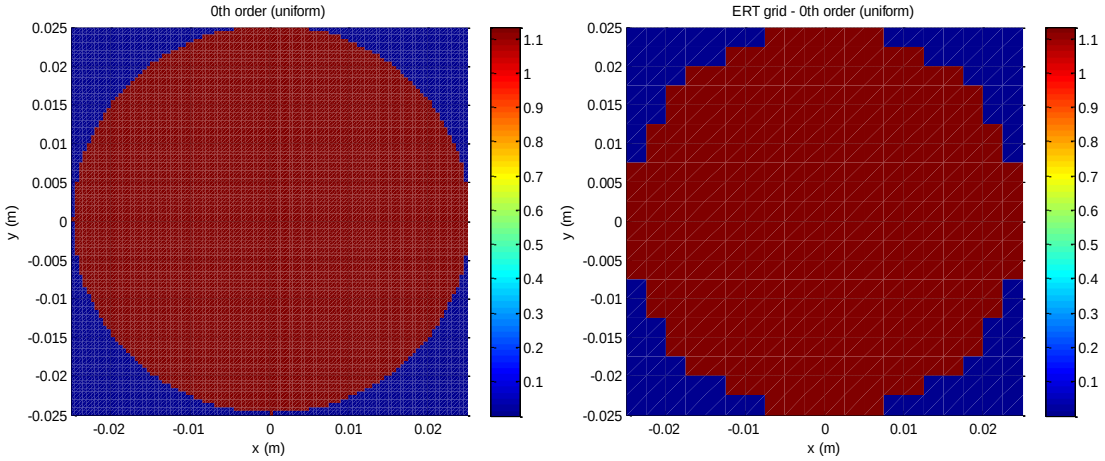

(b) Reconstruction algorithm without use of axisymmetric component

Fig. 7-32 Flow condition fv2: (a) reconstructed velocity profile using the reconstruction algorithm with use of an axisymmetric component; (b) reconstructed velocity profile using the reconstruction algorithm without use of an axisymmetric component. Note that the water velocity profile with higher resolution (100×100) is on the left of the figure and the water velocity profile with low resolution (20×20 ERT grid) is on the right. The water velocities in the colour bars are in ms^{-1}

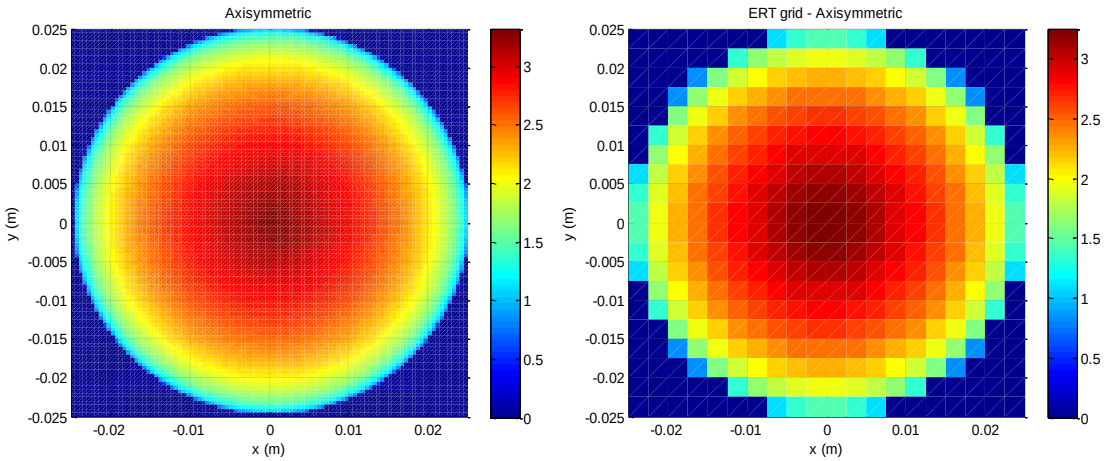

(a) Reconstruction algorithm with use of axisymmetric component

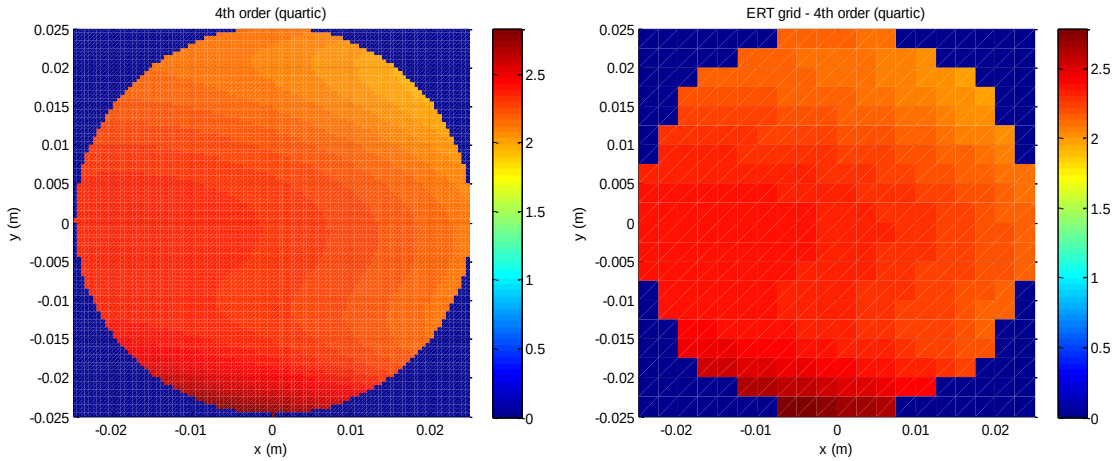

(b) Reconstruction algorithm without use of axisymmetric component

Fig. 7-33 Flow condition fv3: (a) reconstructed velocity profile using the reconstruction algorithm with use of an axisymmetric component; (b) reconstructed velocity profile using the reconstruction algorithm without use of an axisymmetric component. Note that the water velocity profile with higher resolution (100×100) is on the left of the figure and the water velocity profile with low resolution (20×20 ERT grid) is on the right. The water velocities in the colour bars are in ms^{-1}

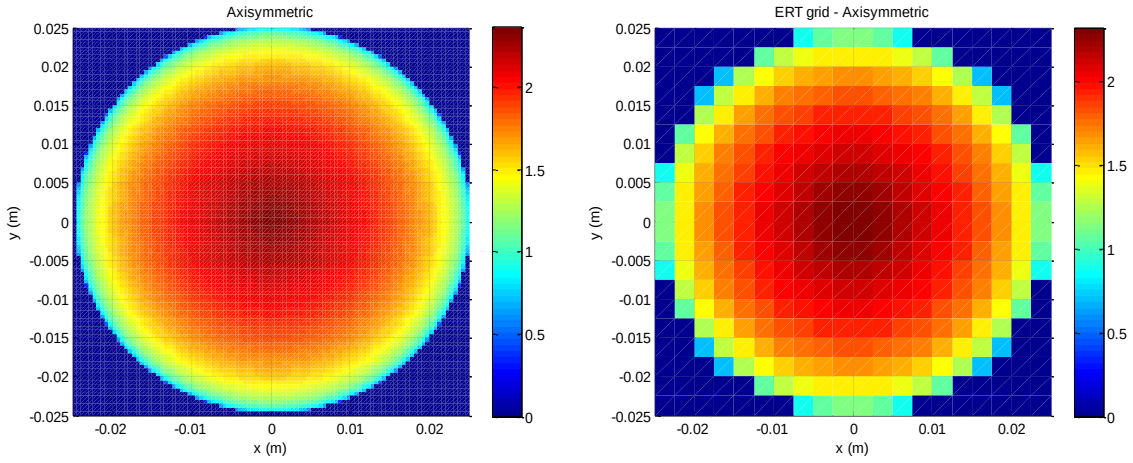

(a) Reconstruction algorithm with use of axisymmetric component

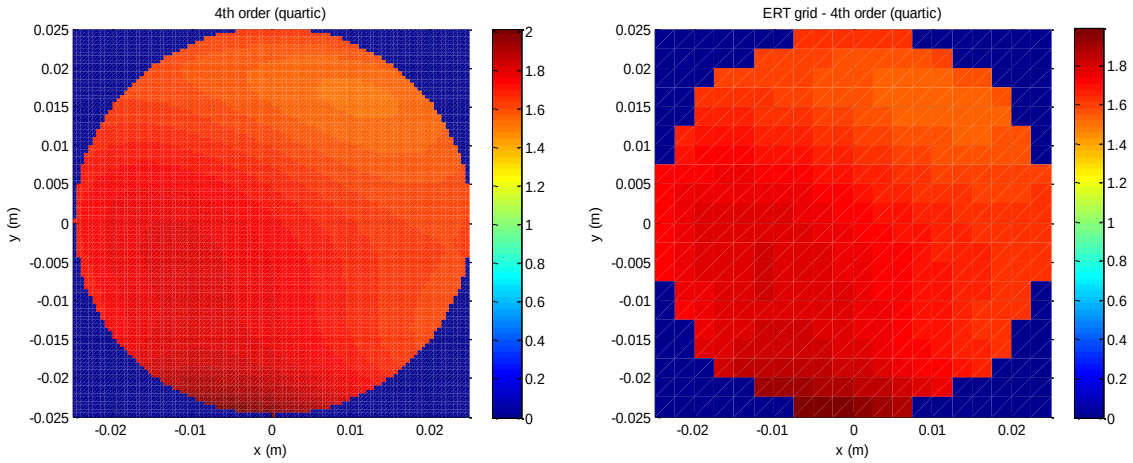

(b) Reconstruction algorithm without use of axisymmetric component

Fig. 7-34 Flow condition fv4: (a) reconstructed velocity profile using the reconstruction algorithm with use of an axisymmetric component; (b) reconstructed velocity profile using the reconstruction algorithm without use of an axisymmetric component. Note that the water velocity profile with higher resolution (100×100) is on the left of the figure and the water velocity profile with low resolution (20×20 ERT grid) is on the right. The water velocities in the colour bars are in ms-1

7.5.3.2 Reconstructed velocity profiles for oil-in-water two phase flow and oil-gas-water three phase flow in a vertical pipe.

In this section, in order to investigate the reconstructed water velocity profiles in oil-in-water two phase and oil-gas-water three phase flow, the procedure used was the same as in Section 7.5.3.1. The water velocity profiles for each flow condition fv5 to fv8 in Table 7-3 were obtained by using the reconstruction algorithm without the use of an axisymmetric component (see Section 3.6) and the reconstruction algorithm with the use of an axisymmetric component (see Section 3.7), respectively. Note that for the results in this section the working section was vertical.

This section describes experimental tests carried out using the same experimental set-up as shown in Section 7.5.2 for the IFT and ERT systems (see Section 3.6 and 3.7), respectively, to obtain the local water velocity distribution and local dispersed phase volume fraction distribution for the flow conditions, from fv5 to fv8. As explained in Section 7.5.2.1, the local water velocity distribution with ERT grid will be used in conjunction with results obtained by the ERT device for determining the water volumetric flow rate according to Equation 7-22. The mean water volume fraction $\overline{\alpha}_w$ and mean dispersed phase (oil or oil and gas) volume fraction $\overline{\alpha}_o$ or $\overline{\alpha}_{o+g}$ were calculated (see Section 7.5.2.1) and are presented at the bottom of each figure.

The water velocity profiles for flow conditions fv5 to fv8 reconstructed by using the first reconstruction algorithm without use of an axisymmetric component (See Section 3.6) are shown in Fig. 7-37 (b), Fig. 7-38 (b), Fig. 7-39 (b) and Fig. 7-40 (b). The colour scale represents the local water velocity $v_{w,i}$ where blue represents minimum velocity, green represents middle values of the velocity and red represents maximum values of velocity. By inspecting these reconstructed water velocity profiles, as shown in Fig. 7-37 (b) to Fig. 7-40 (b), it can be seen that there is a similar behaviour for the different water velocity profiles. In all of the flow conditions (fv5 to fv8), the maximum water velocity occurs at the regions of the pipe near electrode 11 (see Fig. 3-20) and lower values of water velocity occur at the region of the pipe near electrode 4. However, the local dispersed phase volume fraction distribution for the flow conditions fv5 to fv8 shown in Fig. 7-36 is essentially axisymmetric and maximum values of the local dispersed phase volume fraction $\alpha_{o+g,i}$ or $\alpha_{o,i}$ occur close to the centre of the pipe cross-

section. These volume fraction profiles have a good agreetment with Panagiotopuolos's [117] results, as shown in Fig. 7-35. As described in Section 7.5.2, because the density of oil and gas is smaller than water, the dispersed phase (oil or oil and gas) travels faster than the water phase. This would force the water in front of oil or oil and gas bubbles to move faster. Furthermore, Govier and Aziz [118] found that there is a tendency for the large bubbles to rise faster than the small bubbles in two phase flow. This explains why higher values of water velocity are expected to occur at position where higher values of the local dispersed phase volume fraction are located.

The reconstructed local water velocity distributions shown in Fig. 7-37 (a) to Fig. 7-40 (a), were obtained using the reconstruction algorithm which assumes an axisymmetric velocity component, for flow conditions fv5 to fv8. These velocity profiles are axisymmetric, which is similar to the local dispersed phase volume fraction distribution shown in Fig. 7-36.

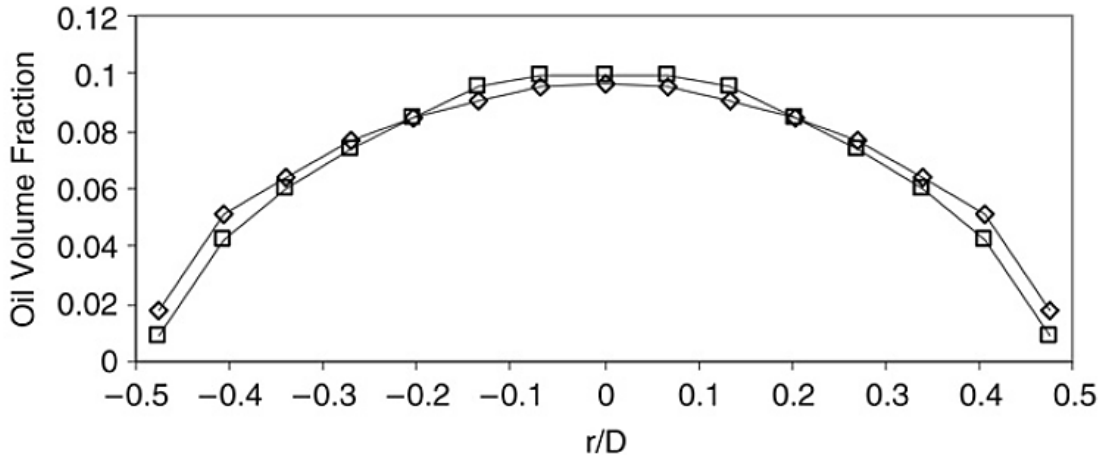

Fig. 7-35 Local oil volume fraction distribution in oil-in-water two phase flow in vertical pipe from Panagiotopuolos [117].

By using the local water velocity distributions shown in Fig. 7-37 to Fig. 7-40, and the local water volume fraction distributions shown in Fig. 7-36 with Equation 7-19, the water volumetric flow rates, $Q_{w,IFT}$, using different velocity reconstruction algorithms were calculated and are shown in Table 7-8 and Table 7-9.

From the calculated values of $Q_{w,IFT}$, as shown in Table 7-8, it can be seen that the percentage difference ε in $Q_{w,IFT}$ with respect to the reference water volumetric flow rate $Q_{w,ref}$ for the reconstruction algorithm which does not assume an axisymmetric velocity component varied from -4.53% to 0.63%. The standard deviation of the this percentage difference was 1.88%.

For the calculated value $Q_{w,IFT}$, as shown in Table 7-9, the percentage difference ε varied from -3.53% to 0.88% for the reconstruction algorithm which assumes an axisymmetric velocity component. The standard deviation of the percentage difference is equal to 1.65%. It is clear then that , for the vertical flows decribed in this section, the errors associated with $Q_{w,IFT}$ are smaller when the reconstruction algorithm which assumes an axisymmetric velocity component is used.

Flow condition	Angle of inclination of working section	Reference measurement $Q_{w,ref}$(m^3/hr)	Calculated $Q_{w,IFT}$ (m^3/hr) using original reconstruction algorithm	Percentage difference ε (%)
fv5	0 º	8	8.05	0.63
fv6	0 º	10	9.91	-0.9
fv7	0 º	15	14.32	-4.53
fv8	0 º	15	14.81	-1.27

Table 7-8 Percentage difference between reference measurement $Q_{w,ref}$ and water volumetric flow rate $Q_{w,IFT}$ based on velocity results calculated by using the reconstruction algorithm without use of an axisymmetric velocity component (see Section 3.6)

Flow condition	Angle of inclination of working section	Reference measurement $Q_{w,ref}$(m^3/hr)	Calculated $Q_{w,IFT}$ (m^3/hr) using original reconstruction algorithm	Percentage difference ε (%)
fv5	0 º	8	8.07	0.88
fv6	0 º	10	10.00	0
fv7	0 º	15	14.47	-3.53
fv8	0 º	15	14.87	-0.87

Table 7-9 Percentage difference between reference measurement $Q_{w,ref}$ and water volumetric flow rate $Q_{w,IFT}$ based on velocity results calculated by using the reconstruction algorithm with use of an axisymmetric velocity component(see Section 3.7)

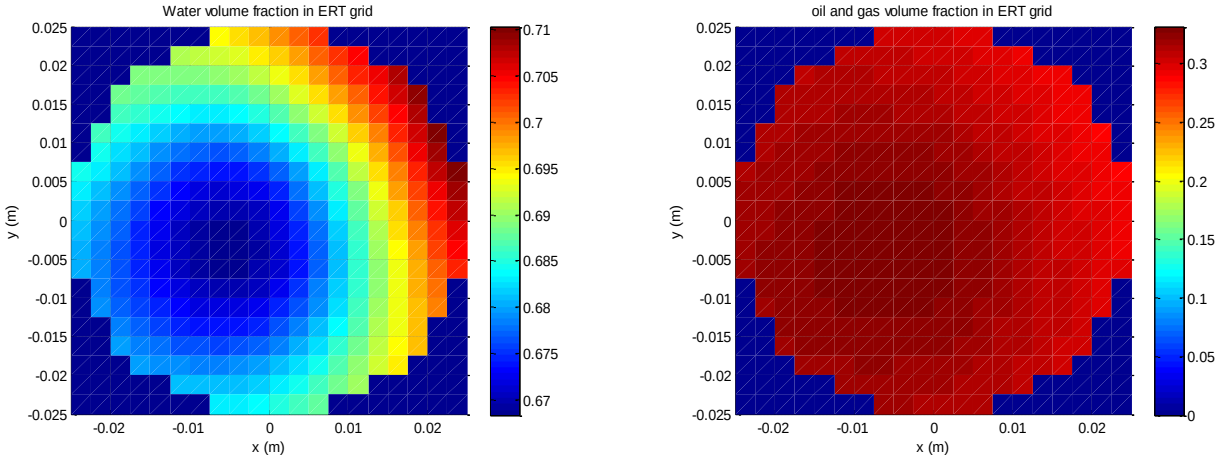

(a) Flow condition fv5 $\overline{\alpha}_w = 0.685 \quad \overline{\alpha}_o = 0.315$

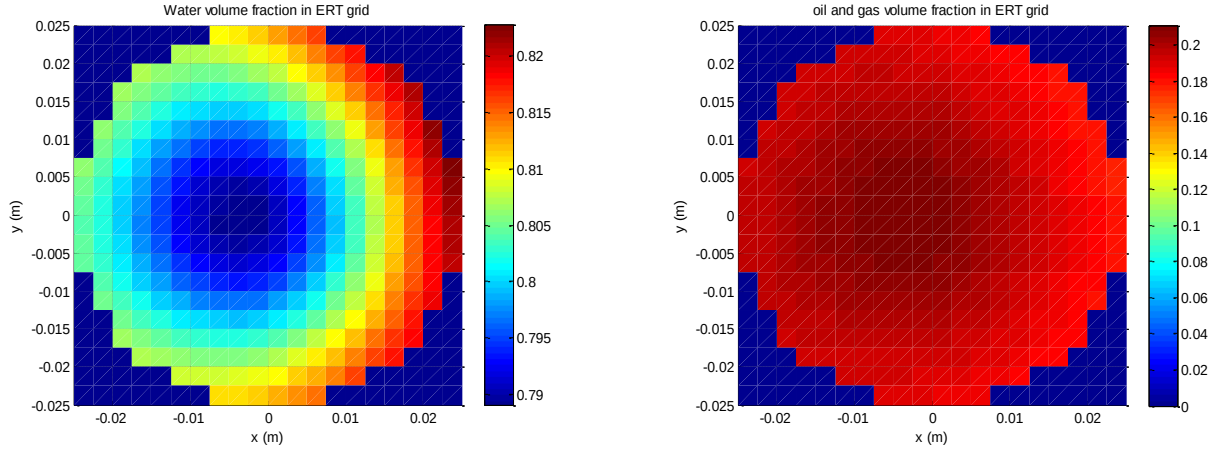

(b)Flow condition fv6 $\overline{\alpha}_w = 0.8045 \quad \overline{\alpha}_{o+g} = 0.1955$

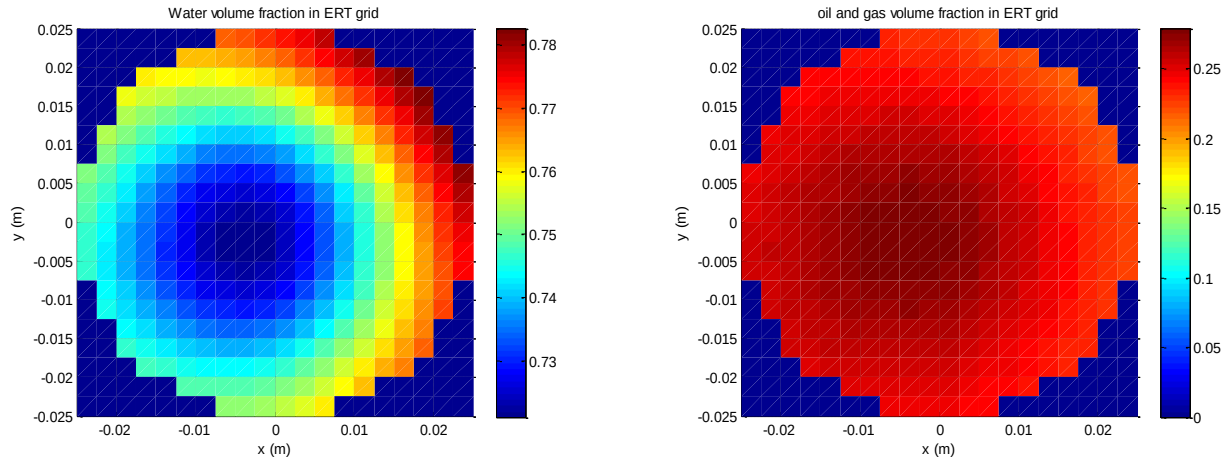

(c) Flow condition fv7 $\overline{\alpha}_w = 0.7489$ $\overline{\alpha}_{o+g} = 0.2511$

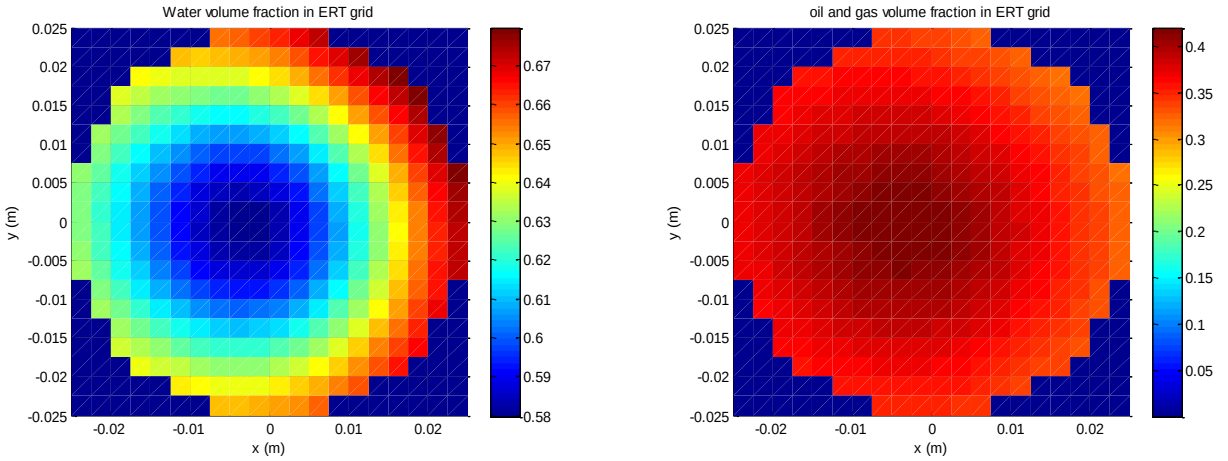

(d) Flow condition fv8 $\overline{\alpha}_w = 0.6276$ $\overline{\alpha}_{o+g} = 0.3724$

Fig. 7-36 Local water volume fraction distribution and local dispersed phase (oil or oil and gas) volume fraction distribution for flow conditions fv5 to fv8.

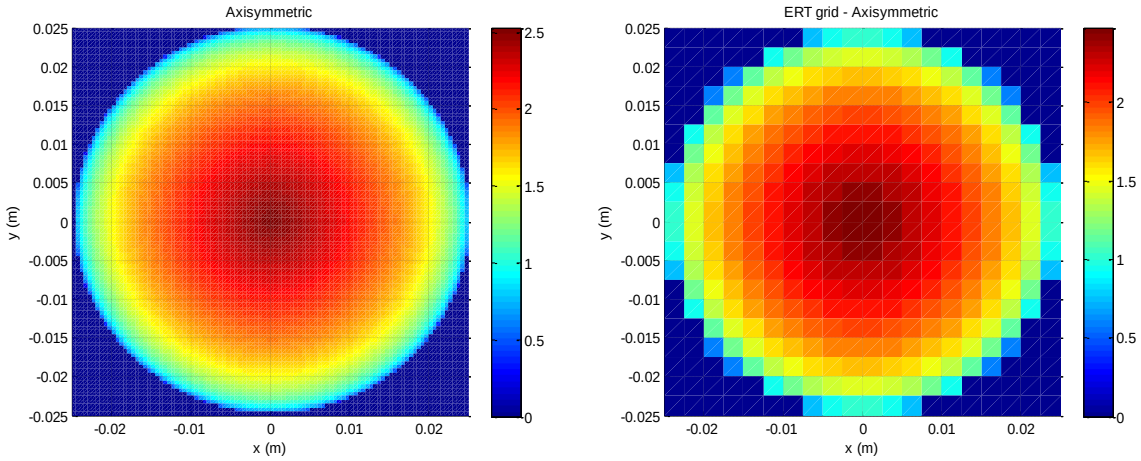

(a) Reconstruction algorithm with use of an axisymmetric component

$\overline{\alpha}_w = 0.685$ $\overline{\alpha}_o = 0.315$

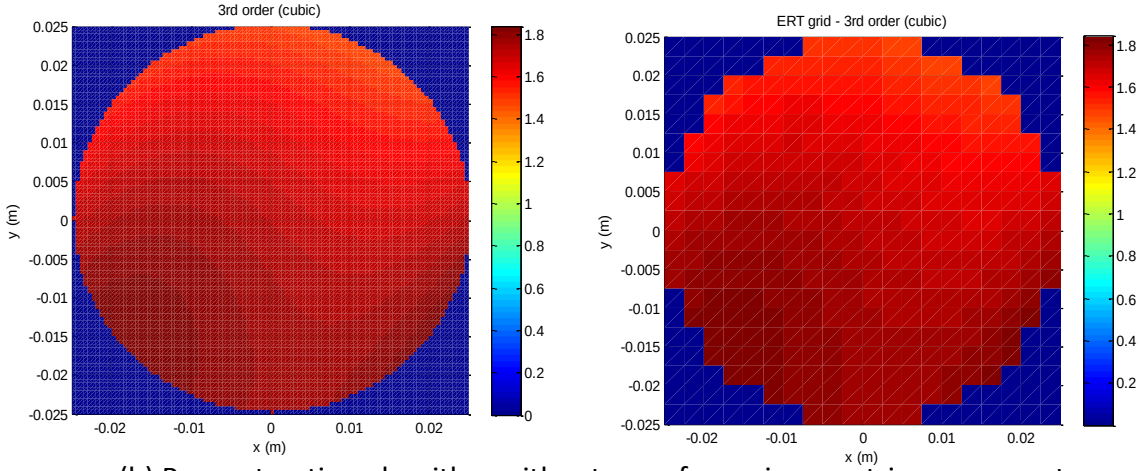

(b) Reconstruction algorithm without use of an axisymmetric component

$\overline{\alpha}_w = 0.685$ $\overline{\alpha}_o = 0.315$

Fig. 7-37 Flow condition fv5: (a) reconstructed velocity profile using the reconstruction algorithm with use of an axisymmetric component; (b) reconstructed velocity profile using the reconstruction algorithm without use of an axisymmetric component. Note that the water velocity profile with higher resolution (100×100) is on the left of the figure and the water velocity profile with low resolution (20×20 ERT grid) is on the right. The water velocities in the colour bar are in ms^{-1}

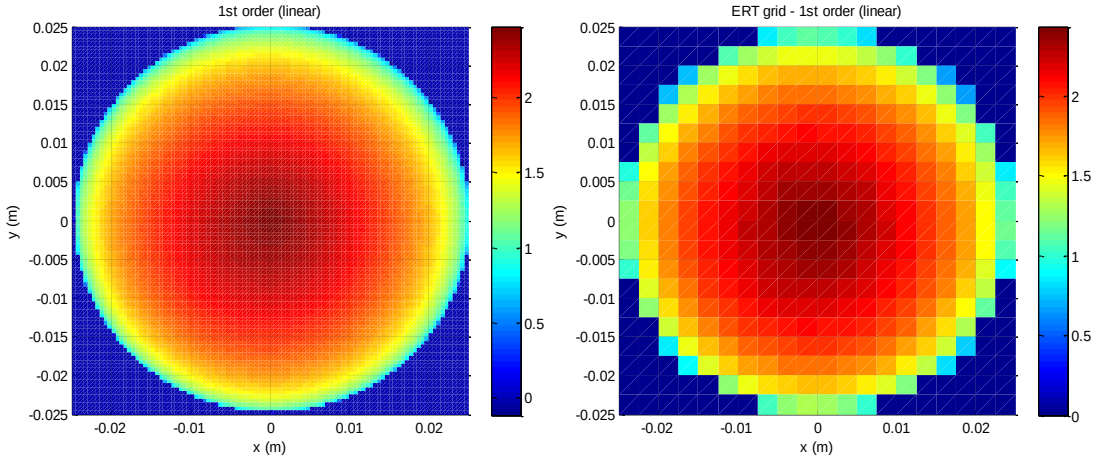

(a) Reconstruction algorithm with use of an axisymmetric component

$$\overline{\alpha}_w = 0.8045 \quad \overline{\alpha}_{o+g} = 0.1955$$

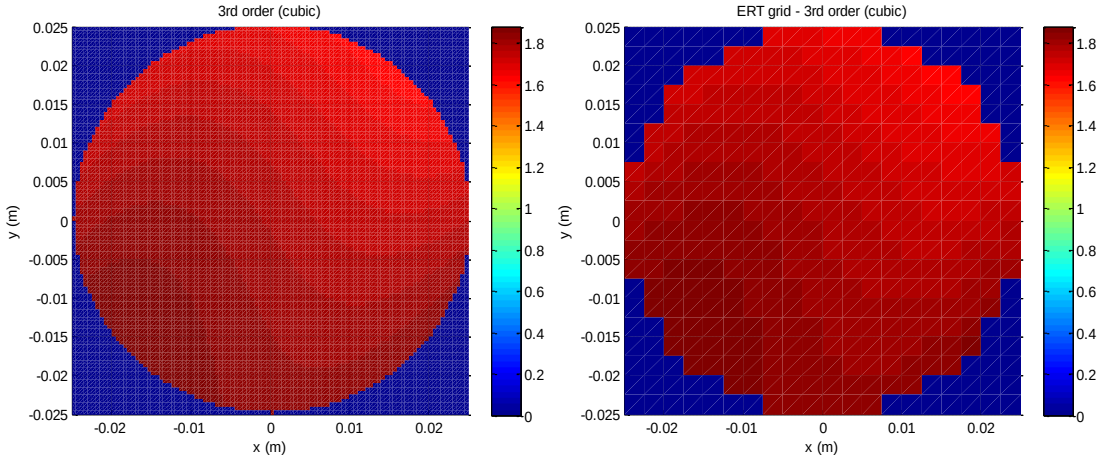

(b) Reconstruction algorithm without use of an axisymmetric component

$$\overline{\alpha}_w = 0.8045 \quad \overline{\alpha}_{o+g} = 0.1955$$

Fig. 7-38 Flow condition fv6: (a) reconstructed velocity profile using the reconstruction algorithm with use of an axisymmetric component; (b) reconstructed velocity profile using the reconstruction algorithm without use of an axisymmetric component. Note that the water velocity profile with higher resolution (100×100) is on the left of the figure and the water velocity profile with low resolution (20×20 ERT grid) is on the right. The water velocities in the colour bar are in ms^{-1}

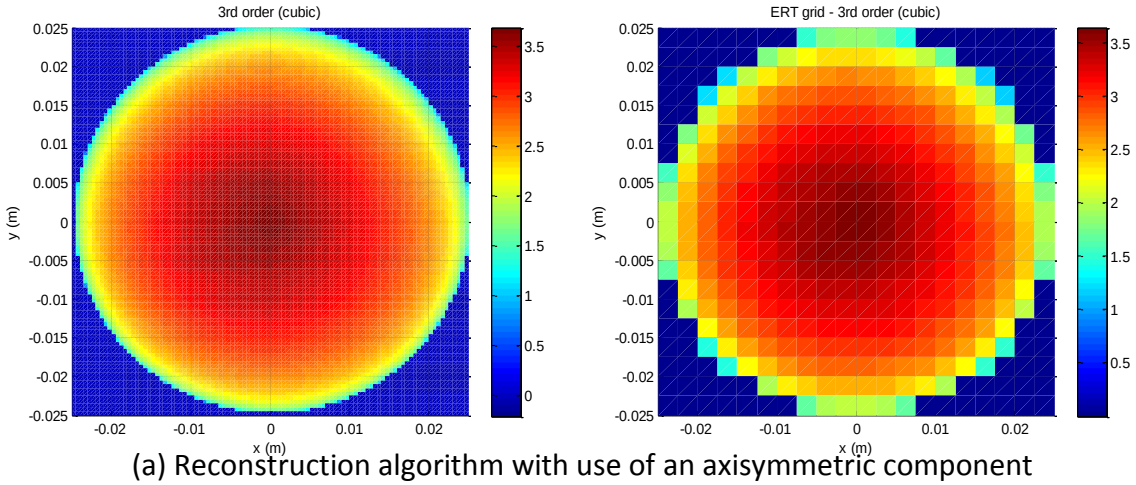

(a) Reconstruction algorithm with use of an axisymmetric component

$$\overline{\alpha}_w = 0.7489 \quad \overline{\alpha}_{o+g} = 0.2511$$

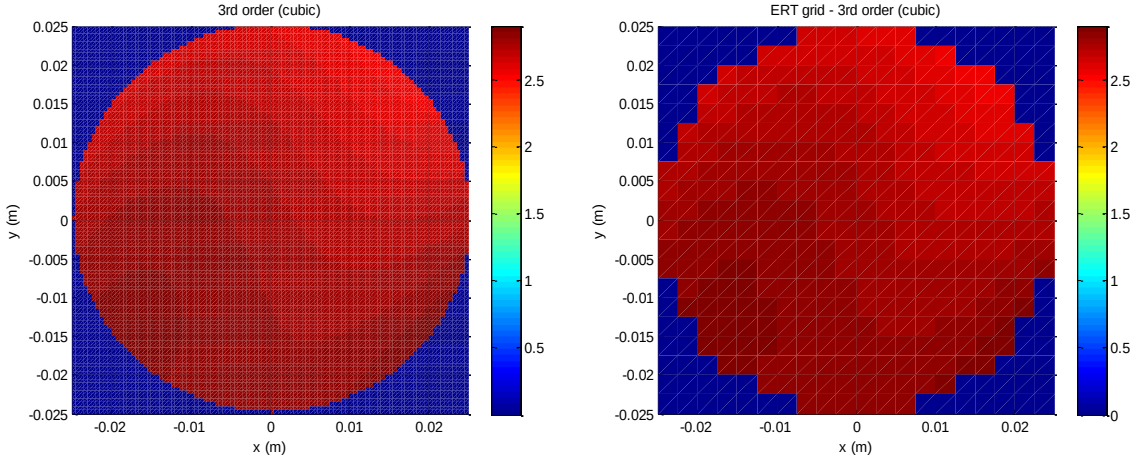

(b) Reconstruction algorithm without use of an axisymmetric component

$$\overline{\alpha}_w = 0.7489 \quad \overline{\alpha}_{o+g} = 0.2511$$

Fig. 7-39 Flow condition fv7: (a) reconstructed velocity profile using the reconstruction algorithm with use of an axisymmetric component; (b) reconstructed velocity profile using the reconstruction algorithm without use of an axisymmetric component. Note that the water velocity profile with higher resolution (100×100) is on the left of the figure and the water velocity profile with low resolution (20×20 ERT grid) is on the right. The water velocities in the colour bar are in ms^{-1}

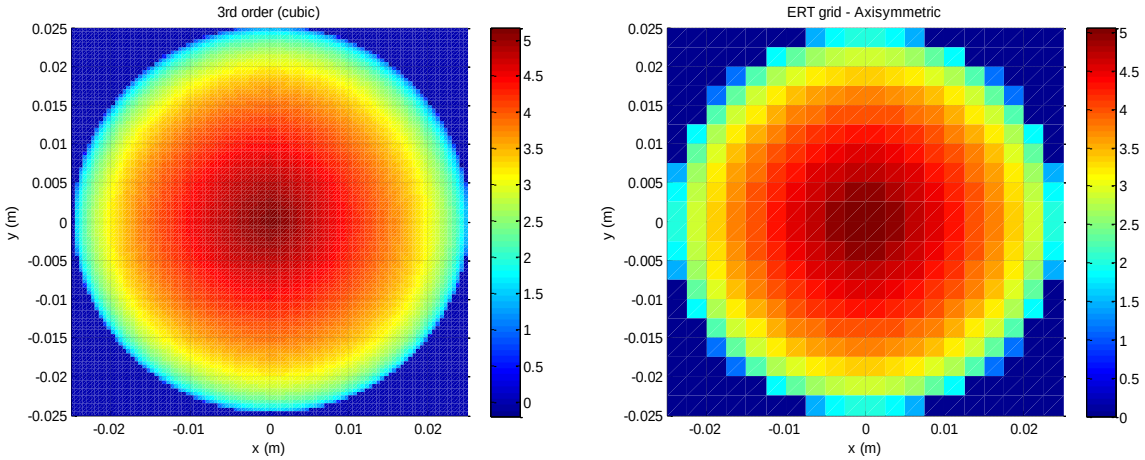

(a) Reconstruction algorithm with use of an axisymmetric component

$\overline{\alpha}_w = 0.6276 \quad \overline{\alpha}_{o+g} = 0.3724$

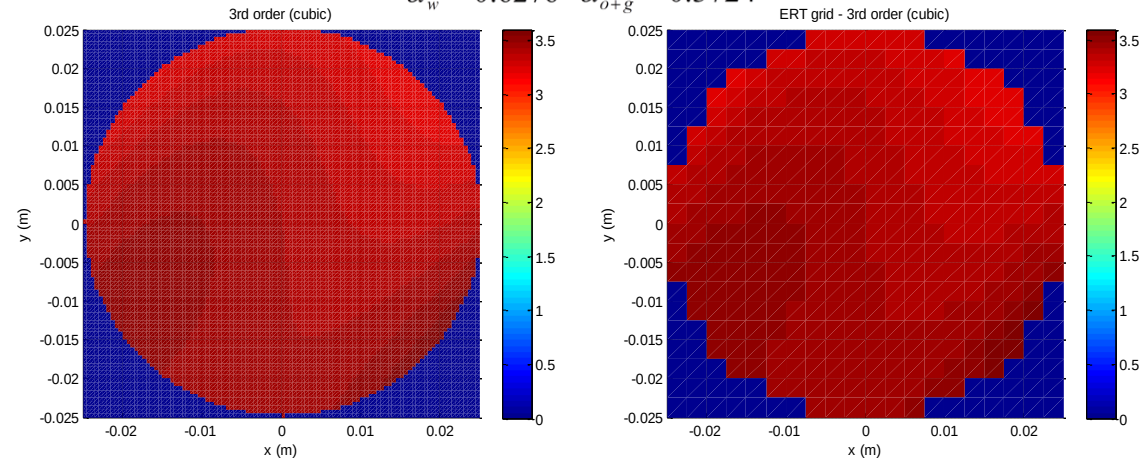

(b) Reconstruction algorithm without use of an axisymmetric component

$\overline{\alpha}_w = 0.6276 \quad \overline{\alpha}_{o+g} = 0.3724$

Fig. 7-40 Flow condition fv8: (a) reconstructed velocity profile using the reconstruction algorithm with use of an axisymmetric component; (b) reconstructed velocity profile using the reconstruction algorithm without use of an axisymmetric component. Note that the water velocity profile with higher resolution (100×100) is on the left of the figure and the water velocity profile with low resolution (20×20 ERT grid) is on the right. The water velocities in the colour bar are in ms^{-1}

7.5.4 Discussion of selection of the original and the improved velocity profile reconstruction algorithms

Comparison of results presented in Table 7-4 to Table 7-9 show that the calculated water flow rate using the first reconstruction algorithm without use of an axisymmetric component and the second reconstruction algorithms with use of an axisymmetric component gave errors that were well within the ±10% usually considered acceptable in multiphase flow measurement applications.

In order to investigate the reliability of both reconstruction algorithms, Fig. 7-41 and Fig. 7-42 show the scatter plot of the error, ε, derived from the first reconstruction algorithm (without use of an axisymmetric component) results and the second reconstruction algorithms (with use of an axisymmetric component) results for all flow experiments (see Table 7-2 and Table 7-3). Note that the percentage difference ε vs. inclination angle θ plot shown in Fig. 7-41 is for the multiphase flow conditions fm1 to fm5 and fv5 to fv8. Note also that the plot of the percentage difference ε vs. inclination angle θ in Fig. 7-42 was obtained from water-only single phase flow (flow conditions fv1 to fv4). In Fig. 7-41 and Fig. 7-42, the triangles represent the errors obtained by using the second reconstruction algorithm and the circles represent the errors obtained by using the first reconstruction algorithm. The different volumetric flow rates are represented by different colours as explained in Table 7-10 and Table 7-11.

From Fig. 7-41, it can be seen that, for inclined flows, $\theta > 0^0$, there is a tendency for the errors in $Q_{w.IFT}$ obtained by the second reconstruction algorithm (with use of an axisymmetric component) to be higher than the errors in $Q_{w.IFT}$ obtained using the first reconstruction algorithm (without use of an axisymmetric component). However, the differences between the two sets of results are neither consistent nor large. For vertical flows (flow conditions fv6 to fv8), $\theta = 0^{o}$, the errors in $Q_{w.IFT}$ for results obtained by the second reconstruction algorithm are in the range -3.53% to 0%, and are consistently lower than the errors in $Q_{w.IFT}$ corresponding to the first reconstruction algorithm. For flow condition fv5 (see Fig. 7-41,coloured in yellow), the error in $Q_{w.IFT}$ obtained using the first reconstruction algorithm was very close to the error obtained using the second

reconstruction algorithm, even though $\varepsilon = 0.63\%$ (using the first reconstruction algorithm) is smaller than $\varepsilon = 0.88\%$ (using the second reconstruction algorithm). Hence, from the results above, we cannot definitely conclude that the second reconstruction algorithm with use of an axisymmetric component better for reconstructing the local water velocity distribution when the deviation $\theta = 0°$.

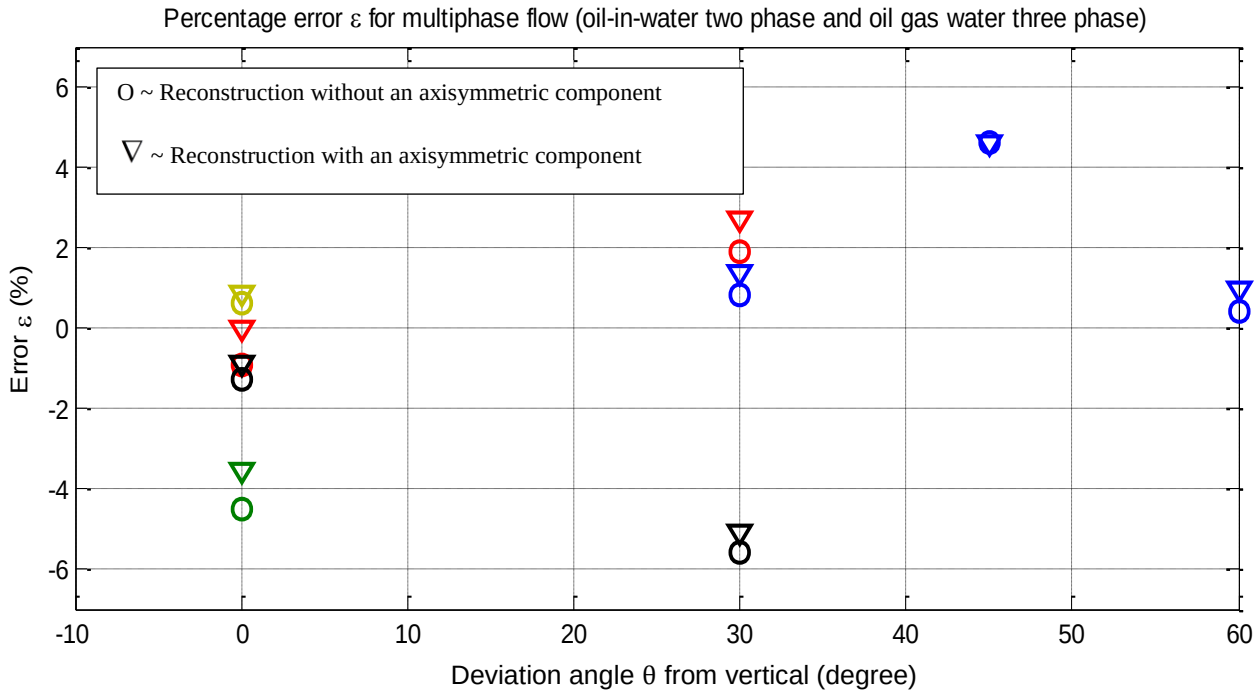

Fig. 7-41 Percentage difference ε plotted against the angle of deviation θ for multiphase flow condition

Water volumetric flow rate (m^3/hr)	Gas volumetric flow rate(m^3/hr)	Oil volumetric flow rate (m^3/hr)	Colour
5	2	3.4	blue
10	2	3.4	red
10	2	8.5	black
15	2	8.5	green
15	2	17.0	purple
8	0	4	yellow

Table 7-10 This table relates to Fig. 7-41 and shows the phase volumetric flow rates corresponding to the colour of the data points in Fig. 7-41

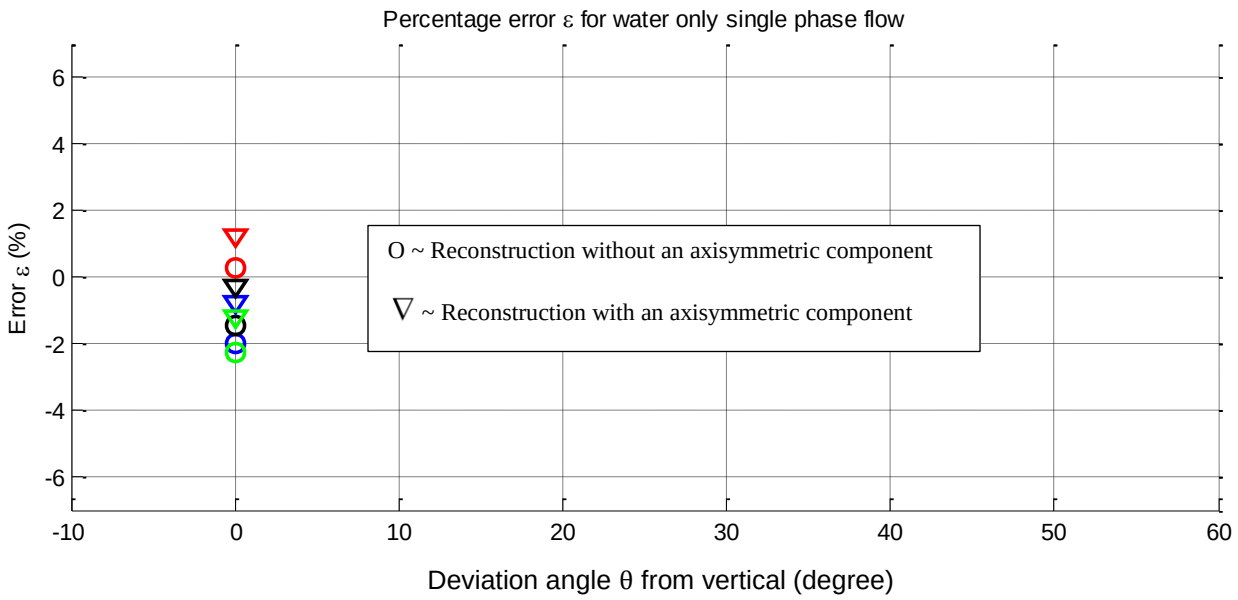

Fig. 7-42 Percentage difference ε plotted against the angle of deviation, θ, for water-only single phase flow

Water volumetric flow rate (m^3/hr)	Gas volumetric flow rate(m^3/hr)	Oil volumetric flow rate (m^3/hr)	Colour
4	0	0	red
8	0	0	blue
16	0	0	black
12	0	0	green

Table 7-11 This table relates to Fig. 7-42 and shows the phase volumetric flow rates relating to the colour of the data points in Fig. 7-42

To better identify the differences in the experimental results between using two reconstruction algorithms, the errors in $Q_{w.IFT}$ for water-only single phase vertical flow were also investigated (see Fig. 7-42). It is worth noting that there were four reconstructed velocity results obtained by the IFT system for vertical water-only single phase flows (flow condition fv1 to fv4). By inspection of Fig. 7-42, it can be seen that, for water volumetric flow rates from 8 m^3/hr to 16 m^3/hr, the percentage difference ε in $Q_{w.IFT}$ for the second reconstruction algorithm is always

smaller than -1.2%, and is also smaller than the value of error ε for the first reconstruction algorithm at the same flow condition (i.e. the error is in the range of -1.44% to -2.25%). However, from inspection of Fig. 7-42, it can be seen that, for a water volumetric flow rate of 4 m^3/hr (i.e. flow condition fv1), the percentage difference $\varepsilon = 1.25\%$ for the second reconstruction algorithm which is greater than the error $\varepsilon = 0.25\%$ for the first reconstruction algorithm. This could be a result of incorrect determination of the exponent q of the 'power law' equation (see Equation 3-23). Referring to Section 3.7, we can see that, if the measured potential differences $U_{j,a}$ are inaccurate in the non-uniform magnetic field, the term A_q has an inaccurate value. The value of A_q is strongly related to the power law exponent q according to the relevant polynomial function (see Fig. 3-19 (a)). With an inaccurate exponent q, the reconstructed local water velocity distribution with axisymmetric component will have a velocity error. There are several possible reasons for causing an inaccurate measurement of $U_{j,a}$, such as electrical noise.

From the above discussion, it is suggested that the results from the first reconstruction algorithm, which does not contain an axisymmetric velocity component, are slightly more accurate when the flow is multiphase and inclined from the vertical. This may be because, in real inclined multiphase flows, an axisymmetric velocity component may be small or even absent. It can, therefore, be concluded that the first velocity profile reconstruction algorithm is more suitable for inclined, stratified flow. For vertical flow, the second velocity reconstruction algorithm, which allows for an axisymmetric velocity component, can provide a more accurate local water velocity profile. This second velocity reconstruction algorithm is most suitable for use with vertical flow.

7.6 Comparing the performance of IFT against MRI in vertical gas-in-water two phase flows

7.6.1 Reference measurement parameters and experimental flow conditions

For additional vertical gas-in-water two phase flow experiments, the IFT flowmeter device was installed with the MRI system in the University of Cambridge multiphase flow loop (see Section 7.2.2). The overall set-up is shown in Fig. 7-3. The IFT flowmeter was oriented such that electrode 5 was positioned at 35 ° relative to the *y*-axis of the MRI system (see Fig. 7-43). All reconstructed velocity profile results were rotated back to the correct position corresponding to the MRI orientation.

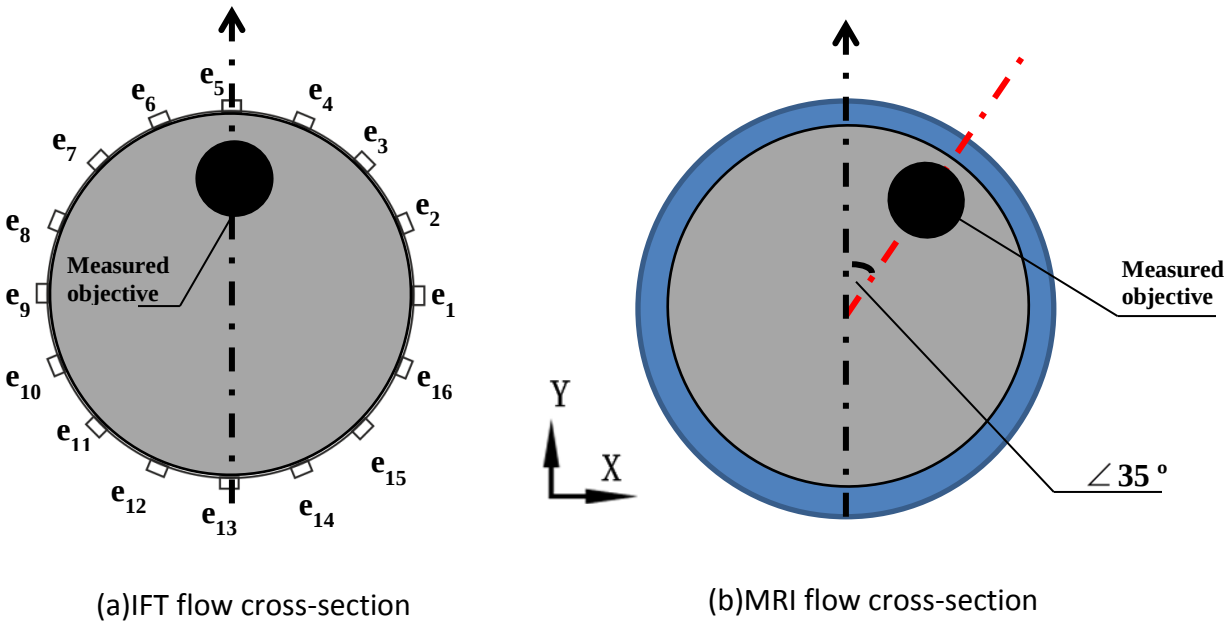

Fig. 7-43 (a) IFT flow cross-section (b) MRI flow cross-section

Referring to the conclusions presented in the previous section, the second water velocity profile reconstruction algorithm, which contains an axisymmetric velocity component, was applied to all experiments which were carried out in vertical two phase flow at the UoC flow loop (see Table

7-13). The relevant reference parameters are shown in Table 7-12 and Table 7-13 shows the gas and water volumetric flow rates for each flow condition. Note that the reference water volumetric flow rate $Q_{w,ref}$ is measured by using a turbine flowmeter (see Section 7.3.1).

Reference measurement parameter	Measurement technique
Mean water velocity, $\bar{v}_{w,ref}$	The mean water velocity as determined from equation: $\bar{v}_{w,ref} = \frac{Q_{w,ref}}{A(1-\bar{\alpha}_g)}$ where $Q_{w,ref}$ is measured by using a turbine meter (see Section 7.2.2)
Mean volume fraction of dispersed phase, (gas) $\bar{\alpha}_g$	The mean volume fraction gas phase as determined by using a differential pressure measurement technique as described in Section 7.3.1.

Table 7-12 Relevant reference measurement parameters

Flow condition	Angle of inclination of the working-section	Water volumetric flow rate (m^3/hr)	Gas volumetric flow rate (m^3/hr)	Gas volume fraction, $\bar{\alpha}_g$
ft1	0 °	5.42	0.24	0.046
ft2	0 °	6.62	0.30	0.041
ft3	0 °	6.45	2.05	0.19
ft4	0 º	5.41	1.04	0.13
ft5	0 º	6.68	1.86	0.17

Table 7-13 Gas-in-water two phase vertical flow conditions

7.6.2 Reconstructed local water velocity distribution for vertical gas-in-water two phase flows using the IFT system

Following a procedure similar to that described in Section 7.5.2, the processed electrical potential differences for both uniform and non-uniform magnetic fields under different flow conditions were as shown in Fig. 7-44.

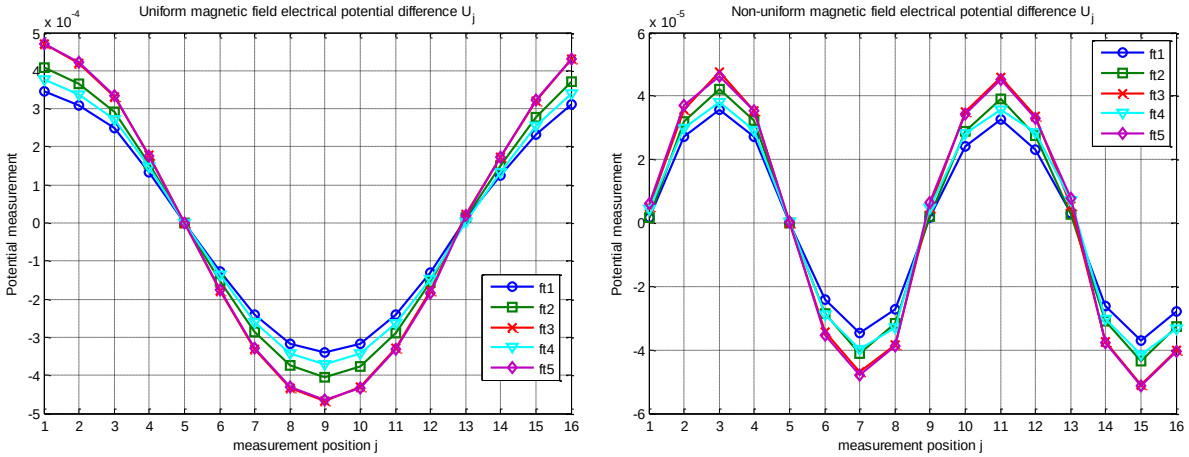

(a) (b)

Fig. 7-44 Measured potential differences for gas-in-water two phase vertical flows: (a) uniform magnetic field, (b) non-uniform magnetic field

It can be seen from Fig. 7-44 that the potential distributions for both uniform and non-uniform magnetic fields are very close to one or two cycles of a sinusoid. With reference to the analysis described in Section 3.5, this phenomenon was observed with all vertical flows because the flow velocity distributions for these flows were likely to be close to axisymmetric. After applying the DFT to the potential distributions, the real parts of the DFT components for the uniform magnetic field and the imaginary parts of the DFT components for the non-uniform magnetic field are shown in Fig. 7-45 (a) and (b), respectively. It is clear from Fig. 7-45 (a) that the terms X_2, X_3 …X_7 are negligible compared to X_1(see Equation 3-60). From Fig. 7-45 (b), it can be seen that the imaginary parts of X_2 are at least 10 times greater than the remaining DFT components; therefore, the imaginary parts of X_2 are dominant. The behaviour of these plots is similar to the

results shown in Section 3.7, which means that the reconstructed local water velocity distributions were very close to being axisymmetric velocity profiles.

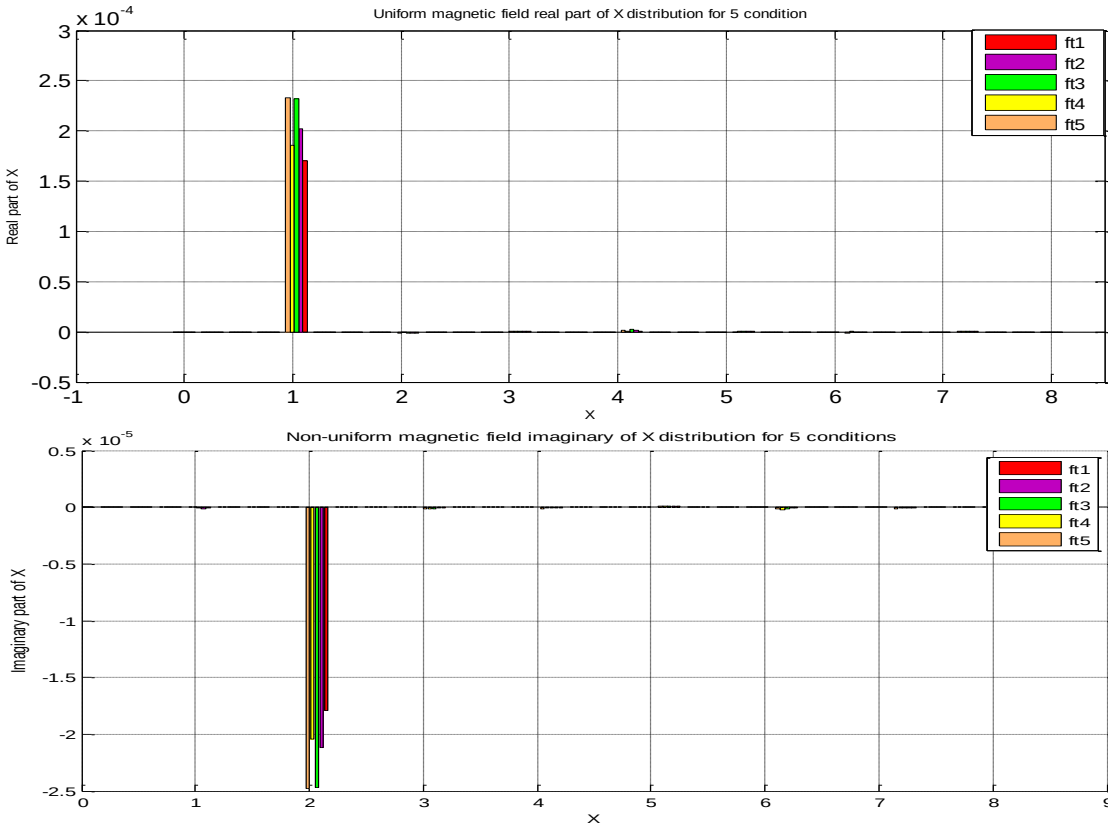

Fig. 7-45 Applying DFT method to the potential distributions shown in Fig. 7-27: (a) the real parts of the DFT components for the uniform magnetic field, (b) the imaginary parts of the DFT components for the non-uniform magnetic field.

The reconstructed local water velocity distributions using MRI and IFT are shown in Fig. 7-46 for the flow conditions ft1 to ft5 given in Table 7-13. The left side and right side of each figure, are used for comparing the reconstructed local water velocity distributions obtained using the MRI and IFT respectively.

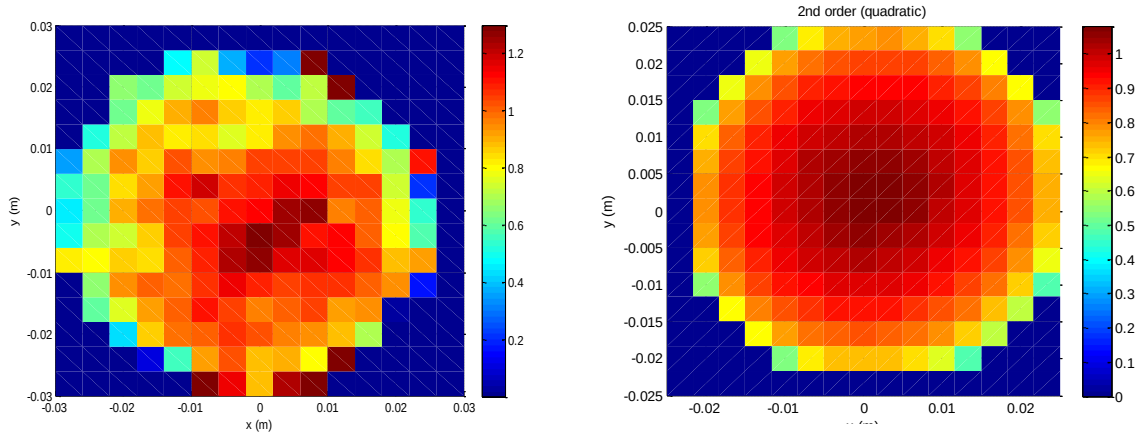

(a) Flow condition ft1

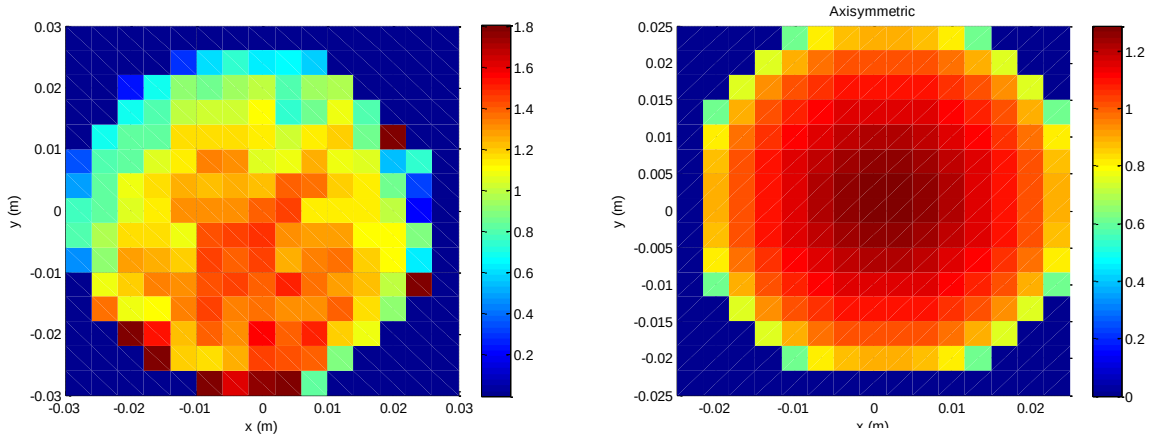

(b) Flow condition ft2

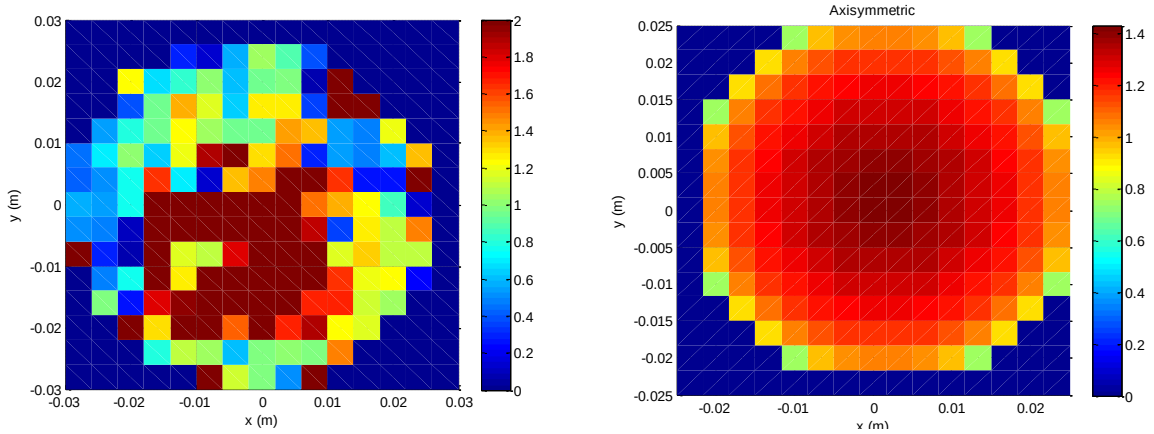

(c) Flow condition ft3

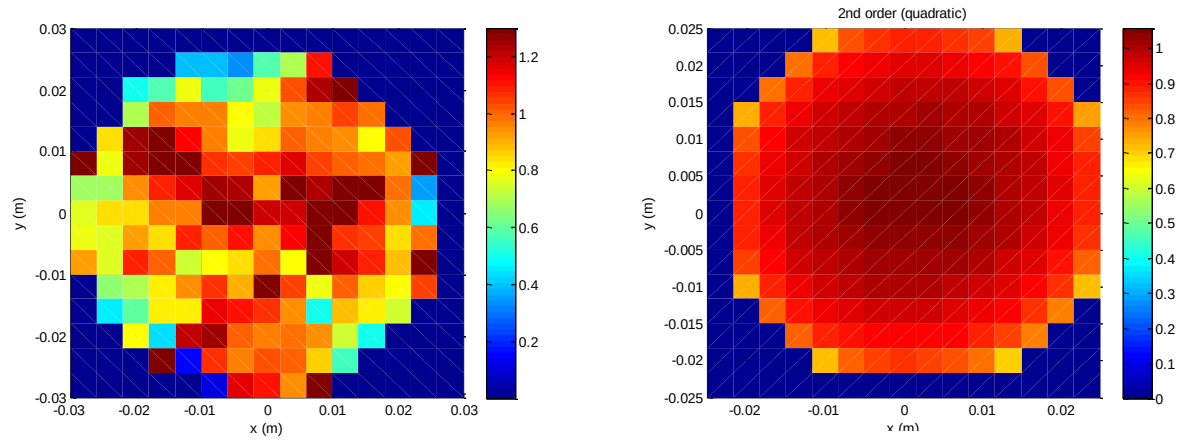

(d) Flow condition ft4

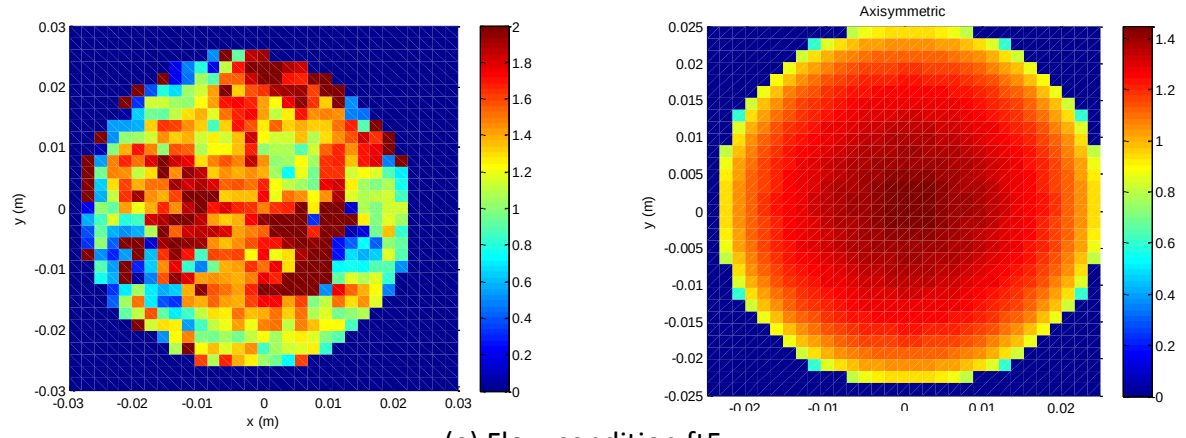

(e) Flow condition ft5

Fig. 7-46 Comparison of local water velocity distribution results for vertical flows. Left side: reconstructed velocity profiles using MRI. Right side: reconstructed velocity profiles using IFT. The water velocities in the colour bars are in ms^{-1}

Fig. 7-46 displays results for vertical gas-in-water two phase flows where the water volumetric flow rate is greater than the gas volumetric flow rate and water is the continuous phase. The mean volume fraction of gas $\bar{\alpha}_g$ which varied from 0.041 to 0.19, was calculated from measurements made using the DP cell. Specifically, in flow conditions ft1 and ft2, the values of $\bar{\alpha}_g$ were 0.046 and 0.041, respectively. For flow conditions ft3, ft4 and ft5, the mean gas volume fraction $\bar{\alpha}_g$ was 0.19, 0.13 and 0.17, respectively. It is therefore to be expected that there will be differences in the gas volume fraction distributions for the different flow conditions.

From inspection of Fig. 7-46, it can be seen that, for all the flow conditions, the reconstructed local water velocities for MRI measurement are generally higher than the reconstructed velocity results obtained from the IFT system. However, by inspection of Fig. 7-46 (a), (b) and (d), it can be seen that the MRI reconstructed local water velocity distributions shows unrealistically high velocities at the pipe wall. In particular, for flow condition ft2, as shown in Fig. 7-46 (b), the local water velocity near the pipe wall is up to 1.8m/s, which is higher than the local water velocity in the centre of the pipe (approximately 1.5m/s). This phenomenon contradicts previous research, which shows a lower velocity near the pipe wall due to the 'wall effect' [55], [111]. Discussions with staff at the University of Cambridge led to the conclusion that this problem was likely to be caused by a slow MRI scanning rate and low image resolution. Furthermore, by inspection of previous experimental results reported by Lucas (see Fig. 7-47) [111], it can be seen that, when the mean gas volume fraction is 0.025 and the water superficial velocity is 0.9m/s, in vertical flow the local gas volume fraction distribution and local gas velocity distributions should be close to axisymmetric profiles. As we know that the velocity profiles for both the water and gas phases are likely to have a similar shape in two phase flow, the water velocity profile is also likely to be axisymmetric [119]. However, the MRI reconstructed local water velocity distribution for each flow condition do not give the expected axisymmetric velocity profile characteristics, especially the expected higher velocity at the pipe centre than at the wall. In comparison, the reconstructed velocity profiles obtained by using the IFT system for each flow condition do show the expected axisymmetric water velocity distribution.

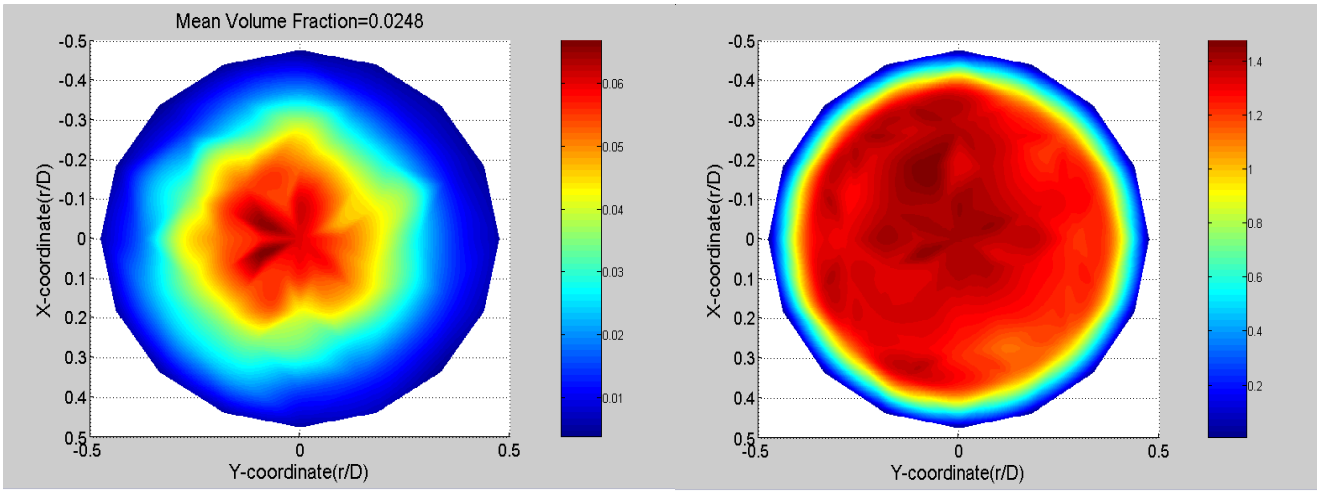

(a) Local gas volume fraction distribution (b) Local gas velocity distribution

Fig. 7-47 Local gas volume fraction distribution and local gas velocity distribution in vertical air-water flow. Mean gas volume fraction is 0.0248, superficial water velocity is 0.9m/s ,superficial gas velocity is 0.033m/s [111]

To improve the MRI reconstructed water velocity profiles, it was believed that the original velocity profiles could be corrected by radially averaging the velocity and applying a correction factor to the entire velocity profile. This correction factor was determined by using data from a series water-only single phase flow experimental results. Further details of the MRI velocity profiles correction process, which were carried out by members of the University of Cambridge, are not described in this thesis.

In order to clearly identify the differences between MRI and IFT velocity profiles, the corrected velocity profiles for the MRI system were also approximated by a 'power law' expression (see Equation 3-23). Fig. 7-48 shows the local axial water velocity results in the radial direction, where the black curve represents the corrected water velocity profile for the MRI system at the given flow condition, the red curve represents the reconstructed water velocity profile using the IFT system under the same flow conditions and the blue curve represents the 'power law' approximation velocity profiles for the MRI system.

Before discussing the results from the IFT and MRI systems, it is necessary to describe how to determine the exponent q and mean water velocity $\bar{v}_{w,MRI}$ for the (MRI) 'power law'

approximation velocity profile. As mentioned above, by assuming the flow velocity profile is axisymmetric, the corrected velocity profile for MRI is described in the form of Equation 3-23. The mean water velocity $\bar{v}_{w,MRI}$ was obtained by averaging the local water velocity in the MRI-corrected water velocity profile (i.e. the black curve in Fig. 7-48). This value for $\bar{v}_{w,MRI}$ was substituted into Equation 3-23 and the exponent q was adjusted until an error ε_t was minimised. ε_t is given by Equation 7-22.

$$\varepsilon_t = \sum_{i=1}^{N} (v_{i,MRI} - v_{i,MRI,c})^2 \qquad \text{Equation 7-22}$$

where $v_{i,MRI}$ represents the local velocity in the i^{th} pixel in the MRI image calculated from the power law approximation and where $v_{i,MRI,c}$ represents the local velocity in the i^{th} pixel in the MRI image associated with the corrected MRI velocity profile described above. N is the number of pixels in the MRI image. It is straightforward to show that the 'power law' velocity profile for MRI can be written as:

$$v_{MRI} = 0.5 \cdot \bar{v}_{w,MRI} \cdot (1 - r/R)^q \cdot (1+q) \cdot (2+q) \qquad \text{Equation 7-23}$$

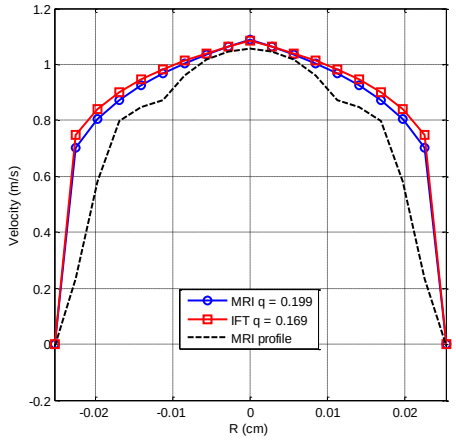

(a) Flow condition ft1 $\bar{\alpha}_g = 0.046$

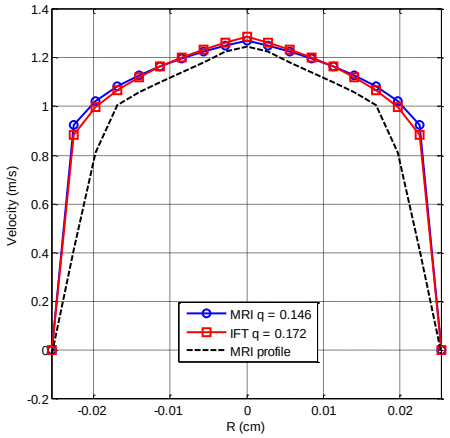

(b) Flow condition ft2 $\bar{\alpha}_g = 0.041$

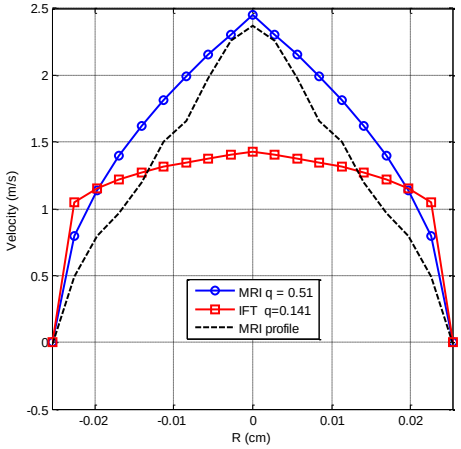

(c) Flow condition ft3 $\bar{\alpha}_g = 0.19$

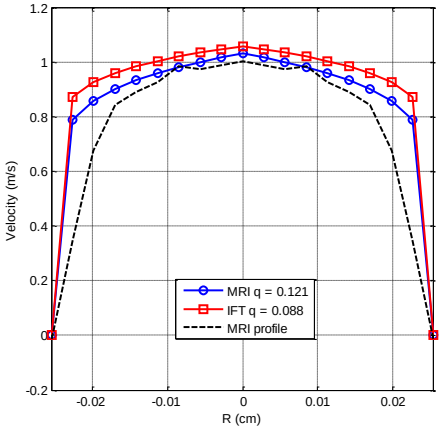

(d) Flow condition ft4 $\bar{\alpha}_g = 0.13$

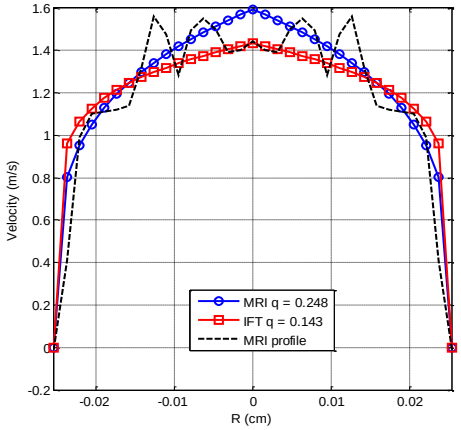

(e) Flow condition ft5 $\bar{\alpha}_g = 0.17$

Fig. 7-48 Local water velocity profiles for vertical gas-in-water two phase flows. The black curve is the corrected MRI velocity profile, the blue curve is the power law approximation to the corrected MRI velocity profile and the red curve is the velocity profile obtained from IFT.

From inspection of the results in each figure for both the IFT and the MRI data, the water velocity has low values near the pipe wall and tends to increase towards the pipe centre. It can also be seen that, for the IFT results, as the mean gas volume fraction $\overline{\alpha}_g$ increases the local water velocity distribution changes from a more pointed shape to a flatter profile. This phenomenon can be explained by referring to previous research on local gas volume fraction distributions. Lucas [90] and van der Welle [91] discovered that, for low mean gas volume fractions, the gas bubbles are relatively highly concentrated at the pipe centre. When the mean gas volume fraction increased, the gas bubbles were more uniformly distributed in the flow cross-section. Due to its lighter density the gas phase always moves faster than the liquid phase and the local water velocity increases where the gas is highly concentrated. Accordingly, if the local gas volume fraction distribution is more uniform, the local water velocity profile will be smoother. From the discussion above and from Section 3.5 it is expected that as the mean gas volume fraction $\overline{\alpha}_g$ increases, the power law exponent *q* will decrease.

In Fig. 7-50 we plot the value of the power law exponent *q* against the mean gas volume fraction $\overline{\alpha}_g$ for both MRI and IFT. The distribution of exponent *q* in Fig. 7-50 (a) tends to agree with previous results obtained by Lucas [90]. However, the results obtained for the MRI (see Fig. 7-50 (b)) show a clear tendency for the exponent *q* to increase with increase in $\overline{\alpha}_g$. This latter observation is probably due to the inaccuracy of the MRI velocity profiles. Furthermore, by comparing the MRI exponent *q* vs. mean gas volume fraction $\overline{\alpha}_g$ shown in Fig. 7-50 (b) with the exponent *q* vs. $\overline{\alpha}_g$ obtained from previous experiments, as shown in Fig. 7-49, it is clear that the value of exponent *q* for the MRI results is often much higher than in the previous literature, e.g. as reported by Lucas [90]. This shows that some of the water velocity profiles obtained by MRI (particularly at ft3) have an unrealistic shape. As explained above, the water velocity profiles from IFT have a value of *q* which are in much better agreement with Lucas's [90] results.

Referring to Fig. 7-48 (c) and (e), the mean gas volume fraction $\overline{\alpha}_g$ was equal to 0.19 and 0.17 respectively, the water volumetric flow rates were 6.45 and 6.68 m^3/hr respectively and the gas volumetric flow rates were 2.05 and 1.86 m^3/hr respectively. Of course, there would be some local fluctuations in the flow rates during testing and, because the image scanning period of MRI

lasts a few seconds, flow fluctuations may perhaps have had an influence and could possibly explain the differences between the two MRI profiles.

The comparison of the reconstructed velocity profiles between the MRI and IFT is discussed in the following section.

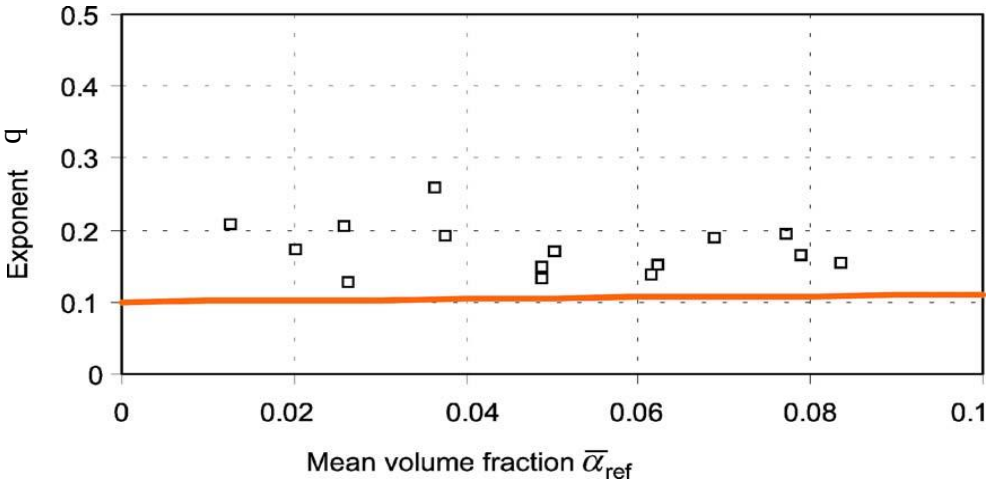

Fig. 7-49 Exponent *q* vs. mean volume fraction[90]

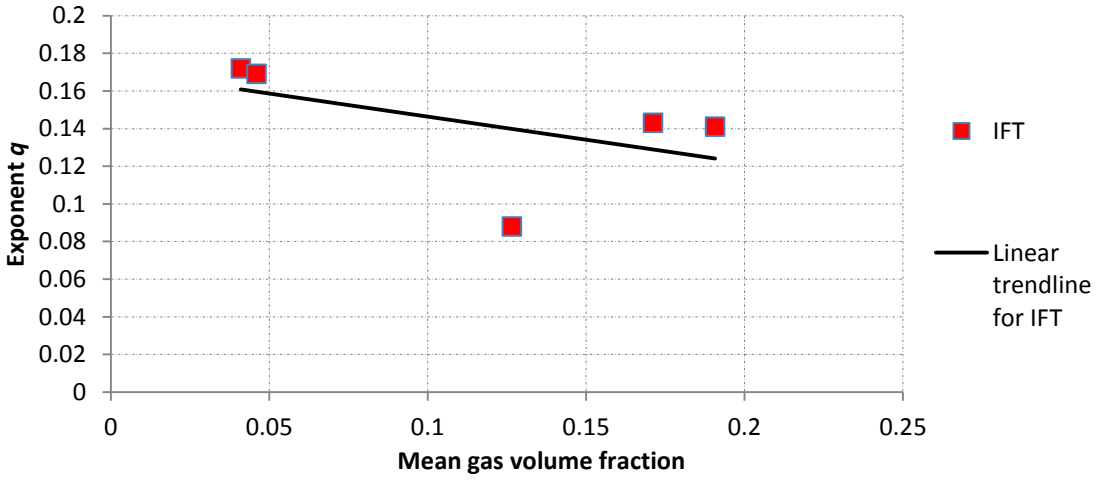

(a)

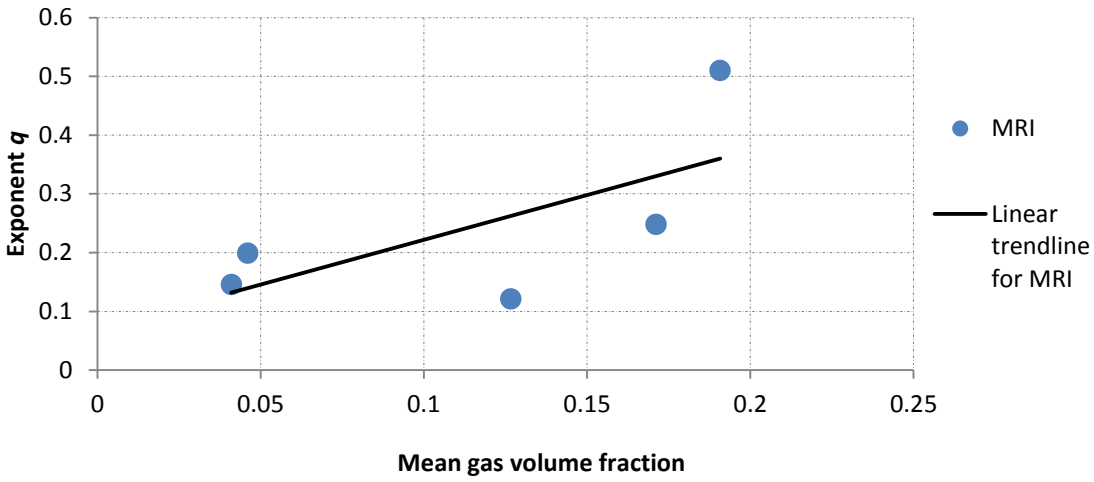

(b)

Fig. 7-50 Plots of power law exponent q vs. mean gas volume fraction (a) q vs. $\bar{\alpha}_g$ for IFT system, (b) q vs. $\bar{\alpha}_g$ for MRI system

7.6.2.1 Comparison of the local water velocity distributions obtained by IFT and MRI

In order to quantitatively analyse the differences in local water velocity as determined by the IFT and MRI, the term δv_i (see Section 4.3.2) was used to calculate the percentage relative difference of velocity value at each of a number of points denoted by the index i. δv_i used in this analysis is defined as follows:

$$\delta v_i = \frac{v_{i,IFT} - v_{i,MRI}}{v_{MRI,\max} - v_{MRI,\min}} \times 100\% \qquad \text{Equation 7-24}$$

where $v_{MRI,\max}$ and $v_{MRI,\min}$ are respectively the maximum and minimum velocities in the MRI velocity profiles.

From the discussion in the last section on the limitations of the MRI technique, it can be seen that, in certain flow conditions, erroneous velocity profiles can be generated. Here, the velocity results for flow conditions ft1, ft2 and ft4 are examined. It should be noted that the reason for ignoring the reconstructed velocity profile of two flow conditions (ft3 and ft5) was due to the MRI reconstructed velocity distribution having an unrealistic flow velocity profile for a real pipe flow. Referring to Fig. 7-49 it is clear that, for a similar mean gas volume fraction condition, the value of exponent q for MRI velocity profiles (ft3 and ft5) is higher than the value of exponent q obtained from previous experimental results [90]. This means that the MRI reconstructed water velocity profile looks too 'peaky', which is unrealistic.

The terms δv_i for 19 points in each of the three flow conditions (ft1, ft2 and ft4) are presented in Fig. 7-51. By inspection of the figure, it can be seen that the maximum value of the local relative difference between the local velocities at a given point is 8%, and appears close to the pipe wall (r/R = 0.9). In the central flow area ($-0.4 \leq r/R \leq 0.4$), the local relative differences are $\leq 4\%$. The results presented in Fig. 7-51 indicate good agreement between IFT velocity profiles and MRI results in these three flow conditions.

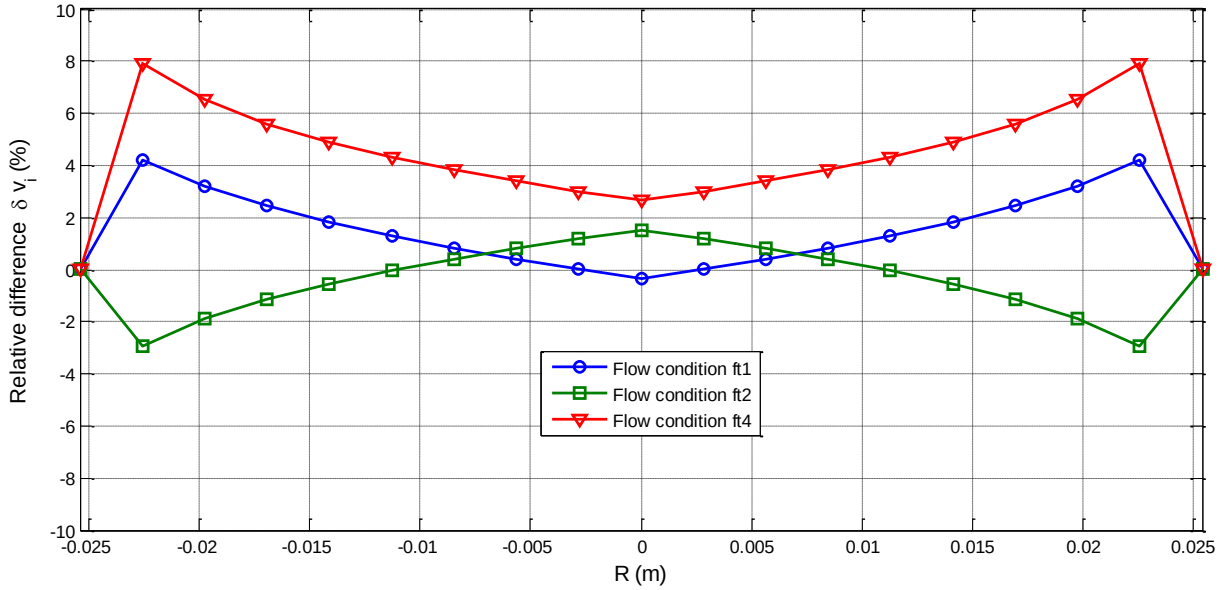

Fig. 7-51 Local relative differences between velocities

7.6.2.2 Comparison of averaged velocity results obtained by MRI and IFT with reference measurements

To more accurately evaluate the performance of the MRI and IFT systems, the averaged water velocities can be compared with reference measurements. From the measurement of mean gas volume fraction $\overline{\alpha}_g$ the reference mean water velocity for each flow condition can be calculated.

The water velocity percentage difference $\varepsilon_{v,w}$ obtained by the IFT system can be expressed as:

$$\varepsilon_{v,w} = \frac{\overline{v}_{w,IFT} - \overline{v}_{w,ref}}{\overline{v}_{w,ref}} \times 100\% \qquad \text{Equation 7-25}$$

where $\bar{v}_{w,IFT}$ is the averaged water velocity obtained by the IFT system and $\bar{v}_{w,ref}$ is the reference mean water velocity. Note that the reference mean water velocity $\bar{v}_{w,ref}$ is calculated according to the equation shown in Table 7-12.

By using Equation 7-25 with the values of $\bar{v}_{w,ref}$ and $\bar{v}_{w,IFT}$ for each flow condition, $\varepsilon_{v,w}$ can be calculated and is listed in Table 7-14. The percentage difference $\varepsilon_{v,w}$ has a maximum value of 3.67% in vertical gas-in-water two phase flow, for flow condition ft1.

The averaged water velocity obtained using the IFT system was referenced against the mean water velocity obtained from the turbine flowmeter, and the gas volume fraction from the differential pressure measurement device (see Table 7-12), and are presented in Fig. 7-52 (a). A comparison was also made between the mean water velocity $\bar{v}_{w,MRI}$, obtained from the raw, uncorrected MRI velocity profiles, and the reference water velocity $\bar{v}_{w,ref}$.

The trend curve in Fig. 7-52 (a) reveals that the average water velocity measurement of IFT system has exceptional linearity. The relationship between $\bar{v}_{w,IFT}$ and $\bar{v}_{w,ref}$ can be expressed as:

$$\bar{v}_{w,IFT} = 0.9479\bar{v}_{w,ref} + 0.0683 \qquad \text{Equation 7-26}$$

A similar trend curve for MRI water velocity is shown in Fig. 7-52 (b) and can be seen to be close to linear. However, it is worth noting that the accuracy of the averaged velocity obtained from the raw MRI data becomes worse with the increasing value of reference mean water velocity $\bar{v}_{w,ref}$. To investigate the linearity of MRI water velocity measurement, it is fairly straightforward to show that the relationship between $\bar{v}_{w,MRI}$ and $\bar{v}_{w,ref}$ can be written in the form:

$$\bar{v}_{w,MRI} = 1.3379\bar{v}_{w,ref} - 0.2972 \qquad \text{Equation 7-27}$$

By comparing Equation 7-26 and Equation 7-27, the conclusion can be drawn that the accuracy of the performance of the IFT system is much better than when raw MRI data is used, especially at high flow rates.

Flow condition	Reference water velocity $\bar{v}_{w,ref}$ (m/s)	Averaged water velocity $\bar{v}_{w,IFT}$ by IFT(m/s)	Relative percentage difference $\varepsilon_{v,w}$ (%)
ft1	0.82	0.85	3.67
ft2	1.00	1.01	1.00
ft3	1.15	1.16	0.87
ft4	0.89	0.91	2.25
ft5	1.16	1.17	0.86

Table 7-14 Averaged water velocity determined using IFT and reference measurement for vertical gas-in-water two phase flow

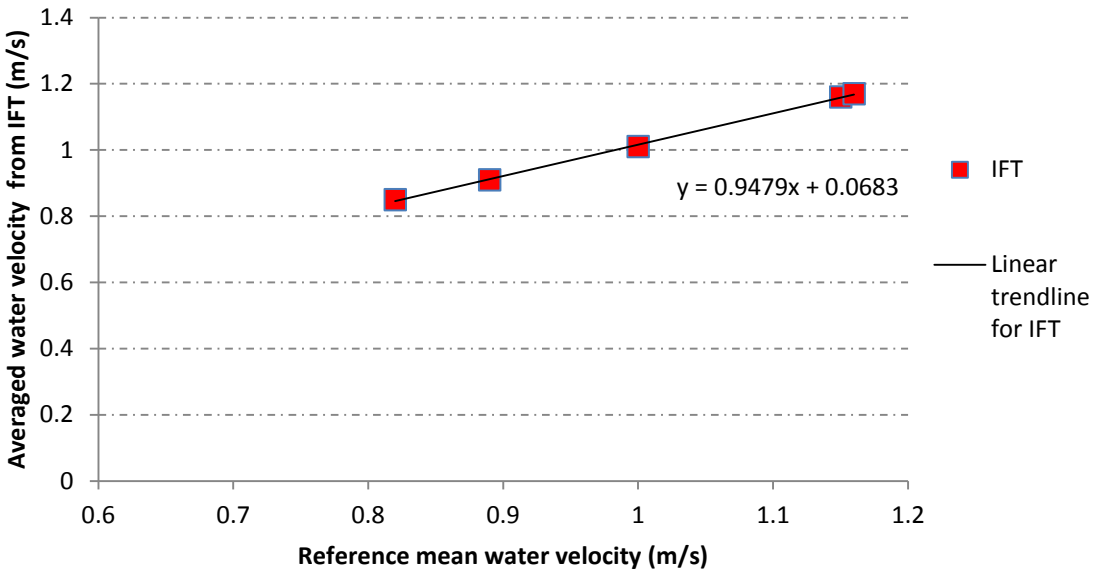

(a)

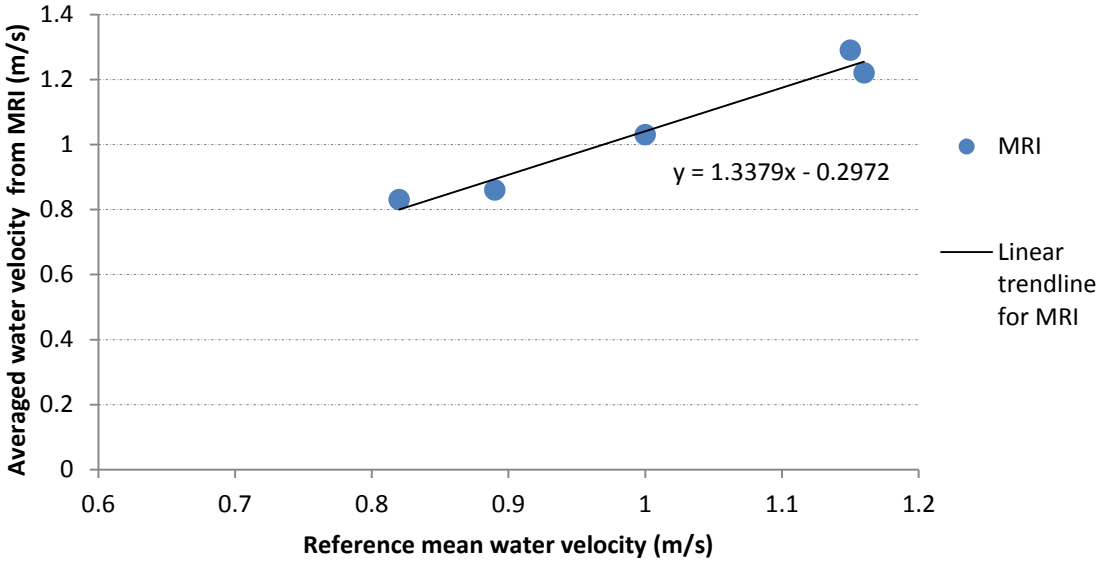

(b)

Fig. 7-52 Averaged water velocity vs. reference water velocity: (a) averaged water velocity obtained by IFT vs. reference mean water velocity, (b) averaged water velocity obtained using uncorrected MRI data vs. reference mean water velocity

7.7 Summary

This chapter has mainly described and reported two different series of multiphase flow experiments, including two and three phase flows. For the oil-gas-water three phase flow experiments, a multiphase flow loop based at the SGR laboratory was used (see Section 7.2.1). A second flow loop at the University of Cambridge used for the gas-in-water two phase flow was described in Section 7.2.2. Related reference instruments to evaluate the accuracy and reliability of the IFT system have been described in Section 7.3.

During the oil-gas-water three phase flow experiments, the central part of the IFT flowmeter body containing the electrodes was fitted in such a way that it was not correctly aligned, and this resulted in errors in the boundary potential measurements. It was necessary to correct for the misalignment, and the method used is described in Section 7.4; the corrective procedures are applicable for the potential measurements in uniform and non-uniform magnetic fields.

With corrected potential difference measurements, the local water velocity distributions were reconstructed for thirteen different flow conditions using two different IFT reconstruction algorithms (see Section 7.5.2). The experiments included the working section as both vertical and inclined.

In inclined oil-gas-water flow experiments, the local water velocity distribution results for both reconstruction algorithms (see Section 3.6 and 3.7) show that the higher water velocities appear close to the uppermost part of the pipe cross-section and are in good agreement with the results of previous research. To evaluate the accuracy of results obtained by the IFT system, the mean water volumetric flow rate for each flow condition was calculated by integrating the local water velocity distribution in conjunction with the results obtained using the ERT system. Using Equation 7-21, the maximum water volumetric flow rate error for three phase flows for both reconstruction algorithms (see Section 3.6 and 3.7) was approximately 5%. Note that this percentage difference is also affected by the accuracy of the ERT system.

The results, as shown in Fig. 7-34 for vertical flow in water-only single phase flow experiments, show that the reconstructed local water velocity distributions obtained using the second velocity reconstruction algorithm, which allows for the use of an axisymmetric velocity component, are similar to previous experimental results obtained by a Pitot static tube [1]. The error of the water

volumetric flow rate is varied from -1.17% to 1.25%. Under the same flow conditions, the reconstructed velocity profile obtained by using the first velocity reconstruction algorithm, without use of an axisymmetric velocity component, have unrealistic flow profiles and higher water volumetric flow rate errors. For oil-in-water and oil-gas-water vertical flows, the reconstructed water velocity profile by using the second velocity reconstruction algorithm (with use of an axisymmetric velocity component) has good agreement with previous published results (see Fig. 7-35), wherein the maximum water velocity was in the centre of the pipe and minimum water velocity near the pipe wall. On the contrary, the reconstructed water velocity profiles by using the first velocity reconstruction algorithm shows unrealistic flow profile in a real vertical pipe flow. By using the reconstructed velocity profiles for both reconstruction algorithms, in conjunction with the corresponding local water volume fraction distribution (see Table 7-1), it is shown that the maximum error for the first velocity reconstruction algorithm is -4.53% and the maximum error for the second velocity reconstruction algorithm is -3.53%.

To better identify the differences in the experimental results between using the two reconstruction algorithms, an numerical analysis has been presented using velocity results obtained for inclined oil-gas-water three phase flows, and vertical water-only single phase and oil-in-water two phase flows (see Fig. 7-41 and Fig. 7-42). Referring to the discussion shown in Section 7.5.4, it is suggested that the results from the first reconstruction algorithm, which does not contain an axisymmetric velocity component, are slightly more accurate when the flow is both multiphase and inclined from the vertical. When the flow is vertical, and hence more likely to be axisymmetric, the results from the second reconstruction algorithm, which allows for an axisymmetric velocity component, are more accurate.

Section 7.6 describes how the IFT and MRI systems respectively obtain the local water velocity distribution in vertical gas-in-water two phase flow. Quantification of the observed performance of the IFT system was done in two ways: firstly, the results obtained using the IFT system were compared with corrected MRI-reconstructed velocity profiles. The local relative percentage difference of water velocity δv_i was less than 10%. Secondly, the averaged water velocity measurements for the IFT system were compared with the reference mean water velocity, obtained under the same flow conditions. The discrepancy between the predicted and reference mean water velocities varied in the range 0.8% to 3.5%. The linearity of the water velocity

results obtained by both IFT and MRI systems was noted and discussed in Section 7.6.2. By inspection of Equation 7-26 and Equation 7-27, it was possible to conclude that the accuracy of the reconstructed water velocity results for the IFT system was much better than the water velocity results obtained from raw, uncorrected MRI data (especially at relatively high flow rates).

8 Conclusions and suggestions for future work

8.1 Introduction

In this chapter, general conclusions are drawn relating to the methodology of local water velocity profile measurement and to the work described in this thesis. In addition, some suggestions and recommendations for future work are given in Section 8.4.

8.2 Conclusions

The aim of this study was to develop a novel non-intrusive multiphase flow meter for determining the local water velocity distribution in multiphase flows, such as gas-in-water two phase and oil-gas-water three phase flows. A further aim was that this flow meter should not include either a radioactive source or an intrusive homogenising mixer.

A review of a previous Electromagnetic Velocity Profiler (EVP) technique indicated that multi-electrode electromagnetic flow metering techniques had demonstrated a promising ability to obtain local axial water velocity profiles in water-only single phase, and solids-in-water two phase flows. However, the EVP technique has several limitations, such as low spatial resolution, which meant it was not able to provide detailed local velocity information across the entire pipe cross-section. More details of the limitations of the EVP device are given in Section 2.3.3.

An objective of this research was, therefore, to develop a multi-electrode electromagnetic flow meter which not only extends the inductive flow tomography (IFT) techniques used in EVP, to enable much greater spatial resolution of the velocity profile within the entire flow cross-section, but also avoids the use of matrix inversion techniques, which are often ill-posed problems, hence leading to inaccurate results.

The IFT flowmeter designed in this study consisted of a non-conducting 50mm internal diameter flow conduit, sixteen stainless steel electrodes (equispaced circumferentially around the pipe), and a Helmholtz coil (see Fig. 5-1).

Using COMSOL Multiphysics software, a 3D finite element analysis model for the IFT metering device was established in order to investigate the magnetic flux density distribution in the pipe cross-section and the effects of the imposed water velocity profile on the electrical potential distribution. The simulation results, shown in Section 3.3 and 3.4, indicated that if equal coil currents were used that were in the same or opposite directions, then the magnetic flux density in the pipe cross-section had, respectively, either an essentially uniform distribution or a non-uniform anti-Helmholtz distribution.

Based on these characteristics, an initial theoretical model was developed which enabled an axisymmetric velocity profile to be reconstructed from potential difference measurements made at the array of boundary electrodes. A study of different axisymmetric flows with the same mean velocity showed that, if the magnetic field is non-uniform, a unique signature can be obtained from the measured electrical potential distribution. With the aid of this unique signature, a parameter A_q was defined and a relationship between A_q and a power law exponent q was established (see Equation 3-34). Having found A_q it was then possible to determine the corresponding exponent q (see Fig. 3-18). By using a power law velocity profile expression (see Equation 3-23), in conjunction with the calculated mean velocity $\bar{v}_z$ obtained in the uniform magnetic field and the exponent q, it was possible to fully determine the local water velocity at all points in the pipe cross-section.

Because the above, initial model was only valid for axisymmetric velocity profiles, an analytical velocity profile reconstruction algorithm was proposed and developed using the electrical potential distribution on the boundary of the pipe to reconstruct more complicated profiles, such as stratified velocity profiles. This analytical reconstruction algorithm was based on the Discrete Fourier Transform (DFT) and an assumption of a polynomial form for the velocity profile (see Section 3.6.1). Specifically, the DFT components of the boundary electrical potential distribution obtained in the uniform magnetic field were used to infer the coefficients of the polynomial expression for the magnitude and angle of direction of each of a series of velocity components of increasing order n (where n=0, 1, 2, … up to a maximum possible value of 6). The polynomial expressions for each of these velocity components were then added together to provide an analytical expression giving the water velocity at any position in the pipe cross-section. Unfortunately, because this technique assumes that the 0^{th} order velocity component is uniform,

it was not possible to apply this algorithm to reconstruct axisymmetric velocity profiles or profiles containing an axisymmetric velocity component.

To overcome the above limitation, the DFT-based velocity reconstruction algorithm was extended by combining the DFT reconstruction algorithm with power law theory (see Section 3.7) to enable the parameter A_q to be determined using the DFT component $\mathrm{Im}\,\hat{X}_2$ obtained from the boundary potential distribution measured in the non-uniform magnetic field. From the value of A_q , the appropriate value of the power law exponent q was obtained. This value of q when used with the mean velocity $\bar{v}_z$ for the axisymmetric velocity component, enable an analytical expression for the axisymmetric component of the velocity profile to be determined (see Equation 3-23).

It was found that the influence of the quadratic (2^{nd} order) velocity profile component on the value of $\mathrm{Im}\,\hat{X}_2$ was much greater than the effects from the other polynomial velocity components (apart from, obviously, the axisymmetric velocity profile commponent) (Section 3.7.2). In other words, $\mathrm{Im}\,\hat{X}_2$ cannot be directly used for calculating A_q. To overcome this problem, a new parameter $A_{2,\theta}$ was defined to enable determination of the contribution of the quadratic velocity component to $\mathrm{Im}\,\hat{X}_2$. Referring to Equation 3-85, by subtracting this contribution $\mathrm{Im}(\hat{X}_2)_2$ from $\mathrm{Im}\,\hat{X}_2$, the remainder $\mathrm{Im}(\hat{X}_2)_0$ can be used to accurately calculate the parameter A_q. With the reconstruction procedure shown above, the power law exponent q was obtained, thereby distinguishing between different axisymmetric velocity components with the same mean velocity. The reconstructed velocity results obtained from this improved reconstruction model which includes an axisymmetric velocity component, enable the reconstruction of velocity profiles containing both axisymmetric and asymmetric velocity components.

Further work was carried out to find the optimum solution from the $n!$ possible reconstructed velocity profiles using either the former reconstruction algorithm without the use of an axisymmetric component or the improved velocity reconstruction algorithm which contains an axisymmetric component. The adopted method was based on weight value theory, which can infer the boundary electrical potential distribution in a non-uniform magnetic field for any of the possible velocity profiles. The optimum velocity profile was then determined by finding the

minimum differences S_U between the predicted and measured boundary electrical potential distributions in the non-uniform magnetic field (see Equation 4-4).

To verify the theoretical work described above, the reconstructed velocity results for both reconstruction algorithms were compared with imposed velocity profiles in COMSOL simulations. The maximum local velocity error for the imposed two flow conditions was approximately 4%. (see Section 4.3.2), which fully satisfies the majority of industrial applications. In addition, the reconstructed velocity profile results also indicated that the two proposed velocity profile reconstruction algorithms are capable of providing a detailed map of the local axial water velocity distribution (in single phase or multiphase flow) by using the boundary potential distributions obtained in both the uniform and the non-uniform magnetic fields. Therefore, it can be concluded that both water velocity profile reconstruction algorithms satisfy the main objective, as shown in Section 1.4.

The electronic hardware developed and built for the physical IFT system included coil excitation circuitry with coil current monitoring circuitry and potential difference measurement circuitry. The author also developed a LabVIEW-based program to control the coil excitation circuitry which generated a hybrid pulsed DC excitation signals for the Helmholtz coil and which simultaneously collected the analogue voltage signals from the potential difference measurement circuitry, via an NI DAQ device.

Increases in the coil temperature due to Ohmic heating resulted in an increase in coil electrical resistance and hence a decrease in coil current and a corresponding decrease in magnetic field strength. The author therefore included coil current monitoring circuitry to continuously measure the current signal via the NI DAQ device and the host computer.

MATLAB-based software was developed for analysing the potential difference signals obtained from the electrodes. The procedure for signal processing included three steps: Firstly, determining the magnitude of the flow induced potential difference U_j (see Equation 6-17). Secondly, using relevant coil current measurement to enable compensated potential difference $U_{j,cp}$ to be obtained. The final step was to use these values of $U_{j,cp}$ to find the properties of the flow induced potential difference signals averaged over 30 excitation cycles.

A further objective of the present study was to quantify the observed performance of the IFT system. A series of experiments was performed on the IFT system with vertical upward, gas-in-water two phase flow and with inclined and vertical, upward, gas-oil-water three phase, water-only single phase and oil-in-water two phase flow. To achieve the flow conditions for these experiments, two multiphase flow loops were used. These were located at the SGR laboratory and at the University of Cambridge (see Section 7.2.1). Reference flow instruments and related multiphase flow metering techniques were mounted in the flow loop to provide reference measurements including the phase volumetric flow rates and the local dispersed phase volume fraction distribution.

The experimental results for the inclined gas-oil-water three phase flows indicated that the calculated volumetric flow rate of water obtained using the reconstructed water velocity profile from both velocity profile reconstruction algorithms (see Section 3.6 and 3.7), in conjunction with the measured local dispersed phase volume fraction, gave good agreement with reference measurements obtained from a water turbine meter. The reconstructed water velocity profiles were obtained using the IFT system. An ERT device was used to obtain the local dispersed phase volume fraction distribution. The relative error for most of the flow conditions was in the range of 0.5% to 2%, with a maximum relative error of approximately -5%. For inclined flows, the experimental results also showed that the relative errors for the water volumetric rate, obtained from the original reconstruction algorithm without the use of an axisymmetric velocity component, were smaller than for the improved velocity reconstruction algorithm which included the use of an axisymmetric component. On the other hand for vertical upward flows, from the relative errors obtained by using both reconstruction algorithms, as shown in Fig. 7-41, it was found that the reconstructed water velocities obtained using the improved reconstruction algorithm were closer to the reference measurements. The maximum error for the water volumetric flow rate was approximately -3.5%. Consequently, it can be said that the original velocity reconstruction algorithm is more suitable for asymmetric and stratified flows while the improved reconstruction algorithm is better for flows containing an axisymmetric velocity component (e.g. vertical multiphase flows).

A further series of experiments was performed using the MRI tomographic technique to quantitatively investigate the reliability of the local water velocity distributions in gas-in-water

two phase vertical flows obtained from the IFT system. Five cases of local water velocity distribution were reconstructed (see Table 7-13) for both techniques. The local relative differences of water velocity value δv_i is less than 10%, which is acceptable for most industrial applications. Furthermore, by comparing the mean water velocity results obtained from both techniques with the reference water velocity, the relative error for the IFT system is in the range 0.86% to 3.67%, which is much smaller than the relative errors obtained using MRI..

8.3 Contribution to knowledge

The theoretical and experimental work presented in this thesis make the following contributions to knowledge:

1) An investigation into the limitations of a previous multi-electrode electromagnetic flowmeter (EVP) for measuring local water axial velocity distributions in multiphase flow, has been conducted.
2) A 3D simulation model for an IFT flowmeter using finite element analysis has been produced.
3) A MATLAB program based on a mathematical model for analytically investigating the magnetic fields of IFT systems with an anti-Helmholtz coil has been developed.
4) DFT-based reconstruction algorithms have been developed for the local conducting continuous phase velocity profile for three phase or two phase flow where water is the continuous phase. These reconstruction algorithms have much higher spatial resolution than for any previous systems.
5) The hardware of an IFT system has been developed.
6) MATLAB-based software for processing potential difference measurements, and LabVIEW-based software for controlling coil excitation and collecting induced voltage signals, has been developed.
7) New methods for correcting the potential difference measurements have been designed.
8) Quantification of the performance of IFT in vertical and inclined single phase, two phase and three phase flows has been carried out in the SGR flow loop. The major conclusion was that an original velocity profile reconstruction algorithm is more suitable for

reconstructing asymmetric and stratified velocity profiles and an improved reconstruction algorithm, which allows for the use of an axisymmetric velocity component, is better for flows containing an axisymmetric velocity component (e.g. single phase flows and vertical multiphase flows).

9) The IFT system has been compared with an MRI system in vertical gas-in-water two phase flows at a University of Cambridge flow loop. From the results, as shown in Section 7.6.2.2, it was concluded that the accuracy of the IFT system was better than the MRI system, especially at high flow rates.
10) Referring to these features of the IFT system shown in the present research, it can be seen that there is no existing electromagnetic flow metering technique capable of non-invasively obtaining the local axial water velocity distribution in single phase and multiphase flows with high spatial resolution. In addition, because the velocity profile reconstruction algorithms are based on an analytical (polynomial) expression for the water velocity profile, the spatial resolution of the technique can be regarded as infinitely small.

8.4 Future work

The primary objectives of this research have been achieved, but the main task for the future is to develop the IFT flowmetering technique for industrial applications. This section provides ideas for further development of the IFT technique.

1. Coil excitation strategy

As described in Chapter 5, the selected coil excitation strategy for the IFT system was based on the hybrid pulsed DC method. This type of magnetic flux density excitation is more commonly used in a multiphase flow, which is not subject to rapid changes. However, most flows in oil and gas fields are not steady and the flow rates of the flowing phases can vary rapidly with time. In particular the local volume fraction of the dispersed phase can vary rapidly with time which can cause rapid variations in the local water velocity. From the description of the IFT excitation signal in Chapter 5, the ON (S1 and S3) and OFF (S2 and S4) times for one excitation cycle of the magnetic flux density were all selected to have a value of 0.5sec. This strategy will cause loss of useful flow information if typical variations in the local water velocity profile take place over periods which are significantly less than 1 second. In such cases, it will be necessary to use other

excitation methods with higher frequencies, such as the AC excitation or trapezoid excitation methods [120-122].

2. Real-time flow velocity reconstruction algorithm

The DFT-based velocity reconstruction algorithms (original and improved) make the image reconstruction procedure easier compared to more conventional methods, such as generalised iterative or back-projection algorithms [41, 123, 124]. Thus, they have the potential to be used for continuously producing real-time images of the water velocity profile. For real-time imaging, the operation must be executed within a time window which provides a transient flow-induced voltage signal that reliably reflects the local flow velocity distribution during that time window. However, as stated in Chapter 3, the DFT-based reconstruction algorithms rely upon potential difference measurements made when the flow passes through a magnetic field. These potential difference measurements are obtained from uniform and non-uniform magnetic fields, respectively. Therefore, in order to reconstruct flow velocity in real-time, the uniform and non-uniform magnetic fields should be generated alternatively within an adequately short time. The procedure of operation could be:

- First stage: Helmholtz coils of the IFT system are energised to create a uniform magnetic field in the flow cross-section while the potential difference measurements are collected. The time of this stage could be set to be 0.5sec.
- Second stage: After the first stage, the anti-Helmholtz configuration is adopted which produces a non-uniform magnetic field in the pipe cross-section. Simultaneously, the potential difference measurements are obtained. The duration of this stage is also set to be 0.5sec.

Thus, after the application of both magnetic fields the local flow velocity profile could be obtained once per second. Note that the time duration relies upon the RL time-constant of the Helmholtz coil circuits.

3. Inline MPFM flowmeter

As stated in Chapter 2, inline MPFMs commonly employ a combination of two or more measurement techniques to obtain the volumetric flow rate for each phase in a multiphase flow (see Equation 1-4). The experimental work presented in this thesis determined the water volumetric flow rate by processing the offline measurement of Inductive Flow Measurement

Tomography (IFT) and Electrical Resistance Tomography (ERT) systems. Once a real-time flow velocity reconstruction algorithm for IFT is fully developed, the IFT and ERT systems could be combined with a densitometer to obtain real-time mass flow rate measurement for each phase in a multiphase flow (e.g. oil-gas-water three phase flow). A possible technique for density measurement is the vibrating pipe densitometer, which has significant advantages for use with an inline MPFM, including independence of flow regime and being non-intrusive.

9 References

1. Leeuncgulsatien, T., *Measurement of velocity profiles in single-phase and multiphase flows using a multi-electrode electromagnetic flow meter*, Ph.D thesis, 2012, Huddersfield.
2. Tan, C. and F. Dong, *16 - Applications of tomography in mineral transportation*, in *Industrial Tomography*, M. Wang, Editor 2015, Woodhead Publishing. p. 431-450.
3. Xie, C.G. and M. Wilt, *23 - Applications of tomography in the oil-gas industry – Part 2*, in *Industrial Tomography*, M. Wang, Editor 2015, Woodhead Publishing. p. 633-665.
4. Chen, J., et al. *Identification of oil-water flow patterns using conductance probe in vertical well*. in *Instrumentation and Measurement Technology Conference (I2MTC), 2015 IEEE International*. 2015. IEEE.
5. Crowe, C.T., *Multiphase flow handbook*2005: CRC press.
6. Thorn, R., G. Johansen, and B. Hjertaker, *Three-phase flow measurement in the petroleum industry.* Measurement Science and Technology, 2013. **24**(1): p. 012003.
7. Thorn, R., G. Johansen, and E. Hammer, *Recent developments in three-phase flow measurement.* Measurement Science and Technology, 1997. **8**(7): p. 691.
8. Falcone, G., G. Hewitt, and C. Alimonti, *Multiphase flow metering: principles and applications*. Vol. 54. 2009: Elsevier.
9. Shoham, O., *Mechanistic Modeling of Gas-liquid Two-phase Flow in Pipes*2006: Society of Petroleum Engineers.
10. Akhnoukh, R., et al., *Keeping producing wells healthy.* Technology, 1998. **10**(4): p. 14-28.
11. Oddie, G., et al., *Experimental study of two and three phase flows in large diameter inclined pipes.* International Journal of Multiphase Flow, 2003. **29**(4): p. 527-558.
12. Govier, G.W. and K. Aziz, *The flow of complex mixtures in pipes*2008: Society of Petroleum Engineers.
13. Al-Hinai, S., *Non-invasive velocity and volume fraction profile measurement in multiphase flows*, Ph.D thesis, 2010, University of Huddersfield.
14. Lucas, G., J. Cory, and R. Waterfall, *A six-electrode local probe for measuring solids velocity and volume fraction profiles in solids-water flows.* Measurement Science and Technology, 2000. **11**(10): p. 1498.
15. Al-Hinai, S. and G. Lucas. *An Impedance Cross Correlation (ICC) Device For Measuring Solids Velocity And Volume Fraction Profiles in Solid-Water Flows*. in *University of Huddersfield Research Festival*. 2009. University of Huddersfield.
16. Muhamedsalih, Y., G.P. Lucas, and Y.Q. Meng, *A two-phase flow meter for determining water and solids volumetric flow rates in stratified, inclined solids-in-water flows.* Flow Measurement and Instrumentation, 2015. **45**(0): p. 207-217.
17. *Three-Phase Well Test Separator*. 2015 [cited 2015 19th June]; Available from: http://alshaheenweatherford.com/weatherford/groups/web/documents/weatherfordcorp/WFT120079.pdf.
18. Syre, B., et al. *Using Multiphase Meters for fiscal purposes-A field experience*. in *31st International North Sea Flow Measurement Workshop*. 2013.

19. Letton C, P.N., Webb B,Ting F, Floyd A, Tyrrel C, Aabro E and Kane M, *Subsea deepwater measurement— technology gaps and solutions*, in *Proc. 28th Int. North Sea Flow Measurement Workshop*2010: St Andrews, UK.
20. JP, C., *Subsea multiphase measurements: where are we and what's next from an oil and gas operator perspective*, in *29th Int. North Sea Flow Measurement Workshop*2011: Tønsberg,Norway. p. 1500.
21. Danielson, T.J., *Transient Multiphase Flow: Past, Present, and Future with Flow Assurance Perspective.* Energy & Fuels, 2012. **26**(7): p. 4137-4144.
22. Jamaluddin, A. and C. Kabir, *Flow assurance: Managing flow dynamics and production chemistry.* Journal of Petroleum Science and Engineering, 2012. **100**: p. 106-116.
23. Zhang, J., et al., *Advances in rheology and flow assurance studies of waxy crude.* Petroleum Science, 2013. **10**(4): p. 538-547.
24. Weatherford. *Red Eye Multiphase Metering System*. 2009 [cited 2015 June]; Available from: http://www.weatherford.com/doc/wft118301.
25. Fiorentini, P. *Flowatch Multiphase Flow Meter* 2010 [cited 2015 June]; Available from: http://www2.fiorentini.com/media/files/506_flowatch_ct-s-507-e_march-010_int3_1_1_1_1_1_1_3_2_1_1.pdf.
26. Ting, V. *Utilization of an Inline rotary Separator as a Wet Gas Meter*. in *19th North Sea Flow Measurement Workshop*. 2001.
27. Corneliussen, S., et al., *Handbook of multiphase flow metering, rev. 2.* Norwegian Society for Oil and Gas Measurement (www. nfogm. no)/Tekna, 2005.
28. Lucas, G.P., *Modelling velocity profiles in inclined multiphase flow to provide a priori information for flow imaging.* The Chemical Engineering Journal and the Biochemical Engineering Journal, 1995. **56**(3): p. 167-173.
29. Jamieson, A.W., *Multiphase metering—the challenge of implementation.* Measurement and Control, 1999. **32**(1): p. 5-9.
30. Åbro, E., et al., *Determination of void fraction and flow regime using a neural network trained on simulated data based on gamma-ray densitometry.* Measurement Science and Technology, 1999. **10**(7): p. 619.
31. Mi, Y., M. Ishii, and L.H. Tsoukalas, *Vertical two-phase flow identification using advanced instrumentation and neural networks.* Nuclear Engineering and Design, 1998. **184**(2–3): p. 409-420.
32. Letton, W., J.A. Svaeren, and G. Conort. *Topside and Subsea Experience with the Multiphase Flow Meter*. in *SPE Annual Technical Conference and Exhibition*. 1997. Society of Petroleum Engineers.
33. Schlumberger. *Schlumberger Vx MPFM* [cited 2015 June]; Available from: http://www.slb.com/services/characterization/testing/multiphase/~/media/Images/testing/multiphase/flow_ani_sm2_.ashx.
34. Al-Bouri, H.A., et al. *Application of New Multiphase Flow Measurement Systems with Satellite Based Monitoring in Offshore Khafji Field*. in *International Petroleum Technology Conference*. 2005. International Petroleum Technology Conference.
35. Ismail, I., et al., *Tomography for multi-phase flow measurement in the oil industry.* Flow Measurement and Instrumentation, 2005. **16**(2–3): p. 145-155.
36. Canière, H., et al., *Horizontal two-phase flow characterization for small diameter tubes with a capacitance sensor.* Measurement Science and Technology, 2007. **18**(9): p. 2898.

37. Irons, G. and J. Chang, *Particle fraction and velocity measurement in gas-powder streams by capacitance transducers.* International Journal of Multiphase Flow, 1983. **9**(3): p. 289-297.
38. Beck, M.S., *Process Tomography: Principles, Techniques and Applications*2012: Butterworth-Heinemann.
39. Wang, M., *2 - Electrical impedance tomography*, in *Industrial Tomography*, M. Wang, Editor 2015, Woodhead Publishing. p. 23-59.
40. Johansen, G.A., *7 - Gamma-ray tomography*, in *Industrial Tomography*, M. Wang, Editor 2015, Woodhead Publishing. p. 197-222.
41. Yang, W. and L. Peng, *Image reconstruction algorithms for electrical capacitance tomography.* Measurement Science and Technology, 2003. **14**(1): p. R1.
42. Devia, F. and M. Fossa, *Design and optimisation of impedance probes for void fraction measurements.* Flow Measurement and Instrumentation, 2003. **14**(4): p. 139-149.
43. Li, L.-p., et al. *The analysis and study on electromagnetic field of conductance water fraction sensor*. in *Image and Signal Processing (CISP), 2010 3rd International Congress on*. 2010. IEEE.
44. Shi, Y., F. Dong, and C. Tan. *Conductance probe for the measurement of liquid volume fraction and axial velocity in gas-liquid two phase flow*. in *Electronic Measurement & Instruments, 2009. ICEMI'09. 9th International Conference on*. 2009. IEEE.
45. Lina, Y. and L. Yingwei. *On Conductance Probe Measurement Model for Measuring Oil-Water Annular Flow*. in *Information Science and Engineering (ICISE), 2009 1st International Conference on*. 2009. IEEE.
46. Ceccio, S. and D. George, *A review of electrical impedance techniques for the measurement of multiphase flows.* Journal of fluids engineering, 1996. **118**(2): p. 391-399.
47. Muhamedsalih, Y. and G. Lucas. *Measuring two phase flow parameters using impedance cross-correlation flow meter*. in *The 7th International Symposium On Measurement Techniques for multiphase flows* 2012. AIP Publishing.
48. Maxwell, J.C., *A treatise on electricity and magnetism*. Vol. 1. 1881: Clarendon press.
49. Tan, C. and F. Dong. *Cross correlation velocity of oil-water two-phase flow by a dual-plane electrical resistance tomography system*. in *Instrumentation and Measurement Technology Conference (I2MTC), 2010 IEEE*. 2010. IEEE.
50. Lei, H., et al. *Research on electrical resistance tomography and cross-correlation technique to measure the two-phase flows*. in *Instrumentation and Measurement Technology Conference, 2004. IMTC 04. Proceedings of the 21st IEEE*. 2004. IEEE.
51. Wang, M., T. Jones, and R. Williams, *Visualization of asymmetric solids distribution in horizontal swirling flows using electrical resistance tomography.* Chemical Engineering Research and Design, 2003. **81**(8): p. 854-861.
52. Lucas, G. and N. Jin, *A new kinematic wave model for interpreting cross correlation velocity measurements in vertically upward, bubbly oil-in-water flows.* Measurement Science and Technology, 2001. **12**(9): p. 1538.
53. Lucas, G. and N. Jin, *Measurement of the homogeneous velocity of inclined oil-in-water flows using a resistance cross correlation flow meter.* Measurement Science and Technology, 2001. **12**(9): p. 1529.
54. Beck, M.S. and A. Pląskowski, *Cross correlation flowmeters, their design and application*1987: CRC Press.

55. Cory, J., *The measurement of volume fraction and velocity profiles in vertical and inclined multiphase flows*, Ph.D thesis, 1999, University of Huddersfield.
56. Kalender, W.A., *X-ray computed tomography.* Physics in medicine and biology, 2006. **51**(13): p. R29.
57. Marashdeh, Q., F.L. Teixeira, and L.S. Fan, *1 - Electrical capacitance tomography*, in *Industrial Tomography*, M. Wang, Editor 2015, Woodhead Publishing. p. 3-21.
58. Breckon, W. and M. Pidcock, *Mathematical aspects of impedance imaging.* Clinical Physics and Physiological Measurement, 1987. **8**(4A): p. 77.
59. Li, J., *Advances in Chemical Engineering: Characterization of Flow, Particles and Interfaces*. Vol. 37. 2009: Academic Press.
60. Wang, M., W. Yin, and N. Holliday, *A highly adaptive electrical impedance sensing system for flow measurement.* Measurement Science and Technology, 2002. **13**(12): p. 1884.
61. Ye, J., H. Wang, and W. Yang. *Evaluation of effect of number of electrodes in ERT sensors on image quality*. in *Imaging Systems and Techniques (IST), 2013 IEEE International Conference on*. 2013. IEEE.
62. Harikumar, R., R. Prabu, and S. Raghavan, *Electrical Impedance Tomography (EIT) and Its Medical Applications: A Review.* International Journal of Soft Computing Engineering, 2013. **3**(4): p. 2231-2307.
63. Deng, X., et al., *The design of a dual-plane ERT system for cross correlation measurement of bubbly gas/liquid pipe flow.* Measurement Science and Technology, 2001. **12**(8): p. 1024.
64. Meng, Y. and G. Lucas. *Two-phase flow meter for determining water and solids volumetric flow rate in stratified solids-in-water flows*. in *Proceedings of Computing and Engineering Annual Researchers' Conference 2013 : CEARC'13*. 2013. University of Huddersfield.
65. Muhamedsalih, Y., et al. *Two-phase flow meter for determining water and solids volumetric flow rate in inclined solids-in-water flows*. in *7th World Congress on Industrial Process Tomography*. 2013. Krakow, Poland.
66. Hassan, Y.A., *Multiphase bubbly flow visualization using particle image velocimetry.* Annals of the New York Academy of Sciences, 2002. **972**(1): p. 223-228.
67. Raffel, M., C.E. Willert, and J. Kompenhans, *Particle image velocimetry: a practical guide*2013: Springer.
68. Kaipio, J.P., et al., *21 - Process tomography and estimation of velocity fields*, in *Industrial Tomography*, M. Wang, Editor 2015, Woodhead Publishing. p. 551-590.
69. Sederman, A.J., et al., *MRI technique for measurement of velocity vectors, acceleration, and autocorrelation functions in turbulent flow.* Journal of Magnetic Resonance, 2004. **166**(2): p. 182-189.
70. Pope, J. and S. Yao, *Quantitative NMR imaging of flow.* Concepts in Magnetic Resonance, 1993. **5**(4): p. 281-302.
71. Gladden, L.F., *Nuclear magnetic resonance in chemical engineering: principles and applications.* Chemical engineering science, 1994. **49**(20): p. 3339-3408.
72. Fukushima, E., *Nuclear magnetic resonance as a tool to study flow.* Annual review of fluid mechanics, 1999. **31**(1): p. 95-123.

73. Hogendoorn, J., et al. *Magnetic resonance technology: An innovative approach to measure multiphase flow*. in *9th North American Conference on Multiphase Technology*. 2014. BHR Group.
74. Hogendoorn, J., et al., *Magnetic Resonance Multiphase Flowmeter.* Upstream Production Measurement forum, 2015.
75. Sederman, A.J., *4 - Magnetic resonance imaging*, in *Industrial Tomography*, M. Wang, Editor 2015, Woodhead Publishing. p. 109-133.
76. Sederman, A. and L.F. Gladden, *Velocity Imaging of Transient Flows.* eMagRes.
77. Gladden, L.F. and A.J. Sederman, *Recent advances in Flow MRI.* Journal of Magnetic Resonance, 2013. **229**(0): p. 2-11.
78. Mantle, M.D. and A.J. Sederman, *Dynamic MRI in chemical process and reaction engineering.* Progress in Nuclear Magnetic Resonance Spectroscopy, 2003. **43**(1–2): p. 3-60.
79. Hori, M., T. Kobori, and Y. Ouchi, *Method for Measuring Void Fraction by Electromagnetic Flowmeters*1966: Japan Atomic Energy Research Inst.
80. Bernier, R.N. and C.E. Brennen, *Use of the electromagnetic flowmeter in a two-phase flow.* International Journal of Multiphase Flow, 1983. **9**(3): p. 251-257.
81. Velt, I., et al., *Correlation technique for flow rate measurement of electroconductive fluids and two-phase media and device for its implementation*, 1982.
82. Krafft, R., *Electromagnetic flowmeters in multiphase flows.* 1993.
83. Leeungculsatien, T. and G. Lucas, *Measurement of velocity profiles in multiphase flow using a multi-electrode electromagnetic flow meter.* Flow Measurement and Instrumentation, 2013. **31**: p. 86-95.
84. Shercliff, J.A., *The theory of electromagnetic flow-measurement*1987: CUP Archive.
85. Meng, Y. and G. Lucas, *Two-phase flow meter for determining water and solids volumetric flow rate in stratified solids-in-water flows.* 2013.
86. Dr. Sen-ben Liao, D.P.D., and Professor John W. Belcher. *Faraday's Law of Induction*. 2004 [cited 2015 25 Feb]; Available from: http://web.mit.edu/viz/EM/visualizations/coursenotes/modules/guide10.pdf.
87. Lipták, B.G. and H. Eren, *Instrument Engineers' Handbook, Volume 1: Process measurement and analysis*. Vol. 1. 1995: CRC press. 211.
88. *E+H PROMAG*. 2006 [cited 2015 26th Jan]; Available from: http://c.gongkong.com/articleDetails?id=41945&this=solution.
89. DeTroye, D.J. and R.J. Chase, *The Calculation and Measurement of Helmholtz Coil Fields*, Report,1994, DTIC Document.
90. Lucas, G., R. Mishra, and N. Panayotopoulos, *Power law approximations to gas volume fraction and velocity profiles in low void fraction vertical gas–liquid flows.* Flow Measurement and Instrumentation, 2004. **15**(5): p. 271-283.
91. Van der Welle, R., *Void fraction, bubble velocity and bubble size in two-phase flow.* International Journal of Multiphase Flow, 1985. **11**(3): p. 317-345.
92. Zhang, Z., Lucas Gary. *Determination of power law velocity profiles by electromagnetic flow measurement*. in *7th World Congress on Industrial Process Tomography*. 2013. Krakow, Poland.
93. Kollár, L.E., G.P. Lucas, and Z. Zhang, *Proposed method for reconstructing velocity profiles using a multi-electrode electromagnetic flow meter.* Measurement Science and Technology, 2014. **25**(7): p. 075301.

94. Miller, S.J., *The method of least squares.* Mathematics Department Brown University, 2006: p. 1-7.
95. Horner, B., F. Mesch, and A. Trächtler, *A multi-sensor induction flowmeter reducing errors due to non-axisymmetric flow profiles.* Measurement Science and Technology, 1996. **7**(3): p. 354.
96. Kollár, L.E., G.P. Lucas, and Y. Meng, *Reconstruction of velocity profiles in axisymmetric and asymmetric flows using an electromagnetic flow meter.* Measurement Science and Technology, 2015. **26**(5): p. 055301.
97. Zhao, Y., G. Lucas, and T. Leeungculsatien, *Measurement and control systems for an imaging electromagnetic flow metre.* ISA transactions, 2014. **53**(2): p. 423-432.
98. Meyrath, T., *Electromagnet design basics for cold atom experiments*, Report,2004, University of Texas: University of Texas, Austin.
99. Lipták, B.G., *Process Control: Instrument Engineers' Handbook*2013: Butterworth-Heinemann.
100. Schukat, M. *A New Approach to Signal Processing for DC-Electromagnetic Flowmeters*. in *ICSP 2004: International Conference on Signal Processing*. 2004. Citeseer.
101. Dyer, S.A., *Wiley survey of instrumentation and measurement*2004: John Wiley & Sons.
102. Inc, R. *Magnetic Flowmeter Fundamentals*. 1995 [cited 2015 14th February]; Available from: http://www.automaatika.ee/pdf/Fundament.pdf.
103. *Coil Voltage and Temperature compensation*. 2013 June [cited 2015 2nd March]; Available from: http://www.te.com/commerce/DocumentDelivery/DDEController?Action=srchrtrv&DocNm=13C9135_Coil_Voltage_Temp_Comp_AppNote&DocType=CS&DocLang=EN.
104. Brand, J.R., *Handbook of electronics formulas, symbols, and definitions*2012: Springer Science & Business Media.
105. *LF353 dual operational amplifier*. [cited 2015 15th March]; Available from: https://www.fairchildsemi.com/datasheets/LF/LF353.pdf.
106. Ali, M. and G. Lucas, *Optimisation of an Analogue Signal Conditioning Circuit for a Novel Imaging Electromagnetic Flow meter.* 2013.
107. Eshbach, O.W., *Eshbach's handbook of engineering fundamentals*1990: John Wiley & Sons. 43.
108. Gopel, W., et al., *Sensors: a comprehensive survey. chemical and biochemical sensors, Part 1*. Vol. 2. 1992: VCH.
109. Malmberg, C. and A. Maryott, *Dielectric Constant of Water from 00 to 1000 C.* Journal of research of the National Bureau of Standards, 1956. **56**: p. 1-8.
110. Oddie, G., *Instruction of SGR flow loop*, Report, 2012, Schlumberger.
111. Lucas, G., *Gas Volume Fraction and Velocity ProfilesVertical and Inclined Bubbly Air-Water Flows.* Journal of visualization, 2006. **9**(4): p. 419-426.
112. Vigneaux, P., P. Chenais, and J. Hulin, *Liquid‐liquid flows in an inclined pipe.* AIChE Journal, 1988. **34**(5): p. 781-789.
113. Zuber, N. and J. Findlay, *Average volumetric concentration in two-phase flow systems.* Journal of Heat Transfer, 1965. **87**(4): p. 453-468.
114. Vedapuri, D., *Studies on oil-water flow in inclined pipelines* Ph.D thesis, 1999, Ohio University.
115. Hasan, A. and C. Kabir, *A simplified model for oil/water flow in vertical and deviated wellbores.* SPE production & facilities, 1999. **14**(01): p. 56-62.

116. Lucas, G. and N. Jin, *Investigation of a drift velocity model for predicting superficial velocities of oil and water in inclined oil-in-water pipe flows with a centre body.* Measurement Science and Technology, 2001. **12**(9): p. 1546.
117. Lucas, G.P. and N. Panagiotopoulos, *Oil volume fraction and velocity profiles in vertical, bubbly oil-in-water flows.* Flow Measurement and Instrumentation, 2009. **20**(3): p. 127-135.
118. Aziz, K. and G.W. Govier, *Pressure drop in wells producing oil and gas.* Journal of Canadian Petroleum Technology, 1972. **11**(03).
119. Ameen, M.S., *Fracture and in-situ stress characterization of hydrocarbon reservoirs: definitions and introduction.* Geological Society, London, Special Publications, 2003. **209**(1): p. 1-6.
120. Torimaru, T., *Electromagnetic flowmeter*, 1996, Google Patents.
121. Togawa, T., T. Tamura, and P.A. Oberg, *Biomedical transducers and instruments*1997: CRC press.
122. Qingfu Du, W.R., *Trapezoidal excitation based low-power dissipation electromagnetic flowmeter and excitation method* 2014.
123. Cao, Z. and L. Xu, *14 - Direct methods for image reconstruction in electrical capacitance tomography*, in *Industrial Tomography*, M. Wang, Editor 2015, Woodhead Publishing. p. 377-399.
124. Hampel, U., *13 - Image reconstruction for hard field tomography*, in *Industrial Tomography*, M. Wang, Editor 2015, Woodhead Publishing. p. 347-376.

Appendix A

```
close all;
clear;
clc;
% Physical constants
pi = 3.1416;
ne = 16;        % Number of electrodes on circumference (it cannot be
                % changed simply here, because the weight values have to be
                % recalculated for a different number of electrodes)
Bm =159.314e-4;%8.358e-3;%1.59314e-2;     % Magnetic flux density in uniform
magnetic field
                % where magnetic field is assumed in the negative y
                % (vertical) direction (T)
Bmnu =45.271e-4;%5.019e-3;%4.5271e-3;  % Maximum magnetic flux density in
non-uniform magnetic field
Rp = 0.025;     % Pipe radius (m)
vslip = 0;  % Slip velocity (non-zero if velocity of non-conductive
                %   phase is plotted)

% Numerical constants
nmax =6;       % Max order of polynomial to consider in reconstruction
                % 0 <= nmax <= 6
m = 100;        % For plot: Number of points in both horizontal and vertical
                % directions in the division of a rectangular section
                % including the pipe
potplot = 0;    % 1: Plot potential distributions in non-uniform magnetic
field
                % 0: No plot of potential distributions
qconc = 2;      % If non-zero, input file with local water volume fraction
                %    'qwater.dat' is needed
                % 0: No calculation of water flow rate, no plot of vol
fraction
                % 1: Calculate water flow rate, no plot of volume fraction
                % 2: Calculate water flow rate, plot volume fraction
om = 0;    % Angle of rotation (deg) of coordiantes
                %    Zero if vertical passes through electrodes 5 and 13
                %    Positive if axis through e5-e13 has to be rotated in
                %    positive direction toward vertical
np1 = 0;        % Lowest and highest max orders of polynomials in optimum
np2 = 1;        % solutions that are used to determine mean velocities in
                % subdomains of ERT grid (Leeds), 0 <= np1, np2 <= nmax
                % If np1 > np2, then there is no calculation and plot of
                %    velocity profiles in the mh x mv resolution.
mh = 20;        % For mean velocities in subdomains of ERT grid (Leeds):
mv = mh;        %    number of subdomains in horizontal and vertical
directions
                %    They must be the same for calculation of water flow rate!

% Constants for axisymm component
%   (in ImX(2)2-theta(Q2) and q-Aq relationships)
% ImX(2)2 = (ac2*cos(2*theta(Q2))+b2)*a22*Bmnu*Rp
% q = qaq3*Aq^3 + qaq2*Aq^2 + qaq1*Aq + qaq0
% These relationships depend on the structure of the experimental device
%   used (or on its COMSOL model). A high velocity (100 m/s) was used to
```

```
%   derive these relationships, because computation error increases
%   considerably for low velocity (below 10 m/s).
% as: In general, ImX(2)0 (axisymm component) is obtained by substructing
%     ImX(2)2 (quadratic component) from ImX(2) (total). It is always like
%     that when max order of polynomial in velocity profile is at least 2.
%     as = 0: ImX(2)2 is not subtracted when max order of polynomial in
%             velocity profile is less than 2 (i.e. axisymm and linear).
%     as = 1: Two plots are shown when max order of polynomial in velocity
%             profile is less than 2 (i.e. axisymm and linear): with and
%             without subtracting ImX(2)2
% Models: LK's 80mm - LK's Mk1 Comsol model for 80-mm pipe, Bop is rounded
%                     to 0.0052 T, 10-cm long pipe with normal mesh
%         LK's 50mm - LK's Mk1a Comsol model for 50-mm pipe (based on Meng's
%                     model with "different" coil geometries), Bop is
%                     calculated as average of abs(min) and abs(max) of B
%         Meng's 50mm red - Meng's Mk1a Comsol model for 50-mm pipe, Bop is
%                           calculated as max of B, short pipe (3 cm) with
%                           normal mesh refined in the pipe section
%         Meng's 50mm blue - Meng's Mk1a Comsol model for 50-mm pipe, Bop is
%                            calculated as average of abs(min) and abs(max)
%                            of B, short pipe (3 cm) with normal mesh
%                            refined in the pipe section
as = 1;
ac2v = [0.0099 0.009653];
b2v = [-0.0172 -0.01665];
curvx2 = 2;             % curvx2=1: LK's 80mm model
ac2 = ac2v(curvx2);     % curvx2=2: LK's 50mm model - short pipe (3 cm) with
b2 = b2v(curvx2);       %           normal mesh refined in the pipe section
qaq3v = [0 -50.5454 -48.9608 0];
qaq2v = [10.79 62.7395 61.4532 11.835];
qaq1v = [-13.32 -30.6971 -30.3993 -13.812];
qaq0v = [3.73 5.4655 5.4770 3.6579];
Aqmaxv = [(-qaq1v(1)-sqrt(qaq1v(1)^2-4*qaq2v(1)*qaq0v(1)))/(2*qaq2v(1))...
    0.3979 0.4034 ...
    (-qaq1v(4)-sqrt(qaq1v(4)^2-4*qaq2v(4)*qaq0v(4)))/(2*qaq2v(4))];
curv = 3;               % curv=1: LK's 80mm model
qaq3 = qaq3v(curv);     % curv=2: Meng's 50mm red model
qaq2 = qaq2v(curv);     % curv=3: Meng's 50mm blue model
qaq1 = qaq1v(curv);     % curv=4: LK's 50mm model - long pipe (30 cm) with
qaq0 = qaq0v(curv);     %         normal mesh
Aqmax = Aqmaxv(curv);


% PART I: RECONSTRUCTION OF POSSIBLE VELOCITY PROFILES

% STEP 1
% Potential distribution in uniform magnetic field from input file
% The input file includes a column vector with 16 elements, where the pth
% element means potential difference ep-e5 in V at electrode p (p = 1 at 0
% deg if angle is measured from the x-axis)
load potdistr_unif.dat

% Potential distribution (length(Uu) = ne)
for i=1:ne
    Uu(i) = potdistr_unif(i)-potdistr_unif(5);
end
```

```
% STEP 2
% Constants for DFT
fs = ne;    % sampling frequency
N = length(Uu);
fn = fs/2;  % Nyquist frequency
f = linspace(0,fn-fn/(N/2),N/2);

% DFT
X = fft(Uu)/N;
XA = X(1:N/2+1);
XAR = real(XA);
XAI = imag(XA);

% STEPS 3-6 for 0th to 6th order terms
A0 = zeros(2,2);
A1 = zeros(1,2);
A2 = zeros(2,3);
A3 = zeros(3,3);
A4 = zeros(4,4);
A5 = zeros(5,4);
A6 = zeros(6,5);

% Uniform (0th order) term
if XAR(N/fs+1) > 0
    a00 = 2*abs(XA(N/fs+1))/(Bm*Rp);
else
    a00 = -2*abs(XA(N/fs+1))/(Bm*Rp);
end

% Linear (1st order) term
a11 = 2*abs(XA(2*N/fs+1))*4/(Bm*Rp);
if XAR(2*N/fs+1)>=0
    psi = atan(XAI(2*N/fs+1)/XAR(2*N/fs+1))*180/pi;
elseif XAI(2*N/fs+1)>=0
    psi = (atan(XAI(2*N/fs+1)/XAR(2*N/fs+1))+pi)*180/pi;
else
    psi = (atan(XAI(2*N/fs+1)/XAR(2*N/fs+1))-pi)*180/pi;
end
theta1 = -psi;

% Quadratic (2nd order) term
a22 = 2*abs(XA(3*N/fs+1))*12/(Bm*Rp);
a20 = -a22/4;
if XAR(3*N/fs+1)>=0
    psi = atan(XAI(3*N/fs+1)/XAR(3*N/fs+1))*180/pi;
elseif XAI(3*N/fs+1)>=0
    psi = (atan(XAI(3*N/fs+1)/XAR(3*N/fs+1))+pi)*180/pi;
else
    psi = (atan(XAI(3*N/fs+1)/XAR(3*N/fs+1))-pi)*180/pi;
end
theta2 = -psi/2;

% Cubic (3rd order) term
a33 = 2*abs(XA(4*N/fs+1))*32/(Bm*Rp);
```

```
a31 = -a33/2;
if XAR(4*N/fs+1)>=0
    psi = atan(XAI(4*N/fs+1)/XAR(4*N/fs+1))*180/pi;
elseif XAI(4*N/fs+1)>=0
    psi = (atan(XAI(4*N/fs+1)/XAR(4*N/fs+1))+pi)*180/pi;
else
    psi = (atan(XAI(4*N/fs+1)/XAR(4*N/fs+1))-pi)*180/pi;
end
theta3 = -psi/3;

% Quartic (4th order) term
a44 = 2*abs(XA(5*N/fs+1))*80/(Bm*Rp);
a42 = -3*a44/4;
a40 = a44/16;
if XAR(5*N/fs+1)>=0
    psi = atan(XAI(5*N/fs+1)/XAR(5*N/fs+1))*180/pi;
elseif XAI(5*N/fs+1)>=0
    psi = (atan(XAI(5*N/fs+1)/XAR(5*N/fs+1))+pi)*180/pi;
else
    psi = (atan(XAI(5*N/fs+1)/XAR(5*N/fs+1))-pi)*180/pi;
end
theta4 = -psi/4;

% Quintic (5th order) term
a55 = 2*abs(XA(6*N/fs+1))*192/(Bm*Rp);
a53 = -a55;
a51 = 3*a55/16;
if XAR(6*N/fs+1)>=0
    psi = atan(XAI(6*N/fs+1)/XAR(6*N/fs+1))*180/pi;
elseif XAI(6*N/fs+1)>=0
    psi = (atan(XAI(6*N/fs+1)/XAR(6*N/fs+1))+pi)*180/pi;
else
    psi = (atan(XAI(6*N/fs+1)/XAR(6*N/fs+1))-pi)*180/pi;
end
theta5 = -psi/5;

% 6th order term
a66 = 2*abs(XA(7*N/fs+1))*448/(Bm*Rp);
a64 = -5*a66/4;
a62 = 3*a66/8;
a60 = -a66/64;
if XAR(7*N/fs+1)>=0
    psi = atan(XAI(7*N/fs+1)/XAR(7*N/fs+1))*180/pi;
elseif XAI(7*N/fs+1)>=0
    psi = (atan(XAI(7*N/fs+1)/XAR(7*N/fs+1))+pi)*180/pi;
else
    psi = (atan(XAI(7*N/fs+1)/XAR(7*N/fs+1))-pi)*180/pi;
end
theta6 = -psi/6;


% PART II: FINDING AXISYMMETRIC COMPONENT

% STEP 7
% Potential distribution in non-uniform magnetic field from input file
% The input file includes a column vector with 16 elements, where the pth
```

```
% element means potential difference ep-e5 in V at electrode p
load potdistr_nonu.dat
for i=1:ne
    theta(i) = 22.5*(i-1);
    Unu(i) = potdistr_nonu(i)-potdistr_nonu(5);
end

% STEP 8
% Apply DFT for potential distribution obtained in non-uniform
%   magnetic field and determine Im X(2)
Xnu = fft(Unu)/N;
XAnu = Xnu(1:N/2+1);
Xnuout = [real(XAnu.') imag(XAnu.') abs(XAnu.')];
imx2 = imag(XAnu(3));

% STEPS 9-11
% Determine Im X(2)_0 (nmax <= 2 means that quadratic component is
%   neglected, so Im X(2) is due to axisymmetric component only)
%   Index ix=1 is used when max order of polynomial is 0 or 1
%   Indeces ix=2 and 3 are used when max order of polynomial is at least 2
imx20(1) = imx2;
ixmax = 1;
if nmax >= 2
    imx221 = (ac2*cosd(2*theta2)+b2)*a22*Bmnu*Rp;
    imx20(2) = imx2 - imx221;
    imx222 = (ac2*cosd(2*(theta2+180/2))+b2)*(-a22)*Bmnu*Rp;
    imx20(3) = imx2 - imx222;
    ixmax = 3;
end
for ix = 1:ixmax
    if imx20(ix) >= 0
        if a00 >= 0
            qaxi(ix) = 0;
        else
            Aq(ix) = abs(2*imx20(ix)/(a00*Bmnu*Rp));
        end
    else
        if a00 < 0
            qaxi(ix) = 0;
        else
            Aq(ix) = abs(2*imx20(ix)/(a00*Bmnu*Rp));
        end
    end
    if Aq(ix) > Aqmax
        qaxi(ix) = 0;
    else
        qaxi(ix) = qaq3*Aq(ix)^3+qaq2*Aq(ix)^2+qaq1*Aq(ix)+qaq0;
    end
end


% PART III: CHOICE OF OPTIMUM SOLUTION

% Weight values are stored in data file wei.dat for a specific division
%   with 30 subdomains in the pipe cross section - areas of subdomains and
%   calculation of mean velocities in those subdomains are in
```

```
%   function vmean30.m
% The data file wei.dat includes 15 rows (i.e. number of electrodes-1) and
%   30 columns (i.e. number of subdomains)
%   1st row - electrode 6 (112.5 deg); 15th row - electrode 4 (67.5 deg)
load wei.dat

% STEPS 12-13
% Division of pipe section
% Rectangular section including the pipe is divided into mxm points where
%   calculations are made - corresponding x and y coordinates are stored
%   in two vectors x and y
for i=1:(m+1)*(m+1)
    if i-(m+1)*floor(i/(m+1)) == 0
        xi = m+1;
        yi = floor(i/(m+1));
    else
        xi = i-(m+1)*floor(i/(m+1));
        yi = floor(i/(m+1))+1;
    end
    x(i) = -Rp + (xi-1)*2*Rp/m;
    y(i) = -Rp + (yi-1)*2*Rp/m;
end
for i=1:m+1
    xM(i) = -Rp + 2*Rp/m*(i-1);
    yM(i) = -Rp + 2*Rp/m*(i-1);
end

% Pixel numbers, and coordinates (x and y) for ERT grid (Leeds)
xc = zeros(1,mh*mv);
yc = zeros(1,mh*mv);
npix = 0;
for i = 1:mh
    for j = 1:mv
        xc((i-1)*mv+j) = -Rp + 2*Rp/mh*(2*i-1)/2;
        yc((i-1)*mv+j) = -Rp + 2*Rp/mv*(2*j-1)/2;
    end
end
for i = 1:mh*mv             % Results in vector form (xcc,ycc,vmean)
    if xc(i)^2+yc(i)^2 <= Rp^2
        npix = npix + 1;
        pix(npix) = npix;
        xcc(npix) = xc(i);
        ycc(npix) = yc(i);
    end
end
pixxyv(:,1) = pix';
pixxyv(:,2) = xcc';
pixxyv(:,3) = ycc';

% Load local water concentration if it is plotted or
%   if total water flow rate is calculated
if qconc ~= 0
    alpm = load('qwater.dat');
    fign = 2*(nmax+1) + np2-np1+2 + 2*as; % Figure number of concentration
plot
end
```

```
% Calculation for each max order of polynomials up to 'nmax'
mindopt = 1e10;
kert = 0;
for kn=1:nmax+1
    % Saving possible velocity components in matrices, A0, ..., A6
    % Each matrix corresponds to a given order polynomial component
    % Each row includes a possible solution component with coefficients
    %   and angle (in deg) of that component (coefficient and exponent for
    %   the axisymmetric component)
    if kn == 1
        A0 = [a00 qaxi(1); 0 0];
    end
    if kn == 2
        A1 = [a11 theta1];
    end
    if kn == 3
        A0 = [a00 qaxi(2); a00 qaxi(3)];
        A2 = [a22 a20 theta2; -a22 -a20 theta2+180/2];
    end
    if kn == 4
        A3 = [a33 a31 theta3; a33 a31 theta3+360/3; a33 a31 theta3+2*360/3];
    end
    if kn == 5
        A4 = [a44 a42 a40 theta4; a44 a42 a40 theta4+360/4; ...
        -a44 -a42 -a40 theta4+180/4; -a44 -a42 -a40 theta4+3*180/4];
    end
    if kn == 6
        A5 = [a55 a53 a51 theta5; a55 a53 a51 theta5+360/5; ...
        a55 a53 a51 theta5+2*360/5; a55 a53 a51 theta5+3*360/5; ...
        a55 a53 a51 theta5+4*360/5];
    end
    if kn == 7
        A6 = [a66 a64 a62 a60 theta6; a66 a64 a62 a60 theta6+360/6; ...
        a66 a64 a62 a60 theta6+2*360/6; -a66 -a64 -a62 -a60 theta6+180/6; ...
        -a66 -a64 -a62 -a60 theta6+3*180/6; -a66 -a64 -a62 -a60
theta6+5*180/6];
    end
    for k=1:factorial(kn-1)
        % Determine the number of row (n2, ..., n6) in each matrix A0, ...,
A6,
        % which must be considered in possible solution k (k = 1, ..., nmax!)
        if (k/2 - floor(k/2)) == 0
            n2 = 2;
        else n2 = 1;
        end
        if (k/6 - floor(k/6)) > 0
            if (k/6 - floor(k/6)) <= 1/3
                n3 = 1;
            elseif (k/6 - floor(k/6)) <= 2/3
                n3 = 2;
            else n3 = 3;
            end
        else n3 = 3;
        end
        if (k/24 - floor(k/24)) > 0
            if (k/24 - floor(k/24)) <= 1/4
```

```
            n4 = 1;
        elseif (k/24 - floor(k/24)) <= 2/4
            n4 = 2;
        elseif (k/24 - floor(k/24)) <= 3/4
            n4 = 3;
        else n4 = 4;
        end
    else n4 = 4;
    end
    if (k/120 - floor(k/120)) > 0
        if (k/120 - floor(k/120)) <= 1/5
            n5 = 1;
        elseif (k/120 - floor(k/120)) <= 2/5
            n5 = 2;
        elseif (k/120 - floor(k/120)) <= 3/5
            n5 = 3;
        elseif (k/120 - floor(k/120)) <= 4/5
            n5 = 4;
        else n5 = 5;
        end
    else n5 = 5;
    end
    if (k/720 - floor(k/720)) > 0
        if (k/720 - floor(k/720)) <= 1/6
            n6 = 1;
        elseif (k/720 - floor(k/720)) <= 2/6
            n6 = 2;
        elseif (k/720 - floor(k/720)) <= 3/6
            n6 = 3;
        elseif (k/720 - floor(k/720)) <= 4/6
            n6 = 4;
        elseif (k/720 - floor(k/720)) <= 5/6
            n6 = 5;
        else n6 = 6;
        end
    else n6 = 6;
    end

    % Possible velocity profiles from matrices A0, ..., A6
    % Velocity values are calculated at points (x,y) and stored in
    %   a vector of the same size as x and y
    for i=1:(m+1)*(m+1)
        if x(i)^2+y(i)^2 > Rp^2
            v(i) = 0;
        else
            v0(i) = A0(n2,1)/2*(1-sqrt(x(i)^2+y(i)^2)/Rp)^A0(n2,2)*...
                (A0(n2,2)+1)*(A0(n2,2)+2);
            v1(i) = A1(1)*(x(i)*cosd(A1(2))+y(i)*sind(A1(2)))/Rp;
            v2(i) =
A2(n2,1)*(x(i)*cosd(A2(n2,3))+y(i)*sind(A2(n2,3)))^2/Rp^2 ...
                + A2(n2,2);
            v3(i) =
A3(n3,1)*(x(i)*cosd(A3(n3,3))+y(i)*sind(A3(n3,3)))^3/Rp^3 ...
                + A3(n3,2)*(x(i)*cosd(A3(n3,3))+y(i)*sind(A3(n3,3)))/Rp;
            v4(i) =
A4(n4,1)*(x(i)*cosd(A4(n4,4))+y(i)*sind(A4(n4,4)))^4/Rp^4 ...
```

```
                    +
A4(n4,2)*(x(i)*cosd(A4(n4,4))+y(i)*sind(A4(n4,4)))^2/Rp^2 ...
                    + A4(n4,3);
                v5(i) =
A5(n5,1)*(x(i)*cosd(A5(n5,4))+y(i)*sind(A5(n5,4)))^5/Rp^5 ...
                    +
A5(n5,2)*(x(i)*cosd(A5(n5,4))+y(i)*sind(A5(n5,4)))^3/Rp^3 ...
                    + A5(n5,3)*(x(i)*cosd(A5(n5,4))+y(i)*sind(A5(n5,4)))/Rp;
                v6(i) =
A6(n6,1)*(x(i)*cosd(A6(n6,5))+y(i)*sind(A6(n6,5)))^6/Rp^6 ...
                    +
A6(n6,2)*(x(i)*cosd(A6(n6,5))+y(i)*sind(A6(n6,5)))^4/Rp^4 ...
                    +
A6(n6,3)*(x(i)*cosd(A6(n6,5))+y(i)*sind(A6(n6,5)))^2/Rp^2 ...
                    + A6(n6,4);
                v(i) = v0(i)+v1(i)+v2(i)+v3(i)+v4(i)+v5(i)+v6(i);
            end
        end

        % Mean velocities in the 30 subdomains where weight values are known
        % Velocities and areas are stored in vector vmA with 30x2 elements
        vmA = vmean30(Rp,m,x,y,v);

        % Potential distribution in non-uniform magnetic field for
        % the possible velocity profiles
        delU = zeros(1,ne-1);
        for j=1:ne-1
            for i=1:30
                delU(j) = delU(j) +
2*Bmnu/(pi*Rp)*vmA(i,1)*wei(j,i)*vmA(i,2);
            end
        end

        % Organize potential values so that j=1 corresponds to electrode 1
        % (0 deg) and j=16 corresponds to electrode 16 (337.5 deg)
        % Potential at electrode 5 (90 deg) is 0
        for j=1:4
            U(k,j) = delU(ne-5+j);
        end
        for j=1:ne-5
            U(k,j+5) = delU(j);
        end

        % Comparison of measured potential distribution to those
        % calculated for each possible velocity profile
        del(k) = 0;
        for i=1:ne
            del(k) = del(k) + (U(k,i)-Unu(i))^2;
        end

        % Save number of rows in matrices A0, ..., A6 for optimum solution
        if kn <= 2
            nopt = [1 1 1 1 1];
        else
            if k == 1
                kopt = k;
```

```
            nopt = [n2 n3 n4 n5 n6];
            kfar = k;
            for j=1:ne
                Uopt(j) = U(k,j);
                Ufar(j) = U(k,j);
            end
        end
        if k > 1
            if del(k) < del(kopt)
            kopt = k;
            nopt = [n2 n3 n4 n5 n6];
                for j=1:ne
                    Uopt(j) = U(k,j);
                end
            end
            if del(k) > del(kfar)
            kfar = k;
                for j=1:ne
                    Ufar(j) = U(k,j);
                end
            end
        end
    end
end

% Collect lowest (delopt) and highest (delfar) sums of differences of
% measured and calculated potentials for each order of polynomial
if kn <= 2
    delopt(kn) = del(k);
    delfar(kn) = del(k);
else
    delopt(kn) = del(kopt);
    delfar(kn) = del(kfar);
end
if delopt(kn) < mindopt
    ndelmin = kn-1;
    mindopt = delopt(kn);
end
n2 = nopt(1);
n3 = nopt(2);
n4 = nopt(3);
n5 = nopt(4);
n6 = nopt(5);

% Plot potential distributions in non-uniform magnetic field
% Measured, closest and farthest calculated distributions
if potplot == 1
    if kn <= 2
        figure(nmax+1+kn)
        plot(theta,Unu,'b',theta,U,'r-')
        xlabel('\theta (deg)')
        ylabel('U (V)')
        legend('measured','calculated')
        if kn == 1
            title('Axisymmetric')
        else
```

```
                title('1st order (linear)')
            end
        else
            figure(nmax+1+kn)
            plot(theta,Unu,'b',theta,Uopt,'r-',theta,Ufar,'r--')
            xlabel('\theta (deg)')
            ylabel('U (V)')
            legend('measured','closest','farthest')
            if kn == 3
                title('2nd order (quadratic)')
            elseif kn == 4
                title('3rd order (cubic)')
            elseif kn == 5
                title('4th order (quartic)')
            elseif kn == 6
                title('5th order (quintic)')
            elseif kn == 7
                title('6th order (sextic)')
            end
        end
    end

    % Optimum velocity profile from matrices A0, ..., A6
    %   with corresponding rows determined above
    % Velocity values calculated at mxm points are stored in matrix form
    for i=1:m+1
        for j=1:m+1
            if xM(i)^2+yM(j)^2 > Rp^2
                vM(j,i) = 0;
            else
                vM(j,i) = A0(n2,1)/2*(1-
sqrt(xM(i)^2+yM(j)^2)/Rp)^A0(n2,2)*...
                    (A0(n2,2)+1)*(A0(n2,2)+2) ...
                    + A1(1)*(xM(i)/Rp*cosd(A1(2)-om)+yM(j)/Rp*sind(A1(2)-om))
...
                    + A2(n2,1)*(xM(i)/Rp*cosd(A2(n2,3)-
om)+yM(j)/Rp*sind(A2(n2,3)-om))^2 ...
                    + A2(n2,2) ...
                    + A3(n3,1)*(xM(i)/Rp*cosd(A3(n3,3)-
om)+yM(j)/Rp*sind(A3(n3,3)-om))^3 ...
                    + A3(n3,2)*(xM(i)/Rp*cosd(A3(n3,3)-
om)+yM(j)/Rp*sind(A3(n3,3)-om)) ...
                    + A4(n4,1)*(xM(i)/Rp*cosd(A4(n4,4)-
om)+yM(j)/Rp*sind(A4(n4,4)-om))^4 ...
                    + A4(n4,2)*(xM(i)/Rp*cosd(A4(n4,4)-
om)+yM(j)/Rp*sind(A4(n4,4)-om))^2 ...
                    + A4(n4,3) ...
                    + A5(n5,1)*(xM(i)/Rp*cosd(A5(n5,4)-
om)+yM(j)/Rp*sind(A5(n5,4)-om))^5 ...
                    + A5(n5,2)*(xM(i)/Rp*cosd(A5(n5,4)-
om)+yM(j)/Rp*sind(A5(n5,4)-om))^3 ...
                    + A5(n5,3)*(xM(i)/Rp*cosd(A5(n5,4)-
om)+yM(j)/Rp*sind(A5(n5,4)-om)) ...
                    + A6(n6,1)*(xM(i)/Rp*cosd(A6(n6,5)-
om)+yM(j)/Rp*sind(A6(n6,5)-om))^6 ...
                    + A6(n6,2)*(xM(i)/Rp*cosd(A6(n6,5)-
om)+yM(j)/Rp*sind(A6(n6,5)-om))^4 ...
```

```
                    + A6(n6,3)*(xM(i)/Rp*cosd(A6(n6,5)-
om)+yM(j)/Rp*sind(A6(n6,5)-om))^2 ...
                    + A6(n6,4);
                % If as = 1, then calculate axisymm and linear velocity
                %   profiles considering the effects of quadratic component
                %   on ImX(2). This is done only once when the quadratic
                %   velocity profile is determined.
                if kn == 3
                    if as == 1
                        vM02(j,i) = A0(n2,1)/2*(1-
sqrt(xM(i)^2+yM(j)^2)/Rp)^A0(n2,2)*...
                            (A0(n2,2)+1)*(A0(n2,2)+2);
                        vM12(j,i) = A0(n2,1)/2*(1-
sqrt(xM(i)^2+yM(j)^2)/Rp)^A0(n2,2)*...
                            (A0(n2,2)+1)*(A0(n2,2)+2) ...
                           + A1(1)*(xM(i)/Rp*cosd(A1(2)-
om)+yM(j)/Rp*sind(A1(2)-om));
                    end
                end
            end
        end
    end

    % Write coefficients of optimum velocity profile in a matrix
    %   1st row: axisymm term, ..., 7th row: 6th order term
    %   1st column: order of term
    %   2nd and 3rd columns for axisymm term: coefficient and exponent 'qaxi'
    %   next column(s) for non-axisymm terms: coefficients
    %   last (non-zero) column for non-axisymm terms: angle
    Ares = [0 A0(n2,1) A0(n2,2) 0 0 0; ...
            1 A1(1) A1(2)-om 0 0 0; ...
            2 A2(n2,1) A2(n2,2) A2(n2,3)-om 0 0; ...
            3 A3(n3,1) A3(n3,2) A3(n3,3)-om 0 0; ...
            4 A4(n4,1) A4(n4,2) A4(n4,3) A4(n4,4)-om 0; ...
            5 A5(n5,1) A5(n5,2) A5(n5,3) A5(n5,4)-om 0; ...
            6 A6(n6,1) A6(n6,2) A6(n6,3) A6(n6,4) A6(n6,5)-om];
    for i = 1:kn
        for j = 1:6
            Aresult(i,j) = Ares(i,j);
        end
    end
    Aresult

    % 3D plot of optimum velocity profile
    figure(kn)
    surf(xM,yM,vM+vslip)
    xlabel('x (m)')
    ylabel('y (m)')
    axis([-Rp Rp -Rp Rp])
    view([0,90])
    shading flat
    colorbar
    if kn == 1
        title('Axisymmetric')
    elseif kn == 2
        title('1st order (linear)')
```

```
    elseif kn == 3
        title('2nd order (quadratic)')
    elseif kn == 4
        title('3rd order (cubic)')
    elseif kn == 5
        title('4th order (quartic)')
    elseif kn == 6
        title('5th order (quintic)')
    elseif kn == 7
        title('6th order (sextic)')
    end
    % If as = 1, then plot axisymm and linear velocity profiles considering
    %   the effects of quadratic component on ImX(2). This is done only
    %   once when the quadratic velocity profile is determined.
    if kn == 3
        if as == 1
            figure(2*(nmax+1)+1)
            surf(xM,yM,vM02+vslip)
            xlabel('x (m)')
            ylabel('y (m)')
            axis([-Rp Rp -Rp Rp])
            view([0,90])
            shading flat
            colorbar
            title('Axisymmetric with quadratic (imx22) effect')
            figure(2*(nmax+1)+2)
            surf(xM,yM,vM12+vslip)
            xlabel('x (m)')
            ylabel('y (m)')
            axis([-Rp Rp -Rp Rp])
            view([0,90])
            shading flat
            colorbar
            title('1st order (linear) with quadratic (imx22) effect')
        end
    end

    % Determine mean velocities in subdomains of ERT grid (Leeds)
    %   if max order of polynomial is between 'np1' and 'np2'
    if kn >= np1+1
        if kn <= np2+1
            kert = kert + 1;
            npix = 0;
            for i = 1:mh*mv             % Results in vector form
(xcc,ycc,vmean)
                if xc(i)^2+yc(i)^2 <= Rp^2
                npix = npix + 1;
                vmean(npix) = A0(n2,1)/2*(1-
sqrt(xcc(npix)^2+ycc(npix)^2)/Rp)^A0(n2,2)*...
                    (A0(n2,2)+1)*(A0(n2,2)+2) ...
                    + A1(1)*(xcc(npix)/Rp*cosd(A1(2)-
om)+ycc(npix)/Rp*sind(A1(2)-om)) ...
                    + A2(n2,1)*(xcc(npix)/Rp*cosd(A2(n2,3)-
om)+ycc(npix)/Rp*sind(A2(n2,3)-om))^2 ...
                    + A2(n2,2) ...
                    + A3(n3,1)*(xcc(npix)/Rp*cosd(A3(n3,3)-
om)+ycc(npix)/Rp*sind(A3(n3,3)-om))^3 ...
```

```
                    + A3(n3,2)*(xcc(npix)/Rp*cosd(A3(n3,3)-
om)+ycc(npix)/Rp*sind(A3(n3,3)-om)) ...
                    + A4(n4,1)*(xcc(npix)/Rp*cosd(A4(n4,4)-
om)+ycc(npix)/Rp*sind(A4(n4,4)-om))^4 ...
                    + A4(n4,2)*(xcc(npix)/Rp*cosd(A4(n4,4)-
om)+ycc(npix)/Rp*sind(A4(n4,4)-om))^2 ...
                    + A4(n4,3) ...
                    + A5(n5,1)*(xcc(npix)/Rp*cosd(A5(n5,4)-
om)+ycc(npix)/Rp*sind(A5(n5,4)-om))^5 ...
                    + A5(n5,2)*(xcc(npix)/Rp*cosd(A5(n5,4)-
om)+ycc(npix)/Rp*sind(A5(n5,4)-om))^3 ...
                    + A5(n5,3)*(xcc(npix)/Rp*cosd(A5(n5,4)-
om)+ycc(npix)/Rp*sind(A5(n5,4)-om)) ...
                    + A6(n6,1)*(xcc(npix)/Rp*cosd(A6(n6,5)-
om)+ycc(npix)/Rp*sind(A6(n6,5)-om))^6 ...
                    + A6(n6,2)*(xcc(npix)/Rp*cosd(A6(n6,5)-
om)+ycc(npix)/Rp*sind(A6(n6,5)-om))^4 ...
                    + A6(n6,3)*(xcc(npix)/Rp*cosd(A6(n6,5)-
om)+ycc(npix)/Rp*sind(A6(n6,5)-om))^2 ...
                    + A6(n6,4);
                end
            end

            % Plot results in ERT grid (Leeds)
            % Increasing indices in xcM,ycM,vmeanM mean increasing x and y
coordinates,
            %   i.e. in vmeanM: x increases from left to right and
            %   y increases from top to bottom
            for i = 1:mh+1              % Results in matrix form
(xcM,ycM,vmeanM)
                xcM(i) = -Rp + 2*Rp/(2*mh)*(2*i-1);
                xcMM(i) = -Rp + 2*Rp/(2*mh)*(2*i-2);
                for j = 1:mv+1
                    ycM(j) = -Rp + 2*Rp/(2*mv)*(2*j-1);
                    ycMM(j) = -Rp + 2*Rp/(2*mv)*(2*j-2);
                    if xcM(i)^2+ycM(j)^2 > Rp^2
                        vmeanM(j,i) = 0;
                    else
                        vmeanM(j,i) = A0(n2,1)/2*(1-
sqrt(xcM(i)^2+ycM(j)^2)/Rp)^A0(n2,2)*...
                            (A0(n2,2)+1)*(A0(n2,2)+2) ...
                            + A1(1)*(xcM(i)/Rp*cosd(A1(2)-
om)+ycM(j)/Rp*sind(A1(2)-om)) ...
                            + A2(n2,1)*(xcM(i)/Rp*cosd(A2(n2,3)-
om)+ycM(j)/Rp*sind(A2(n2,3)-om))^2 ...
                            + A2(n2,2) ...
                            + A3(n3,1)*(xcM(i)/Rp*cosd(A3(n3,3)-
om)+ycM(j)/Rp*sind(A3(n3,3)-om))^3 ...
                            + A3(n3,2)*(xcM(i)/Rp*cosd(A3(n3,3)-
om)+ycM(j)/Rp*sind(A3(n3,3)-om)) ...
                            + A4(n4,1)*(xcM(i)/Rp*cosd(A4(n4,4)-
om)+ycM(j)/Rp*sind(A4(n4,4)-om))^4 ...
                            + A4(n4,2)*(xcM(i)/Rp*cosd(A4(n4,4)-
om)+ycM(j)/Rp*sind(A4(n4,4)-om))^2 ...
                            + A4(n4,3) ...
                            + A5(n5,1)*(xcM(i)/Rp*cosd(A5(n5,4)-
om)+ycM(j)/Rp*sind(A5(n5,4)-om))^5 ...
```

```
                            + A5(n5,2)*(xcM(i)/Rp*cosd(A5(n5,4)-
om)+ycM(j)/Rp*sind(A5(n5,4)-om))^3 ...
                            + A5(n5,3)*(xcM(i)/Rp*cosd(A5(n5,4)-
om)+ycM(j)/Rp*sind(A5(n5,4)-om)) ...
                            + A6(n6,1)*(xcM(i)/Rp*cosd(A6(n6,5)-
om)+ycM(j)/Rp*sind(A6(n6,5)-om))^6 ...
                            + A6(n6,2)*(xcM(i)/Rp*cosd(A6(n6,5)-
om)+ycM(j)/Rp*sind(A6(n6,5)-om))^4 ...
                            + A6(n6,3)*(xcM(i)/Rp*cosd(A6(n6,5)-
om)+ycM(j)/Rp*sind(A6(n6,5)-om))^2 ...
                            + A6(n6,4);
                    end
                end
            end
            % 3D plot of optimum velocity profile
            %   with order of polynomial chosen by the user
            figure(2*(nmax+1)+kert+2*as)
            surf(xcMM,ycMM,vmeanM+vslip)
            xlabel('x (m)')
            ylabel('y (m)')
            axis([-Rp Rp -Rp Rp])
            view([0,90])
            shading flat
            colorbar
            if kn == 1
                title('ERT grid - Axisymmetric')
            elseif kn == 2
                title('ERT grid - 1st order (linear)')
            elseif kn == 3
                title('ERT grid - 2nd order (quadratic)')
            elseif kn == 4
                title('ERT grid - 3rd order (cubic)')
            elseif kn == 5
                title('ERT grid - 4th order (quartic)')
            elseif kn == 6
                title('ERT grid - 5th order (quintic)')
            elseif kn == 7
                title('ERT grid - 6th order (sextic)')
            end

            % Save results to file vmean.out
            % Columns: 1-number of pixel, 2-x coordinate, 3-y coordinate, 4-
mean velocity
            % First 4 columns for max order of polynomial is np1;
            %   last 4 columns for max order of polynomial is np2
            % Pixel number increases from bottom to top and in columns from
left to right
            pixxyv(:,3+kert) = vmean';
            if qconc ~= 0
                if kert > 1
                    qconc = 1;
                end
                qvol(kert) = flowrate(qconc,fign,mh,Rp,vmean,alpm);
            end
        end
    end
end
```

```
save vmean.out pixxyv -ascii
if qconc ~= 0
    'Total water flow rate (m^3/h):'
    qvol*3600      % Water flow rate in m^3/h
end

% Write lowest (delopt) and highest (delfar) sums of differences 'SU' of
% measured and calculated potentials for each order of polynomial and
% the ratio of min sum of differences to sum of differences for each
% order of polynomial 'SUmin/SU'
for i=1:size(delopt,2)
    suminsu(i) = mindopt/delopt(i);
end
delopt
suminsu
```

Appendix B

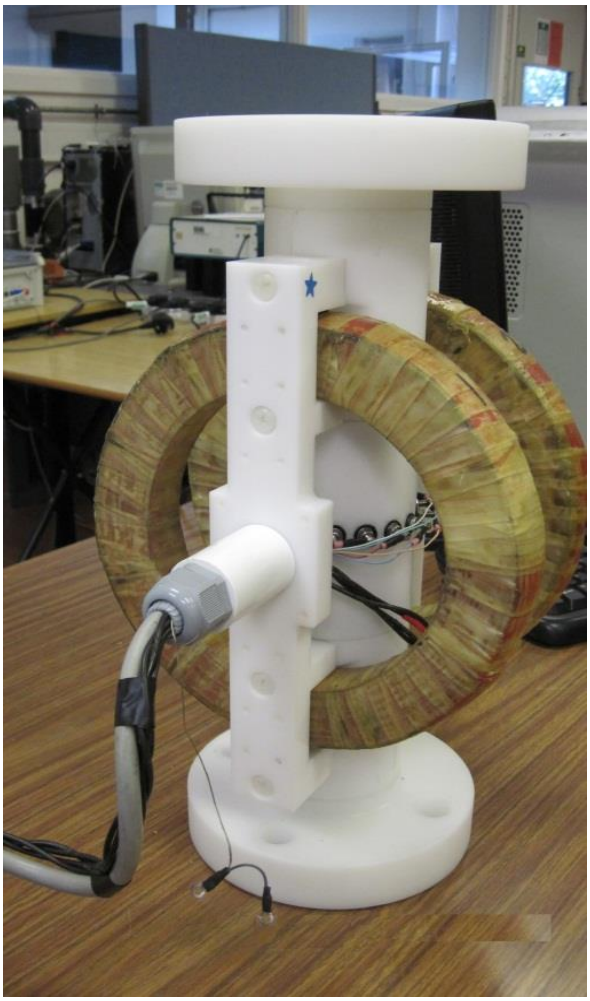

The flow meter body of the IFT device without casing

The flow meter body of the IFT device with casing

The IFT flow meter in the flow loop